
Multi-Method Chronometric Constraints on the Thermal, Structural and Morphotectonic Evolution of the Eastern and Western Sierras Pampeanas with Special Emphasis on K-Ar Dating of Fault Gouges

Dissertation

zur Erlangung des mathematisch-naturwissenschaftlichen Doktorgrades

„Doctor rerum naturalium“

der Georg-August-Universität Göttingen

im Promotionsprogramm Geowissenschaften

der Georg-August University School of Science (GAUSS)

vorgelegt von

Frithjof Alfons Bense

aus Braunschweig

Göttingen 2012

Betreuungsausschuss

Prof. Dr. Siegfried Siegesmund

Abt. Strukturgeologie and Geodynamik

Geowissenschaftliches Zentrum der Georg-August-Universität Göttingen

Dr. Klaus Wemmer

Abt. Isotopengeologie

Geowissenschaftliches Zentrum der Georg-August-Universität Göttingen

Mitglieder der Prüfungskommission

Referent: **Prof. Dr. Siegfried Siegesmund**

Geowissenschaftliches Zentrum der Georg-August-Universität Göttingen

Korreferent: **Dr. Georg Grathoff**

Abt. Ökonomische Geologie and Mineralogie

Institut für Geographie and Geologie der Ernst-Moritz-Arndt Universität Greifswald

Weitere Mitglieder der Prüfungskommission

Prof. Dr. Bent T. Hansen

Abt. Isotopengeologie

Geowissenschaftliches Zentrum der Georg-August-Universität Göttingen

Prof. Dr. Jonas Kley

Abt. Strukturgeologie and Geodynamik

Geowissenschaftliches Zentrum der Georg-August-Universität Göttingen

Prof. Dr. Sharon Webb

Abt. Experimentelle and Angewandte Mineralogie

Geowissenschaftliches Zentrum der Georg-August-Universität Göttingen

Dr. Klaus Wemmer

Abt. Isotopengeologie

Geowissenschaftliches Zentrum der Georg-August-Universität Göttingen

Tag der mündlichen Prüfung: 26/01/2013

Preface

The thesis presented here is part of the DFG project SI438/31-1, which is focused on the investigation of the thermochronological, structural and morphological evolution of the Sierras Pampeanas in central and northwest Argentina between 26°S and 34°S latitude.

Because of the sheer size of the study area being approximately 1000 x 500 km, a large number of samples to be prepared and analyzed and the complexity of the methodological tools involved, as well as the laborious and time-consuming sample preparation, the project has been handled collaboratively by two PhD students (Stefan Löbens 2012 and thesis presented here).

Where possible and/or reasonable, the methodological work was divided between colleagues. S. Löbens performed the apatite fission-track analyses, while the analysis and dating of fault gouges was my responsibility. (U-Th)/He dating was performed in a collaboration in which S. Löbens handled the apatite dating, while the zircon dating and mass spectroscopy was performed by me. Additionally, key aspects of the basic research goals were assigned to both of the theses. While the work of Löbens (2012) concentrates on the thermal history of the western and northern Sierras Pampeanas, the thesis presented here focuses on the thermal evolution of the Eastern as well as parts of the Western Pampean ranges (see Chapters 3-5 and 7). The main focal point is set on the investigation of gouge-bearing fault systems (Chapters 5 and 6). The focus of both theses is also well illustrated by the first-authorship of priorly published and submitted papers (see list below).

Structure of the Thesis

The Chapters 1 and 2 give a general introduction and methodological overview. Chapters 3 to 5 present and discuss the results of detailed thermochronological and geochronological studies. Each chapter is comprised of a brief introduction to its specific scope as well as a brief recapitulation of regional and geological aspects involved. Chapters 3 to 5 focus on individual mountain ranges of the southern Sierras Pampeanas and roughly follow a geographical line through the study area from the east to the west. Chapters 6 and 7 synthesize results from fault-gouge analyses and thermochronological investigations of the entire Sierras Pampeanas, also incorporating findings from Löbens (2012). Chapter 8 summarizes the most important conclusions drawn by this thesis. Finally, Chapter 9 gives a brief outlook on ideas for potential further studies raised within the scope of this study.

Chapter 1 gives a general introduction, elucidating the aims of this thesis as well as summarizing the regional geology and the current state of scientific knowledge of the geodynamic, morphotectonic and thermochronologic evolution of the Sierras Pampeanas.

Chapter 2 gives a methodological introduction to the thermochronological and chronological tools used. The principles of (U-Th)/He dating on zircon and apatite, apatite fission-track analyses and K-Ar illite fine-fraction dating are illustrated. An approach to forward and inverse modeling of thermochronological data is also elucidated.

Chapter 3 presents a study of the southern Sierra de Comechingones. It depicts thermochronological data from the Yacanto area as well as K-Ar illite fine-fraction ages from fault gouges in the Merlo area. Findings from both methods are interpreted and discussed in relation to established cooling and uplift scenarios. This chapter was written in collaboration with Stefan Löbens (see Löbens 2012).

Chapter 4 represents a study from the southern Sierra de San Luis. It presents thermochronological and fault-gouge analysis data from an elevation profile in the Nogolí area. Results are discussed regionally and, along with findings from the Sierra de Comechingones (Chapter 2), summarized in a morphotectonic model for the easternmost Pampean ranges. Additionally, thermochronological implications for the development of paleolandsurfaces are discussed. This chapter was written in collaboration with Stefan Löbens (see Löbens 2012).

Chapter 5 is focused on the thermal history of the Sierra de Pie de Palo, which represents the westernmost branch of the Sierras Pampeanas. Based on AFT and (U-Th)/He data, the thermochronological development of the Sierra de Pie de Palo is illustrated and discussed in a regional context. This chapter was written in collaboration with Stefan Löbens (see Löbens 2012).

Chapter 6 is dedicated to the analyses of gouge-bearing brittle fault zones in the Eastern Sierras Pampeanas. The data presented are derived from several methodological approaches, e.g. clay mineralogy, illite polytype quantification and K-Ar illite fine-fraction dating, as well as structural observations of gouge-bearing fault systems. In addition to data presented in Chapters 2 and 3, new data are presented from almost all ranges of the Eastern Sierras Pampeanas. Detailed discussion of results is focused on both regional and methodological aspects. The latter include a thorough review of existing K-Ar fault-gouge analysis concepts as well as a discussion of possibilities for cross-evaluation of illite ages with results from other methods, e.g. thermochronology, geochronology and illite mineralogy.

Chapter 7 presents new data from key positions in the Sierras Pampeanas, which allow us to extend the regional interpretations and thermal evolution models, discussed in Chapters 3 to 5, to the entire Pampean region. Results reveal significant differences in the Late Paleozoic to Neogene post-accretional cooling history between the northern, central and southern Pampeanas ranges. Spatially and timely differences in thermal history are illustrated and discussed in relation to main geodynamic and tectonic events as well as to established geological hypotheses. The results are condensed into a cooling and exhumation history model for the entire Sierras Pampeanas. This chapter was written in collaboration with Stefan Löbens (see Löbens 2012).

Chapter 8 thoroughly summarizes conclusions which can be drawn from results presented in the Chapters 3 to 7 concerning (a) the geological, thermochronological and morphological evolution of the Sierras Pampeanas and (b) methodological aspects and interpretational models of the K-Ar illite fine-fraction dating technique, as well as their significance in terms of dating brittle deformation events.

Chapter 9 presents a brief outlook, suggesting methodological approaches for further studies to (a) further constrain the low-temperature thermal history and morphotectonic evolution of the Sierras Pampeanas as well as (b) to further extend and evaluate the validity of illite fault-gouge analysis data.

This thesis incorporates the following publications and manuscripts:

- Löbens, S., Bense, F.A., Wemmer, K., Dunkl, I., Costa, C.H., Layer, P. and Siegesmund, S. (2011): Exhumation and uplift of the Sierras Pampeanas: preliminary implications from K–Ar fault gouge dating and low-T thermochronology in the Sierra de Comechingones (Argentina). *International Journal of Earth Sciences*, 100: 671-694.
- Löbens, S., Sobel, E.R., Bense, F.A., Wemmer, K., Dunkl, I. and Siegesmund, S. (2013): Refined thermochronological aspects of the Northern Sierras Pampeanas. *Tectonics*, 32(3): 453-472
- Bense, F.A., Wemmer, K., Löbens, S. and Siegesmund, S. (in press): Fault gouge analyses: K-Ar illite dating, clay mineralogy and tectonic significance – A study from the Sierras Pampeanas, Argentina. Submitted to the *International Journal of Earth Sciences*. DOI: 10.1007/s00531-013-0956-7
- Bense, F.A., Löbens, S., Dunkl, I., Wemmer, K., Costa, C.H. and Siegesmund, S. (in review): Exhumation history and landscape evolution of the southeastern Sierras Pampeanas, Argentina – a low-temperature multichronometer approach. Submitted to the *Journal of South American Earth Sciences*.
- Löbens, S., Bense, F.A., Dunkl, I., Wemmer, K. and Siegesmund, S. (in review): Thermochronological constraints of the exhumation and uplift of the Sierra de Pie de Palo, NW Argentina. Submitted to the *Journal of South American Earth Sciences*.
- Bense, F.A., Löbens, S., Dunkl, I., Wemmer, K., Siegesmund, S. (in review): Is the exhumation of the Sierras Pampeanas just related to Neogene flat-slab subduction? Implications from a multi-thermochronological approach. Submitted to the *Journal of South American Earth Sciences*.

Abstract

The thesis presented here is focused on the investigation of the thermochronological, structural and morphological evolution of the Eastern and Western Sierras Pampeanas in Argentina between 26°S and 34°S latitude.

Chapter 3 discusses results from K-Ar fault-gouge dating and low-temperature thermochronology (Apatite Fission Track, Zircon and Apatite (U-Th)/He) along two transects within the Sierra de Comechingones, as well as Ar-Ar ages from the San Luis Volcanic Belt (Eastern Sierras Pampeanas). Data reveal a minimum age for the onset of brittle deformation of about 340 Ma, very low exhumation rates since Late Paleozoic times and a total exhumation of about 2.3 km since the Late Cretaceous. New Ar-Ar ages (7.54–1.91 Ma) of volcanic rocks from the San Luis volcanic belt support the eastward propagation of the flat-slab subduction-related magmatic front, confirming the onset of flat-slab-related deformation in this region at 11.2 Ma. Although low-temperature thermochronology does not clearly constrain the signal of the Andean uplift, it is understood that the total amount of uplift due to the Andean deformation is possibly of more minor importance than previously assumed.

Chapter 4 presents the, as yet, first low-temperature thermochronological data as well as K-Ar ages from retrograde grown illite from brittle fault-gouges along one transect in the Sierra de San Luis (Eastern Sierras Pampeanas). K-Ar fault-gouge data reveal long-lasting brittle fault activity which started subsequent to the end of the Chanic orogenic cycle and the cessation of ductile deformation at around 320 Ma. Cooling of the samples below illite formation temperatures confines the youngest K-Ar illite ages to 222–172 Ma, representing the last illite forming event but not the end of brittle deformation. This stands in good accordance with the cooling history derived from the other thermochronometers used. Carboniferous K-Ar illite ages are interpreted in relation to an orogenic event. Thermochronological data derived from (U-Th)/He ages of apatite and zircon, as well as apatite fission-track dating, reveal an onset of exhumation in the transect studied during Permian times. Exhumation is possibly related to the San Rafael orogenic phase and dominated by slow cooling rates. Slow cooling and, thus, persistent residence of the samples in the partial annealing / retention zone temperature conditions of apatite and zircon (PRZ_A , PRZ_Z and PAZ_A) during cooling influenced the ages obtained. Final exhumation to surface temperatures is not well constrained but most likely happened during Jurassic or Late Cretaceous times. Published data for the evolution of the Sierra de San Luis and Sierra de Comechingones as well as the new data presented here are condensed in an evolutionary model, revealing significant differences in the cooling and deformation history of both ranges.

Chapter 5 illustrates the thermochronological evolution of the Sierra de Pie de Palo, a distinct basement range located in the Western Sierras Pampeanas. Integrated cooling histories constrained by apatite fission-track data and (U-Th)/He measurements of zircon and apatite reveal that the structural evolution of this mountain range commenced during the Late Paleozoic and was mainly controlled by tectonically triggered erosion. Although decelerated, exhumation controlled by erosion persisted on even during the Mesozoic. The present-day topography of the Pie de Palo range was generated by en-block uplift and related denudation during the earliest stage of the Andean deformation during the Late Mesozoic to Paleogene. Deformation associated with this event propagated from the east to west during this time interval. Since the Early Paleogene, total vertical block uplift has been about 3.7-4.2 km, while exhumation has been between 1.7-2.2 km with a rate of 0.03-0.04 mm/a. In contrast to previous assumptions, the amount of Late Pliocene uplift may be significantly lower in favor of Mesozoic to Paleogene uplift.

Chapter 6 introduces a method for the detailed interpretation of K-Ar illite fine-fraction ages of fault gouges from non-sedimentary host rocks. Ages derived from fault gouges are cross-evaluated with several independent parameters, e.g. illite crystallinity, illite polytype quantification, grain-size, mineralogical observations, K-Ar muscovite and biotite host-rock cooling ages, as well as low-temperature thermochronological data (Apatite Fission Track, Zircon and Apatite (U-Th)/He). This interpretation approach is applied in a regional study to constrain the "deformation path" of the Eastern Sierras Pampeanas in northwest Argentina. In the course of this study, a large number of gouge-bearing fault zones were analyzed and systematically sampled. The K-Ar illite fine-fraction ages obtained range from Devonian to Cretaceous times, documenting a long-lasting brittle fault activity in this region. Ages >320 Ma are synchronous with a period of wide-spread intra-Carboniferous compressional tectonism, whereas Permo-Triassic ages are contemporaneous to a flat-slab subduction episode of the Farallon plate beneath the South American plate. In addition, K-Ar illite ages reveal a propagation of brittle deformation from north to south in the Sierras de Córdoba and San Luis. Data integrity and consistency with other chronometers and geological evidence show that the interpretation suggested here is valid and can provide a powerful tool for the evaluation of cooling and deformation histories. Despite that, we were able to show that the reliability of fault-gouge data strongly depends on the regional thermal history.

Chapter 7 synthesizes thermochronological data from zircon and apatite (U-Th)/He as well as apatite fission-track dating from samples derived from the entire Sierras Pampeanas. Data reveal that cooling below 200°C commenced locally in Carboniferous times. During Permo-Triassic times, pronounced cooling in the southern Sierras Pampeanas propagated from east to west, being timely and spatially equivalent to a flat-slab subduction period at these latitudes. Mesozoic rifting, accompanied by sedimentation and burial re-heating, only locally affected ages obtained, suggesting

that substantial sedimentary thicknesses were only accumulated along the narrow and spatially restricted Cretaceous rift basins. Final cooling in the northern Pampean ranges occurred during the Neogene. In contrasting, cooling to near-surface temperatures occurred in the southern and southwestern Sierras Pampeanas between the Late Cretaceous and the Paleogene, supporting the idea that a positive topography already existed in these areas before the Cenozoic. This contradicts the previous hypothesis that the uplift of the Pampean ranges was entirely related to the Neogene flat-slab subduction. Instead, we suggest that this process merely accentuated a pre-existing relief built up by diachronously developed Mesozoic land surfaces. Calculated long-term denudation rates vary between 0.010 and 0.024 km/Ma, indicating stable conditions since at least Cretaceous times.

Kurzfassung

Die hier präsentierte Studie umfasst detaillierte Untersuchungen zur thermochronologischen, strukturellen sowie morphologischen Entwicklung der Östlichen und Westlichen Sierras Pampeanas in Argentinien, zwischen 26°S to 34°S südlicher Breite.

Kapitel 3 diskutiert thermochronologische Daten (Apatit Spaltspuren, Zirkon und Apatit (U-Th)/He) sowie K-Ar Illit-Datierung an Störungsletten aus der Sierra de Comechingones sowie Ar-Ar Alter an Vulkaniten des vulkanischen Gürtels von San Luis (Östliche Sierras Pampeanas). K-Ar Illitalter belegen den Beginn spröder Deformation vor etwa 340 Ma. Thermochronologische Daten dokumentieren geringe Exhumationsraten seit dem späten Paläozoikum sowie eine maximale Exhumierung von etwa 2,3 km seit der späten Kreidezeit. Ar-Ar Datierungen an vulkanischen Gesteinen des San Luis Vulkanischen Gürtels ergeben Alter zwischen 7,54 Ma und 1,91 Ma. Dies belegt ein ostwärts gerichtetes Fortschreiten der magmatischen Front, welches mit einer Verflachung des Subduktionswinkels der Nazca Platte unter die Südamerikanische Platte vor etwa 11.2 Ma assoziiert wird. Darüber hinaus deuten die hier präsentierten thermochronologischen Daten an, dass der Anteil Andiner Exhumation und Hebung an der Gesamthebung und Exhumation der Sierras Pampeanas von geringer ist als gemeinhin angenommen.

Kapitel 4 präsentiert Ergebnisse von Niedrig-Temperatur thermochronologischen Untersuchungen sowie K-Ar Alter retrograd gewachsener Illite aus spröden Störungszonen der Sierra de San Luis (Östliche Sierras Pampeanas). K-Ar Illitalter belegen eine lang andauernde Aktivität spröder Deformation welche unmittelbar nach dem Ende der Chanic Phase der Famatinischen Orogenese vor etwa 320 Ma einsetzte und zeitlich mit dem Übergang von duktilen zu spröden Deformationsmechanismen übereinstimmt. Jüngste Illitalter liegen zwischen 222-172 Ma. Diese können als Abkühlalter des Grundgebirges unter die zur Illitbildung benötigten Temperaturen interpretiert werden, jedoch nicht als Ende der spröden Deformation. Diese Interpretation wird von den Ergebnissen thermochronologischer Untersuchungen bestätigt. (U-Th)/He Datierungen an Apatiten und Zirkonen, sowie Apatit Spaltspuranalysen dokumentieren die Exhumation seit dem Perm, welche möglicherweise in Verbindung zur San Rafael Orogenese steht. Die ermittelten Abkühlalter belegen geringe Exhumationsraten sowie die damit einhergehende lange Verweildauer der Proben in den Temperaturbereichen der partial annealing bzw. parial retention zone von Apatit und Zirkon (PRZ_A , PRZ_Z und PAZ_A). Die finale Abkühlung auf Oberflächentemperaturen fand im Verlauf des Jura und der späten Kreide statt. Die Abkühlgeschichten der Sierra de San Luis und Sierra de Comechingones werden in einem Entwicklungsmodell zusammengefasst, welches signifikante Unterschiede in der thermischen Entwicklung beider Gebirgszüge offenbart.

Kapitel 5 diskutiert die thermochronologische Entwicklung der Sierra de Pie de Palo, einem ausgeprägten Höhenzug in den Westlichen Sierras Pampeanas. Thermochronologische Untersuchungen zeigen, dass die strukturelle Entwicklung der Sierra Pie de Palo bereits im späten Paläozoikum einsetzte und von jeher durch tektonisch kontrollierte Erosion geprägt wurde, welche sich im Verlauf des Mesozoikums aufgrund extensionaler Tektonik zwar verlangsamte, jedoch andauerte. Die heutige Topographie des Gebirgszuges bildete sich im Zuge Andiner Kompression im Verlauf des Späten Mesozoikums und Paläogens durch die Hebung und damit einhergehender Denudation einzelner Grundgebirgsblöcke. Die mit der Hebung assoziierte Deformation schritt dabei von Ost nach West voran. Der Gesamtbetrag vertikaler Hebung seit dem frühen Paläozoikum kann auf ca. 3,7-4,3 km eingegrenzt werden, wobei die Gesamtexhumation etwa 1,7-2,2 km bei einer Exhumationsrate von 0,03-0,04 mm/a beträgt.

Kapitel 6 stellt eine Methode zur Interpretation von K-Ar Illit Feinfraktionsaltern aus Störungsletten aus nichtsedimentären Gesteinen vor. Gemäß der vorgestellten Methode werden die ermittelten K-Ar Illitalter in Kombination mit den Untersuchungsergebnissen unabhängiger Parameter, z.B. Illitkristallinität, Illit-Polytypie und Polytyp-Quantifizierung, Korngröße, Tonmineralogie, K-Ar Abkühlaltern des Nebengesteins sowie mit Ergebnissen thermochronologischer Untersuchungen (AHe, ZHe, AFT) evaluiert. Dieser Interpretationsansatz wird im Rahmen einer regionalen Studie innerhalb der Östlichen Sierras Pampeanas exemplarisch angewandt. Im Zuge dessen wurde eine große Zahl von Störungsletten systematisch beprobt und analysiert. Ermittelte K-Ar Illitalter decken die Zeitspanne vom Devon bis in die Kreidezeit und dokumentieren eine lang anhaltende Phase bruchhafter Deformation in der Region. Alter >320 Ma sind synchron mit einer Periode kompressiver intra-Platten Tektonik, während Permische und Triassische Alter mit einer Periode flacher Subduktion der Farallon Platte unter die Südamerikanische Platte assoziiert werden können. Darüber hinaus belegen die K-Ar Illitalter ein von Nord nach Süd Fortschreiten der spröden Deformation in den Sierras de San Luis und Comechingones. Die Integrität und Konsistenz der analysierten Daten belegt die Leistungsfähigkeit und tektonische Signifikanz der hier vorgestellten Methode, welche somit einen bedeutenden Beitrag zur Entschlüsselung komplexer Abkühlungs- und Deformationsereignisse bieten kann. Jedoch kann gezeigt werden, dass die Aussagekraft der hier vorgestellten Methode stark von der Abkühlgeschichte des Untersuchungsgebietes abhängt.

Kapitel 7 präsentiert thermochronologische Daten aus den gesamten Sierras Pampeanas. Darüber hinaus werden alle verfügbaren thermochronologischen und geochronologischen Daten zur Abkühlgeschichte der Sierras Pampeanas diskutiert und in ein Abkühlmodell zusammengefasst. Die Daten belegen eine Abkühlung unter 200°C im Verlauf des Karbons. Im Verlauf des Perms und der Trias schritt die Abkühlung von West nach Ost fort, räumlich und zeitlich einhergehend mit dem Fortschreiten eines flachen Subduktionsereignisses der Farallon-Platte unter die heutige

Südamerikanische Platte. Mesozoische Riftereignisse und damit einhergehende Sedimentation und Versenkung zeigen nur lokal Einfluss auf die ermittelten Abkühlalter. Dies deutet darauf hin, dass die zum Verlust der Altersinformation der thermochronologischen Systeme notwendige Versenkungstiefen nur entlang der schmalen, räumlich eingeschränkten Kretazischen Riftbecken erreicht werden. Die finale Abkühlung auf Oberflächentemperaturen verlief diachron in den nördlichen und südlichen Sierras Pampeanas. So können im Norden Neogene Alter beobachtet werden, während die südlichen und westlichen Sierras Pampeanas spätestens seit der Kreide bzw. frühen Paleogens auf Oberflächentemperaturen abgekühlt waren. Letzteres deutet auf die Existenz einer positiven Topographie in den südlichen Sierras Pampeanas, bereits vor dem Einsetzen Cenozoischen Andinen Kompression und der im Neogenen einsetzenden flachen Subduktion der Nazca-Platte hin. Dies wiederum widerspricht der allgemein akzeptierten Hypothese, dass die Exhumation und Hebung der Sierras Pampeanas allein mit der Neogenen flachen Subduktion der Nazca-Platte in Verbindung stehen. Im Gegensatz dazu wird vorgeschlagen, dass diese Neogenen Prozesse lediglich zu einer Überprägung und Akzentuierung des bereits existierenden Reliefs führten. Diese Vermutung kann durch die Berechnung auffallend niedriger Denudationsraten in den Östlichen und Westlichen Sierras Pampeanas von 0,010-0,024 km/a gestützt werden, welche auf stabile Bedingungen, zumindest seit der späten Kreidezeit, hindeuten.

Table of Contents

Preface	i
Abstract.....	iv
Kurzfassung.....	vii
Table of Contents	x
1 General Introduction.....	1
1.1 Aims of the Thesis	1
1.2 Geographical Overview and Location of the Study Area	4
1.3 Paleozoic to Mesozoic Geodynamic Evolution of the Sierras Pampeanas.....	8
1.4 Cenozoic Geodynamic Evolution	12
1.5 Neotectonic Activity	16
1.6 Recent Crustal Deformation	17
1.7 Low-Temperature Thermochronology	17
2 Methodology	20
2.1 (U-Th)/He Thermochronometry	20
2.1.1 Introduction.....	20
2.1.2 Principles of Application	22
2.1.3 Analytical Procedure	24
2.2 Apatite Fission Track Thermochronology.....	25
2.2.1 Introduction.....	25
2.2.2 Principles of Application	26
2.2.3 Principles of Application	28
2.2.4 Analytical Procedure	29
2.3 Thermal Modeling	29
2.4 K-Ar Illite Fine-Fraction Dating	30
3 The Sierra de Comechingones.....	32
3.1 Introduction.....	32
3.2 Regional Setting and Geodynamic Evolution	33
3.3 Applied Methods	36
3.3.1 Mineralogy and K-Ar Dating of Fault Fougues.....	36
3.3.2 Apatite Fission Track and (U-Th)/He Thermochronology.....	38
3.3.3 Ar-Ar Dating of Volcanic Rocks	38
3.4 Results	38
3.4.1 K-Ar Dating	38

3.4.2	Zircon (U-Th)/He Ages	40
3.4.3	Apatite Fission Track Ages	41
3.4.4	Apatite (U-Th)/He Ages	42
3.4.5	Ar-Ar Dating.....	43
3.5	Discussion	44
3.5.1	Constraints on Regional Cooling and Fault Activity by K-Ar Dating	44
3.5.2	Thermal Modeling	49
3.5.3	AFT and AHe Ages.....	50
3.5.4	Low Temperature Exhumation Model	51
3.5.5	Ar-Ar Data on the Age of Volcanic Activity.....	52
3.6	Conclusions.....	54
4	The Sierra de San Luis	55
4.1	Introduction.....	55
4.2	Geologic and Morphotectonic Setting	57
4.3	Post-Metamorphic Cooling History	60
4.4	Applied Methods	60
4.4.1	Mineralogy and K-Ar Dating of Fault Gouges	60
4.4.2	Thermochronology	64
4.5	Results	64
4.5.1	K-Ar Dating	64
4.5.2	Illite Polytypism and Illite Crystallinity	68
4.5.3	Zircon (U-Th)/He Ages	69
4.5.4	Fission Track Ages.....	69
4.5.5	Apatite (U-Th)/He Ages	70
4.6	Discussion	71
4.6.1	Brittle Fault Activity Constrained by K-Ar Ages	71
4.6.2	Thermal Modeling	74
4.6.3	Evolution Model	76
4.6.4	Regional Constraints.....	81
4.7	Conclusions.....	82
5	The Sierra de Pie de Palo.....	87
5.1	Introduction.....	87
5.2	Geologic Setting.....	88
5.3	Applied Methods	91
5.4	Results	92

5.4.1	Zircon (U-Th)/He Ages	92
5.4.2	Apatite Fission-Track Analyses	92
5.4.3	Apatite (U-Th)/He Ages	92
5.5	Discussion	94
5.5.1	Thermal Modeling	94
5.5.2	General Structural Evolution of the Sierra de Pie de Palo.....	94
5.5.3	Internal Structure and Related Exhumation.....	99
5.5.4	Cenozoic Thermal Evolution and Amount of Exhumation	100
5.6	Conclusions.....	101
6	Fault Gouge Analyses	102
6.1	Introduction.....	102
6.2	Geological Setting.....	103
6.3	Methodology	105
6.3.1	Sample Preparation	105
6.3.2	Analytical Methods and Procedures	105
6.4	Results	107
6.4.1	Gouge-Bearing Faults Systems	107
6.4.2	Fault Gouge Analyses	112
6.5	Discussion	117
6.5.1	Fault Zones Orientations and Paleostress	117
6.5.2	Mineralogical Observations.....	119
6.5.3	K-Ar Fault Gouge Dating	120
6.5.4	Illite Crystallinity	120
6.5.5	Illite Polytypism and Interpretation of 2M ₁ Illite.....	121
6.5.6	Age Constraints on Brittle Deformation in the Sierras Pampeanas	124
6.5.7	Implications on Regional Cooling, Deformation History and Tectonic Significance ...	130
6.6	Conclusions.....	132
7	Synthesis of Thermochronological Data	139
7.1	Introduction.....	139
7.2	Regional Geology of the Sierras Pampeanas.....	140
7.3	Methodology	142
7.4	Results	142
7.4.1	Zircon (U-Th)/He Ages	142
7.4.2	Apatite (U-Th)/He Ages	143
7.4.3	Apatite Fission-Track Ages.....	143

7.5	Discussion	146
7.5.1	Thermal Modeling	146
7.5.2	Thermal Evolution of the Basement Ranges	153
7.5.3	Spatial and Temporal Variability of Cooling	158
7.5.4	Paleosurfaces and Denudation Rates.....	160
7.5.5	Comparison of the Northern and Southern Pampean Ranges.....	163
7.6	Conclusions.....	165
8	General Conclusions.....	166
9	Outlook	175
10	References	176
	Acknowledgment	191

1 General Introduction

1.1 Aims of the Thesis

The main objectives of this thesis are twofold: on one hand, to contribute to scientific research on the geological, thermochronological and morphological evolution of the southwestern and eastern Sierras Pampeanas and, on the other hand, to evaluate the tectonic significance of K-Ar illite fine-fraction ages from fault gouges in order to date fault formation, activity and reactivation (Fig. 1.1).

More specific objectives are:

- (1) *Determining the time-space disaggregation of the Late Paleozoic to Paleogene post-accretional cooling history of the Sierras Pampeanas.*

The high temperature cooling history of the Eastern Sierras Pampeanas, which has been examined in detail in several other investigations (e.g. Steenken et al. 2004, 2008, 2010), should be extended to a low-temperature cooling branch (Fig. 1.1). In particular, the repeated change from extensional to compressional settings since Late Carboniferous times (see Chapter 1.3.) should be correlated with thermochronological and geochronological findings. Results should also be brought into a regional context by evaluating established concepts of the regional evolution of the Sierras Pampeanas.

- (2) *The identification of a potential modification in the exhumation and uplift history since Neogene times.*

It is proposed that the incorporation of the Juan-Férrandez Ridge into the subduction of the Nazca plate beneath the South American Plate in Neogene times resulted in a southward-propagating flat-slab subduction segment beneath the Pampean region between approximately 27°S and 33°S. It is assumed that the latter led to uplift and exhumation of the Pampean ranges (e.g. Ramos et al. 2002; see also Chapter 1.4). This modification should be traced using thermochronological methods (apatite fission-track analysis and (U-Th)/He dating) and discussed in relation to established concepts and the regional framework (Fig. 1.1). Aside from locations above the flat-slab segment, samples were collected from adjacent areas to the north and south, where normal subduction persisted (Fig. 1.2). Evaluation of thermochronological data from both flat and steep-subducting slabs should provide valuable information about any flat-slab subduction influence on the exhumation and uplift of the Pampean ranges. If the flat-slab exhumation and uplift scenario cannot be confirmed, alternative scenarios should be proposed.

- (3) *Improvement of knowledge on the formation time of erosional surfaces in the Pampean ranges as well as confining the existence of a pronounced positive relief in the eastern Sierras Pampeanas in pre-Cenozoic times.*

Especially in the eastern Sierras Pampeanas, several extensive erosional surfaces have developed, e.g. in the Pampa de Achala in the Sierra de Córdoba (Fig. 1.4). Until now, the timing of formation of these surfaces has not been well understood and is a matter of ongoing debate. Two main scenarios have been proposed: (1) Erosional surfaces are the result of Neogene processes in relation to Andean compression and flat-slab subduction and, thus, represent an initial synchronous surface which nowadays is juxtaposed with Neogene faults and (2) erosional surfaces represent a diachronous surface, developed due to multiple erosional events since Late Paleozoic / Early Mesozoic times (Fig. 1.1; e.g. Carignano et al. 1999; Rabassa et al. 2010; see also Chapter 1.4). The latter idea additionally raises the question of to what extent a positive relief may have developed in pre-Cenozoic times before Andean compression and flat-slab subduction began, which are generally interpreted to have caused the uplift of the Pampean ranges in Neogene times (see Chapter 1.4).

- (4) *Analysis of gouge-bearing fault systems and the evaluation of the brittle deformation activity in the Eastern Sierras Pampeanas as revealed by K-Ar illite fine-fraction dating on clay gouges.*

The Sierras Pampeanas have been affected by brittle deformation processes since Carboniferous times (see Chapters 4 and 6). Deformation is accommodated by numerous faults, of which most exhibit well developed clay gouges. The large number of gouge-bearing faults as well as good exposure conditions make the area an excellent testing ground for the exemplarily evaluation of data derived from fault-gouge analyses in terms of its tectonic significance (see Chapters 4 and 6).

- (5) *Development of concepts to constrain K-Ar illite fine-fraction ages by integrating results from clay mineralogy, thermochronology and geochronology, as well as the evaluation of its tectonic significance in terms of gouge formation and fault activity.*

In order to constrain the timing of brittle deformation in the Sierras Pampeanas, a method for the detailed interpretation of the K-Ar illite fine-fraction ages of fault gouges from non-sedimentary host rocks should be introduced. Ages should be cross-evaluated with several independent parameters, e.g. illite crystallinity, illite polytype quantification, grain-size, mineralogical observations, K-Ar muscovite and biotite host-rock cooling ages, as well as low-temperature thermochronological data (apatite fission-track, (U-Th)/He on zircon and apatite) to evaluate their tectonic significance (Fig. 1.1, see also Chapters 4 and 6).

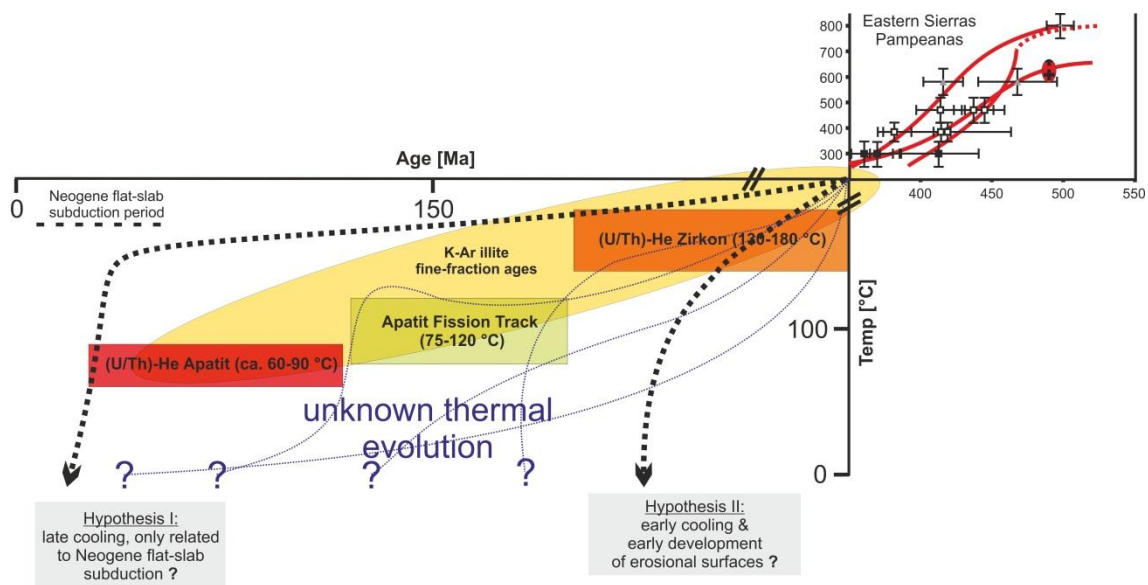


Fig. 1.1: Schematic sketch illustrating the multichronometrical approach and summarizing the main topics of the here presented thesis. As continuation to the high temperature cooling history (upper right; modified from Steenken et al. 2004, 2008, 2010) the low-temperature thermal evolution of the Sierras Pampeanas should be investigated. The thermal history below 300°C is unknown until now (blue and black lines). To illustrate the possible span of plausible low-temperature cooling histories, two contrasting hypotheses are formulated (black lines); 1) the exhumation and cooling of the Sierras Pampeanas is entirely related to a Neogene flat-slab subduction event and 2) The exhumation and cooling of the Sierras Pampeanas is substantially older, maybe of Mesozoic age. In order to decipher the real time-temperature path (a path between the black lines) the displayed methods will be used, each with a different temperature sensibility, which will allow the evaluation of cooling through time. Additionally K-Ar illite dating from brittle fault gouges will be performed in order to evaluate the timing of brittle deformation in the Sierras Pampeanas, subsequent to the cooling of the basement below ductile deformation temperatures (approximately 300°C).

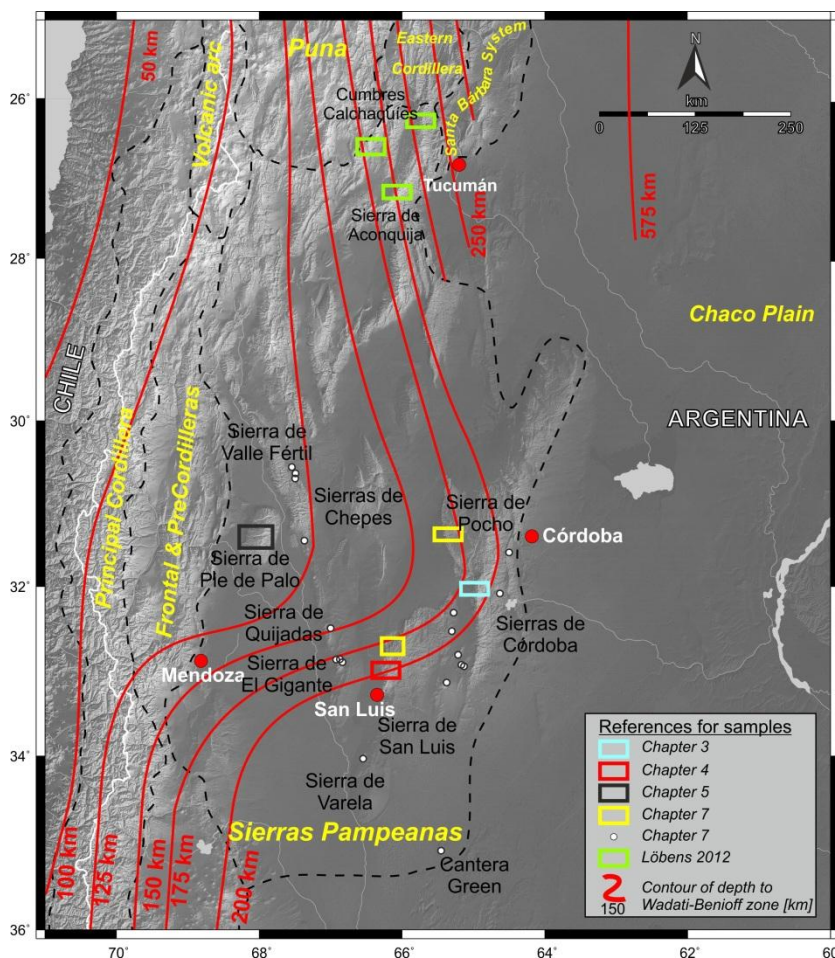


Fig. 1.2: Location of sampled profiles (marked by rectangles) and single locations (white circle). Contours show depth of Wadati-Benioff zone, indicating the position of the Pampean flat-slab segment beneath the Sierras Pampeanas. In order to evaluate any influence of the flat-slab subduction episode on the low-temperature thermal evolution of the Sierras Pampeanas samples were collected within the central zone of flat-slab (i.e. northern and central Sierra de San Luis and Sierras de Comechingones and Pocho, see Chapters 3, 4 and 7), as well as to the north and south of flat-slab, were normal subduction persists (i.e. Sierra de Aconquija and Cumbres Calchaquies and Sierra de Varela and Gantera Green; see Chapter 7 and Löhens (2012). Contour of depth to the seismic slab after Cahill and Isacks (1992).

1.2 Geographical Overview and Location of the Study Area

The study area of the Sierras Pampeanas is located in central and northwestern Argentina between 26°S and 34°S latitude and comprises an area of approximately 1000 x 500 km (Fig. 1.3). The Sierras Pampeanas are represented by several individual, north-south trending mountain ranges which show elevations of up to 5,550 m (Fig. 1.3; e.g. González Bonorino 1950; Caminos 1979; Jordan and Allmendinger 1986; Ramos et al. 2002).

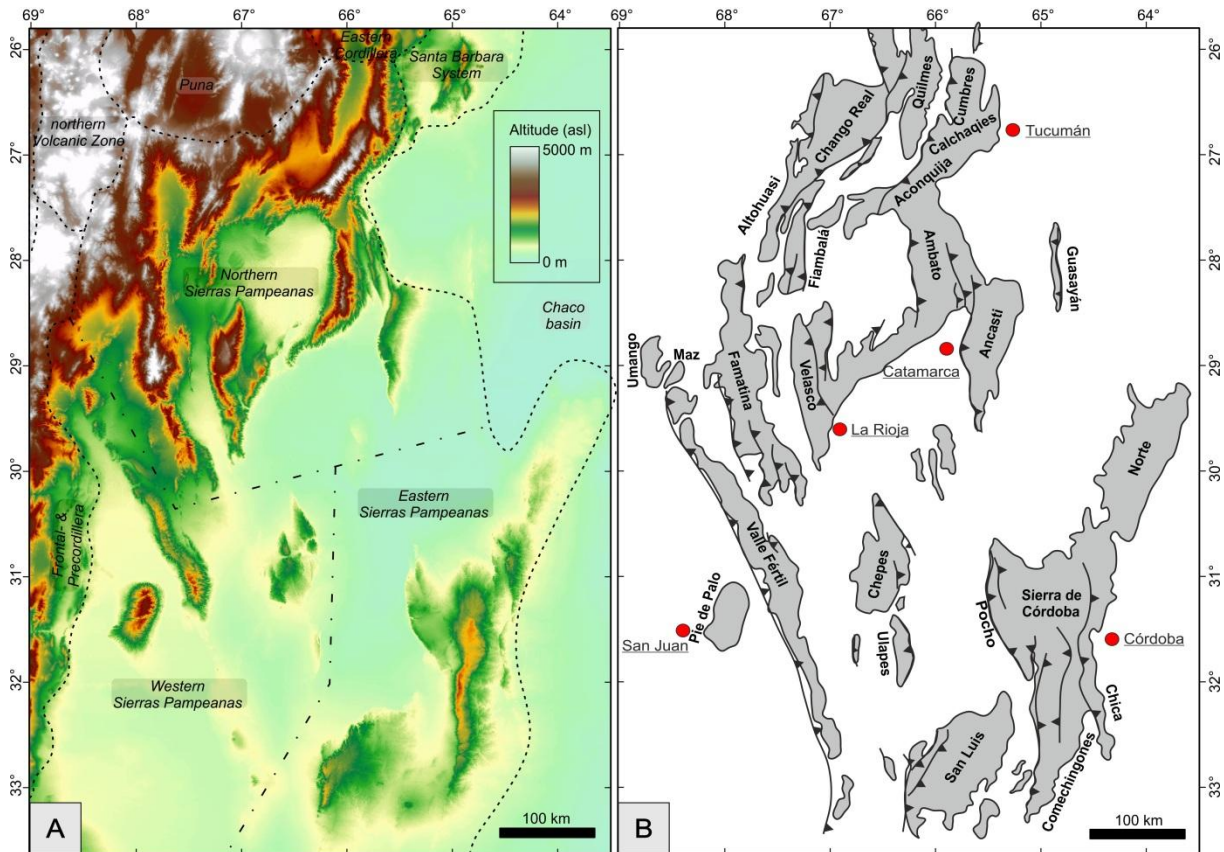


Fig. 1.3: Hypsographic map of the SP. They are divided into two main regions, the northwestern mountains reaching heights above 3500 m a.s.l. and the eastern mountains, showing heights below 3000 m a.s.l. A) Digital elevation model illustrating the topography of the Pampean ranges. Outline of morphotectonic provinces according to Hilley and Coutand (2010). B) Schematic map of individual Pampean basement-block uplifts and associated bounding faults. Major fault vergence based on González Bonorino (1950) and Jordan and Allmendinger (1986).

The Pampean ranges correspond to thirteen major basement block uplifts, comprising a distinct morphotectonic domain east of the Central Cordillera and south of the Puna Plateau (Fig. 1.3 and 1.4). In general, these basement blocks consist of Late Pre-Cambrian to Early Paleozoic metamorphic and igneous rocks, which are surrounded by intermountain sedimentary basins of flat topography that widely crop out in central-western Argentina, e.g. the Chaco-Paraná-basins in the east and the Las Salinas and Bermejo basins in the west (e.g. González Bonorino 1950; Caminos 1972; Jordan et al. 1983; Gordillo and Lencinas 1979; Jordan and Allmendinger 1986; Milani and Thomaz Filho 2000; Ramos et al. 2002; see also Chapter 1.3). The individual mountain ranges of the Sierras Pampeanas show a strong topographic asymmetry represented by a steep western and a gentle eastern slope (Figs. 1.4 b,c,d and 3.2). Observed asymmetry has been linked to Neogene uplift along bounding

reverse faults which are commonly located at their steeply dipping western side (Fig. 1.3; e.g. González Bonorino 1950; Jordan and Allmendinger 1986). The gently dipping eastern slope is usually characterized by the remains of Paleosurfaces, which have traditionally been envisaged as a continuous and essentially synchronous surface, exhumed and disrupted during the Andean Orogeny (e.g. González Díaz 1981; Criado Roque et al. 1981). In contrast, more recent studies suggested that, at a regional scale, these erosion surfaces are diachronous in age, formed by several events in Late Paleozoic to Paleogene times (Jordan et al. 1989; Carignano et al. 1999, see also Chapters 4.6.3 and 7.5.4). Previous researchers divided the Pampean mountain ranges into the northern, western and eastern Sierras Pampeanas (Caminos 1973; 1979, Dalla Salda 1987). Within this context, the basement blocks of the Sierra de San Luis and Sierra de Córdoba (with the Sierras de Norte, Pocho (Fig. 1.4 f,g), Grande, Chica and Comechingones; see Fig. 1.3), representing the southernmost expressions of the Pampean ranges, are part of the Eastern Sierras Pampeanas (Fig. 1.3). In the Eastern Sierras Pampeanas, peak elevations of 2200 m to 2400 m a.s.l. are observed in the Sierras de San Luis and Córdoba, towering over the adjacent basins with nearly 2000 m. The Western Sierras Pampeanas (Fig. 1.3) comprise the Sierras de Pie de Palo (Fig. 1.4 j,k) and Valle Fértil, which reach altitudes of 3400 m a.s.l., rising above the adjacent basins >2500 m. The Sierras de Chango Real, Aconquija, Ambato, Ancasti, Famatina, Fiambalá, Quilmes and Velasco represent the northern Sierras Pampeanas (Fig. 1.3), where elevations above 3500 m a.s.l. are realized.



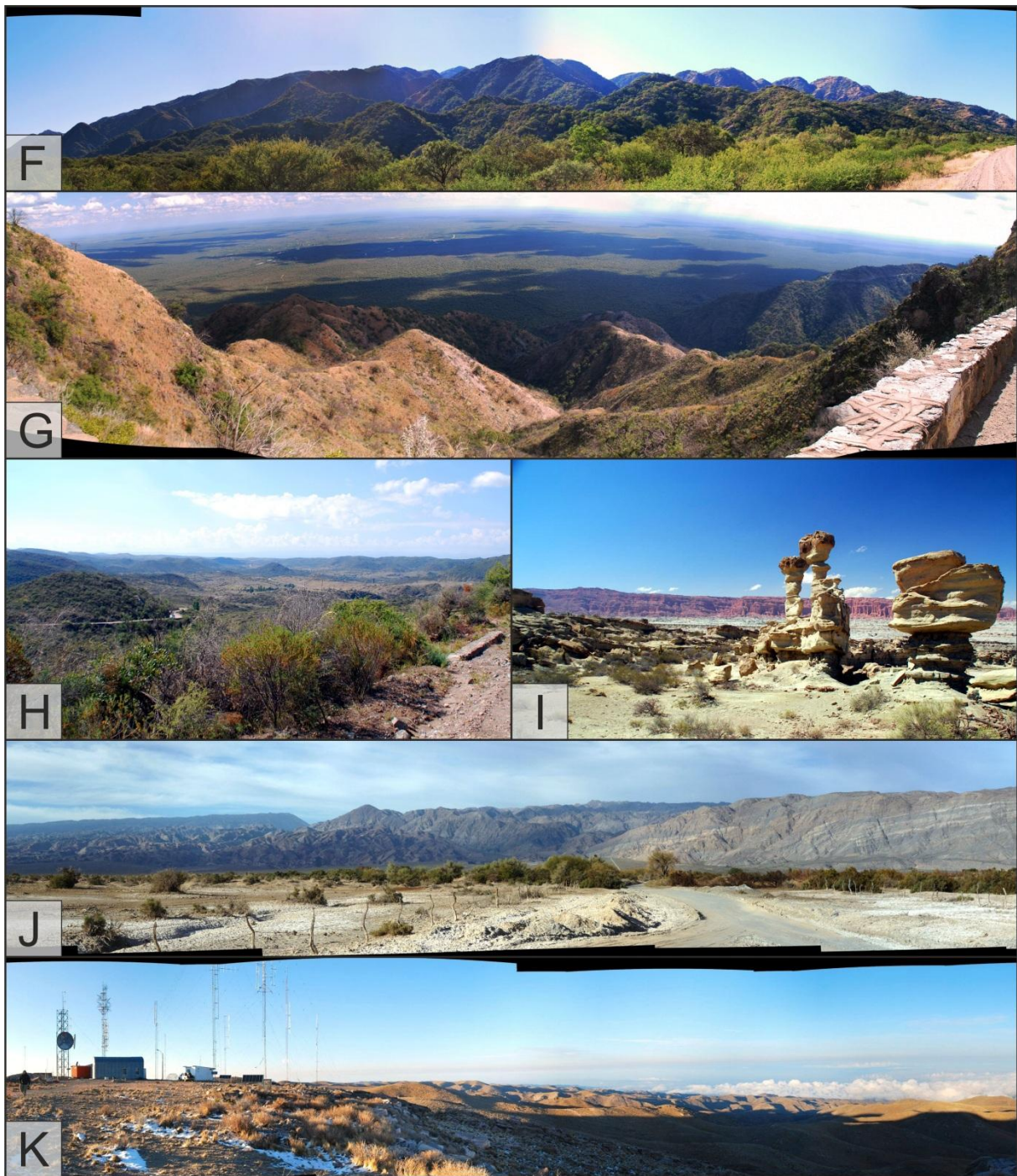


Fig. 1.4: Photos show the topographical and morphological inventory of the Eastern and Western Sierras Pampeanas. A-F: Sierra de San Luis; F-H: Sierra de Pocho; I: Sierra de Valle Fértil; J-K: Sierra Pie de Palo. A) View from the western footslope of the Sierra de San Luis (Nogolí area) towards the west, Nogolí river in foreground. In the far background in the upper right corner is the Sierra del Gigante. View up (B) and down (C) the fault-facing slope of the Sierra de San Luis, illustrating the strong topographic asymmetry of the Pampean ranges. D and E) low-inclined fault-averted side of the Sierra de San Luis. E) Cenozoic volcanoes of the San Luis Volcanic Belt in the background. Sierra de Pocho, view up- (F) and downhill (G). H) Sierra de Pocho, view towards the east along the flat dipping, fault-averted side. I) Remnant of Triassic sediments in the Valle de La Luna, northern Sierra de Valle Fértil. J) Southwestern Sierra de Pie de Palo. K) Top of the Sierra de Pie de Palo.

1.3 Paleozoic to Mesozoic Geodynamic Evolution of the Sierras Pampeanas

The metamorphic, magmatic and structural history of the Eastern and Western Sierras Pampeanas is the result of several accretional phases. Accretion occurred from Late Proterozoic to Devonian times and corresponds with the docking of different allochthonous and parautochthonous terranes along the southwestern continental margin of Gondwana. According to the terranes involved, these phases can be divided into the Pampean, Famatinian and Achaian cycles (e.g. Ramos 1988; Rapela et al. 1998; Sims et al. 1998; Astini and Thomas 1999; Astini and Dávila 2004; Steenken et al. 2004; 2006, Miller and Söllner 2005). Potential sutures indicate the margins of adjacent terranes, e.g. between the Río de la Plata Craton and the Pampia, Famatina and Cuyania terranes (Fig. 1.5).

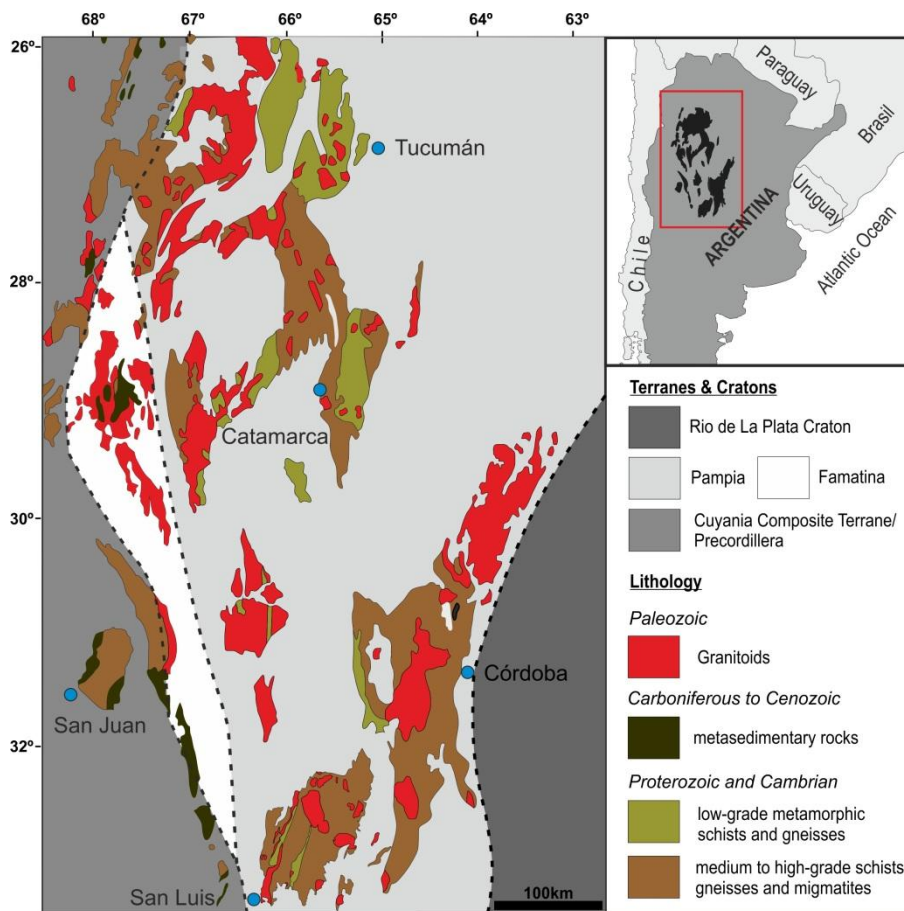


Fig. 1.5: Simplified geological sketch map of the Sierras Pampeanas. Dashed lines indicate inferred position of Precambrian terrane boundaries (modified according to Ramos 2010, based on van Gosen 1998).

Post-accretional basement cooling in the eastern and western Sierras Pampeanas is traced by Ar-Ar and K-Ar cooling ages (see also Figs. 1.1 and 8.1). In general, high-temperature cooling propagated from the east to west (e.g. Steenken et al. 2004, 2010). In the Sierra de Córdoba, Ar-Ar ages from Muscovite document passage through Ar-retention temperatures (ca. 400°C; McDougal and Harrison 1999) in Cambrian times (500-480 Ma; Krol and Simpson 1999; Martino et al. 2007). Subsequent cooling is documented by Ar-Ar and K-Ar biotite cooling ages, recording passage through temperatures between 350°C and 300°C, respectively (McDougal and Harrison 1999; Willigers et al. 2001), in Ordovician to Silurian times (480-420 Ma; Krol et al. 2000, Martino et al. 2007). In the more western Sierras de San Luis and Chepes, passage through Ar-retention temperatures occurred in

Ordovician to Devonian times (460-380 Ma; Sims et al. 1998; Steenken et al. 2004, 2007a). The youngest K-Ar biotite ages even yield Early Carboniferous ages (Steenken et al. 2004, 2010). Those differences in thermal evolution between the eastern (Sierra de Córdoba) and western (Sierras de San Luis and Chepes) basement domains were caused by differential movement. The latter was accommodated by westward thrusting along ~north-south-striking crustal shear zones, developed during the Famatinian Orogenic cycle, e.g. in the most western parts of the Sierra de Córdoba (Fig. 1.6; Whitmeyer and Simpson 2003, 2004; Simpson et al. 2003; Martino 2003). Ar-Ar and K-Ar muscovite ages of mylonites from these shear zones indicate that deformation persisted until the Late Devonian (Krol and Simpson 1999; Martino et al. 2005). In addition, K-Ar-dating on Illite fine-fraction ages from phyllitic rocks of the San Luis Formation (Sierra de San Luis; Fig. 1.6) indicates that differential movement between basement blocks were reactivated in Carboniferous to Permian times (Wemmer et al. 2011). The authors note that ages are synchronous to a widespread period of intra-Carboniferous compressional tectonism, e.g. the Toco Orogeny of Bahlburg and Breitzkreuz (1991). The latter defines a compressional tectonic phase expressed, for example, by a hiatus between Lower Carboniferous (Mississippian) and Permian sequences of the Paganzo Formation (e.g. Bahlburg and Breitzkreuz 1991).

In the Late Paleozoic, the Paganzo basin was formed due to the final orogenic collapse and extension as a consequence of Early Paleozoic mountain building (Salfity and Gorustovic 1983; Mpodozis and Ramos 1989; Ramos et al. 2002). Sediments of the Paganzo basin were widely developed in northwest Argentina (Fig. 1.7; e.g. Gonzalez and Aceñolaza 1972), comprising mainly Carboniferous alluvial sediments, tillites, claystones and lacustrine sediments which are overlain by Lower Permian (Cisuralian) arid to semi-arid aeolian sequences (Limarino and Césari 1988; Césari and Guitiérrez 2000; Limarino et al. 2002; Martins-Neto et al. 2007). Additionally, relicts of alkaline volcanism are associated with the formation of the Paganzo basin (e.g. Ramos et al. 2002).

In the northern Sierras Pampeanas, the maximum accumulated thickness of Paganzo strata is about 1800 m (Azcuy 1999), while, in the study region, the record of Paganzo strata is scarce. Trapped and preserved sedimentary records of this time period can be found in minor outcrops at the foot of the Sierra de Pocho and the Sierra de Chepes, as well as in the Bajo de Veliz region in the northeastern Sierra de San Luis (Fig. 1.7 and 1.8; Hünicken and Penza; 1980; Hünicken et al. 1981; Limarino and Spalletti 2006). The latter region is also considered to represent the southeasternmost branch of the Paganzo basin (Fig. 1.7; e.g. Fernandez-Seveso and Tankard 1995; Césari and Guitiérrez 2000; Limarino and Spalletti 2006; Martins-Neto et al. 2007).

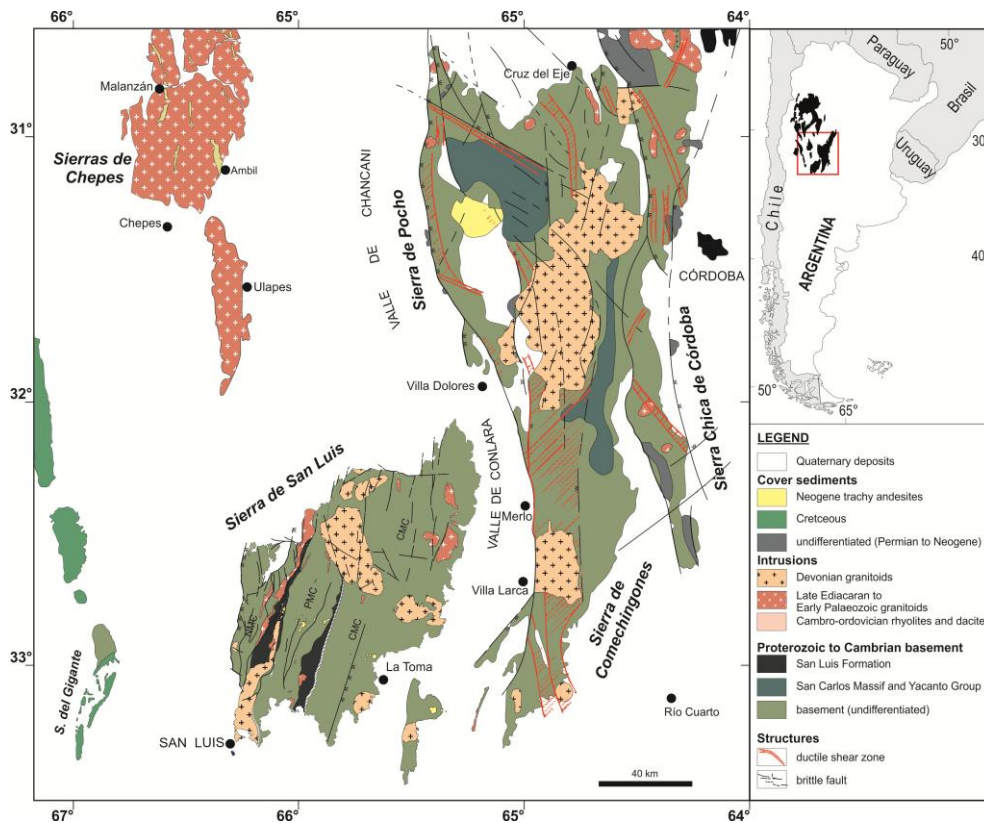


Fig. 1.6: Simplified geological map of the Eastern Sierras Pampeanas with indicated location of main brittle and ductile fault zones.

The re-onset of compressional tectonics after Late Paleozoic extension is documented by the rhyolitic volcanism of the Choiyoi Group, which discordantly overlay the Paganzo Formation to the west of the Sierras Pampeanas (e.g. Llambías et al. 2003; Japas and Kleimann 2009). Additional indications come from the scarce remnants of clastic sediments and the emplacement of granitoids in the area of the Cuyania terrane (see Llambías and Sato 1990; Mpodozis and Kay 1992).

A second phase of extensional tectonism during the Late Triassic to Early Jurassic led to reactivation of Late Proterozoic to Palaeozoic terrane boundaries (Fig. 1.5). Extensional movement along these faults resulted in the formation of localized, NNW-trending basins and the deposition of non-marine, clastic sediments (Figs. 1.7 and 1.8). Remnants of these depocenters can be found along the Valle Fértil fault in the Western Sierras Pampeanas, i.e. the Ischigualasto (Valle de la Luna; Fig. 1.4 i), Marayes, Las Salinas and Beazley basins (Criado Roque et al. 1981; Aceñolaza and Toselli 1988; Ramos et al. 2002), where thicknesses of up to 2000 m can be observed (Fig. 1.8). In the Eastern Sierras Pampeanas, significant lower thicknesses are developed (e.g. Jordan et al. 1989), of which potential relicts can be found south of the Sierra de San Luis (Costa et al. 2001). In addition to sedimentation, rifting was accompanied by alkaline intraplate volcanism (e.g. Ramos et al. 2002).

A third extensional episode, linked to the opening of the South Atlantic Ocean, occurred during Early Cretaceous times (e.g. Schmidt et al. 1995, Rossello and Mozetic 1999). Major but narrow rift basins developed, which are mainly located along the eastern and western boarder of the Pampia terrane (Fig. 1.7), partially superimposing the Triassic basins. In the northern Sierras Pampeanas, cretaceous extension caused the formation of the Salta Rift (Salfity and Marquillas 2000). In the Eastern and

Western Sierras Pampeanas, Cretaceous basins accumulated non-marine sediments of up to 2500m thicknesses (e.g. Santa Cruz 1979; Gordillo and Lencinas 1979; Criado Roque et al. 1981; Battaglia 1982; Jordan et al. 1983; Schmidt et al. 1995; Gardini et al. 1996; Gardini et al. 1999; Costa et al. 2000; Costa et al. 2001; Ramos et al. 2001; Ramos et al. 2002). Sedimentary remnants of those basins can be found in the Sierra de Norte and along the western side of the Sierra Chica and Sierra de Valle Fértil (Fig. 1.7 and 1.8). In the Western Sierras Pampeanas, extension and basin formation was accompanied by alkaline magmatism (Ramos et al. 2002).

Late Triassic to Early Jurassic as well as Early Cretaceous sedimentation caused highly variable sediment distribution throughout the Sierras Pampeanas and resulted in a quite irregular sedimentary basement cover (Fig. 1.8). Although the original extent of the Mesozoic depocenters is masked by erosion of the basin remnants (Furque 1968; Gonzalez and Aceñolaza 1972; Lucero Michaut and Olsacher 1981; Ramos 1982; Salfity and Gorustovich 1983; Jordan et al. 1983; Schmidt et al. 1995) the rather asymmetrical pattern of Mesozoic sediment distribution (Fig. 1.8) indicates that large areas of the central and eastern Sierras Pampeanas had little or no sedimentary cover (e.g. Jordan et al. 1983, Schmidt et al. 1995). Additionally, the continuance of a pronounced positive relief in the Sierras Pampeanas is indicated by the absence of marine sediments of the Paleozoic or Mesozoic age (e.g. Lencinas and Timonieri 1968).

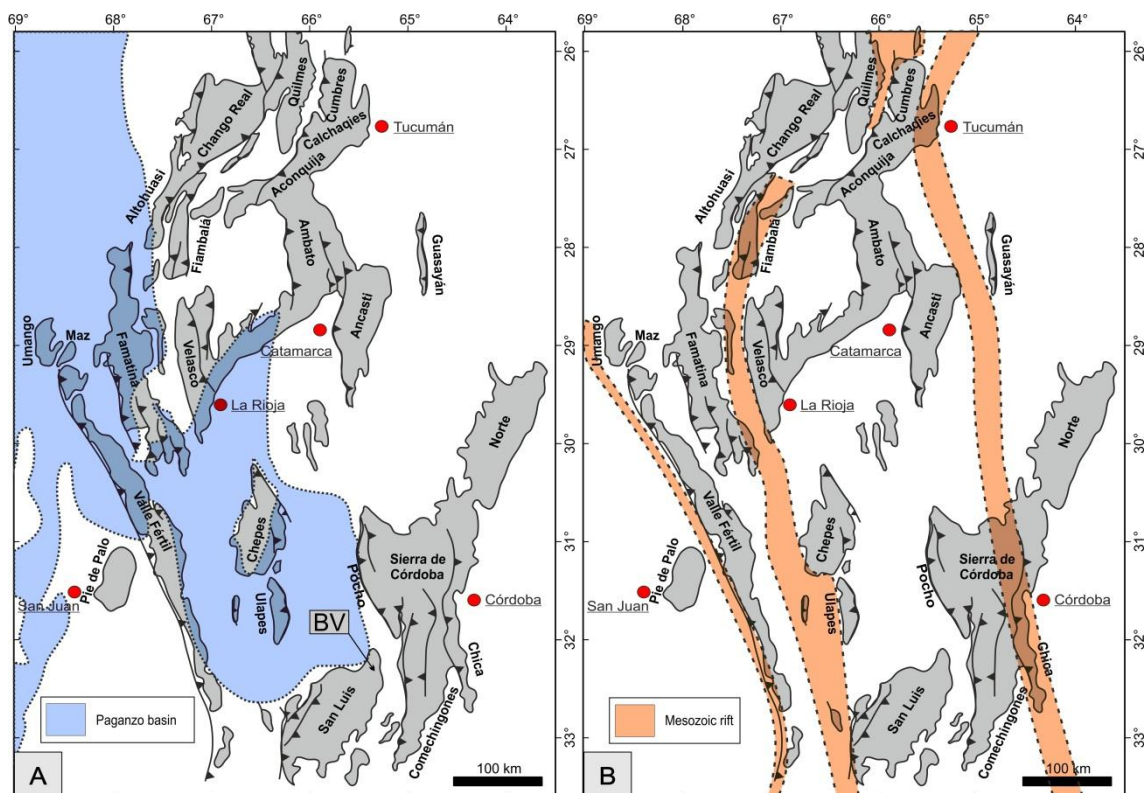


Fig. 1.7: A) Late Paleozoic Paganzo basin with main depocentres (based on Salfity and Gorustovich (1984) and Koukharsky et al. (2002), modified from Ramos et al. 2002). B) Location of major rift systems of Triassic-Early Jurassic and Early Cretaceous ages (based on Ramos 2000, modified from Ramos et al. 2002). BV: Bajo de Véliz.

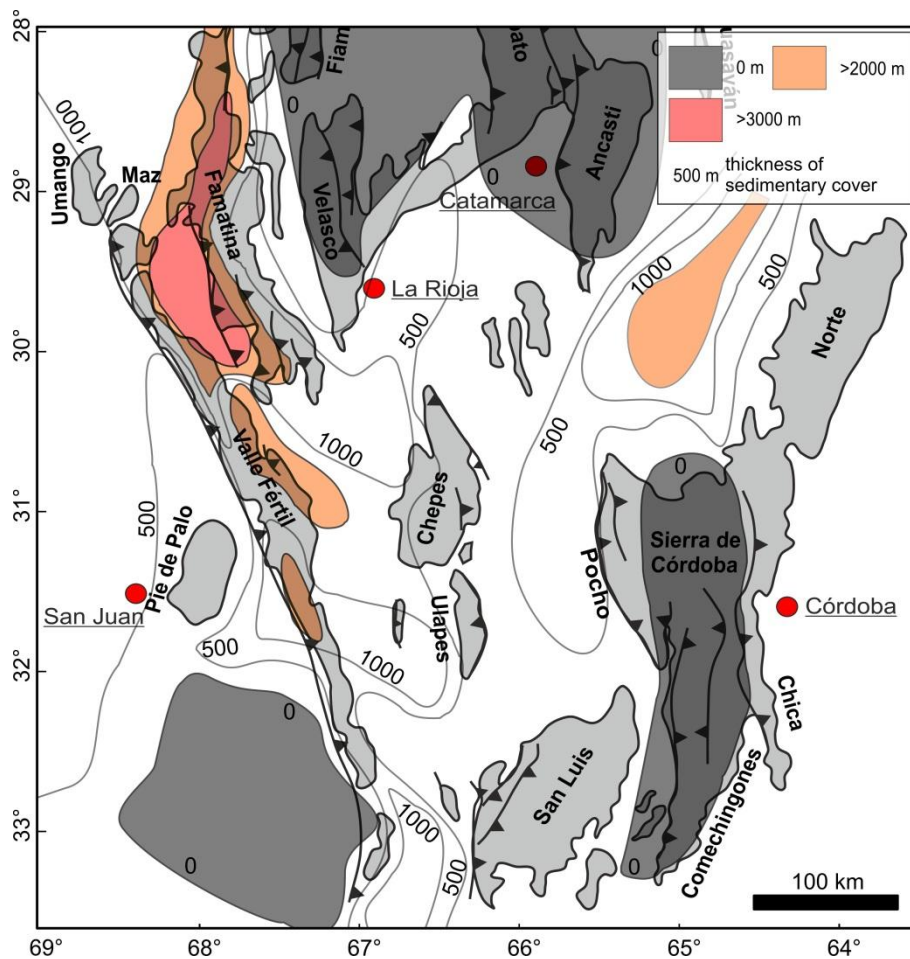


Fig. 1.8: Geographical distribution of Mesozoic sediments in the Sierras Pampeanas. Sedimentary thicknesses according to Jordan et al. 1989 and Carignano et al. 1999.

1.4 Cenozoic Geodynamic Evolution

In the Cenozoic, the almost orthogonal subduction of the Nazca Plate beneath the South American Plate resulted in the onset of Andean compression, which led to the development of the Andean orogen (e.g. Windley 1995). ENE-directed subduction with rates of up to 85 mm/a led to crustal shortening and, in general, to an east-verging geometry of the Andean Orogen. Eastward propagation of crustal shortening resulted in the progressive exhumation of individual mountain ranges which are oriented almost parallel to the Andes (e.g. Mpodozis and Ramos 1989; Russo and Silver 1996; Yañez et al. 2002; Ramos et al. 2002). The present-day Sierras Pampeanas south of 26°S comprise an exception to this trend (Figs. 1.3 and 1.9). Here, the Cenozoic reactivation of Paleozoic and Mesozoic basement structures resulted in generally west-verging geometry (see above).

During Miocene times (18-11 Ma), the Juan Fernández ridge was incorporated into the subduction of the Nazca plate, which resulted in a shallowing of the subduction angle from around 30° to about 5-10° in the area between 27°S and 33°S, just below the extent of the present-day Sierras Pampeanas (Fig. 1.9; Barazangi and Isacks 1976; Pilger 1981; Jordan and Allmendinger 1986; Yañez et al. 2001; Ramos et al. 2002). During Upper Miocene to Pliocene times, the subduction-related volcanic activity shifted, associated with the shallowing of the subduction angle, from the Andes eastward to the Sierras de San Luis and Pocho, more than 650 km away from the Peru-Chile trench (e.g. Pilger 1984;

Isacks 1988; Gütscher et al. 2000; Kay and Mpodozis 2002; Ramos et al. 2002). The eastward shift of magmatic activity towards the Sierras Pampeanas left a gap in the chain of active arc volcanism of the Andes from 28°S to 33°S, between the central volcanic zone in the north and the southern volcanic zone in the south (Fig. 1.9).

In the Sierra de San Luis, magmatic activity formed a WNW trending belt between La Carolina and El Morro (Fig. 1.9; Kay et al. 1991). Volcanic rocks of this belt comprise andesites, dacites, latites and trachytes with a typical subduction signature (Kay et al. 1991; Kay and Gordillo 1994). Along this "San Luis Volcanic Belt", ages decrease from 9.5-6.3 Ma in the west to 1.9 Ma in the east, documenting an ongoing eastward propagation of volcanic activity, which is correlated with the eastward propagation of the flat-slab beneath. The latter age represents the youngest magmatic manifestation associated with this flat-slab subduction event (Llambías and Brogioni 1981; Sruoga et al. 1996; Urbina et al. 1997; Urbina 2005; Ramos et al. 1991, 2002). A similar trend of eastward rejuvenating Miocene to Pliocene volcanic activity is also reported for the Sierras de Aconquija and Cumbres Calcaquies, the Sierra de Famatina and for the Sierra de Pocho (see Ramos et al. 2002 and references therein).

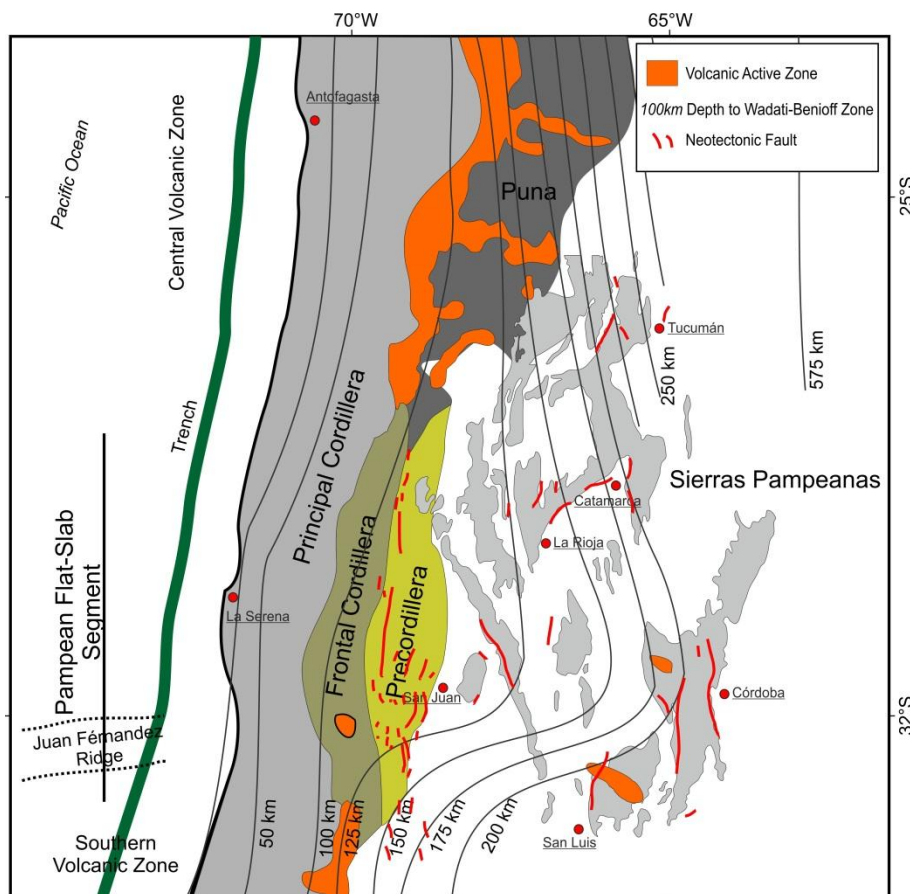


Fig. 1.9: Location of the Pampean flat-slab segment in Argentina and Chile and associated volcanism. Contours indicate depth to Wadati-Benioff zone, indicating the oceanic slab, modified from Ramos and Folguera 2009 and Ramos et al. 2002; Location of neotectonic faults associated to flat-slab subduction according to Costa et al. 2006; outline of Wadati-Benioff zone according to Cahill and Isacks (1992).

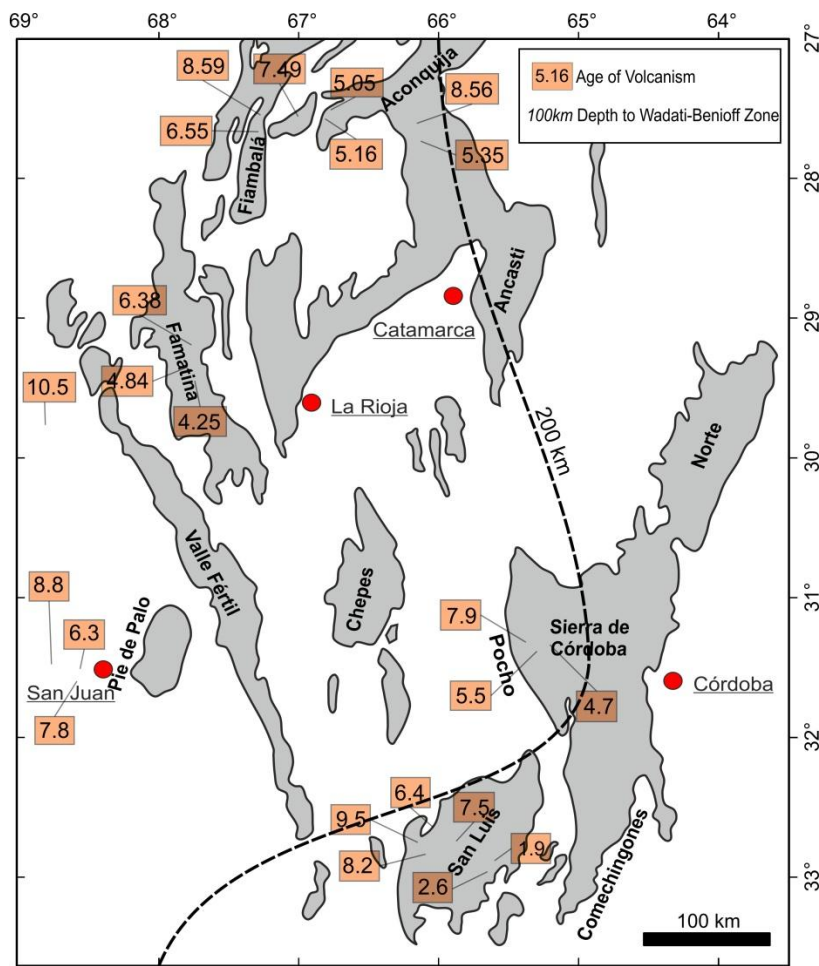


Fig. 1.10: Evolution of arc magmatism through time in the Pampean flat slab segment. Ages after Ramos et al. (2002) and references therein. Countourline indicate 200 km depth corresponding to the oceanic slab. Modified, from Ramos and Folguerea 2009

Isacks et al. (1982) and Jordan et al. (1983) were the ones to first introduce the hypothesis that the flat-slab subduction segment and associated Neogene compressional tectonic can be linked to the formation of the present-day Sierras Pampeanas. This idea was corroborated by further studies, e.g. Jordan and Allmendinger (1986), Ramos et al. (1991), Kay and Abbruzzi (1996) and Ramos et al. (2002). In short, models suggest that the uplift of the Sierras Pampeanas is related to an increase in heat flow associated with the eastward migration of the magmatic arc activity due to the flat-slab subduction. After a residence time of 2.6 – 4 Ma, the increased heat flow led to thermal weakening of the crust which caused an elevation of the brittle–ductile deformation transition. This led to the development of décollements and, together with pre-existing crustal anisotropies, to a failure of the crust. The latter resulted in the thick-skinned basement uplifts of the Sierras Pampeanas through tilt and rotation of the basement-cored blocks (González Bonorino 1950; Jordan and Allmendinger 1986; Intracaso et al. 1987; Ramos et al. 2002). Seismic data reveal the position of the main décollement near the crust-mantle boundary at 38 km depth (Fig. 1.11; e.g. Snyder et al. 1990; Regnier et al. 1992; Cristallini et al. 2004; Fromm et al. 2004; Brooker et al. 2004).

The uplift of the Pampean basement blocks was mainly controlled by older structures such as Proterozoic to Paleozoic sutures and the extensional Mesozoic fault systems (see Chapter 1.3), as well as inherited crustal weaknesses (e.g. Criado Roque et al. 1981; Schmidt et al. 1995; Gardini et al.

1996, 1999; Costa et al. 2000, 2001). The Neogene inverse reactivation of these structures (Fig. 1.9) generally resulted in a listric fault shape with a dominant dip to the east, which is expressed by a distinct morphologic asymmetry of the Pampean mountain ranges, i.e. a steep western and gentle eastern slope (see Figs. 1.4 b,c,d; e.g. González Bonorino 1950; Gordillo and Lencinas 1979; González Díaz 1981; Jordan and Allmendinger 1986; Introcaso et al. 1987; Costa and Finzi 1996; Urreiztieta et al. 1996). The main uplift phase of the Sierras Pampeanas, due to the flat-slab subduction period, is thought to have been completed in Late Pliocene times (Ramos et al. 2002). Additionally, it is inferred that Neogene block uplift led to the development of the present-day mountainous landscape with peak elevations of 2200-2800 m in the Sierras de San Luis and Córdoba, which tower the surrounding Pampa by 2300 m (see Chapter 1.1).

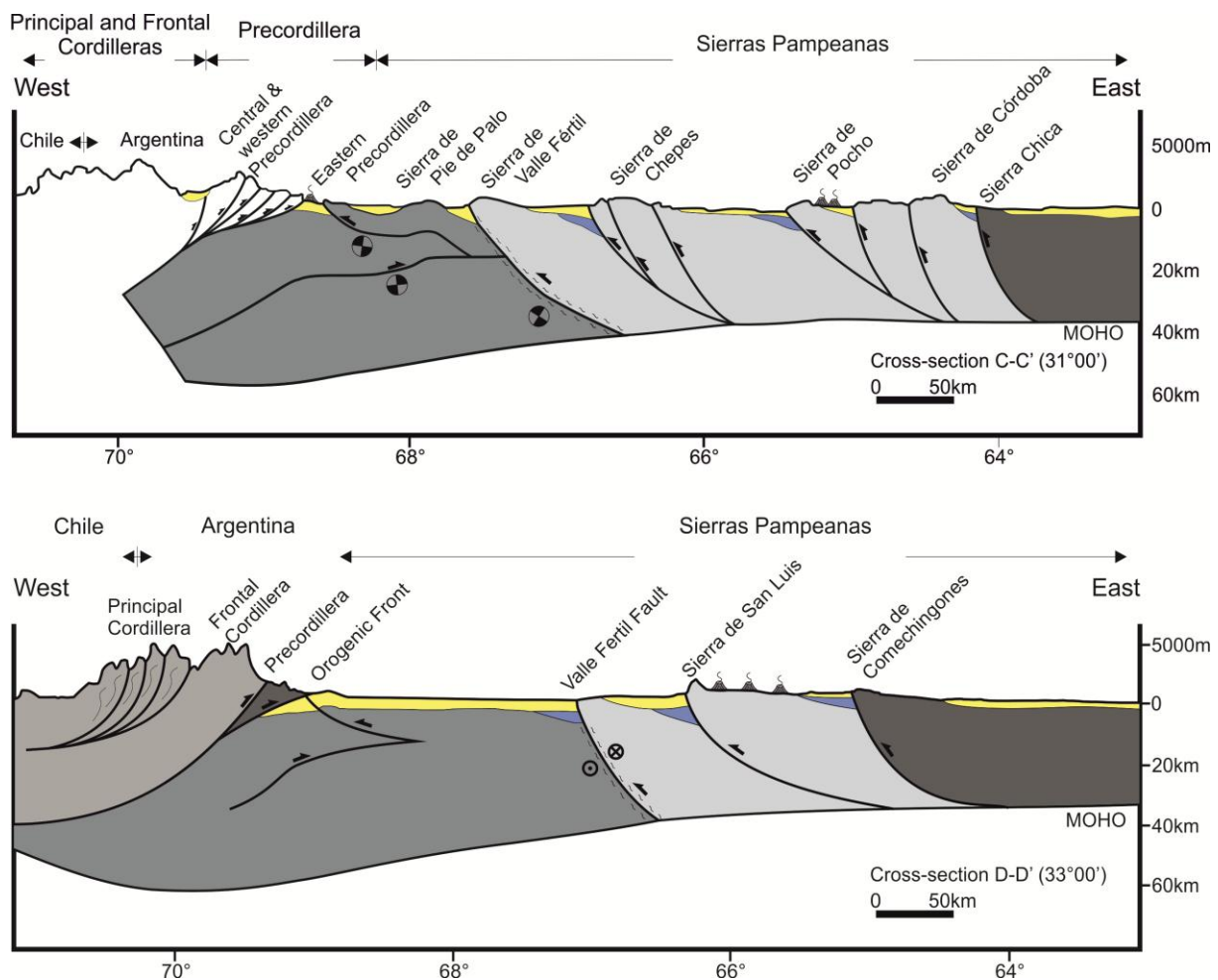


Fig. 1.11: Schematic crustal cross-section of the Andes and Sierras Pampeanas at 31° and 33°S; see Fig. 1.3 (modified, from Ramos et al. 2002).

After the Mesozoic, sedimentation did not resume until the Eocene (Santa Cruz 1972). Sediments of the Late Miocene age are scarce in the Eastern Sierras Pampeanas but can be found in the Valle de Punilla between the Sierras Grande and Chica. Those sediments are interpreted as synorogenic deposits, indicating the existence of a positive relief in this region prior to Neogene Andean Orogeny. In Neogene times, sedimentation continued due to the onset of Andean compression and the uplift

of the Eastern Sierras Pampeanas (see Chapter 1.4). Upper Miocene to Pliocene sedimentation in the eastern Sierras Pampeanas led to deposition of fluvial and alluvial piedmont sediments of up to 180 m thicknesses (Casa Grande Formation in the Valle de Punilla in between the Sierras Grande and Chica; Lencinas 1971). Andean deformation can also be traced in Pleistocene piedmont deposits derived from the Pampean ranges, which are mostly comprised of conglomerates. The thickness of sediments above the Casa Grande Formation is restricted to a maximum of 90 m (Kull and Methol 1979; Sayago 1979; Carignano 1997).

1.5 Neotectonic Activity

The latitudes affected by flat-slab subduction also concentrate about 90 % of the Quaternary deformation currently documented in Argentina (Costa et al. 2000a), which is mainly made evident by the rise of the Precordillera fold-and-thrust belt (Ramos 1988). In the Eastern Sierras Pampeanas, neotectonic activity is mainly concentrated in the Pie de Palo complex (Ramos et al. 2002; Vita-Finzi 2009), especially the Ampacama-Niquizanga fault (Fig. 5.1) which comprises an area of high intracrustal seismicity (Kadinsky-Cade et al. 1985; Regnier et al. 1992; Costa et al. 2006; Ramos and Folguerea 2009). Although main Quaternary structures (Fig. 1.9) are located between the Precordillera and the western Sierras Pampeanas (i.e. Sierra de Pie de Palo), Quaternary deformation can also be traced in the Eastern Sierras Pampeanas (Costa et al. 2006). For instance, Quaternary deformation has been reported along many of the main boundary faults of the Pampeanas ranges, overprinting Paleozoic, Mesozoic and Cenozoic structures. The majority of these faults with suspected or proven compressional Quaternary activity show a north-south trend dip between 20 and 65° to the east (e.g. Massabie 1976, 1987; Costa 1987, 1992, 1996, 1999; Kramer et al. 1995; Costa and Vita Finzi 1996; Costa et al. 2001; 2006 and many others). Only one fault with Quaternary activity, located in the southernmost Sierra de San Luis, shows normal displacement (Costa and Cortés 1993).

As during Neogene uplift, models of fault geometry based on the uplifted blocks' topographic asymmetry favor a listric fault shape (e.g. González Bonorino 1950; Jordan and Allmendinger 1986; Costa and Vita-Vita-Finzi 1996; Intracoso et al. 1987; Richardson et al. 2012), but planar fault geometries have also been proposed (e.g. Martino et al. 1995).

It is commonly understood that these Quaternary intraplate faults have long recurrence intervals (Costa et al. 2006). However, in contrast to geological field evidence of Quaternary movement along some of the larger, range-bounding faults in the Eastern Sierras Pampeanas (e.g. Costa et al. 2001), Richardson et al. (2012) found little seismicity along these. It is not yet clarified whether these faults are no longer active or accumulating stress instead of slipping. Regardless, Costa (1992) proposed a neotectonic uplift rate in the Eastern Sierras Pampeanas (i.e. Sierra de San Luis) of <0.1mm/a.

1.6 Recent Crustal Deformation

GPS-derived velocity fields for the Andes (26°-36°S) show that recent shortening due to compression in relation to the ongoing subduction of the Nazca plate beneath the South American plate is mainly accompanied by underthrusting along the décollement beneath the Argentine Precordillera (see also Fig. 1.11; Kendrick et al. 1999; Brooks et al. 2003; Klotz et al. 2006). Surface velocities measured in the Precordillera are around 10-20 mm/a but are decreasing significantly towards the Sierras Pampeanas in the east (Fig. 1.9; Brooks et al. 2003). Finite element modeling of the GPS-velocity field indicates that the Precordillera and the Sierras Pampeanas regions behave as two separate microplates. Differential movement between both plates is approximately 4.5 mm/a, mainly accommodated by continuous creep along a sub-horizontal décollement, which has its surface expression at the transition of the Precordillera and the Western Sierras Pampeanas (Brooks et al. 2003).

1.7 Low-Temperature Thermochronology

Previous to the study presented here, detailed thermochronological investigations are restricted to the northernmost branches of the Sierras Pampeanas as well as the adjacent areas of the Puna Plateau and Altiplano (Fig. 1.12; e.g. Jordan et al. 1989; Coughlin et al. 1998; Sobel and Strecker 2003; Carrapa et al. 2005, 2006; Mortimer et al. 2007; Coutand et al. 2006; Carrapa et al. 2011). The following chapter gives a brief summary of the knowledge of low-temperature thermal evolution of the Northern, Eastern and Western Sierras Pampeanas, which is entirely derived from apatite fission-track analyses. For more details, see discussion in the Chapters 3-7.

Northern Sierras Pampeanas

For the northernmost Sierras Pampeanas, Sobel and Strecker (2003) show that, after the deposition of clastic sediments along Cretaceous rifts valleys, the existing relief was completely leveled by erosion until the Middle Miocene. This episode was followed by deposition of shallow marine strata atop the basement, until exhumation of the ranges started in Late Miocene times (Fig. 1.12). It is possible that total uplift reached 6 km in the Cumbres Calchaquies and 11 km in the Sierra de Aconquija (Sobel and Strecker 2003).

Thermochronological data from the northwestern Pampean ranges (Fig. 1.12) gathered by Coughlin (1998) document a pre-Andean cooling history with periods of accelerated cooling during the Carboniferous-Permian and the Middle Jurassic. Final exhumation occurred during the Middle Miocene (see also Kleinert and Strecker 2001).

In contrast to the northern Sierras Pampeanas, Oligocene to Miocene apatite fission-track ages are reported by Carrapa et al. (2006) for the southernmost branches of the Puna plateau, adjacent to the

northwesternmost Pampean ranges (Fig. 1.12). This indicates that exhumation and development of a distinct relief commenced earlier than in the Northern Sierras Pampeanas.

For the basement domains of the central Sierras Pampeanas, thermochronological data (Fig. 1.12) were presented by Jordan et al. (1989). Based on the position of the samples in relation to the erosional surface atop the ranges, Jordan et al. (1989) defined two groups of ages. One group, comprised of samples collected below the erosional surface, show apparent fission-track ages between 135-115 Ma. On the basis of an indicated track-length shortening, Jordan et al. (1989) interpret this group as being affected by Late Cenozoic cooling and exhumation of the samples from the shallow portions of the partial-annealing zone (see Chapter 2.1). In contrast, the second group contains samples collected near the erosional surface. The apparent ages of these samples are significantly older, lying between 237-208 Ma, and show no evidence of Cenozoic cooling. Based on these observations, Jordan et al. (1989) conclude that cooling was slow during Mesozoic to Late Cenozoic times. However, in contrast to data from the northern Pampean regions, the data of Jordan et al. (1989) do not illuminate the uplift of the Pampean ranges during the Neogene. Additionally, the data of Jordan et al. (1989) support the idea of a diachronous development of the erosional surfaces (with Mesozoic-to-Neogene development of surfaces), contrasting previous ideas (e.g. Gonzalez Diaz 1981 and Criado Roque et al. 1981) of a continuous and essentially old, but synchronous erosional surface, which was uplifted and disrupted during the Andean Orogeny (see also Chapters 4.6.3 and 7.5.4).

Eastern and Western Sierras Pampeanas

Within the southern Sierras Pampeanas (the study area of this thesis), only scarce thermochronological data are available. Jordan et al. (1989) present apatite fission-track data for only a single sample from the Sierra de Córdoba (Fig. 1.11). On the basis of this single age (apparent age 115 ± 10 Ma), they extrapolate their interpretation of the cooling history of the northern Pampean ranges (see above) to the entire Eastern and Western Sierras Pampeanas, concluding slow cooling until Late Cretaceous times. Although available data are scarce, especially for the more southern Pampean ranges, available thermochronological data indicate differences in apatite fission-track cooling ages from the different Pampean ranges. In general, cooling ages from the northern Sierras Pampeanas clearly document the influence of Cenozoic Andean compression. In contrast to the northern Sierras Pampeanas, a Cenozoic exhumation event is not evident based on thermochronological data, although this may be related to the fact that only one age was determined in this region.

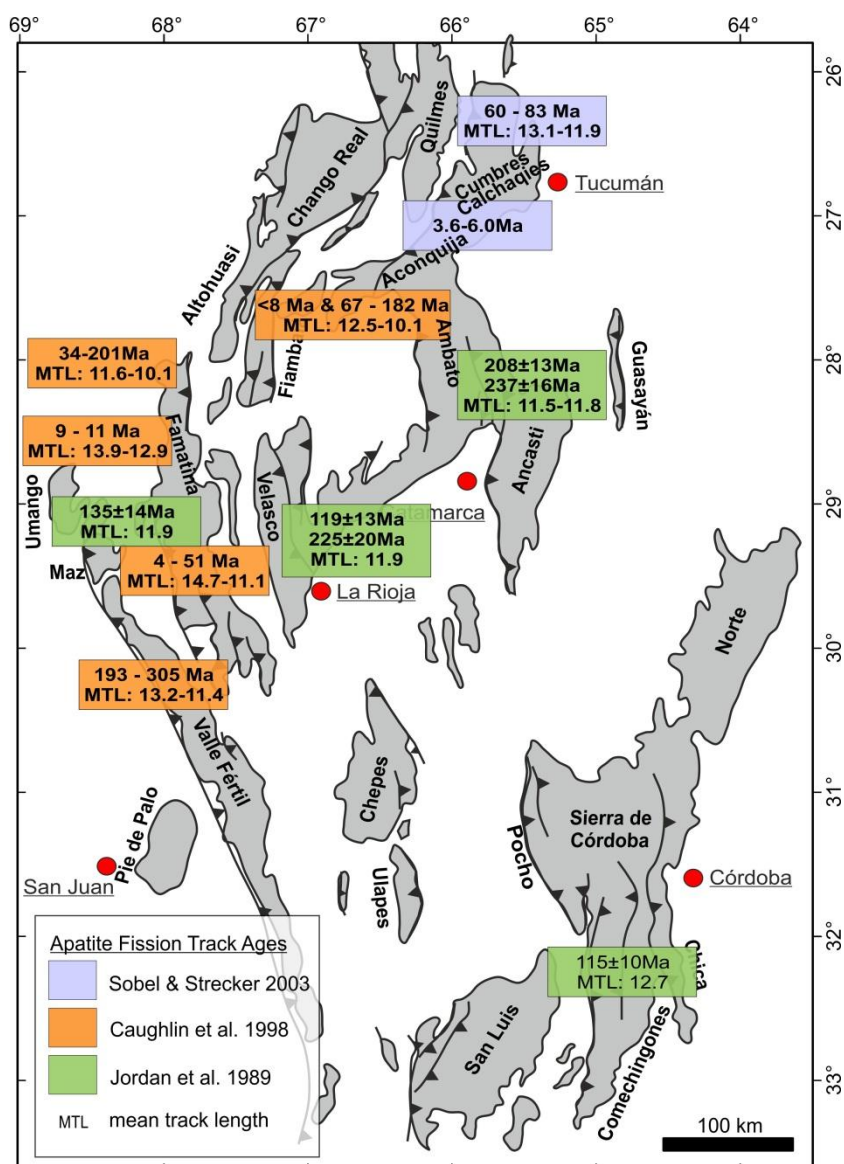


Fig. 1.12: Compilation of low-temperature thermochronological data for the Sierras Pampeanas.

2 Methodology

2.1 (U-Th)/He Thermochronometry

2.1.1 Introduction

The possibility of dating minerals based on the accumulation of ^4He produced by the decay of U and Th was recognized over a hundred years ago (e.g. Strutt 1905). Additionally, the (U-Th)/He-dating method represents the first attempt to date rocks and minerals by using the radioactive decay of isotopes (by Ernest Rutherford in 1905). However, the rapid diffusion of He out of the minerals especially resulted in apparent ages much younger than ages obtained from other, newer and, apparently, more reliable methods (e.g. K-Ar, Rb-Sr, U-Pb). The interest in the He-dating method waned, and the method was essentially abandoned for several decades. The discrepancies in the early works can, at least in part, be attributed to a lack of understanding of the closure-temperature concept as well as the distinction between emplacement and cooling ages (see Farley 2002 for a review).

Scientific research since the 1980s has refocused on the He-dating method. Zeitler et al. (1987) proposed that, in the case of apatite, He ages might be meaningfully interpreted as ages of cooling through very low temperatures. In the following years, the work of Lippolt, Zeitler, Farley and Wolf, as well as their colleagues, established the currently widespread thermochronological use of the He-dating method (e.g. Lippolt and Weigel 1988; Bähr et al. 1994; Lippolt et al. 1994;; Farley et al. 1996; Farley 2000; Wolf et al. 1996, 1997, 1998). Especially since Wolf et al. (1996a) found that He ages increase systematically with sample elevation in a mountain range, He ages are interpreted in terms of an exhumation-induced cooling through low temperature conditions. Subsequently, the (U-Th)/He thermochronometry emerged to an important tool for geochronological and thermochronological studies quantifying the cooling history of rocks as they pass through relatively shallow crustal levels (e.g. Farley et al. 2002, Ehlers et al. 2003). Today the (U-Th)/He method is applied in many geoscientific tasks, e.g. to understand orogenic process (dating the final phase of exhumation or evaluate tectonic-climate feedback), basin evolution (study sediment provenience by dating detrital grains or evaluate low temperature overprints), near surface tectonic (age and offset of faults), geomorphology (age of relief formation), as well as hydrothermal fluid migration and kerogen transformation (e.g. Reiners and Brandon 2006; Wölfler et al. 2010).

In the here presented study, we used zircon and apatite (U-Th)/He-dating methods. The sensitivity interval of these minerals, often referred to as partial-retention zones (PRZ), is between 180-140°C and 80 to 40 °C, respectively (see Fig. 2.1; Green et al. 1986; Wagner and Van den Haute 1992; Wolf et al. 1996).

Apatite has the lowest closure temperature currently known (ca. 70°C Reiners and Brandon 2006; see also Chapter 2.1.2). Additionally, its high abundance in a wide range of lithology make the apatite He dating (AHe) one of the most applicable low-temperature thermochronological methods, providing an important tool for quantifying the cooling history of rocks as they pass through the upper 1-3 km of the crust (e.g. Farley 2002; Ehlers et al. 2003). In contrast, the zircon He thermochronometer has a much higher closure temperature (ca. 180°C Reiners and Brandon 2006, see also Chapter 2.1.2). The usually high U and Th content in zircon, its frequent occurrence in rocks and resistance to physical and chemical weathering as well as its refractory nature under metamorphic conditions make zircon He dating (ZHe) suitable for thermochronological and geochronological dating. Especially the position of the ZHe closure temperature in between those of the AFT (see Chapter 2.2) and K-Ar mica system (Fig. 2.1; e.g. Willigers et al. 2001), provide valuable information for deciphering the cooling history (e.g. Farley 2002; Reiners and Brandon 2006). Additionally, ZHe ages can provide temporal constraints on the exhumation history of rocks through the PRZ_Z which high temperature boundary is near the onset of brittle behavior in an exhuming orogen (see also Chapter 6).

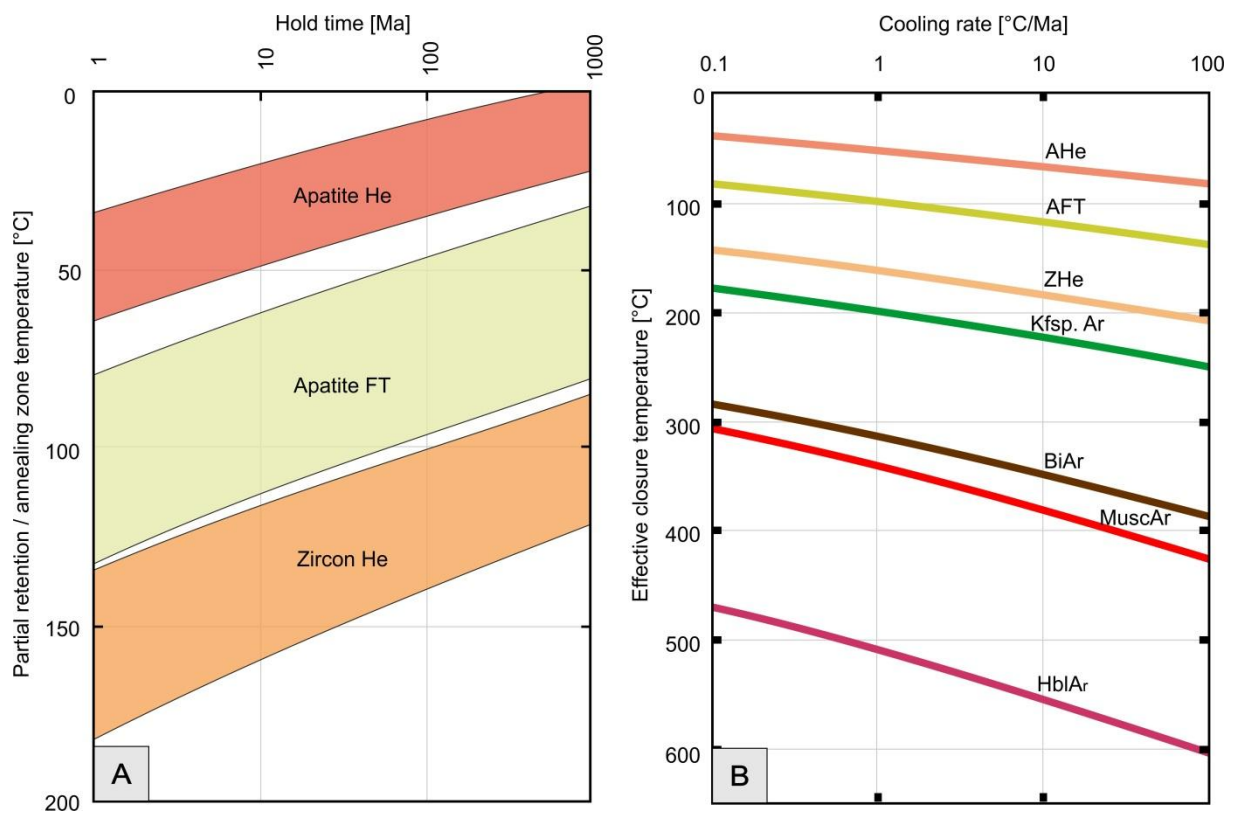


Fig. 2.1: A) Loss-only partial retention / annealing zone for apatite helium (AHe), zircon He (ZHe) and apatite fission track (AFT) thermochronometers. The PRZ / PAZ for each thermochronometer is defined by upper and lower boundaries, indicating 90% and 10% retention after being held at a steady temperature for a specific amount of time (modified, from Reiners and Brandon 2006). B) Effective closure temperature (T_c) as a function of cooling rate for AHe, ZHe and AFT thermochronometers, as well as other common Ar thermochronometers (modified, from Reiners and Brandon 2006; AHe = apatite helium, AFT = apatite fission track, ZHe = zircon helium, Kfsp = potassium feldspar, Ar = argon, Bi = biotite, Musc = muscovite, Hbl = hornblende).

2.1.2 Principles of Application

The (U-Th)/He-dating method is based on accumulation of ^4He (α -particle), produced by the radioactive decay of the parent isotopes ^{238}U , ^{235}U , ^{232}Th and ^{147}Sm .

The decay chain of U and Th to the respective stable isotopes ^{206}Pb and ^{208}Pb is composed of several stages, thus, producing several α particles (up to 8 particles in the decay chain of U). The resulting high He accumulation rates in U and Th-bearing minerals, a low He concentration in the air and a high sensitivity to measurement of U, Th and He make it possible to date both young materials with a high content of the parent isotopes U and Th and old materials with only a trace of the parent isotopes left (see Farley 2002; Reiner and Brandon 2006 and references therein).

Radiogenic ^4He is highly mobile and can diffuse through the crystal lattice of most solid phases and out of a mineral. The loss of ^4He by diffusion is mainly determined by the temperature the mineral is exposed too. Thus, the measured concentration of the parent isotopes and the daughter isotope ^4He can be used to calculate a He cooling age (e.g. Farley 2002; Reiner and Brandon 2006 and references therein). At relatively high temperatures, calculated ages are zero because ^4He is not retained in the mineral due to high diffusion. In contrast, at sufficiently low temperatures, ^4He is completely retained within the crystal lattice. In this case, the He age is finite and might be meaningfully interpreted as the age of cooling through a mineral-specific effective closure temperature (T_c). The temperature interval between the complete gain or loss of radiogenic He is defined as the partial-retention zone (PRZ, see Fig. 2.1 and 2.2; Baldwin and Lister 1998; Wolf et al. 1998; Reiner and Brandon 2006).

Apart from the diffusivity of He, the closure temperature of a mineral depends on the size of the dated crystal (i.e. the dimension of the diffusion domain) and the cooling (see Fig. 2.1; Reiners and Brandon 2006). Hence, individual crystals from the same sample can show small variations in closure temperature and, thus, show different He cooling ages. Additionally, the retention of He in a crystal is not proportional to time, i.e. He diffuses out of the crystal lattice during cooling through the PRZ. Subsequently, He ages change during the passage through the PRZ by achieving a balance between He loss and He production (Fig. 2.2). Ultimately, depending on equilibration time and temperature, an equilibrated steady-state age will be achieved (e.g. Wolf et al. 1998).

In order to evaluate this effect, several individual crystals need to be dated (see Chapter 2.1.3). Modeling of He diffusion and closure temperature of those grains can be used to reveal a more detailed thermal history from the different apparent ages (e.g. Dodson 1973; Kelley 2002; Farley 2002; Reiners and Brandon 2006; see also Chapter 2.3). An effective closure temperature (T_c) can be defined for a given crystal and represents the temperature of a rock at its thermochronologic cooling age under the assumption of a monotonic cooling history. In general, closure temperatures of around 180°C and 70°C can be estimated for zircon and apatite, respectively (Reiner and Brandon 2006). The typically observed zone of partial He retention in apatite and zircon extends from 180-140°C and 80-

40°C respectively (Fig. 2.1; Reiners and Brandon 2006). Although He diffuses rapidly from apatite at shallow crustal levels, He ages are nearly unaffected by surficial processes (Wolf et al. 1998).

Several factors bias the reliability of obtained He ages, of which the main factors are: (a) ejection of α -particles during the decay, (b) Actinide-bearing inclusions and (c) the zonation of α -particle-emitting sources in the crystal.

The α -particles which are produced during the decay process of U, Th and Sm are emitted from their source with substantial kinetic energy (e.g. Farley et al. 1996; Hourigan et al. 2005). Depending on grain size and the position of the emitting source in relation to the external crystal boundaries, a portion of the α -particles is ejected from the parent crystal instantaneously. Stopping distances for α -particles vary depending on decay energy and mineral density/composition (e.g. U/Th ratio) but are typically within the range of 10 – 30 μm , considerably long compared to the size of a typically analyzed crystal grain (approx. 80-100 μm). For instance, a spheroid crystal of 100 μm radius only retains ca. 82 % of its α -particles (Farley et al. 1996; Hourigan 2005). An estimation of the sensitivity of a crystal to He loss can be expressed by the surface-area-to-volume ratio of a crystal. Especially platy crystals as well as diffusion channels represented by fractures, crack or radiation damage (e.g. Shuster et al. 2006) in the grain may contribute significantly to the ejection loss of He; therefore euhedral crystals are preferred for dating (see Chapter 2.1.3). As a consequence, an α -ejection correction factor is required to account for those He atoms ejected from the crystal. This correction factor is called F_T (F_T = fraction of total), expressing the proportion of the radiogenic He remaining in the crystal after radioactive decay (e.g. Farley et al. 1996; Farley 2002; Hourigan et al. 2005).

The second biasing factor concerns the role of crystal inclusions. Because especially Actinide-bearing inclusions can produce errors in age determination by contributing the U, Th and Sm content of the "pure" crystal and by producing additional He themselves, the selection criteria for crystals used in He dating are very strict, e.g. no visible inclusions are allowed. Fluid inclusions may also contain He, which is undistinguishable from the radiogenic one. In both cases, excess He will produce erroneously high He ages.

The third main biasing factor is the zoning of the α -particle-emitting elements within the dated grain, i.e. their enrichment in the core or rim of the crystal. If the emitting elements are enriched in the crystal core, the α -ejection is smaller compared to a crystal with homogeneous element distribution. The result is an overestimated percentage of ejected He and, thus, an overcorrection of the presumed He-loss. Therefore, the corrected He content is higher than the real one, resulting in an erroneously high age. On the contrary, if emitting elements are enriched in the rim, more α -particles are ejected than expected. The underestimation of α -ejection results in an undercorrected, erroneously young age (see Hourigan et al. 2005). If samples are also analyzed by fission-track dating,

the effect of zonation of α -particle-emitting elements can be evaluated by fission-track density maps, which allow a more accurate α -ejection correction of He ages (see also Chapter 2.3).

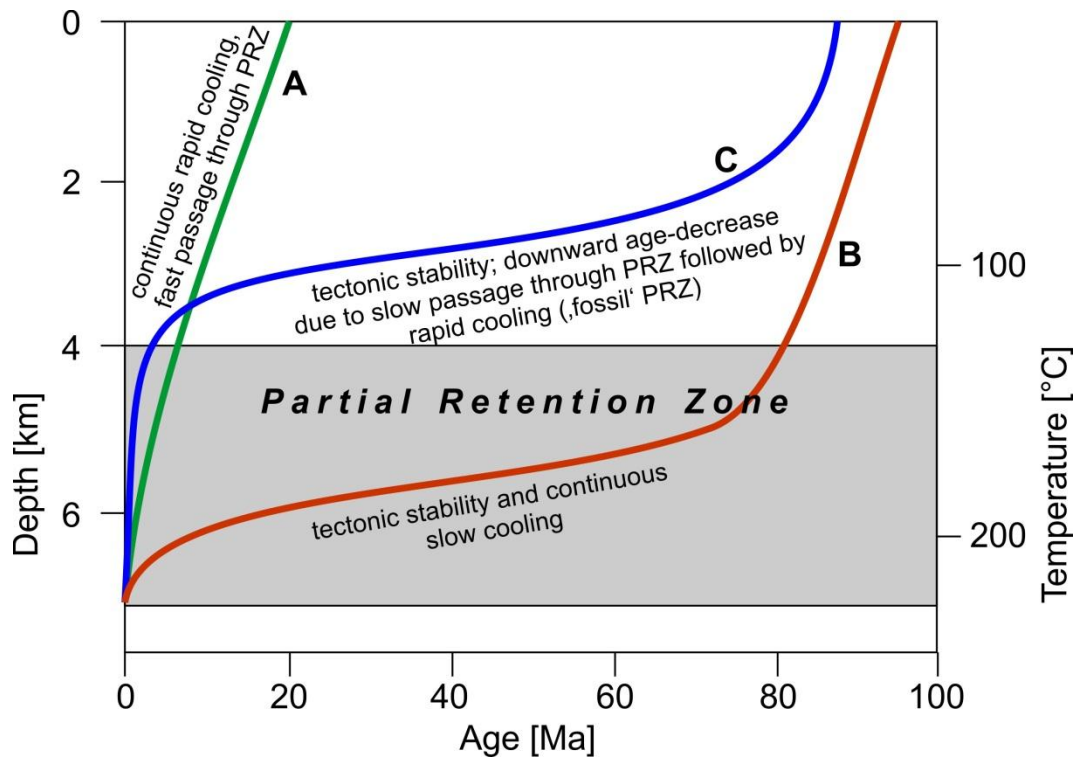


Fig. 2.2: Schematic age-elevation diagram (e.g. a deep borehole) across the partial-retention zone (PRZ) for a He thermochronometer. A geothermal gradient of 30 °C/km is assumed; A) illustrates an idealized elevation profile in the upper continental crust where substantial exhumation-related cooling has continued at a constant rate for >20 Ma. The gradient above the PRZ approximately gives an average rate of cooling and exhumation (i.e. 9°C/Ma or 0.3 km/Ma). B) In tectonically stable regions, the age profile is primarily governed by the vertical temperature profile. Due to slow passage of samples through the PRZ (and associated slow age increase due to He retention) results in a characteristic downward age-decrease profile characterising the passage through the PRZ. The age profile above the PRZ reflects the rate of exhumation-related cooling that precedes the time of tectonic stability (i.e., 0.3 km/Ma or 9 °C/Ma before 80 Ma). C) If the extended period of tectonic stability is followed by a recent, rapid exhumation event, i.e. for ~3 km in the past ~3 My, the characteristic age-decrease profile may be preserved as a fossil PRZ (modified, from Tagami 2012).

2.1.3 Analytical Procedure

Between 1 and 6 apatite and zircon single crystal aliquots from each sample were carefully handpicked using binoculars and petrologic microscope. Only inclusion and fissure-free grains showing a well-defined external morphology were used, wherein euhedral crystals were preferred. The shape parameters of each single crystal were determined, e.g. length and width, and archived by digital microphotographs in order to apply the correction of alpha ejection described by Farley et al. (1996). Subsequently, the crystals were wrapped in an approximately 1 x 1 mm sized platinum capsule and analyzed following a two-stage analytical procedure (Reiners and Brandon 2006). This is characterized by (a) measuring the ^4He extraction and (b) by analyzing the ^{238}U , ^{232}Th and Sm content of the same crystal. During the first step, which was operated by HeLID automation software through a K8000/ Poirot interface board, the Pt capsules were degassed in a high vacuum via heating with an infrared diode laser. The extracted gas was purified using an SAES Ti-Zr getter at 450°C, and the inert noble gases as well as a minor amount of rest gases were measured by a Hiden triple-filter

quadrupole mass spectrometer equipped with a positive-ion-counting detector. Re-extraction was performed for each sample to control the quantitative amount of extracted He. During the He measurement, 240 readings of the mass spectrometer were recorded for every standard and sample.

After degassing, the samples were retrieved from the gas extraction line and spiked with calibrated ^{230}Th and ^{233}U solutions. Zircon crystals were dissolved in pressurized Teflon bombs using distilled 48% HF + 65% HNO_3 for five days at 220°C. For apatite 2%, HNO_3 was used. These spiked solutions were then analyzed with the isotope dilution method using a Perkin Elmer Elan DRC II ICP-MS equipped with an APEX micro flow nebulizer.

To process and evaluate the He signal as well as the data of the ICP-MS measurements, the factory-made software of the mass spectrometer MASsoft and the freeware software PEPITA (Dunkl et al. 2008) were used. Regarding the latter evaluation, 40 to 70 readings of the ICP-MS were considered and individual outliers of the $^{233}\text{U}/^{238}\text{U}$ as well as $^{230}\text{Th}/^{233}\text{Th}$ ratios were tested and rejected according to the 2σ deviation criterion.

Finally, the raw (U-Th)/He ages of zircon and apatite were form-corrected (Ft correction) following Farley et al. (1996) and Hourigan et al. (2005). Replicate analyses of Durango apatite over the period of this study yielded a mean (U-Th)/He age of 30.4 ± 1.7 Ma, which is in good accordance with the reference (U-Th)/He age of 31.12 ± 1.01 Ma (McDowell et al. 2005). Replicate analyses of the Fish Canyon zircon standard yielded a mean (U-Th)/He age of 28.0 ± 1.6 Ma, which also coincides well with the reference Ar–Ar age of 27.9 ± 1.01 Ma (Hurford and Hammerschmidt 1985) and the reference U-Pb age of $28,479 \pm 0.029$ Ma (Schmitz and Bowring 2001).

2.2 Apatite Fission Track Thermochronology

2.2.1 Introduction

Apatite fission-track (AFT) analysis includes both the determination of an AFT age as well as modeling of time-temperature paths based on the measured fission-track length distributions. In the last decade, apatite fission-track analysis has become a standard technique and tool for investigating the low-temperature thermal evolution of rocks. It has been used in numerous geoscientific tasks, e.g. tectonic modeling, landscape development, tectonic geomorphology, mountain building and temperature history of hydrocarbon source rocks, as well as thermal and burial histories of sedimentary basins (e.g. Ravenhurst et al. 1994; House et al. 1999). Additionally, as with the (UTh)/He method, by assuming a geothermal gradient and a surface temperature, AFT data can be used to infer burial depth and denudation rates (see Reiners and Brandon 2006 and references therein).

The main advantage of fission-track analysis over many other thermochronological methods, e.g. the (U-Th)/He method (see Chapter 2.1), is the fact that much more information than just a cooling age

can be obtained (Fig. 2.3). Especially when several thermochronometers are used to constrain the low temperature thermal evolution of a rock, the combination of fission-track chronology and (U-Th)/He dating is heavily recommended (e.g. Brandon and Reiners 2006). On one hand, the closure temperature of the FT system is higher than that of the He system; thus, a more detailed thermal-evolution path can be drawn by using both methods (Fig. 2.3). On the other hand, the FT method can be used to constrain reliable results from the (U-Th)/He method (see also Chapter 2.3).

2.2.2 Principles of Application

The fission-track technique is based on the spontaneous fission of the natural, unstable isotope ^{238}U in U-bearing minerals such as apatite. Emitted fission products move diametrically to each other, resulting in atomically-scaled linear damage zones within the crystal lattice, which are named fission tracks (FT). The number of tracks within a sample depends on the U-concentration of the crystal and can be described by the decay constant of the ^{238}U isotope $\lambda = 8.46 \times 10^{-17}/\text{a}$. If the concentration of U within the crystal is known, the density of spontaneous fission tracks (named ρ_s = number of spontaneous tracks/cm²) can be used as a direct indicator of the age of the crystal. In order to determine the fission-track density, the atomically scaled fission tracks are etched with a chemical treatment to make them visible in optical methods. Subsequently, fission tracks are counted at high magnifications under an optical microscope (see Chapter 2.2.3).

The concentration of ^{238}U is determined indirectly by irradiating the etched crystal with thermal neutrons in a nuclear reactor. Neutron irradiation induces the fission of the isotope ^{235}U which itself, producing fission tracks which are traced by a U-free external detector atop the crystal (usually muscovite, see Chapter 2.2.3). The density of these induced fission tracks (named ρ_i = number of induced tracks/cm²) is obtained analogue to ρ_s by etching and counting under the microscope. Because only the external detector and not the crystal will be etched again after irradiation, the induced fissions do not interfere with the counting of spontaneous tracks. Since the $^{235}\text{U}/^{238}\text{U}$ ratio is a constant in nature, the initial ^{238}U content can be calculated from counted ρ_s and the known neutron flux used for irradiation.

Spontaneous fission tracks in apatite have approximately the same length. However, because fission tracks are thermally unstable, they are only retained within the crystal lattice below a specific temperature (see below; e.g. Ketcham et al. 1999). If mineral grains are heated above their closure temperatures, both the number and mean length of tracks are subsequently annealed, i.e. they become partially or even totally shortened due to restoration of the crystal lattice. In this respect, AFT ages can be considered as cooling ages, dating the cooling of the sample to a temperature at which the fission tracks became stable. For example, if fission tracks are completely annealing, the apatite fission-track age provides a cooling age recording the time the apatite passed through its

closure temperature. A fission-track age does not generally reflect a discrete event (Donelick et al. 2005).

The extent of thermal annealing can be expressed by the length-distribution of the fission tracks in the sample. Measurements of the confined track length (horizontal tracks, i.e. tracks interior to the crystal, where both ends can be seen and are parallel to the cut surface of the crystal) in combination with the AFT age yield additional information about the samples' thermal history. For example, the track-length distribution of an apatite from rapidly cooled rocks (e.g. vulcanites) show characteristic long-track length and small standard deviations of $14\text{--}15 \pm 0.8\text{--}1.3 \mu\text{m}$ (Gleadow et al. 1987). In contrast, slow cooling will result in shorter track length and higher standard deviation $12\text{--}14 \pm 1\text{--}2 \mu\text{m}$ (Fig. 2.3; Gleadow et al. 1987).

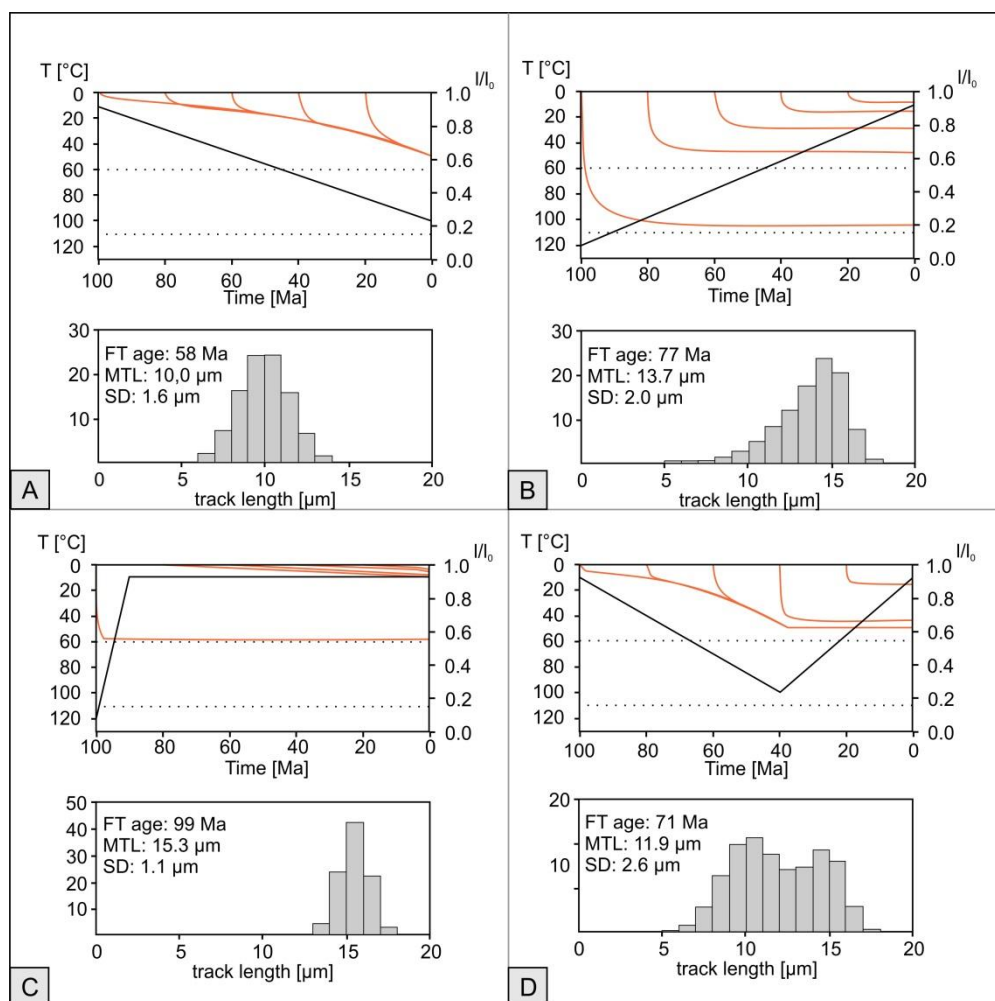


Fig. 2.3: Models of apatite fission-track length distribution (heavy lines in upper panels) and predicted track length parameters (lower panels) for apatite. I/I_0 = present track length divided by the initial length. The two lines at 60°C and 110°C indicate partial annealing zone (PAZ). A) Linear heating. All tracks have more or less the same length at present, as they all experience the same maximum paleotemperature. The track length distribution is unimodal, symmetrical, and has a short mean length. The fission track age does not relate to any discrete event. B) Linear cooling. Each track experiences a different maximum paleotemperature as cooling progresses, which is reflected in the characteristic negatively skewed length distribution. The age does not relate to any discrete event. C) Rapid cooling. Nearly all tracks are formed after the cooling episode, thus all are relatively long. In this case, the fission track age is a reasonable indication of the timing of cooling, compared with the age estimate for (b). D) Heating and cooling. The tracks formed during the heating period have similar lengths, while those formed after reflect the progressive cooling. The track length distribution is typically bimodal, and once again, the fission track age does not relate directly to the timing of cooling or timing of maximum paleotemperature (modified, from Gallagher et al. 1998).

2.2.3 Principles of Application

The temperature interval between the partial or complete annealing of spontaneous fission tracks in the apatite crystal is referred to as the apatite partial-annealing zone (PAZ_A; e.g. Gleadow and Duddy 1981). The temperature range of the PAZ_A depends on two major factors: (a) the crystallographic orientation of the tracks and (b) the chemical composition of the apatite.

Green and Durrani (1977) were the first to describe a connection between the annealing behavior and the crystallographic orientation of fission tracks. Tracks which are oriented perpendicularly to the crystallographic c-axis are more rapidly annealed than those parallel to the c-axis (e.g. Green 1988; Laslett et al., 1984; Donelick et al., 1990, 1999; Galbraith et al., 1990; Donelick, 1991, Barbarand et al. 2003b).

In addition to the crystallographic orientation, the annealing of fission tracks strongly depends on the chemical composition of the dated apatite crystal, specifically, the concentration of F and Cl, respectively the F/Cl-ratio. In general, F-rich apatites show more annealing than Cl-rich samples at the same time and temperature conditions (Gleadow and Duddy 1981; Green et al. 1985, 1986). Differences in the annealing behavior can be significant, as expressed by the total annealing temperature of the F-rich Durango apatite (90-100°C), in contrast to a Cl-rich apatite (110°C-150°C; see Burtner 1994, O'Sullivan and Parrish 1995).

Conclusions for the Cl and F contents can be drawn from the etching behavior of a sample, which is expressed by the kinetic parameter Dpar. The Dpar is defined as the mean diameter of the etch figures (geometrical figures formed by the intersection of an etch pit, i.e. the etched fission track and the etched surface) parallel to the crystallographic c-axis. The Dpar is measured on a polished and etched surface and is specified in µm. (e.g. Carlson et al. 1999; Donelick et al. 2005 and references therein). The Dpar has been shown to be an effective expression of the apatite annealing kinetics (e.g. Ketcham et al. 1999). Values of Dpar observed in nature range from approximately 1.50 µm for apatites that are least resistant to annealing to approximately 5.00 µm or higher for apatites that are most resistant to annealing (e.g. Ketcham 2005).

Experimental studies on the annealing behavior of fission-tracks in apatite have yielded the basis for numerical algorithms accounting for both mixed-compositional apatite and crystallographic effects (see Ketcham et al. 2000 and references therein). Numerical computer modeling (e.g. AFTSolve software; Ketcham et al. 2000) can be used to combine the information derived from track-length distribution, age determination and annealing kinetics of a sample and, thus, yield valuable information on the thermal history of a sample by constraining the low temperature cooling history (see also Chapter 2.3).

2.2.4 Analytical Procedure

Following standard density and magnetic mineral separation techniques, the apatite samples were mounted on a glass slide with epoxy. According to Donelick et al. (1999), the mounts were etched at 21°C for 20 s using 5.5 M nitric acid after grinding and polishing procedures in order to reveal spontaneous tracks within the apatite crystals. The external detector method described by Gleadow (1981) was used, while low-uranium muscovite sheets (Goodfellow mica) represent the external detector for induced tracks. For age determination, the zeta calibration approach was adopted (Hurford and Green 1983), and 25 good-quality grains per sample were randomly selected and dated. The fission-track ages were calculated using the software TRACKKEY version 4.2 (Dunkl 2002). Additionally, for track length analysis, about 50–60 horizontal confined tracks of each sample were measured considering their angle to the c-axis (Donelick et al. 1999). In order to account for all the effects influencing the apatite age as well as annealing behavior and, thus, the track length distribution, AFT data are modeled using the numerical simulation software AFTSolve (Ketcham et al. 2000), which accounts for crystallographic effects as well as mixed compositions in apatite (see Chapter 2.2.2). For more details on the analytical procedures and AFT modeling applied, the reader is referred to Löbens (2012).

2.3 Thermal Modeling

Thermal modeling techniques incorporate kinematic formulations of individual thermochronological systems. Forward and inverse models can be developed for reconstructing the range of corresponding time-temperature paths from thermochronological data. The combination of fission-track data with (U-Th)/He data can especially provide a diagnostic and sensitive tool for evaluating low-temperature thermal history (e.g. Gallagher 1995; Ketcham 2005; Wolf et al. 1998).

For modeling, diffusion of daughter nuclides, thermal-annealing behavior and partial retention (see Chapters 2.1.2 and 2.2.2) are formulated in an equation with time and temperature as variables (e.g. Dunai 2005; Ketcham 2005; Tagami 2012). In general, numerical simulation programs such as HeFTy are based on equations which are derived from a combination of laboratory diffusion and annealing experiments, as well as data from natural, key study areas where the time-temperature history is very well known (e.g. Green et al. 1986, 1989; Laslett et al. 1987; Gallagher 1995; Ketcham et al. 1999; Barbarand et al. 2003; Ketcham 2005).

In the present study, we followed a two-stage approach of forward and inverse modeling of data using the computer program HeFTy (Ketcham 2005). HeFTy was designed to allow simultaneous evaluation of thermochronometric data sets from one sample, derived from multiple methods, such as AFT and (U-Th)/He dating. One of the principal features of HeFTy is the integrative evaluation of multiple parameters which constrain the interpretation of the thermochronometers used, e.g. kinetic parameters, annealing behavior and track-length measurement considerations for the AFT system

(see Chapter 2.2), as well as U, Th, Sm zonation or He diffusion effects such as radiation damage and α -stopping distance for the (U-Th)/He system (see Chapter 2.1). For a detailed review of the analytical capabilities and function of HeFTy, the reader is referred to Ketcham (2005) and references therein.

In HeFTy, the term "forward modeling" describes the process of predicting thermo-chronometer measurements for a given time-temperature history. Kinetic equations are used to describe the evolution of kinetic parameters, e.g. FT length distribution and age. By superimposing both the measured and predicted results, the reliability of the inferred thermal history can be evaluated. Through the manual adjustment of the inferred time-temperature path, model predictions are continuously updated, allowing the user to fit measured and predicted data interactively (see also Ketcham 2005).

In a second step, inverse modeling is performed on the basis of forward modeling results. The term "inverse modeling" in HeFTy describes the process by which a large number of forward models (i.e. time-temperature paths) are automatically generated by HeFTy using a Monte-Carlo inversion routine, while optimal fits of the kinetic parameters are searched computationally between the forward-model calculation and the measured data. The predicted thermochronometer results are compared to the measured values for each path tried. Based on the grade of congruence between predicted and real measurements, which is expressed by their goodness-of-fit (see Ketcham et al. 2000 and Ketcham 2000), tried paths are classified as "good" or "acceptable" forward models. Simply speaking, these terms can be thought of as "relative degrees of fitting". A "good" result implies that the modeled time-temperature path is supported by the data, while an acceptable path is not ruled out by the data (see Ketcham 2005).

2.4 K-Ar Illite Fine-Fraction Dating

In brittle near-surface faults, rocks are broken and crushed by tectonic movements. In those localized zones, the increased surface creates a high chemical reactivity, allowing retrograde processes to produce fault gouges composed of authigenic hydrosilicates such as illite. During the formation of illite, K is fixed within the illite crystal lattice. During the radioactive decay of the K isotope ^{40}K , the decay product ^{40}Ar is retained within the crystal lattice, allowing illite to act as a radiometric clock. Thus, by measuring the amount of ^{40}K and ^{40}Ar in authigenic illite, the age of the fault-developing event can be determined (e.g. Lyons and Snellenberg 1971; Kralik et al. 1987).

Although K-Ar illite dating of faulting and thrusting has gained more and more interest in the last decade as expressed by an increasing number of recent publications (e.g. Solum et al. 2005; Schleicher et al. 2006; Haines and van der Pluijm 2008; Zwingmann et al. 2010; Surace et al. 2011; Wolff et al. 2011), only minor attention has been paid to the methodological improvement of illite

age interpretation. The integrating of other methodological approaches into fault-gouge analysis, e.g. illite mineralogy or thermochronology, can provide valuable information and constraints on the timing of fault-gouge formation and fault activity. For instance, information derived from illite crystallinity and illite polytype analyses can be used to illuminate the illite formation history during retrograde metamorphic conditions. The integration of cooling ages derived from thermochronological and geochronological dating methods (AFT, (U-TH)/He dating, K-Ar mica) into the interpretation of K-Ar illite ages can also provide valuable constraints on fault-gouge formation and fault activity by, for example, setting constraints on temperature conditions (Fig. 4.4).

In Chapter 6, we present a multi-methodological approach to fault-gouge analysis in order to constrain the “deformation path” of the Eastern Sierras Pampeanas. All key issues of K-Ar fine-fraction dating, analytical procedures and principles of application are discussed there in detail. Additionally, the chapter offers an integrative discussion of data derived from illite dating, clay mineralogy and thermochronological and geochronological methods in order to elucidate regional tectonic influences and is brought into context with established models of the regional evolution of the Eastern Sierras Pampeanas.

3 The Sierra de Comechingones

3.1 Introduction

The Sierras Pampeanas in central and north-western Argentina represent an area of north-south trending mountain ranges showing elevations of up to 5550 m that are divided by intermountain basins (Fig. 3.1; González Bonorino 1950; Caminos 1979, Jordan and Allmendinger 1986; Ramos et al. 2002; among others). Mainly consisting of Late Pre-Cambrian to Early Paleozoic basement rocks, i.e. igneous and metamorphic rocks (e.g. González Bonorino 1950; Caminos 1979; Gordillo and Lencinas 1979), these mountain ranges comprise twelve main tectonic blocks (Jordan and Allmendinger 1986) which represent distinct morphotectonic features above the shallowing Nazca plate within the area of 27°S-33°S east of the Precordillera (e.g. Jordan et al. 1983; Jordan and Allmendinger 1986; Ramos et al. 2002 and many others). The uplift and type of deformation of the Sierras Pampeanas is interpreted to be closely related to the flat-slab subduction of the Nazca plate beneath the South American plate since the Miocene and after the collision of the Juan Fernández Ridge (e.g. Jordan et al. 1983; Yañez et al. 2001; Ramos et al. 2002).

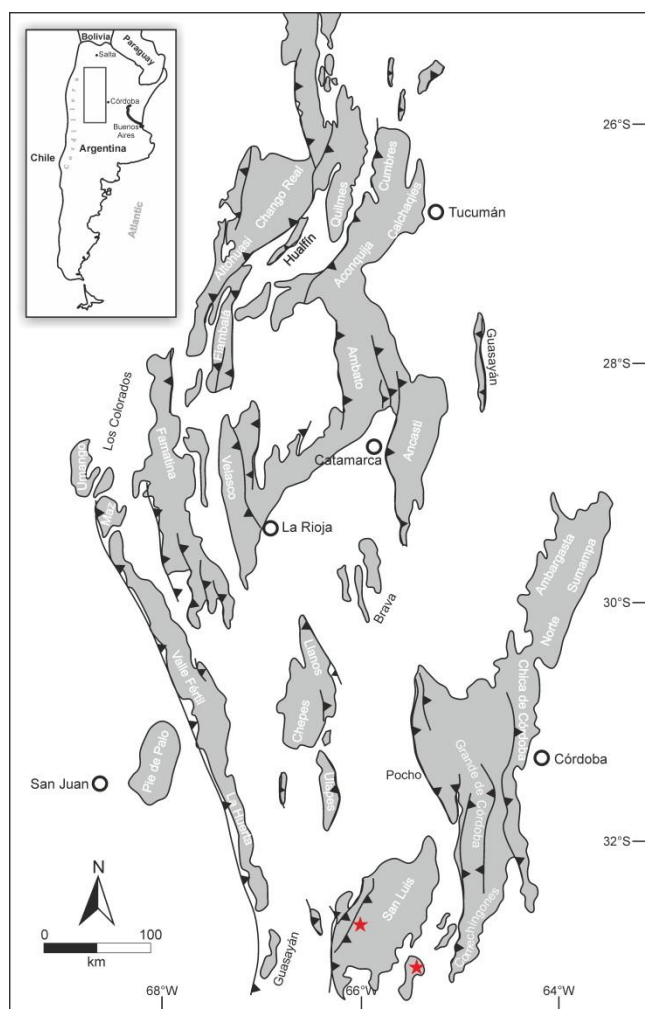


Fig. 3.1: Schematic overview of the Sierras Pampeanas with the main thrusts (modified after Ramos et al. 2002). The mountain ranges are shown in grey and intermountain basins are white but not named. For reference a schematic map of Argentina is shown in the upper left, where the grey frame marks the area of the Sierras Pampeanas. The red stars indicate the sample locations (La Carolina volcanic field in the west and Sierra del Morro in the east) of volcanic rocks taken for Ar-Ar analysis.

Two main morphotectonic features stand out at most of these faulted blocks: a topographic asymmetry, with a steep western slope and a gentle eastern slope where preserved remains of erosion surfaces stand out. Such paleolandscapes have traditionally been envisaged as a continuous and essentially synchronous surface, exhumed and disrupted during the Andean orogeny (González Díaz 1981; Criado Roque et al. 1981). However, Jordan et al. (1989) suggested that these erosion surfaces are diachronic in age at a regional scale. Later, Carignano et al. (1999) postulated that many paleosurfaces scarps and slope breaks result from juxtaposition of diachronous surfaces (ranging from Late Paleozoic to Paleogene ages), rather than being a consequence of the Andean tectonism.

Current uncertainties about the ages and evolutionary paths of these currently exposed erosion surfaces precludes a suitable analysis of core issues regarding the tectonic evolution of the Sierras Pampeanas (i.e. the structural relief related to the Andean orogeny).

In order to investigate the Neogene uplift and exhumation history of the Sierras Pampeanas low temperature thermochronologic dating methods, e.g. apatite fission track and (U-Th)/He dating, can provide constraints, because these techniques are suitable to constrain time, amounts and rate of cooling/erosion associated with mountain building, crustal deformation, extensional tectonics and landscape evolution (e.g. Gallagher et al. 1998; Farlay 2002; Ehlers et al. 2003; Stockli et al. 2003; Fitzgerald et al. 2006). To contribute to the knowledge of the exhumation history of the Sierras Pampeanas as well as an attempt to clarify its relationship to the Andean flat-slab subduction, we followed three different approaches investigating two different elevation profiles in the Sierra de Comechingones. We performed *i)* K-Ar dating on illite fine-fractions from brittle fault gouges to examine the brittle deformation history, *ii)* apatite fission track analysis and (U-Th)/He measurements of zircon and apatite, to reconstruct the exhumation and uplift history of the Sierra de Comechingones and to extend the post-metamorphic cooling path of basement (Steenken et al. 2010) to the low-temperature thermal history, as well as *iii)* Ar-Ar dating on volcanic rocks to evaluate the youngest flat-slab subduction related magmatism possibly indicating the eastward migration of the deformation into the foreland (e.g. Ramos et al. 2002).

3.2 Regional Setting and Geodynamic Evolution

The basement complex of the Sierras Pampeanas was developed by accretion of different allochthonous and parautochthonous terranes during the Late Proterozoic and the Early Paleozoic (e.g. Ramos 1988, 2009; Ramos et al. 2002; Steenken et al. 2004; Miller and Söllner 2005). Potential sutures indicating the margins of adjacent terranes, e.g. Río del la Plata Craton, Pampia, and Cuyania, are illustrated by Ramos et al. (2001, 2002).

During the Late Triassic - Early Jurassic and the Early Cretaceous, the basement was affected by extensional deformation (e.g. Uliana et al. 1989; Ramos et al. 2002), whereby the latter period was

related to the opening of the South Atlantic Ocean at these latitudes (Uliana et al. 1989; Rossello and Mozetic 1999). According to Ramos et al. (2002) master faults related to the rift events were generated by reactivating the sutures between the different cratonic terranes. Continental basins, usually with a half-graben geometry, were developed all over this region, recording mostly the Early Cretaceous stages of rifting (Schmidt et al. 1995).

The extensional fault systems were inverted during the Andean compression caused by subduction of the Nazca Plate beneath the South American plate in the Cenozoic, thus controlling the inception and uplift of the basement blocks forming the Sierras Pampeanas. Accordingly, these basement uplifts have been recognized as a broken foreland of the Andean orogeny (Jordan and Allmendinger 1986) and regarded to be part of the Andean building (Regnier et al. 1992; Costa et al. 2006). The geometry of these reverse faults and thrusts is controlled by basement structures generally resulting in a listric shape and a dominant dip to the east, which is expressed by the referred morphologic asymmetry of the basement blocks (Fig. 3.2a, b; e.g. González Bonorino 1950; Gordillo and Lencinas 1979; Criado Roque et al. 1981; González Diaz 1981; Jordan and Allmendinger 1986; Introcaso et al. 1987; Massabie 1987; Costa and Vita Finzi 1996; Ramos et al. 2002).

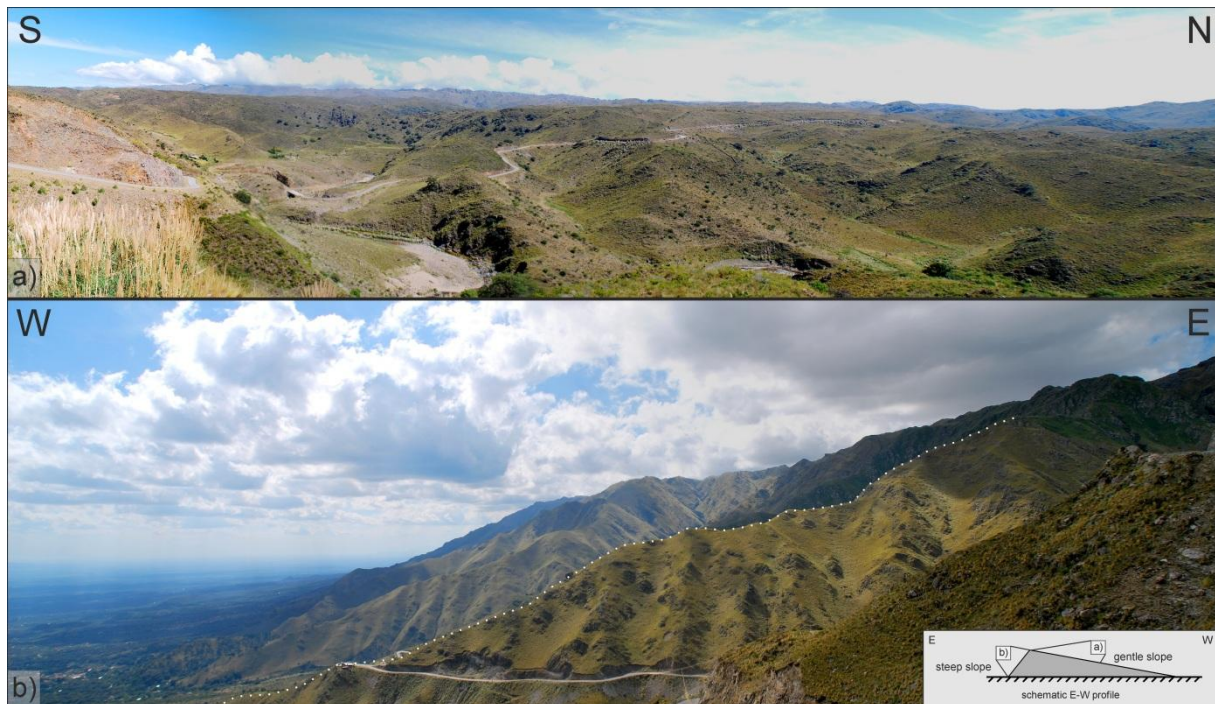


Fig. 3.2: Photos showing the two extremities of relief within the Sierras Pampeanas. a) The gentle inclined, low relief slope on the eastern side of the Sierras de San Luis near the village of El Trapiche (view to the west). b) The steep inclined, high relief slope on the western side of the Sierra de Comechingones near the village of Merlo (view to the north). The schematic sketch in the lower right indicates point of view.

Within Miocene times (18-11 Ma) the Juan Fernández ridge is incorporated into the subduction (Fig. 3.3; e.g. Yañez et al. 2001; Ramos et al. 2002) resulting in a shallowing of the Nazca Plate subduction angle (Barazangi and Isacks 1976; Pilger 1981; Jordan and Allmendinger 1986). This flat-slab subduction (Fig. 3.4) is set to be indicated by *i*) the depth of the Wadati-Benioff zone, *ii*) a gap of

active arc volcanism between 27°S and 33°S, *iii*) the uplift and deformation of Sierras Pampeanas starting at the Late Miocene-Pliocene transition, and *iv*) the timing and location of magmatic activity within the area of the Sierras Pampeanas broken foreland (e.g. Barazangi and Isacks 1976; Pardo Casas and Molnar 1987; Smalley and Isacks, 1987, 1990; Cahill and Isacks 1992; Ramos et al. 2002; and references therein).

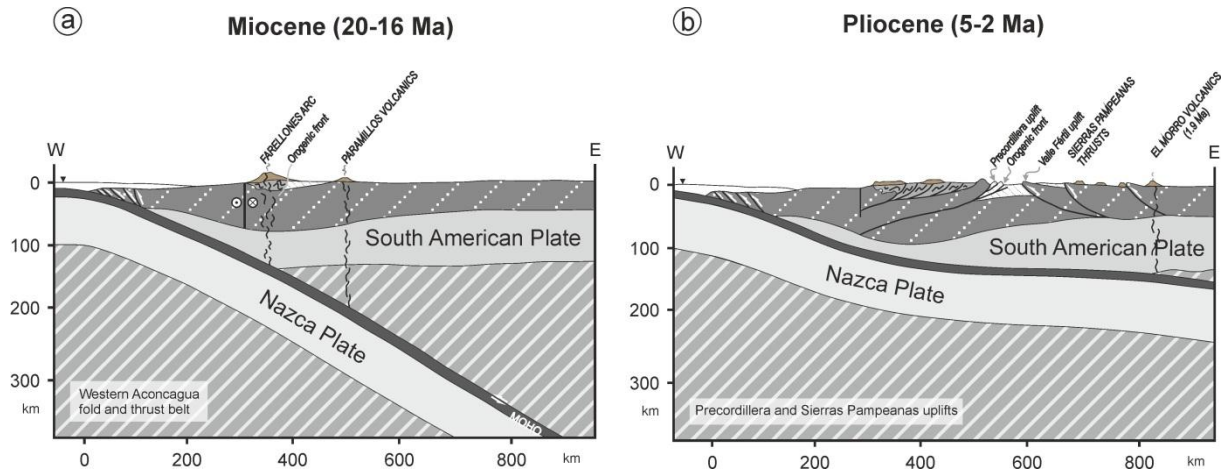


Fig. 3.3: Evolutional stages of the Andean system, including the Sierras Pampeanas, related to the shallowing Nazca plate during the Cenozoic (modified after Ramos et al. 2002). a) Subduction prior to the collision of the Juan Fernandez Ridge. b) Last stage of arc related magmatism within the Sierra del Morro prior to the present setting.

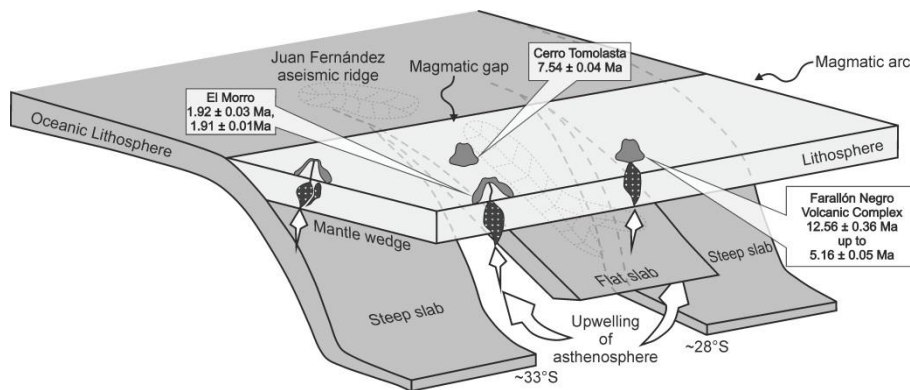


Fig. 3.4: Schematic sketch of the shallowing Nazca Plate (modified from Kerrich et al. 2000; Urbina 2005). The ages for Cerro Tomolasta and El Morro are from this publication. The ages for the Farallón Negro Volcanic Complex 12.56 ± 0.36 Ma up to 5.16 ± 0.05 Ma represent K-Ar data from Ramos et al. (1991).

During the Upper Miocene and the Pliocene the outcropping area of magmatic and hydrothermal activity was shifted eastward to the eastern part of the Sierras Pampeanas (Kay et al. 1991). Here, volcanic buildings crop out along a WNW trending belt between the volcanic field of La Carolina (Fig. 3.5) in the west and the Sierra del Morro in the east, standing out from the erosion surfaces smooth landscape. These rocks comprise andesites, dacites, latites, trachytes and hydrothermal altered rocks showing decreasing ages from 11.2-6.3 Ma in the west to 1.9 Ma in the east (Llambías and Brogioni 1981; Sruoga et al. 1996; Urbina et al. 1997; Urbina 2005; Ramos et al. 1991, 2002; Urbina and Sruoga 2008, 2009; and this study). Further, these volcanic rocks show a typical subduction signature (Kay et al. 1991; Kay and Gordillo 1994), thus marking the easternmost and youngest magmatic manifestation associated with the shallowing of the Nazca plate in the Andean flat-slab segment located 650-750 km east of the Peru-Chile trench (e.g. Ramos et al. 1991; 2002).

The uplift of the southeastern Sierras Pampeanas, e.g. Sierra de San Luis, Comechingones, and El Morro, as well as the termination of the magmatism within the Sierra del Morro in the Late Pleistocene indicates the formation of the present structure of the Andean system (Costa 1992; Ramos et al. 2002). Subduction related shortening and deformation in the Sierras Pampeanas during the Quaternary is mainly accommodated by the ranges bounding reverse faults mostly located at the western footslope of the Sierras (Massabie 1976, 1987; Costa 1987, 1992, 1996, 1999; Kramer et al. 1995; Costa and Vita Finzi 1996; Costa et al. 2001; 2006).



Fig. 3.5: Photo showing the Late Miocene volcanic body of the Cerro Tomolasta in the La Carolina area (view from the Pampa de la Invernada towards the east). The volcanic edifices build up hills, dominating the landscape on the otherwise flat eastern hillslope of the Sierra de San Luis.

3.3 Applied Methods

3.3.1 Mineralogy and K-Ar Dating of Fault Fougues

In brittle near-surface faults, rocks are broken and crushed by tectonic movements. In these localized zones the increased surface creates a high chemical reactivity, allowing retrograde processes to produce fault gouges composed of authigenic hydrosilicates such as illite. Thus, formation time of the authigenic illite in a fault gouge can be correlated with periods of motion along the fault (e.g. Lyons and Snellenberg 1971; Kralik et al. 1987).

The illite crystallinity (IC) and polytypism are important indices for determining the grade of thermal evolution and very low-grade metamorphism grades. The IC values, which are inversely proportional to the illite crystallinity, are defined after Kübler (1964) as half-height width of the 10 Å XRD peak. The values for the illite crystallinity may range from 0.06 $\Delta^{\circ}2\theta$ for ideally ordered muscovite up to 1 $\Delta^{\circ}2\theta$ for illite/smectite mixed layers (Kübler 1964, 1967, 1968).

Kübler (1967) used boundary values of 0.42 $\Delta^{\circ}2\theta$ and 0.25 $\Delta^{\circ}2\theta$ to divide the zones of the very low grade metamorphism into, from lower to higher grade, diagenetic zone (IC > 0.42 $\Delta^{\circ}2\theta$), anchizone (0.42 $\Delta^{\circ}2\theta$ < IC < 0.25 $\Delta^{\circ}2\theta$) and epizone (IC < 0.25 $\Delta^{\circ}2\theta$), in which the corresponding temperatures for the two boundaries are around 150 °C and 300 °C respectively.

Thus, the IC values of authigenic fault gouge illite can be used to estimate the temperature experienced by the fault gouge sample. This information helps to interpret the dating results concerning the thermal evolution.

Polytypism (Bailey et al. 1977; Guinier et al. 1984) is a common phenomenon for layered silicate minerals such as mica, chlorite and kaolinite. For illite the most common polytypes are the $1M_d$, $1M$ and $2M_1$ (e.g. Reynolds and Thomson 1993). With raising temperature, illite shows irreversible polytype transformation of $1M_d \rightarrow 1M \rightarrow 2M_1$ (Hunziker et al. 1986). Generally, illite has $1M_d$ and $1M$ polytypes in a diagenetic zone, a mixture of $1M$ and $2M_1$ polytypes in the anchizone and sole $2M_1$ polytypes in the epizone (e.g. Bailey 1966; Środoń and Eberl 1984). We measured a total of six fault gouge samples taken from the Merlo profile (Fig. 3.6). Details on the analytical procedure are given in the Chapter 0.

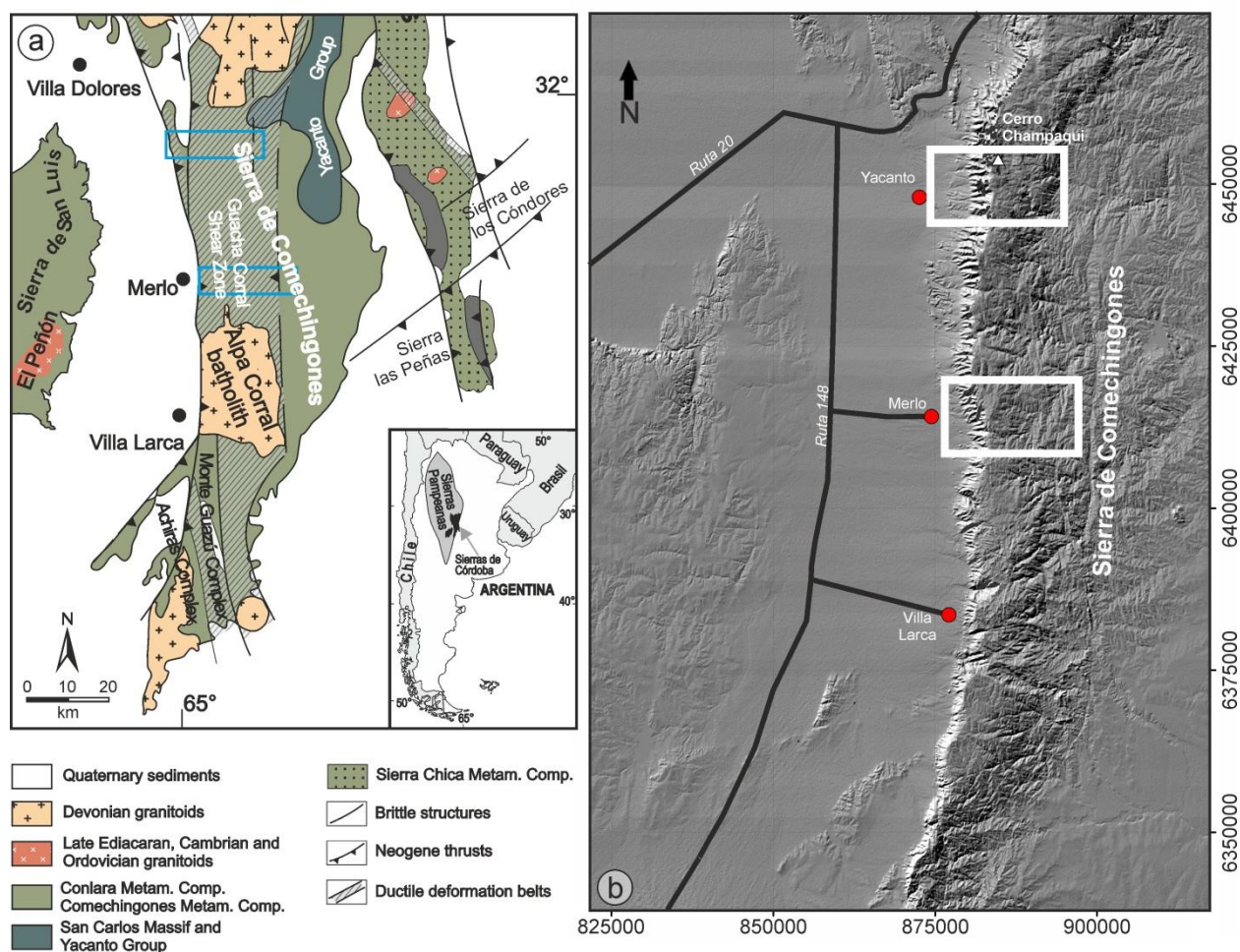


Fig. 3.6: Overview of the working area. a) Schematic geological map of the Sierra de Comechingones (modified after Martino et al. 2003; Siegesmund et al. 2006; Steenken et al. 2010). The coordinates are given in longitude and latitude. The blue frames mark both sampled profiles (referred to as Merlo and Yacanto profile in the text). For reference a schematic map of Argentina, including the Sierras Pampeanas, is shown in the lower right. b) Digital elevation model of the working area. The coordinates are given in UTM coordinates. The white frames define the sampled profiles.

3.3.2 Apatite Fission Track and (U-Th)/He Thermochronology

The combination of apatite fission track dating (AFT) as well as (U-Th)/He dating on zircon (ZHe) and apatite (AHe) allows the reconstruction of low temperature exhumation history (e.g. Hurley 1954; Armstrong 1966; Wagner and van Den Haute 1992; Farley et al. 1996; Wolf et al. 1996). The thermal sensitivity of the apatite fission track method referred to as partial annealing zone (PAZ; Gleadow and Fitzgerald 1987) ranges between 130-70 °C (e.g. Donelick et al. 1999; Ketcham et al. 1999). Regarding the (U-Th)/He method this interval is called partial-retention zone (PRZ; e.g. Baldwin and Lister 1998; Wolf et al. 1998). The temperature of the PRZ for the (U-Th)/He system ranges from around 65°C to approximately 30°C for apatite and from about 185°C to 135°C for zircon (e.g. Reiners and Brandon 2006).

A total of eight samples were collected from the Yacanto profile (Fig. 3.6). Three of them were dated by the AFT and ZHe method. AHe ages were obtained from all samples. Details on the analytical procedure are given in the appendix.

3.3.3 Ar-Ar Dating of Volcanic Rocks

Ar-Ar ages in volcanic rocks can be interpreted as the age of effusion as closing temperatures for different mineral species are negligible due to rapid cooling (e.g. McDougall and Harrison 1999). In this study Ar-Ar dating was performed following standard methods quoted elsewhere (e.g. Layer et al. 1987).

Hornblende and whole rock samples of three trachyandesites from discrete exposures have been dated (Fig 3.1). Details on the analytical procedure are given in the appendix.

3.4 Results

3.4.1 K-Ar Dating

Eighteen K-Ar ages from fractions of six samples were obtained from the Merlo profile (Fig. 3.6) in this study (Table 3.1; Fig. 3.7). The ages range from Early Mississippian to Early/Middle Jurassic (342–174 Ma).

All samples show an age gap between fractions, ranging from 1.5 Ma up to 53.3 Ma (Fig. 3.8). Only the two smallest fractions of sample APG 82-09 show overlapping ages within error.

Radiogenic ^{40}Ar content ranges from 81.0 % to 99.7 % indicating reliable analytical conditions for all analyses. Potassium contents range from 1.03 % (APG 82-09, <0.2 μm) to 5.88 % (APG 85-09, 2–6 μm).

XRD analyses of all samples confirm that illite, chlorite and kaolinite are the major clay mineral components in the various fractions, with minor traces of quartz in almost all sample fractions. Minor traces of potassium feldspar might be present in the 2–6 μm fractions but none is found in the

<0.2 μm and <2 μm fractions. Glycolated XRD analyses were carried out to investigate the potential occurrence of expandable mixed-layers of illite and smectite. Major amounts of illite/smectite were found in the <0.2 μm fraction and minor amounts also in the <2 μm fractions. No illite/smectite mixed-layers were observed in the 2-6 μm fractions (Table 3.2).

Table 3.1: K-Ar ages, illite crystallinity and illite polytypism of the investigated mineral fractions.

Sample No.	Grain size fraction	K-Ar data				Illite crystallinity			Illite polytypism
		K ₂ O [wt%]	⁴⁰ Ar* [nl/g] STP	⁴⁰ Ar* [%]	Age [Ma]	±2σ-error [Ma]	air dry [Δ°2θ]	glycolated [Δ°2θ]	
APG 82-09	< 0.2 μm	1.03	8.68	89.80	244.0	6.1	0.281 ²	0.244 ³	1Md > 2M ₁ > 1M
	< 2 μm	1.69	14.04	84.69	240.9	6.3	0.282 ²	0.275 ²	1Md > 2M ₁ > 1M
	2-6 μm	4.90	43.71	91.79	257.3	5.6	0.180 ³	0.211 ³	2M ₁ ≥ 1Md > 1M
APG 85-09	< 0.2 μm	2.33	18.84	89.63	234.8	5.0	0.491 ¹	0.373 ²	1Md > 2M ₁ > 1M
	< 2 μm	3.32	30.62	95.52	265.5	5.7	0.296 ²	0.272 ²	1Md > 2M ₁ > 1M
	2-6 μm	5.88	57.14	94.81	278.6	5.9	0.161 ³	0.164 ³	2M ₁ > 1Md > 1M
APG 89-09	< 0.2 μm	1.44	8.68	87.39	177.9	4.5	0.428 ¹	0.377 ²	1Md > 2M ₁ > 1M
	< 2 μm	2.58	19.73	96.69	222.7	7.0	0.273 ²	0.234 ³	1Md > 2M ₁ > 1M
	2-6 μm	5.37	48.27	98.17	259.2	5.5	0.163 ³	0.155 ³	2M ₁ > 1Md > 1M
APG 90-09	< 0.2 μm	1.62	9.54	81.01	174.0	4.9	0.530 ¹	0.332 ²	1Md > 2M ₁ > 1M
	< 2 μm	2.33	17.41	91.56	218.0	6.1	0.400 ²	0.313 ²	1Md > 2M ₁ > 1M
	2-6 μm	3.61	33.65	97.03	268.1	5.7	0.171 ³	0.173 ³	2M ₁ > 1Md > 1M
APG 91-09	< 0.2 μm	2.11	17.05	93.43	234.6	6.7	0.390 ²	0.358 ²	1Md > 2M ₁ > 1M
	< 2 μm	3.39	35.67	97.11	299.9	6.4	0.272 ²	0.266 ²	2M ₁ > 1Md > 1M
	2-6 μm	4.17	48.81	98.55	330.7	7.1	0.187 ³	0.179 ³	2M ₁ >> 1Md > 1M
APG 92-09	< 0.2 μm	2.21	18.62	95.07	244.0	5.7	0.441 ¹	0.331 ²	1Md > 2M ₁ > 1M
	< 2 μm	3.57	38.97	98.65	310.2	7.2	0.260 ²	0.247 ³	2M ₁ > 1Md > 1M
	2-6 μm	3.81	46.21	98.44	341.6	7.9	0.168 ³	0.170 ³	2M ₁ >> 1Md > 1M

* = radiogenic, STP = standard pressure and temperature conditions, ¹ = diagenetic, ² = anchizonal, ³ = epizonal, > more, >> much more

The illite crystallinity (IC) of all analyzed samples varies from 0.155 Δ°2θ to 0.530 Δ°2θ (Table 3.1). The IC values from the air-dried <0.2 μm fractions indicate, that all but one developed under diagenetic conditions, whereas the fractions of <2 μm and 2-6 μm yield anchi- to epimetamorphic values. Variations in the Δ°2θ between the glycolated and the air-dry measurements correspond to the presence of illite/smectite mixed-layers (Table 3.2). No systematic variation with respect to the sample location is observed.

The analyzed illite fractions are composed mainly of the 1M_d and 2M₁ polytypes and only subordinate 1M illite. The 1M_d polytype is dominant in the <0.2 μm fractions throughout all analyzed samples. In the <2 μm fraction, the 1M_d is also the dominant polytype, except samples APG 91-09 and APG 92-09 showing the 2M₁ polytype as dominant. The 2-6 μm fractions are mostly made up by 2M₁ illite. The content of different polytypes correlates with obtained IC values (Table 3.2).

3.4.2 Zircon (U-Th)/He Ages

The zircon samples yield (U-Th)/He ages between 276.8 ± 6.4 Ma (Early Triassic) and 141.5 ± 3.4 Ma (Early Cretaceous) showing a positive correlation with elevation (Fig. 3.9). The weighted means of the four samples varies from 263.6 Ma to 198.9 Ma (Table 3.3).

Table 3.2: Results of X-ray diffraction analyses from the sample material fractions.

Sample No.	grain size fraction	Mineralogy					
		Illite	Chlorite	Kaolinite	Smectite	Quartz	K-feldspar
APG 82-09	< 0.2 μm	+	+	o/-	-	o	-
	< 2 μm	+	+	o/-	+	-	-
	2-6 μm	+	+	o/-	o	-	-
APG 85-09	< 0.2 μm	+	-	+	+	o	-
	< 2 μm	+	o	+	o	o	-
	2-6 μm	+	-	o	-	+	o/-
APG 89-09	< 0.2 μm	o	+	o	++	-	-
	< 2 μm	+	+	+	o	o	-
	2-6 μm	+	+	+	-	o	o/-
APG 90-09	< 0.2 μm	+	-	+	+	-	-
	< 2 μm	+	o	+	o	o	-
	2-6 μm	o	o	+	-	+	o/-
APG 91-09	< 0.2 μm	+	+	-	+	-	-
	< 2 μm	+	+	+	o	o	-
	2-6 μm	+	+	+	-	+	o/-
APG 92-09	< 0.2 μm	o	+	o	+	-	-
	< 2 μm	+	+	o/-	o	-	-
	2-6 μm	+	++	o	-	+	o/-

++ = dominant, + = abundant, o = less abundant, o/- = unclear, possibly traces, - none

3.4.3 Apatite Fission Track Ages

The three analyzed samples show apparent apatite fission track ages that range between the Early Jurassic and the Early Cretaceous (Table 3.4). Although less constrained than in the (U-Th)/He ages, which is due to less analyzed samples, a distinct positive correlation of age with increasing altitude is obvious between the samples APM 14-08 and APM 09-08 along the investigated elevation profile (Fig. 3.9). The apparent age of the topographic lower sample APM 14-08 is 143.7 ± 13.6 Ma, whereas APM 09-08 (on the top of the range) shows an age of 169.7 ± 14.4 Ma. However, an exception of this trend depicts APM 15-08. This sample is located at 831 m a.s.l. and has an apparent age of 196.1 ± 17.8 Ma (Table 3.4).

Regarding the fission track length, all three samples are characterized by distinct shortened tracks. The mean track length varies between 12.13 μm and 12.5 μm with s.d. of ± 1.34 -1.75 μm (Table 3.4). Further, the track length distribution of APM 15-08 and APM 14-08 is unimodal distributed (Fig. 3.9). In contrast, APM 09-08 is characterized by a bimodal track length distribution (Fig. 3.9). The mean Dpar values (etch pit diameter) for the three samples range between 1.64 μm and 1.75 μm (Table 4).

Table 3.3: Zircon and apatite (U-Th)/He data of the samples from the elevation profile near Yacanto.

Sample No. (rocktype)		⁴ He vol. [ncc]	s.e. [%]	²³⁸ U mass [ng]	s.e. [%]	²³² Th mass [ng]	s.e. [%]	Th/U ratio	Sm mass [ng]	s.e. [%]	Ejection correct. (Ft)	uncorrect. He age [Ma]	Ft- correct. He age [Ma]	1s [Ma]	Sample weighted average age [Ma]
Zircon															
APM-09-08 (migmatite)	z1	85.368	1.6	3.186	1.8	0.533	2.4	0.2	0.070	7.5	0.80	209.6	262.6	6.2	263.6
	z2	64.745	1.6	2.601	1.8	0.206	2.4	0.1	0.030	7.1	0.79	198.9	250.2	5.9	
	z3	135.567	1.6	4.397	1.8	1.262	2.4	0.3	0.077	10.1	0.85	234.3	276.8	6.4	
APM-11-08 (granite)	z1	44.875	1.6	2.118	1.8	0.396	2.4	0.2	0.056	5.8	0.74	165.7	224.9	5.3	253.6
	z2	35.791	1.6	1.494	1.8	0.133	2.5	0.1	0.010	6.3	0.75	191.1	255.7	6.1	
	z3	42.684	1.6	1.581	1.8	0.350	2.4	0.2	0.019	5.9	0.76	208.7	275.2	6.4	
APM-12-08 (migmatite)	z1	23.449	1.6	1.056	1.8	0.081	2.5	0.1	0.004	6.9	0.73	177.9	242.9	5.8	232.0
	z2	12.829	1.6	0.606	1.8	0.085	2.5	0.1	0.005	6.8	0.73	167.2	228.4	5.4	
	z3	12.208	1.6	0.584	1.8	0.093	2.5	0.2	0.006	6.7	0.74	164.5	223.8	5.3	
APM-15-08 (granite)	z1	171.524	1.6	12.877	1.8	0.649	2.4	0.1	0.140	30.3	0.76	108.0	141.5	3.4	198.9
	z2	81.171	1.6	4.470	1.8	1.480	2.4	0.3	0.890	29.6	0.76	137.7	181.2	4.2	
	z3	136.096	1.6	5.345	1.8	0.917	2.4	0.2	0.909	27.7	0.81	199.1	245.2	5.8	
Apatite															
APM 9-08 (migmatite)	a1	1.876	1.7	0.119	1.9	0.006	5.7	0.05	0.880	5.1	0.83	120.1	145.2	3.5	120.0
	a2	3.060	1.7	0.242	1.8	0.009	4.6	0.04	1.787	4.9	0.91	97.1	106.8	2.5	
	a3	0.507	1.9	0.051	2.2	0.001	17.6	0.02	0.397	4.9	0.83	76.7	92.6	2.5	
	a4	1.625	1.7	0.118	1.9	0.002	12.3	0.02	0.726	4.9	0.86	107.0	124.3	3.1	
APM 10-08 (migmatite)	a1	0.859	1.8	0.073	2.0	0.004	7.2	0.05	1.074	5.8	0.85	85.8	100.9	2.5	94.9
	a2	0.925	1.8	0.090	1.9	0.004	7.1	0.04	0.886	5.7	0.89	77.8	87.9	2.2	
APM 11-08 (granite)	a1	0.115	2.3	0.017	4.6	0.000	638.9	0.00	0.223	5.0	0.75	50.3	67.0	3.1	76.9
	a2	0.119	2.5	0.014	5.0	0.004	7.1	0.31	0.119	5.0	0.74	62.5	84.4	4.1	
APM 12-08 (migmatite)	a1	0.133	2.4	0.021	3.0	0.009	4.50	0.41	0.607	5.7	0.86	39.0	45.2	1.5	77.5
	a2	0.885	1.8	0.083	1.9	0.004	4.2	0.05	1.969	15.1	0.79	80.1	101.6	2.7	
	a3	1.085	1.7	0.151	1.8	0.004	4.3	0.03	1.160	15.7	0.80	53.3	66.7	1.9	
	a4	0.731	1.8	0.091	1.9	0.005	3.9	.06	1.209	16.0	0.75	59.4	79.0	2.3	
APM 13-08 (migmatite)	a1	1.595	1.7	0.105	1.9	0.001	20.2	0.01	0.952	4.9	0.87	115.4	133.2	3.3	108.3
	a2	0.970	1.8	0.114	1.9	0.003	4.7	0.03	1.209	16.4	0.71	63.8	89.7	2.5	
	a3	4.434	1.7	0.428	1.8	0.003	5.1	0.01	1.950	16.8	0.72	82.0	113.9	2.8	
	a4	1.259	1.7	0.143	1.8	0.003	5.3	0.02	2.046	17.1	0.73	64.8	88.8	2.6	
APM 14-08 (migmatite)	a1	0.295	2.0	0.054	2.2	0.009	4.5	0.17	0.558	5.0	0.76	39.9	52.3	1.4	56.7
	a2	0.396	1.9	0.059	2.1	0.003	8.2	0.06	0.352	4.8	0.76	52.2	68.5	1.9	
	a3	0.463	1.9	0.070	2.0	0.006	5.6	0.09	0.479	4.9	0.75	50.4	67.1	1.8	
	a4	0.055	3.1	0.014	4.7	0.001	32.4	0.05	.0134	5.0	0.73	29.6	40.8	2.1	
APM 15-08 (granite)	a1	1.742	1.7	0.102	1.9	0.069	2.7	0.67	2.044	4.9	0.81	106.2	130.5	3.0	113.3
	a2	1.820	1.7	0.118	1.9	0.245	2.5	2.08	2.476	5.0	0.89	76.4	85.9	1.9	

⁴He, amount of in nano-cubic centimetre at standard pressure and temperature; s.e., standard error in percent; U²³⁸/Th²³², amount of in nanogram; uncorrect. age, uncorrected age; Ft, ejection correction factor calculated after Farley et al. (1996); correct. age, corrected age; 1s, standard deviation.

3.4.4 Apatite (U-Th)/He Ages

Apatite (U-Th)/He weighted mean ages vary from 57 Ma (APM 14-08) at the foothill to 108 Ma (APM 09-08) on the top of the profile showing a distinct positive correlation of age with increasing altitude (Fig. 3.9 and Table 3.3). The obtained ages of APM 11-08 and APM 12-08 are similar lying at around 75 Ma. In contrast, sample APM 10-08 is significantly older than APM 11-08.

Exceptions of the positive age with elevation correlation are represented by APM 13-08 and APM 15-08 (Fig. 3.9). These two samples show ages of 108.3 Ma and 113.3 Ma, respectively. The (U-Th)/He

ages of every apatite sample are younger or overlap within their 1σ error with its corresponding AFT-age in this profile (Table 3.3 and 3.4).

Table 3.4: Apatite fission track data of the samples from the elevation profile near Yacanto.

Sample No. (rocktype)	Latitude Longitude	Elevation (m)	n	ρ_s	N_s	ρ_i	N_i	ρ_d	N_d	$P(\chi^2)$ (%)	Age (Ma)	$\pm 1\sigma$ (Ma)	MTL (μm)	SD (μm)	N (L)	Dpar (μm)
APM 09-08 (migmatite)	32°03.252' 064°56.157'	2682	25	20.83	2670	14.994	1922	7.66	7368	42	169.7	14.4	12.5	1.75	58	1.72
APM 14-08 (migmatite)	32°03.007' 064°58.122'	1447	25	16.84	1279	14.404	1094	7.6	7368	2	143.7	13.6	12.3	1.34	50	1.75
APM 15-08 (granite)	32°02.818' 065°01.761'	831	25	17.22	1612	11.016	1031	7.83	7368	10	196.1	17.8	12.13	1.67	61	1.64

n , number of dated apatite crystals; ρ_s/ρ_i , spontaneous/induced track densities ($\times 10^5$ tracks cm^{-2}); N_s/N_i , number of counted spontaneous/induced tracks; N_d , number of tracks counted on dosimeter; $P(\chi^2)$, probability obtaining chi-squared value (χ^2) for n degree of freedom (where n is the number of crystals – 1); age $\pm 1\sigma$ is central age ± 1 standard error (Galbraith and Laslett 1993); ages were calculated using zeta calibration method (Hurford and Green 1983); glass dosimeter CN-5, and zeta value of 323.16 ± 25.31 a cm^{-2} ; MTL, mean track length; SD, standard deviation of track length distribution; N , number of tracks measured; Dpar, etch pit diameter.

3.4.5 Ar-Ar Dating

Three trachyandesitic rock samples from discrete outcrops have been investigated (Fig 3.1). The sample APM 6-09 was taken from trachyandesitic lava in a near top position (approx. 1950 m altitude) on the eastern side of Cerro Tomolasta. The rock displays a porphyritic texture and is build up by plagioclase, sanidine and amphibole phenocrysts in a fine-grained, dark grey groundmass of plagioclase, K-feldspar and amphibole. With 20–30 vol. % and up to 3 cm size, subhedral sanidine phenocrysts are the volumetrically dominant phase. The sample APM 7-09 represents a volcanic bomb, taken from a small outcrop within volcanoclastic layers on the southeastern slope of El Morro. The sample CT3 (Table 3. 5) represent a trachyandesitic lava, taken from the slope of Cerro Tala, directly east of the Sierra de Morro, approx. 2.5 km south of the village La Esquina. This sample shows sanidine phenocrysts up to 5 mm (10-20 vol. %) as well as microcrysts of plagioclase, hornblende and pyroxene in a pale grey groundmass of feldspar, amphibole and pyroxene.

All samples show whole rock and hornblende spectra with well-defined flat plateaus (Fig. 3.10). The whole rock ages exhibit better constrained plateau ages due to smaller errors of their individual degassing steps (Table 3.5, shown in bold, Fig. 3.10). The obtained ages range from 7.54 ± 0.04 Ma for the Cerro Tomolasta (APM 6-09 WR) to 1.91 ± 0.02 Ma for the Cerro Tala (CT3 Hbl., Fig. 3.4)

Table 3.5: Results of Ar-Ar analyses on trachyandesites sampled within the La Carolina volcanic field and the Sierra del Morro.

Sample No. (rocktype)	Locality Latitude Longitude	Mineral	Integrated age (Ma)	Plateau age (Ma)	Plateau information	Isochron age (Ma)	Isochron information
APM 6-09 (trachyandesite)	Cerro Tomolasta, La Carolina district -32.812719° -66.075278°	WR	7.60 ± 0.04	7.54 ± 0.04	4 of 7 fractions, 89% ³⁹ Ar release, MSWD = 0.70	7.45 ± 0.06	7 of 7 fractions, 89% ⁴⁰ Ar/ ³⁹ Ar _i = 312±5, MSWD = 1.86
APM 7-09 (trachyandesitic lava bomb)	Cerro El Morro, El Morro district -33.194399° -65.377763°	WR	1.92 ± 0.02	1.92 ± 0.03	6 of 7 fractions, 99% ³⁹ Ar release, MSWD = 2.03	1.95 ± 0.03	6 of 9 fractions, 89% ⁴⁰ Ar/ ³⁹ Ar _i = 293±2, MSWD = 1.71
		Hbl.	2.19 ± 0.15	2.17 ± 0.14	7 of 9 fractions, 98% ³⁹ Ar release, MSWD = 0.82	2.10 ± 0.23	9 of 9 fractions, 89% ⁴⁰ Ar/ ³⁹ Ar _i = 296±2, MSWD = 0.96
CT3 (trachyandesite)	Cerro Tala, El Morro district ~ -33.165472° ~ -65.366944°	WR	1.87 ± 0.03	1.91 ± 0.02	4 of 7 fractions, 82% ³⁹ Ar release, MSWD = 0.00	1.92 ± 0.03	6 of 7 fractions, 89% ⁴⁰ Ar/ ³⁹ Ar _i = 295±2, MSWD = 0.05
		Hbl.	1.93 ± 0.12	1.90 ± 0.13	6 of 9 fractions, 87% ³⁹ Ar release, MSWD = 0.80	1.85 ± 0.20	5 of 9 fractions, 89% ⁴⁰ Ar/ ³⁹ Ar _i = 296±3, MSWD = 1.29

Bold values indicate the ages which were used for discussion and explanation within the text. These ages represent whole rock ages showing better constrained plateau ages due to smaller errors of their individual degassing steps (Fig. 3.10).

3.5 Discussion

3.5.1 Constraints on Regional Cooling and Fault Activity by K-Ar Dating

The high-temperature (>300 °C) cooling history of the basement rocks of the Sierra de Comechingones was determined by K-Ar ages taken from biotite, muscovite and hornblende mineral separates from the hanging wall and footwall blocks of Guacha Corral shear zone, as well as from the shear zone itself (Steenken et al. 2010). The post-Pampean cooling of the basement of the Sierra de Comechingones took place in the Cambrian to Early Ordovician, as recorded by the K-Ar ages of pegmatitic hornblendes and muscovite booklets (513 Ma and 498 to 474 Ma, respectively). Based on the closure temperature for the K-Ar system between 500–430 °C (for non-recrystallised, coarse-grained muscovite booklets; e.g. Kirschner et al. 1996, Villa 1998) these ages allow the estimation of a cooling rate of approximately 9 °C/Ma after the Pampean granulite facies metamorphism (780–725 °C, 6–5.5 kbar; Guerreschi and Martino 2008). With a hypothetical geothermal gradient of 35 °C/km a maximum exhumation rate of about 0.1 mm/a can be estimated (Steenken et al. 2010). Middle to Late Silurian K-Ar biotite ages (426–420 Ma) document the cooling of the Sierra de Comechingones basement to approximately 300 °C (e.g. Purdy and Jäger 1976) and the final transition from ductile to brittle deformation regime - between 290–300 °C due to the onset of brittle

behavior of quartz below this temperature (e.g. van Daalen et al. 1999, Passchier and Trouw 2005 and references therein).

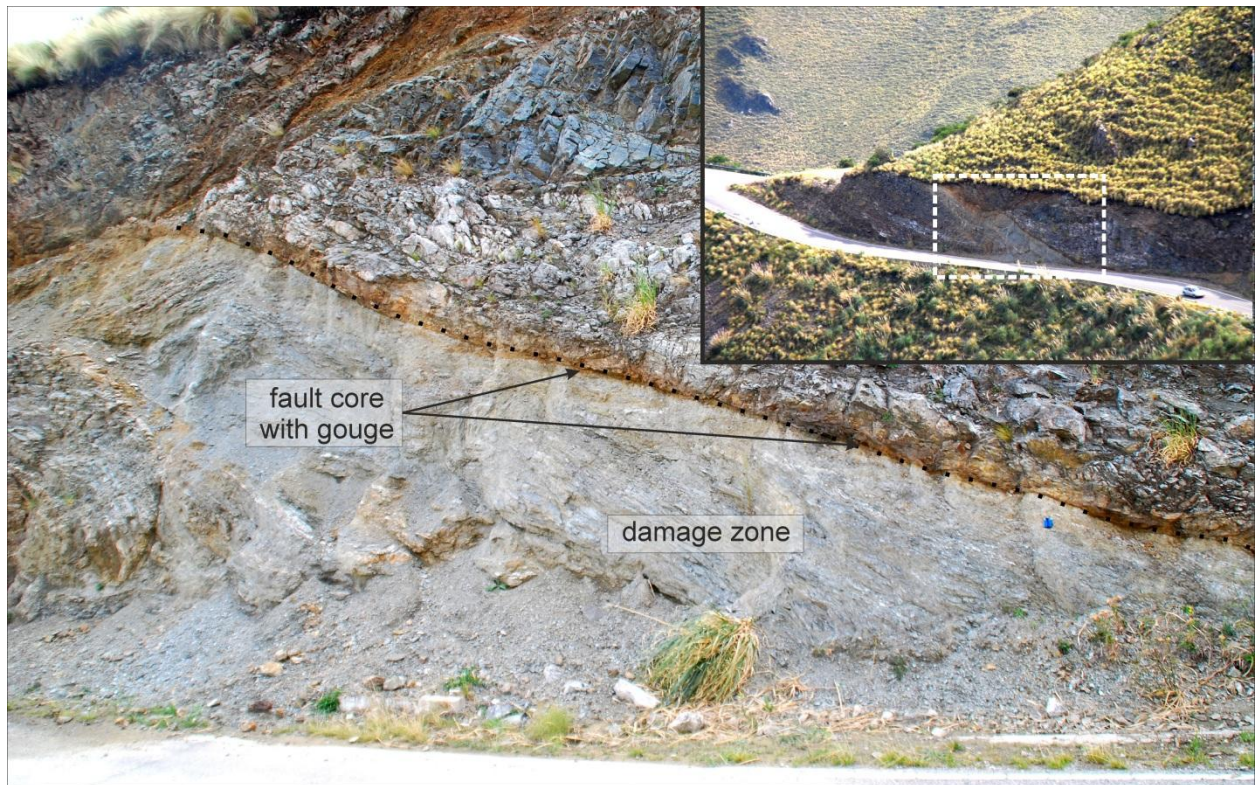


Fig. 3.7: Pictures of a brittle fault zone with a broad cataclastic zone and an approximately 8 cm wide fault gouge (sample APG 90-09) on the western slope of the Sierra de Comechingones, east of the village of Merlo (car in top right picture for scale, in lower picture blue compass on right side for scale).

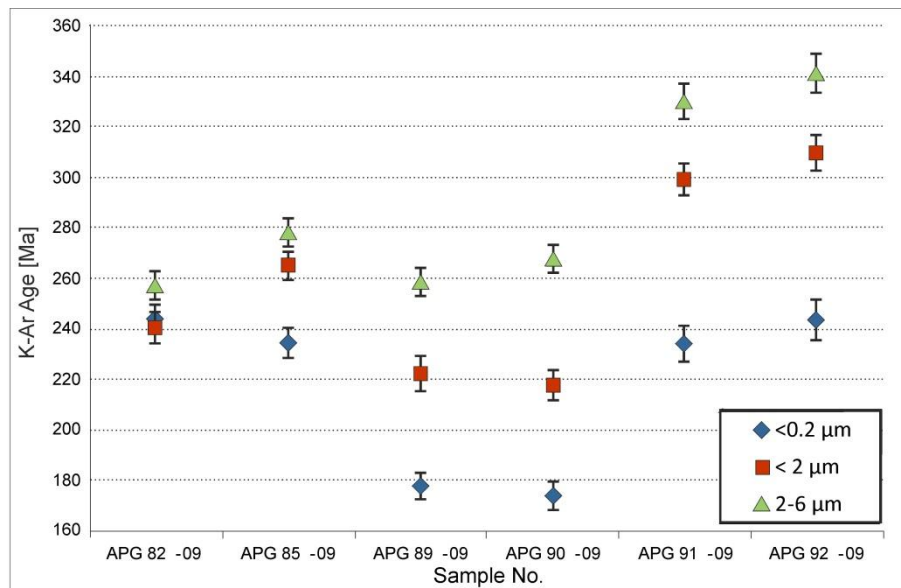


Fig. 3.8: K-Ar ages with errorbars (2σ) of all analyzed grain-size fractions and samples.

K-Ar data may also provide valuable information on fault activities by dating authigenic illites taken from fault gouges. In any case, the correlation of geological events and K-Ar ages from authigenic illite separates requires a careful consideration of the fundamental assumptions of the K-Ar- illite method (e.g. Clauer and Chaudhuri 1998).

One of the most important assumptions involved in the interpretation of K-Ar dating is a closed system behavior, thus no gain or loss of either ^{40}K or ^{40}Ar after the formation of the illite. A loss of Ar might be possible due to thermal diffusion effects or exchange reactions with hydrothermal fluids (e.g. Villa 1998). The importance of the effective diffusion radius on the closure temperature for the Ar-system has been demonstrated throughout a large number of publications (e.g. Dahl 1996, Villa 1998, Hodges 2003). These publications are focused on white micas with grain sizes $>200\text{ }\mu\text{m}$. In case of illite fine-fractions, available information is sparse. Hunziker et al. (1986) reported a closure temperature interval for the mica fractions $<2\text{ }\mu\text{m}$ of $260\pm30\text{ }^{\circ}\text{C}$, whereas Wemmer and Ahrendt (1997) found indication that fine-grained white micas (sericite $<2\text{ }\mu\text{m}$) did not behave as open systems, even at temperatures of $275\text{ }^{\circ}\text{C}$. Therefore, the closure temperature of fine grained mica has to be estimated somewhere between $275\text{--}350\text{ }^{\circ}\text{C}$ (Wemmer and Ahrendt 1997). Furthermore, errors in the acquisition of accurate K-Ar ages can arise from contamination by other K-bearing phases. Potassium-feldspar for example can, even being very much older, rejuvenate the age due to its low closure temperature of about $150\text{ }^{\circ}\text{C}$ (e.g. Fitz-Gerald and Harrison 1993). The major problem which must be considered is the possible mixture of illite formed by different events at different times. For authigenic, neocrystallised illite, the finest illite fraction should represent the most recently grown illite. Coarser grain-size fraction should yield older ages representing earlier illite forming events (e.g. Clauer et al. 1997).

In this study, we used the different illite polytypes to decipher different illite forming events, thus the time span of the deformation history. In low grade sedimentary rocks, the 2M_1 illite polytype is considered as detrital component, due to its restriction to epizonal conditions. The 1M_d and 1M polytypes are considered as authigenic products formed under diagenetic to anchimetamorphic, prograde conditions during subsequent burial (e.g. Grathoff and Moore 1996). In contrast to sedimentary environment, the illite investigated in this study originates from fault gouges developed from granitoid host rocks under retrograde conditions. Thus, the development of 2M_1 illite polytypes in a brittle fault gouge is possible due to subsequent cooling of the host rock and its passage through epizonal conditions, which are more or less equivalent with the ductile-brittle transition. Therefore, the 2M_1 polytype should record the onset of brittle deformation.

Contamination of mineral fine fractions ($<2\text{ }\mu\text{m}$, $<0.2\text{ }\mu\text{m}$) by cataclastically crushed muscovite of the host rock is very unlikely because of the very strong mechanical resistance of this mineral. Muscovite flakes would rather rotate parallel to the faulting plane than being grinded to extremely small particles (e.g. Wemmer 1991). If so, they could be identified by their excellent crystallinity (ca. $0.060\text{ }^{\circ}2\theta$).

Following the above stated assumptions, we interpret all illite to be neoformed, i.e. to be fault gouge related. Thus, the wide age span of the dated sample fractions documents a long lasting fault activity

from 341 Ma to 174 Ma, whereby the relationship of increasing K-Ar ages with increasing grain size (Table 3.1, Fig. 3.8) is consistent with increasing content of older $2M_1$ illite. Still, larger grain-size fractions have to be considered as mixtures of illites formed at different times and thus to be younger than the oldest illite forming event.

This interpretation is constrained by K-Ar ages from pegmatitic large-grained host-rock muscovites in the Merlo profile showing ages from 487 Ma to 431 Ma (Steenken et al. 2010), thus they are significantly older than all obtained K-Ar illite ages, even from fractions with high $2M_1$ polytype content (Table 3.1).

The six analyzed fault gouge samples show three different age groups, depending on their location along the sampled profile (Fig. 3.8). The samples from the footslope of the Sierra de Comechingones (samples 91-09 and 92-09) show the oldest ages of all analyzed samples. Neglecting a possible potassium contamination of the 2-6 μm fractions (Table 3.2), these samples are interpreted to document the onset of brittle deformation in this region. The onset of deformation under epizonal conditions is supported by the highest amount of $2M_1$ illite polytype in all analyzed samples (see Table 3.1). Thus, the oldest age of the 2-6 μm fraction of around 340 Ma (Fig. 3.8, APG 92-09) has to be considered as minimum age for the onset of brittle deformation in this region. This result is similar to a K-Ar muscovite age of 335 Ma from a fault scarp in the Sierras de Córdoba (Los Gigantes) obtained by Jordan et al. (1989). Additionally, this interpretation is supported by the mentioned K-Ar biotite ages from the Sierra de Comechingones, documenting the cooling below the ductile-brittle transition at Middle to Late Silurian times (K-Ar biotite ages, 426-420 Ma, Steenken et al. 2010). Deformation along the sampled faults in the footslope area ceased around 240 Ma, but brittle deformation continued along other faults, e.g. APG 82-09 to APG 90-09 (Fig. 3.8). The samples taken from the uppermost hillslope area (APG 82-09 and 85-09) show a narrower age span between fractions than the other samples, indicating a shorter period of activity along these faults. We interpret the comparatively small age span of sample APG 82-09 to represent a major short lived deformation event between 260 Ma and 240 Ma without any further reactivation of this fault. The samples APG 89-09 and 90-09 derived from the middle slope area show the youngest ages of all samples. Activity along these faults is interpreted to have started at similar times than the deformation on the uppermost hillslope area (around 260 Ma). The <2 μm fractions yield ages of 223 Ma and 210 Ma. As these fractions include the younger <0.2 μm fractions the onset of brittle deformation around 260 Ma is likely, matching the ages obtained from the 2-6 μm fraction. This gives evidence to a major Permo-Triassic (240-260 Ma) deformation event, which might be related to an earlier flat-slab subduction episode with subsequent compression at these latitudes during the Early-Middle Permian as proposed by Ramos and Folguera (2009). This event might also be related to the Permian deformed rocks of the Bajo de Velis (e.g. Costa et al. 1998; Azcuy et al. 1999).

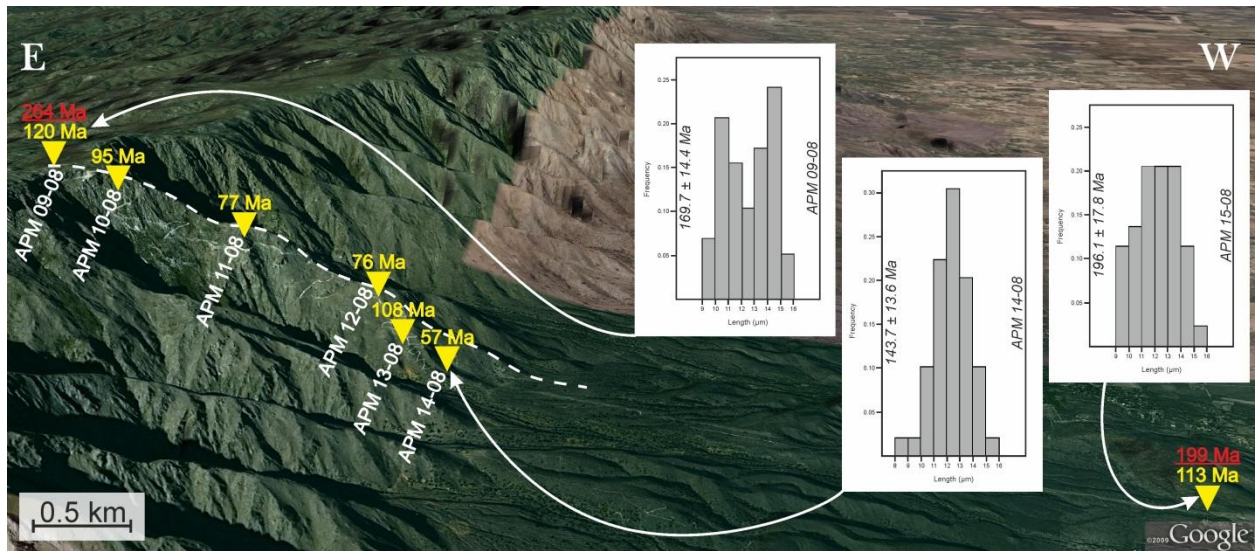


Fig. 3.9: Sampled elevation profile near Yacanto based on a satellite image from Google Earth proTM (2010), which is vertically exaggerated by a factor of 1.25. The yellow triangles mark the sample locations and the sample number is indicated by the white font. Also inserted are the apatite (U-Th)/He ages (yellow font), the zircon (U-Th)/He ages (red and underline font), and the apparent apatite fission track ages with their associated track length distribution is shown by the diagrams (also contain the sample number). The white, dashed line indicates the morphology along the profile.

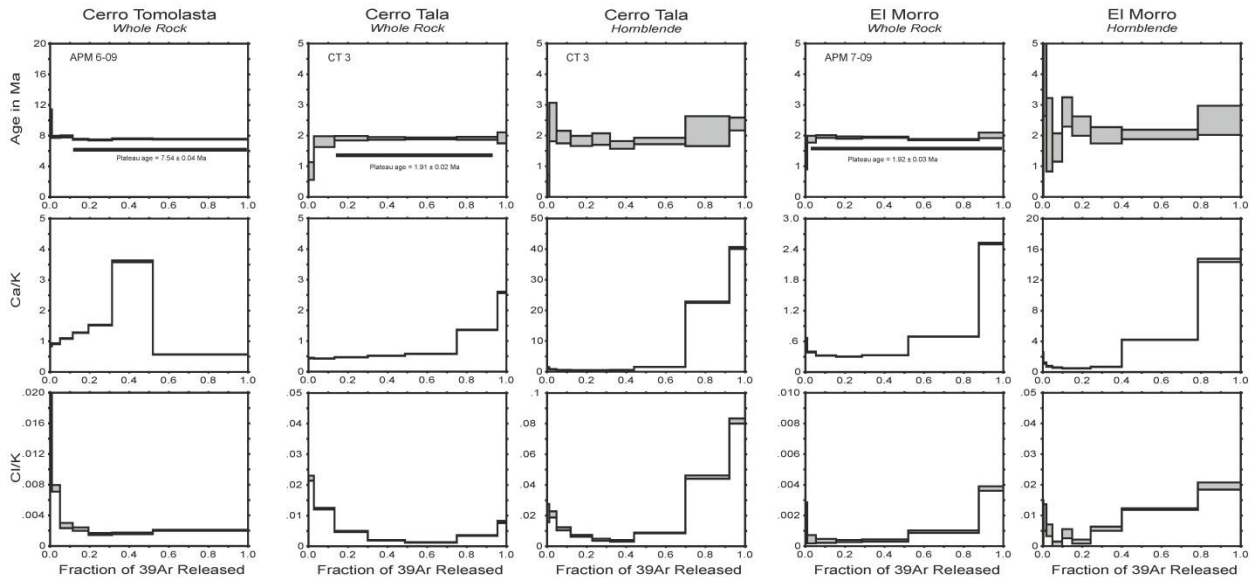


Fig. 3.10: Ar-Ar age spectra from analyzed trachyandesites showing whole rock (WR) and hornblende ages. A sample is considered to have a plateau if it has 3 or more contiguous fractions constituting at least 50% ^{39}Ar release and is significant at the 95% confidence level (as indicated by a Mean Square Weighted Deviates; MSWD $< \sim 2.5$). A sample is considered to form an isochron if it has 3 or more contiguous fractions that form a linear array that is significant at the 95% confidence level (MSWD $< \sim 2.5$).

The $<0.2 \mu\text{m}$ fraction documents a further reactivation around 175 Ma in the Middle Jurassic. This reactivation could be related to rifting processes in the region of the Sierras Pampeanas generated during the earliest stage of opening of the Southern Atlantic Ocean. These rifting processes are also documented by basaltic rocks at the Sierra de Las Quijadas (westernmost San Luis province), with K-Ar ages ranging from 164 to 107 Ma (González 1971; González and Toselli 1973; Yrigoyen 1975), 10–20 Ma younger than the youngest K-Ar age of 174 Ma (APG 90-09, $<0.2 \mu\text{m}$ fraction). The latter age is also interpreted to represent the last illite forming deformation event in this region, while brittle faulting may have continued below illite forming temperatures. These temperatures are estimated to

be approximately 75-110°C (e.g. Hamilton et al. 1992). Cooling below the illite forming temperature is constrained by apatite fission track and apatite (U-Th)/He ages from the Yacanto profile (Table 3.3). In fact, the youngest illites must overlap with the apatite fission track ages (cooling below 130-60°C), whereas the apatite (U-Th)/He ages (60-40°C) always must be younger. This can be observed for all analyzed samples. Non deformational illite formation by fluid percolation cannot be excluded but is unlikely due to consistency of the data set.

3.5.2 Thermal Modeling

Based on the apatite fission track ages and the length distribution as well as on the (U-Th)/He ages of zircon and apatite thermal modeling on two samples was performed following the approach of Ketcham (2005) using HeFTy, a computer program, which comprises tools to obtain more information from thermochronometric data through forward and inverse modeling.

These samples were chosen due to their position on the top (APM 9-08) and at the base (APM 15-08) of the vertical profile, containing the longest thermal memory of all samples and information of the youngest PRZ passage event, respectively. Two constraints were set to the thermal modeling: (1) the beginning of the time-temperature path was constrained by the zircon (U-Th)/He data and (2) the end of the time-temperature paths was set to 17 °C, according to annual mean temperatures in the study area (Müller 1996).

Both modeled samples show slow cooling until 210 Ma (APM 15-08) and 180 Ma (APM 09-08) (Fig. 3.11). Cooling rates are between 4 °C/Ma and 1.5 °C/Ma during this time, followed by a time of more or less constant temperature conditions, lasting for about 80 Ma. This behavior is also confirmed by the length distribution of the apatite fission tracks (Fig. 3.9) indicating a slow to moderate cooling through the PAZ. Final cooling below the effective (U-Th)/He closure temperature of apatite started around 90 Ma for APM 09-08 showing a cooling rate of 1.75 °C/Ma reaching near surface conditions at around 80 Ma. Additionally, modeling revealed a possible burial event between 130 Ma and 90 Ma which might be related to the Early Cretaceous rifting event mentioned above. In contrast to sample APM 09-08, the onset of final cooling for APM 15-08 is far less constrained. Cooling below 60 °C probably started around 120 Ma with an average cooling rate of less than 0.5 °C/Ma. However, these cooling rates are just a rough approximation concerning the possible range of good fitting time-temperature paths (Fig. 3.11), but are similar to cooling rates obtained by Jordan et al. (1989) based on fission track data from one single sample nearby the area regarded in this study.

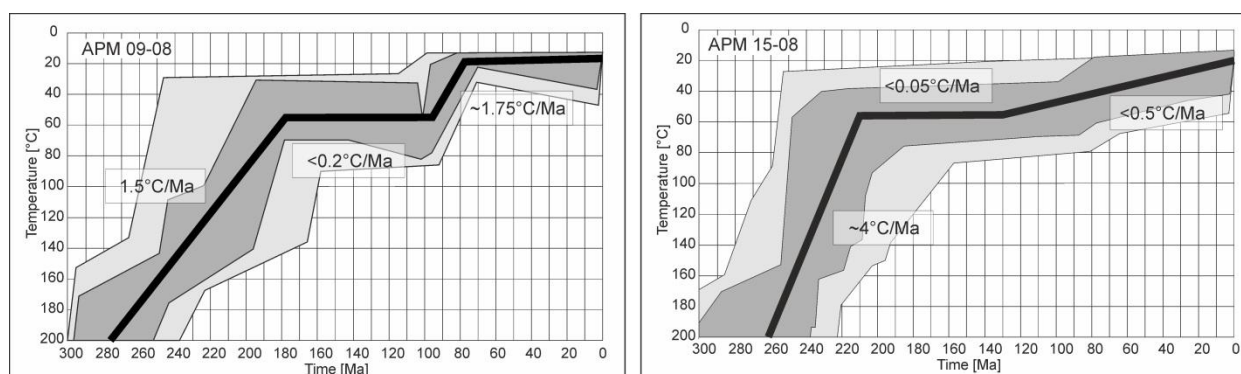


Fig. 3.11: Apatite fission track and (U-Th)/He thermal history modeling results using HeFTy (Ketcham 2005); light grey paths: acceptable fit, dark grey: good fit, black line: best fit. Also given are cooling rates considering the best fit path. a) for sample APM 09-08. b) for sample APM 15-08.

A positive age-elevation trend, constrained by the used low temperature geochronometers, usually allows a direct estimation of long-term exhumation rates, assuming that the closure isotherm of the employed systems remained flat and stationary during cooling (Stüwe et al. 1994). However, our samples are not from a pure vertical profile but show considerably horizontal distances between samples wherefore we abstained from calculating denudation rates.

3.5.3 AFT and AHe Ages

Many apatite grains show (U-Th)/He ages around 70-80 Ma (Table 3.3) indicating cessation of the thermochronological record within the Yacanto profile implying that our samples left the PRZ at that time (Fig. 3.12; e.g. Fitzgerald 2002, Fitzgerald et al. 1999, 2006). Thus, no cooling history younger than Late Cretaceous is recorded by the used methods. The apparent Early Cretaceous ages of APM 13-08 – APM 15-08 are too old and can be explained by *i)* APM 13-08 is probably related to a rockslide evidenced in aerial photographs *ii)* a single grain age of APM 15-08 is contaminated by He-bearing inclusions. Excluding this single grain age a weighted mean age of 85 Ma is calculated still being older than sample APM 14-08. This discrepancy in the age-elevation trend is due to thrusting sample APM 14-08 above APM 15-08 (Fig. 3.13). This is also supported by the apatite fission track ages of these samples, indicating that APM 15-08 passed the partial annealing zone earlier than APM 14-08 (Fig. 3.9, Table 4). In contrast, the relatively decreased apatite (U-Th)/He age of APM 14-08 compared to the samples APM 11-08 and APM 12-08 is probably related to the small radius of crystal four which shows an age of around 40 Ma (Table 3.3). Rejecting this grain due to its size results in a mean age of nearly 70 Ma, confirming the mentioned time when the investigated samples left the PRZ (Fig. 3.12).

A geothermal gradient of approximately 26 °C/km as suggested by Sobel and Strecker (2003) for the Northern Sierras Pampeanas was used to characterise the depth of the PRZ. Using this gradient the upper thermal boundary of the PRZ is located in 2300 m depth. Thus, the final uplift, including the younger Andean deformation, is constrained to a maximum of 2300 m since the passage of analyzed samples through the PRZ at around 80-70 Ma. Due to the difference in elevation of approximately

1850 m between sample APM 15-08 and APM 09-08 within the vertical profile, the amount of eroded thickness from the top of the profile can be constrained to not exceed 450 m since 80 Ma. Otherwise, the apatite (U-Th)/He ages from the footslope area of the profile would yield younger ages. This information is used to calculate a very rough approximation of the erosion rate, affecting the area of the profile, yielding a value of ≤ 6.4 m/Ma (0.006 mm/a), indicating very stable conditions concerning erosional processes since around 80 Ma. These rates confirm denudation rates of 0.01 mm/a between approximately 260 Ma and 120 Ma estimated by Jordan et al. (1989). Therefore, it is appropriate to extend the period of a quiet stable setting within the Sierras Comechingones, basing on our new thermochronological data, to the Late Paleozoic. Anyway, this does not contradict with the structural evolution model usually accepted for the Sierras Pampeanas (Criado Roque et al. 1981; Jordan and Allmendinger 1986; Costa 1992; Ramos et al. 2002; among others) but places constraints on the maximum possible uplift during the Andean orogeny. If the Comechingones fault had evolved from a Mesozoic extensional fault later inverted by Neogene shortening, then the overall displacement related to the Andean orogeny might be larger than the current topographic relief at the conducted crosssections.

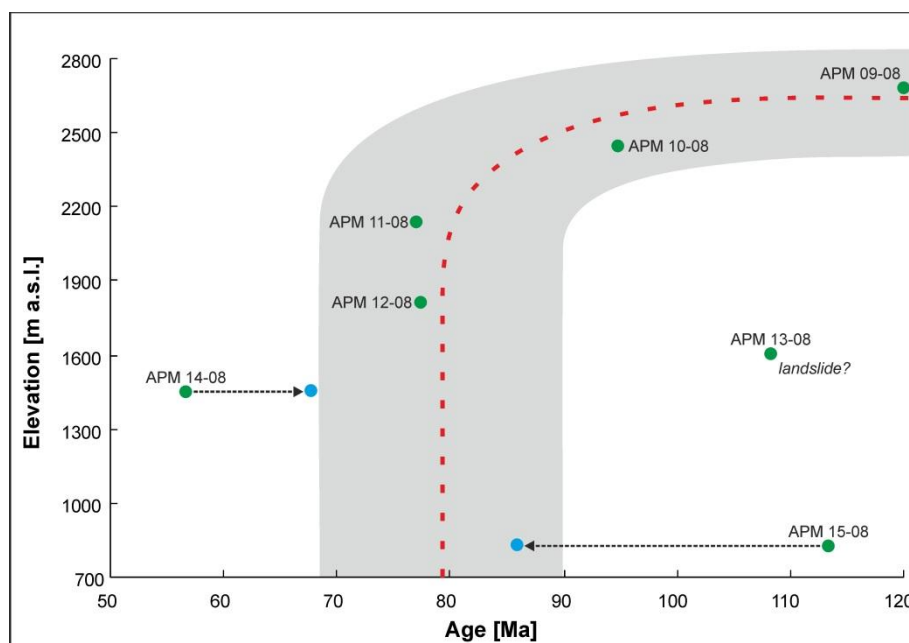


Fig. 3.12: Elevation of the samples plotted against their AHe age showing a cluster at around 80 Ma indicating that they passed the PRZ at that time (e.g. Fitzgerald 2002; Fitzgerald et al. 1999, 2006). Arrows indicate shifting of the age after recalculating (further details are explained in the text). The grey area indicates an error in age of approximately 10 Ma. APM 13-08 is probably affected by a landslide.

3.5.4 Low Temperature Exhumation Model

The exhumation history for the period before 80 Ma is less constrained due to the lack of e.g. zircon fission track data. Two scenarios can be discussed based on the obtained low temperature data. First, the exhumation of our samples above the 60 °C isotherm is induced by erosion commencing during the Early Cretaceous (Fig. 3.13). This suggests that the area of the Sierra de Comechingones was already characterized by a positive relief, a relatively stable setting, whereby the morphologic height acted as sedimentary source (Fig. 3.13a). The new, modeled cooling path of APM 9-08 (Fig. 3.11a) shows a cooling rate of less than 0.2°C/Ma between 180 Ma and 100 Ma, comparable to the less

constrained data presented by Jordan et al. (1989). Also Carignano et al. (1999) postulated that the area of the Sierras Pampeanas were characterized by geomorphological positive elements showing evidence of erosional cycles forming several planation surfaces during the Jurassic and the Cretaceous. The related sediment flux was deposited in Cretaceous intracratonic rift basins (i.e. Sierra Chica Basin and General Levalle Basin) connected to the opening of the South Atlantic Ocean (Uliana et al. 1989; Schmidt et al. 1995; Webster et al. 2004). The sedimentary record represented by thick basal conglomerates in the General Levalle Basin or by two thick megasequences in the Sierra Chica Basin of up to 650 m. K-Ar ages of lava flows found in the basin deposits vary between 151 ± 10 Ma and 114 ± 5 Ma (Gordillo and Lencinas 1967; Stipanovic and Linares 1975).

The second scenario is characterized by a burial event between 130 Ma and 90 Ma as indicated by thermal modeling and bimodal track length distribution of sample APM 09-08 (Figs. 3.11a and 3.9). The time-temperature path from thermal modeling indicates a maximum burial of approximately 2 km (Fig. 3.11a, dashed line). However, further data is needed to constrain this possible burial event.

3.5.5 Ar-Ar Data on the Age of Volcanic Activity

The Ar-Ar ages presented in this study strongly support and constrain the older K-Ar ages presented above (Table 3.5). Older K-Ar geochronological data as well as new Ar-Ar WR and mineral ages show that the volcanic rocks of the San Luis and Sierra de Morro area formed during a volcanic episode occurring between 11.2 Ma and 1.9 Ma. The ages become progressively younger from the west to the east (Table 3.5). The volcanic activity of the belt began in the sectors of Cañada Honda and La Carolina between 11.2 and 8.2 Ma and expanded to the entire belt between 6.4 Ma and 6.3 Ma (Ramos et al. 1991, Sruoga et al. 1996; Urbina and Sruoga 2008, 2009). The magmatic activity in the La Carolina region ceased around 6.3 Ma, whereas it lasted until 2.6 Ma in the Cerros del Rosario and the easternmost sector of El Morro and Cerro Tala. The westernmost sector of the Sierra del Morro shows activity until 1.9 Ma recording the youngest volcanic activity in the entire Sierras Pampeanas (Ramos et al. 1991; this study).

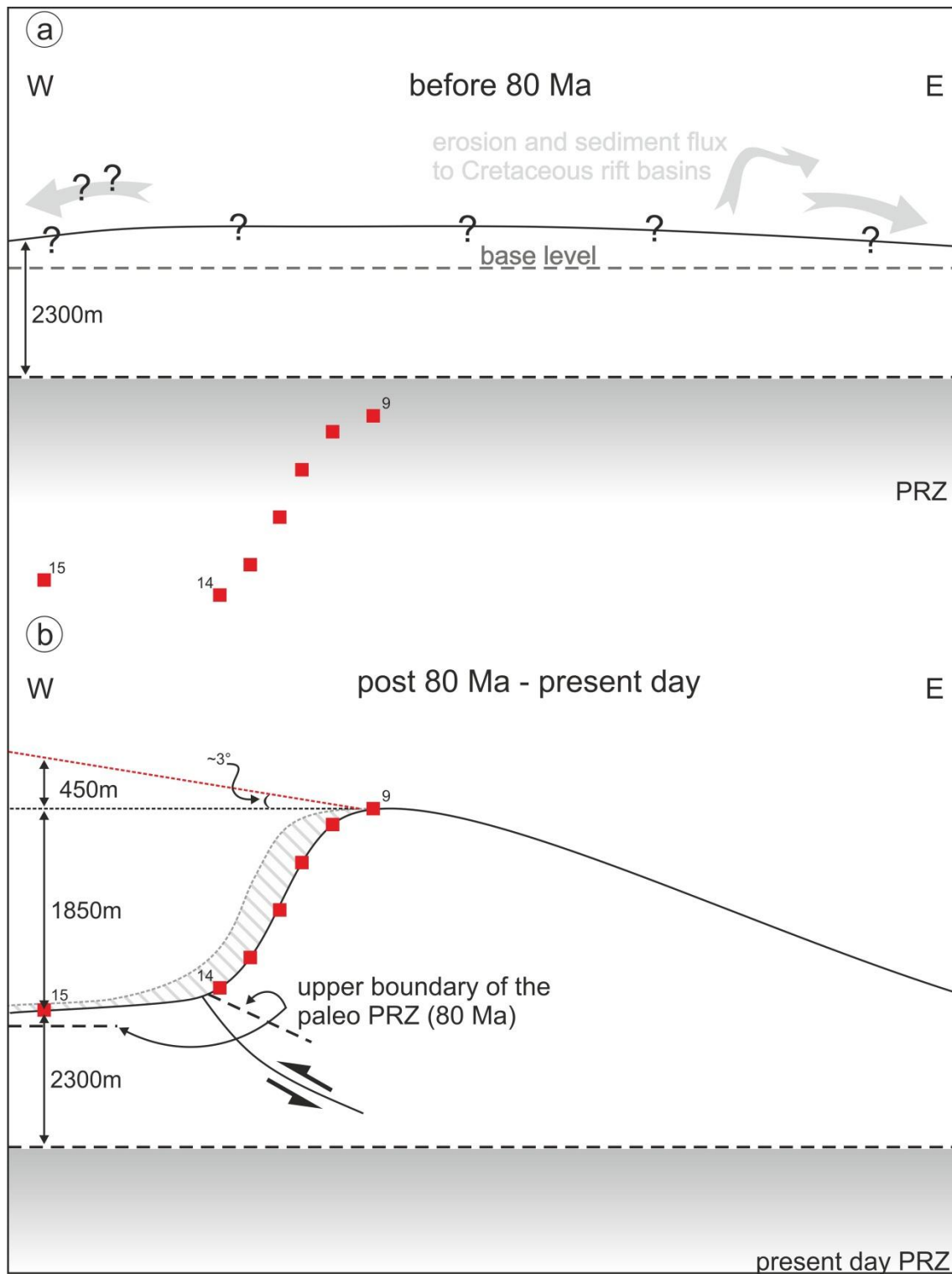


Fig. 3.13: Cooling history of the Sierra de A) Before 80 Ma the area probably was characterized by a slightly elevated relief, hence acting as sedimentary source for adjacent basins to the east and northeast. Whether sedimentation also occurred to the west is arguable. Assuming a geothermal gradient of about $26^\circ\text{C}/\text{km}$ the PRZ of the (U-Th)/He system was located in 2300 m depth. All investigated samples lay within this PRZ before 80 Ma, whereby APM 15-08 was located at a higher crustal level than APM 14-08. B) At present day all investigated samples are at the surface and the PRZ is located in 2300 m depth assuming the same geothermal gradient. Due to passing the PRZ at around 80 Ma, indicated by the upper boundary of the paleo PRZ, the investigated samples could be uplifted by a maximum of 2300 m since the Late Cretaceous. The difference in altitude between APM 15-08 and APM 09-08 is 1850 m representing the minimum amount of uplift. The maximum uplift of 2300 m is constrained by the depth of the paleo PRZ and a dip of 3° of the eastern slope. Also concerning erosional processes the real uplift is in between these values since 80 Ma. Thrusting to the west along the main boundary fault located between APM 15-08 and APM 14-08 post 80 Ma resulted in the sample altitudes observed today.

3.6 Conclusions

- 1) K-Ar dating on illite fine-fractions from fault gouges shows a long lasting brittle deformation history. The minimum age for the onset of brittle deformation is constrained to lay around 340 Ma. This is consistent with the 426-420 Ma K-Ar biotite ages from basement rocks (Steenken et al. 2010), which determine the brittle-ductile transition temperature.
- 2) There is strong indication for a major Permo-Triassic (260-240 Ma) deformation event as indicated from several K-Ar illite fine fraction ages of all analyzed fault gouge samples.
- 3) The last illite forming event dated around 174 Ma, indicating cooling below the minimum formation temperature of illite.
- 4) Assuming a geothermal gradient of 26°C/km our new thermochronological data constrain the total uplift of the Sierra de Comechingones to a maximum of about 2.3 km since the passage of the analyzed samples through the PRZ during the Late Cretaceous (80-70 Ma).
- 5) Thermal modeling yield very low cooling rates, ranging from 4°C/km to <0.2 °C/Ma
- 6) Regarding denudation processes, our thermochronological data indicate relatively stable conditions since at least 80 Ma. This fact agrees with the remarkable preservation of paleolandsurfaces at the eastern slope of the Comechingones uplifted block.
- 7) The propagation of flat slab subduction as expressed by volcanic activity is reconfirmed by new Ar-Ar data on amphiboles and whole rock, yielding ages from 7.54-1.92 Ma.
- 8) Considering the present day difference in altitude between top and base of the Sierra de Comechingones (1850 m), as well as the depth to the AHe paleo PRZ at 80 Ma, the amount of maximum eroded thickness from the top region of the Sierras can be constrained to a maximum of 450 m ever since, although more probably is close to zero.
- 9) The new thermochronological data do not clearly illuminate the uplift of the Pampean ranges during the Neogene, but give no indication that the maximum uplift of 2.3 km of the Sierra de Comechingones is only related to the Andean deformation during the Cenozoic flat-slab subduction. Cenozoic flat-slab subduction. It is preliminary understood that the Post-Cretaceous uplift related to the Comechingones fault at the study section is comprised between 1850 and 2300m. However, several uncertainties related to the dynamic evolution of this structure might biasing such estimation

4 The Sierra de San Luis

4.1 Introduction

The Sierra de San Luis (SSL) is one of the southernmost ranges of the Sierras Pampeanas region. These ranges correspond to around twelve basement block uplifts (González Bonorino 1950; Caminos 1972; Gordillo and Lencinas 1979; Jordan and Allmendinger 1986; Ramos et al. 2002) surrounded by basins of flat topography, which widely crop out in central-western Argentina between 27° to 33° S (Fig. 4.1). In general, they consist of Late Pre-Cambrian to Early Paleozoic metamorphic and igneous rocks and show a topographic asymmetry represented by a steep western and a gentle eastern slope (Fig. 4.2). The latter is usually characterized by several erosional paleosurfaces of diachronous age (Jordan et al. 1989; Carignano et al. 1999; Costa et al. 1999). In the SSL, the planation surfaces are tilted by 2-8° E and are generally characterized by a gentle undulated relief, exposing a crystalline basement which is partially covered by Quaternary sediments. The topographic asymmetry is interpreted as being linked to neotectonic uplift along reverse faults with listric geometry (González Bonorino 1950; Jordan and Allmendinger 1986), which are commonly located at the western sides of the ranges (Fig. 4.1). The last significant uplift episode is considered to be related to the onset of the Andean flat-slab subduction and associated thermal weakening and crustal thickening (e.g. Stauder 1973; Barazanghi and Isacks 1976; Jordan et al. 1983; Pilger 1984; Costa 1999; Ramos et al 2002; Ramos 2009). Due to this deformation style, Jordan and Allmendinger (1986) regarded the region of the Sierras Pampeanas as a modern analogue of the Rocky Mountains foreland uplifts during the Laramide Orogeny in North America.

The geologic knowledge of the Pampean ranges has traditionally been focused on the lithology and evolution of the exposed igneous-metamorphic basement. Generally, the tectonometamorphic evolution of the basement is considered completed by Early Carboniferous times. Later deformation of these blocks was dominated by brittle deformation, leading to a characteristic N-S trending fault blocks bounded by major reverse faults.

The evolutionary paths of these ranges during the different tectonic regimes that have prevailed since the Gondwana break-up as well as the significance of those regimes in relation to the regional mountain building through time is still a matter of ongoing debate. Low-temperature thermochronological data and geochronological dating which support quantitative estimations on Neogene block uplift, as well as the proposed morphotectonic evolution (as proposed by Jordan et al. 1983; Jordan and Allmendinger 1986; Ramos et al. 2002; Ramos 2009; Ramos and Folguera 2009, among others) are still scarce in the Sierras Pampeanas. Low-temperature thermochronologic dating methods, such as fission track and (U-Th/He) analysis, as well as K-Ar illite fine-fraction ages from

fault gouges, are powerful tools to investigating the cooling and exhumation history (*sensu* England and Molnar 1990) in association with mountain building, crustal deformation and landscape evolution (e.g. Gallagher et al. 1998; Farley 2002; Ehlers et al. 2003; Stöckli et al. 2000; Fitzgerald et al. 2006).

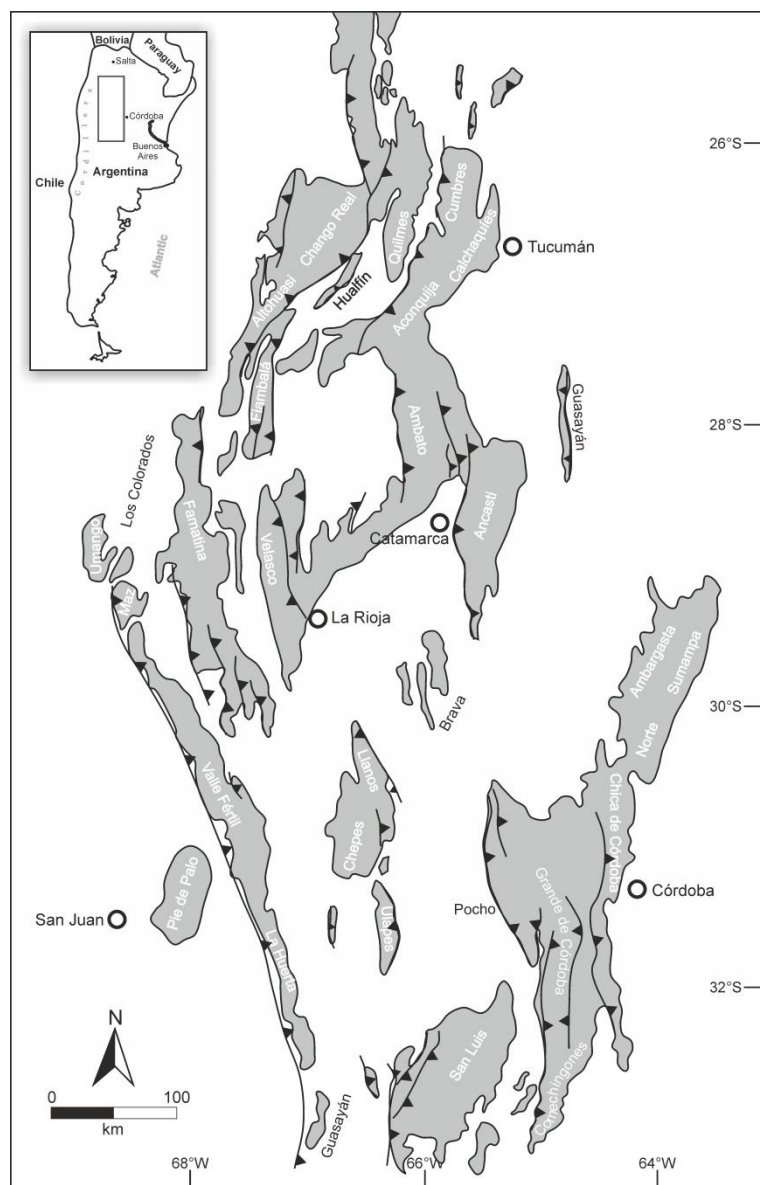


Fig. 4.1: Schematic map of the Sierras Pampeanas modified after Ramos et al. (2002). The Pampean ranges are shown in grey and the intermountain basins in white. A schematic overview of Argentina is given in the upper left corner.

In this study, we investigated an approximately 20 km long cross-section within the western part of the SSL, between the villages of Nogolí in the west and the Rio Grande in the east (Figs. 4.2 and 4.3) in order to *i)* delineate an exhumation model of the SSL, *ii)* to extend the postmetamorphic thermal history of the crystalline basement within this range (Steenken et al. 2004) to the low-temperature thermal regime, *iii)* to compare the thermal history to that of the Sierra de Comechingones (Löbens et al. 2011) and *iv)* to test if the uplift signal related to the Andean Orogeny could be isolated from previous exhumation processes

In order to accomplish these objectives, three different approaches were conducted: (a) K–Ar dating on brittle fault gouges to evaluate the timing of the brittle deformation activity, (b) apatite fission

track analysis (AFT) and (c) (U-Th)/He measurements of zircon (ZHe) and apatite (AHe). Gouge-bearing small-scale fault zones were sampled and dated by the K-Ar illite method in several grain-size fractions. Additionally, illite polytype quantification, illite crystallinity determination and mineralogical classification of gouges were done by X-ray diffraction. The two latter methods were used to decipher the cooling and exhumation history of the sampled region by dating the passage of samples through a mineral-dependent temperature range.

Samples for K-Ar dating were taken from well-developed clay fault-gouges in the crystalline basement. Apatite fission track and (U-Th)/He samples were taken from basement rocks, comprised of predominantly granitic rocks.

4.2 Geologic and Morphotectonic Setting

Accretion of different allochthonous and parautochthonous terranes during the Pampean, Famatinian and Achalian Orogeny in the Late Proterozoic and Early Paleozoic formed the basement complex of the Sierras Pampeanas (e.g. Ramos 1988; Ramos et al. 2002; Steenken et al. 2004; Miller and Söllner 2005; Ramos 2008). The Sierras de San Luis mainly consists of metamorphic and igneous rocks, including mainly schists, migmatites, gneisses and phyllites (Ortiz Suarez *et al.* 1992; von Gosen 1998; Costa et al. 2000; 2001 and others), which are intruded by granitoids of Cambrian to Early Carboniferous age (López de Luchi et al. 2004; Siegesmund et al. 2004).

Terrane sutures and crustal anisotropies, formed in the Late Proterozoic and Early Paleozoic due to terrane accretion, were extensionally reactivated during the Mesozoic (e.g. Criado Roque et al. 1981; Schmidt et al. 1995; Gardini et al. 1996; 1999; Costa et al. 2000; 2001; Ramos et al. 2001; 2002). Rifting led to the development of continental basins which are usually characterized by a half-graben structure and mainly contain Early Cretaceous deposits (Schmidt et al. 1995; Costa et al. 2000; 2001). Around some parts of the SSL, the stratigraphic record is characterized by isolated Gondwanian lacustrine-fluvial deposits bearing *Glossopteris* flora (e.g. Bajo de Véliz, Agua Dorada, La Estanzuela and Suco region; Hünicken and Penza; 1980; Hünicken et al. 1981; Limarino and Spalletti 2006). Cretaceous and Neogene volcanic rocks with clastic deposits of the same age are in a periclinal arrangement around the range (Santa Cruz 1979; Criado Roqué et al.; 1981; Costa et al.; 1998; 2000; 2001). Additionally, Solá (1981) described isolated outcrops of volcanic rocks in inner parts of the SSL, with ages of ca. 85.5 Ma and 83.5 Ma, related to Mesozoic rifting.

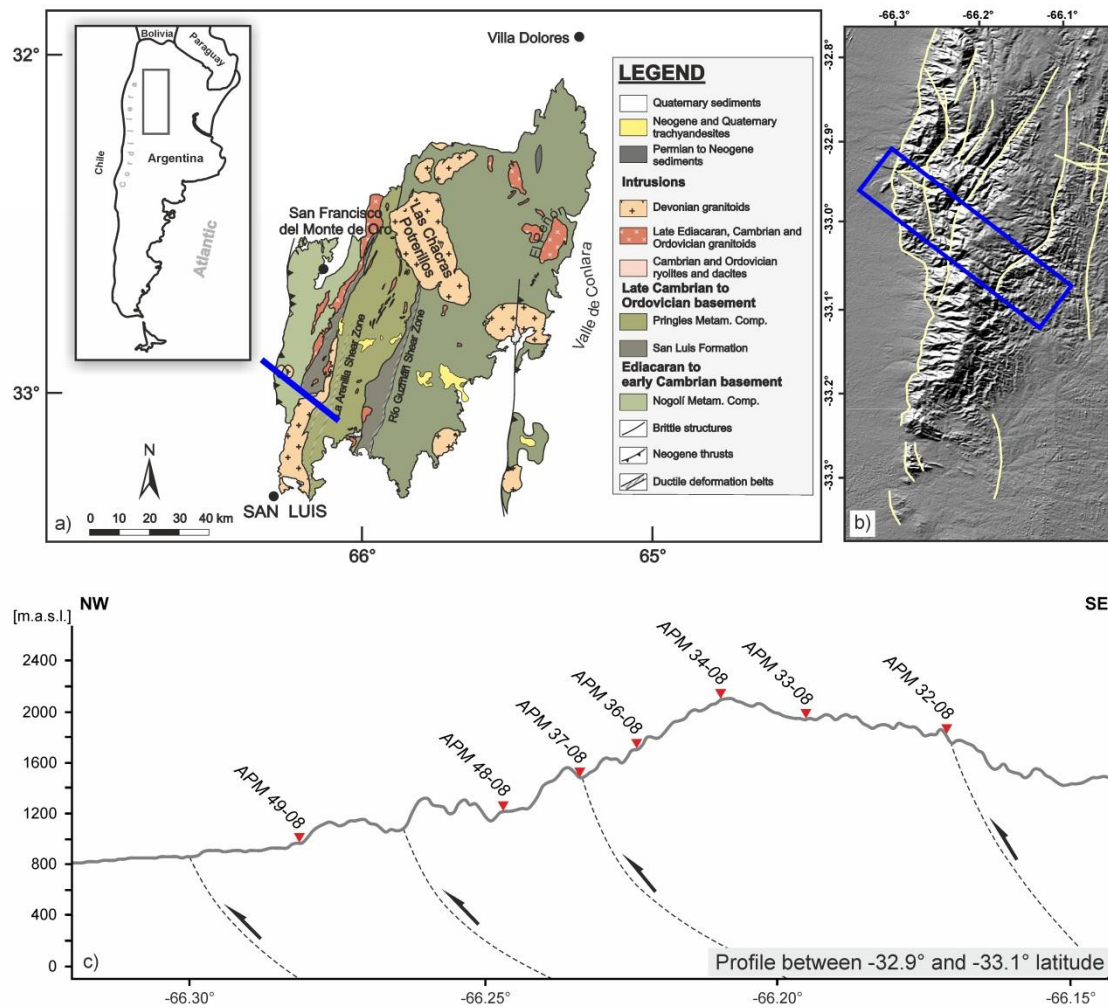


Fig. 4.2: a) Geological map of the Sierra de San Luis (study area marked by grey bar); b) SRTM elevation model of southern Sierra de San Luis (study area marked by rectangle, main faults indicated by yellow lines); c) Elevation profile and sample location of inferred major fault zones (location of fault zones based on geological maps from San Luis and San Francisco del Monte de Oro (Costa et al. 2001b); please note that major fault zones illustrated here does not have a surface expression exposed).

Cenozoic crustal shortening as well as flattening of the subduction angle of the Nazca Plate (Stauder 1973; Barazanghi and Isacks 1976; Pilger 1984), which is related to the collision of the Juan Fernandez Ridge in the Miocene (Yañez et al. 2001; Ramos et al. 2002), led to uplift and tilting of the Pampean basement blocks (González Bonorino 1950; Gordillo and Lencinas 1979; Criado Roque et al. 1981; González Díaz 1981; Jordan and Allmendinger 1986; Introcaso et al. 1987; Massabie 1987; Costa and Vita Finzi 1996; Ramos et al. 2002). Furthermore, Kay et al. (1991), Ramos et al. (2002), Cristallini et al. (2004), Ramos and Folguera (2009) and Ramos (2010) suggest that the eastward migration of the magmatic activity towards the foreland induced crustal thermal weakening, hence block uplift soon after the magmatic emplacement. These uplifts were usually controlled by former main bounding faults of the Mesozoic rift system, which were inverted during the Andean compression together with inherited zones of crustal weakness (e.g. Criado Roque et al. 1981; Schmidt et al. 1995; Gardini et al. 1996; 1999; Costa et al. 2000; 2001). To what extent the current structural relief of the Pampean ranges is related to the Andean compression is not yet well known.

Recent studies suggest that the exhumation component as a result of Andean compression might be less significant than formerly assumed (e.g. Löbens et al. 2011).

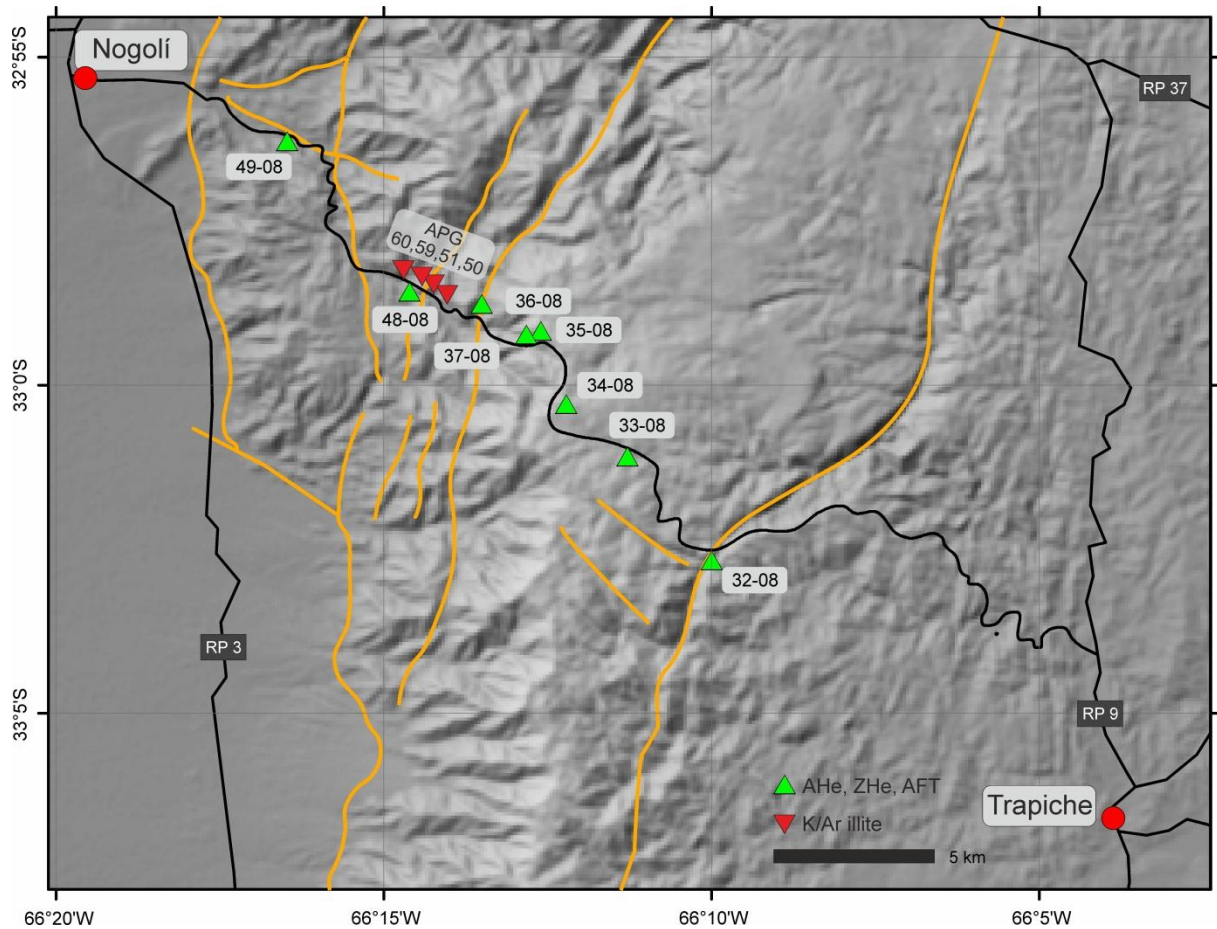


Fig 4.3: Simplified map of the study area with locations of thermo-chronological samples (green triangles) and K-Ar illite fault-gouge samples (red triangles). For location of map extent see Fig. 4.1a,b.

At least in their present day final structural configuration the Sierras Pampeanas uplifts can be characterized, as distinctive surficial characteristics of the Pampean flat-slab segment of the subducting Nazca Plate (Jordan et al. 1983; Jordan and Allmendinger 1986; Ramos et al., 2002). However, their morphotectonic evolution has not been completely clarified yet. Because no pre-Quaternary sedimentary cover was developed or preserved atop the ranges for constraining the geometry and characteristics of the post-Paleozoic structural relief, the erosional surfaces (see above), were envisaged as a key geometric marker for this purpose. These paleolandsurfaces, already described by the early geologic works within the Sierras Pampeanas (e.g. Stelzner 1885; Brackebusch 1891; Bodenbender 1895; 1911; Gross 1948; González Bonorino 1950), have been regarded in two ways. González Díaz (1981) and Criado Roque et al. (1981) considered them as a continuous and essentially synchronous surface, which was uplifted and disrupted during the Andean Orogeny. Alternatively, Carignano et al. (1999) suggested that topographic scarps, preserved in inner areas of the erosional surfaces separating their different topographic levels, are a result of juxtaposition of diachronous surfaces. According to these authors, scarps show ages between the Late Paleozoic and

Paleogene. A similar idea was previously raised by Jordan et al. (1989), who extended their interpretation of only four thermochronologic data points (one age each for the Sierras Ancasti, Córdoba, Famatina and Velasco) to the entire Sierras Pampeanas and suggested that the chronological development of these surfaces were essentially diachronous. Moreover, the assumption of alleviated block uplift related to eastward migration of magmatic activity (Kay et al. 1991) implies a diachronous uplift wave, starting at 7.6-6 Ma in the Sierra de Aconquija and arriving around 2.6 Ma at the SSL (Yañez et al. 2001; Ramos et al. 2002; Ramos and Folguera 2009). The latter would link the morphotectonic evolution with the main tectonic episodes along the Andes during the Neogene.

4.3 Post-Metamorphic Cooling History

The post-metamorphic thermal history of the basement domains of the Sierra de San Luis (SSL) has been assessed by Rb-Sr and K-Ar dating on micas by various studies (e.g. Varela et al. 1994; Sims et al. 1998; González and Sato 2000; Sosa et al. 2002; Steenken et al. 2004; 2008).

Also K-Ar biotite ages from these studies indicate that cooling occurred earlier in the western part of the SSL and migrating over time to the east, recorded differences in K-Ar ages are negligible. Thus, it is assumed that the entire SSL reached epimetamorphic conditions (300-350 °C) during the middle Mississippian (345-328 Ma, Steenken et al. 2008). The distribution of K-Ar ages suggests that the differential cooling of the basement of the SSL was not the result of a rotational 'en-bloc' exhumation but was rather accommodated by the two belts of the San Luis Formation, as recorded by K-Ar fine-fraction ages from the San Luis Formation. This formation, lying several kilometres to the north of the study area, is comprised of two narrow belts of low-grade phyllites and quartz arenites. Here, K-Ar fine-fraction ages range from the middle Mississippian to the lower Cisuralian (345-299 Ma; Steenken et al. 2008; Wemmer et al. 2011). Thereby, ages >320 Ma are synchronous with a period of intra-Carboniferous compressional tectonics, which Wemmer et al. (2011) attributed to the Toco Orogeny (Bahlburg and Breitzkreuz 1991). However, the tectonics of this Upper Mississippian event are poorly understood. A relationship to the accretion of a terrane has been proposed (Ramos et al. 1986; Gohrband 1992; Davis et al. 2000; Ramos 2001), but this contradicts the hypothesis of an Early Devonian docking of the Chilenia terrane (Achalian orogenic cycle) to the southwestern margin of Gondwana (Sims et al. 1998; Siegesmund et al. 2004). These Carboniferous ages are considered to have documented the end of ductile deformation.

4.4 Applied Methods

4.4.1 Mineralogy and K-Ar Dating of Fault Gouges

In brittle near-surface faults, tectonic movement causes the crushing of rocks and grain-size reduction. In these localized fault zones, the increased rock surface together with water creates high

chemical reactivity, allowing retrograde processes to produce fault gouges composed of authigenic hydrosilicates such as illite. Thus, the formation time of the authigenic illite in a fault gouge can be correlated with periods of motion along the fault (e.g. Lyons and Snellenberg 1971; Kralik et al. 1987). In addition to interpreting K-Ar illite ages in terms of the timing of faulting and thrusting (e.g. Wemmer 1991, Solum et al. 2005, Haines et al. 2008, Zwingmann et al. 2010, Surace et al. 2011, Wolf et al. 2011, Löbens et al. 2011), K-Ar illite dating has been used to constrain the age of hydrothermal fluid migration as well as oil and gas migration (Hoffman et al. 1976, Aronson and Burtner 1983, Lee et al. 1985, Hay et al. 1988, Hamilton et al. 1989, Pevear et al. 1997, Pevear 1999, Grathoff et al. 2001, van der Pluijm et al. 2001, Clauer et al. 2012).

One of the most important assumptions involved in the interpretation of K-Ar fault gouge ages is that of closed-system behaviour – in other words, no gain or loss of either ^{40}K or ^{40}Ar after the formation of the illite. A loss of Ar might be possible due to thermal diffusion effects, especially because of the very small size of illite grains or exchange reactions with hydrothermal fluids (e.g. Villa 1998). The importance of the effective diffusion radius on the closure temperature for the Ar-system has been demonstrated throughout a large number of publications (e.g. Dahl 1996; Villa 1998; Hodges 2003). However, these publications are focused on white micas with grain sizes $>200\text{ }\mu\text{m}$. In the case of illite fine-fractions (grain size as small as $<0.2\text{ }\mu\text{m}$), available information is scarce. Hunziker et al. (1986) reported a closure temperature interval for the mica fractions $<2\text{ }\mu\text{m}$ of $260\pm30\text{ }^{\circ}\text{C}$, whereas Wemmer and Ahrendt (1997) found that fine-grained white micas (sericite $<2\text{ }\mu\text{m}$) did not behave as open systems, even at temperatures of $275\text{ }^{\circ}\text{C}$. Therefore, the blocking temperature for Ar in fine-grained mica is estimated somewhere between 275 and 350°C (Wemmer and Ahrendt 1997).

Further errors in the acquisition of accurate K-Ar ages can arise from contamination by other K-bearing phases. Potassium-feldspar, for example, even while much older in formation, can rejuvenate its age due to its low closure temperature of about $150\text{ }^{\circ}\text{C}$ (e.g. Fitz-Gerald and Harrison 1993). Another major problem which must be considered is the possible mixture of illite formed by different events at different times. For authigenic, neocrystallized illite, the finest illite fraction should represent the most recently grown illite. Coarser grain-size fraction should yield older ages, representing earlier illite-forming events (e.g. Clauer et al. 1997). However, we recognize that ages are not usually specific times but represent an integration of events.

Mineral identification was done by XRD analysis on randomly-oriented sample powders as well as oriented (textured) compounds using a Phillips PW 1800 X-ray diffractometer in a step-scan mode ($0.020\text{ }^{\circ}2\theta$) in the range of $4 - 70\text{ }^{\circ}2\theta$. Preparation, sample treatment and mineral identification followed the methods described by Moore and Reynolds (1997). In order to support the identification of clay minerals, samples were measured in different conditions, e.g. under air-dry and

ethylene-glycol-solvated conditions. For more details, the reader is referred to Wemmer (1991). Selected samples were also analysed by TEM to verify mineral identification done by XRD analyses.

In addition to mineralogy, the illite crystallinity and polytypism are determined, which can provide important indices for the assessment of thermal evolution and very low metamorphism grades. The KI (Kübler Index or crystallinity index) values, which are inversely proportional to the illite crystallinity, are defined after Kübler (1964) as the half-height width of the 10 Å XRD peak. The values for the illite crystallinity (IC) may range from $0.060\text{ }^\circ 2\theta$ for ideally ordered muscovite up to $1\text{ }^\circ 2\theta$ for illite/smectite mixed layers (Kübler 1964; 1967, 1968). Kübler (1967) suggested boundary values of $0.420\text{ }^\circ 2\theta$ and $0.250\text{ }^\circ 2\theta$ to divide the zones of the very low-grade metamorphism into, from lower to higher grade, diagenetic zone ($KI > 0.420\text{ }^\circ 2\theta$), anchizone ($0.420\text{ }^\circ 2\theta < KI < 0.250\text{ }^\circ 2\theta$) and epizone ($KI < 0.250\text{ }^\circ 2\theta$; see also Gharrabi et al. 1998, Jaboyedoff et al. 2000, Jaboyedoff et al. 2001). Temperatures corresponding to the two boundaries are around $150\text{ }^\circ\text{C}$ and $300\text{ }^\circ\text{C}$, respectively (Fig. 4.4).

It is important to keep in mind that the analysed samples represent mixtures of illite of different ages and polytypism. Thus, IC as an indicator for temperature experienced by the fault gouge cannot be interpreted easily because samples give mixed IC-values by integrating the IC of all abundant illite phases. However, the KI values of authigenic fault gouge illite, even of mixtures, can be used to estimate the minimum temperature experienced by the fault gouge sample (Table 4.1). Additionally, KI values may help to decipher evolutionary differences between grain-size fractions within one sample as well as between samples.

Polytypism (Bailey et al. 1977; Guinier et al. 1984) is a common phenomenon for layered silicate minerals such as mica, chlorite and kaolinite. For illite, the most common polytypes are the $1M_d$, $1M$ and $2M_1$ (e.g. Reynolds and Thomson 1993). With rising temperature, illite shows irreversible polytype transformation of the $1M_d \rightarrow 1M \rightarrow 2M_1$ (Hunziker et al. 1986). The $2M_1$ polytype is considered to be the most stable at the earth's surface, whereas the $1M_d$ and $1M$ polytypes can be considered metastable. Yoder and Eugster (1955), as well as Weaver (1989), concluded that the transition from $1M_d$ and $1M$ to $2M_1$ begins at a temperature of approximately $200\text{--}210\text{ }^\circ\text{C}$ (Fig. 4.4). Generally, illite has $1M_d$ and $1M$ polytypes in the diagenetic zone, a mixture of $1M$ and $2M_1$ polytypes in the anchizone and more or less sole $2M_1$ polytypes in the epizone (Fig. 4.4; e.g. Bailey 1966; Środoń and Eberl 1984).

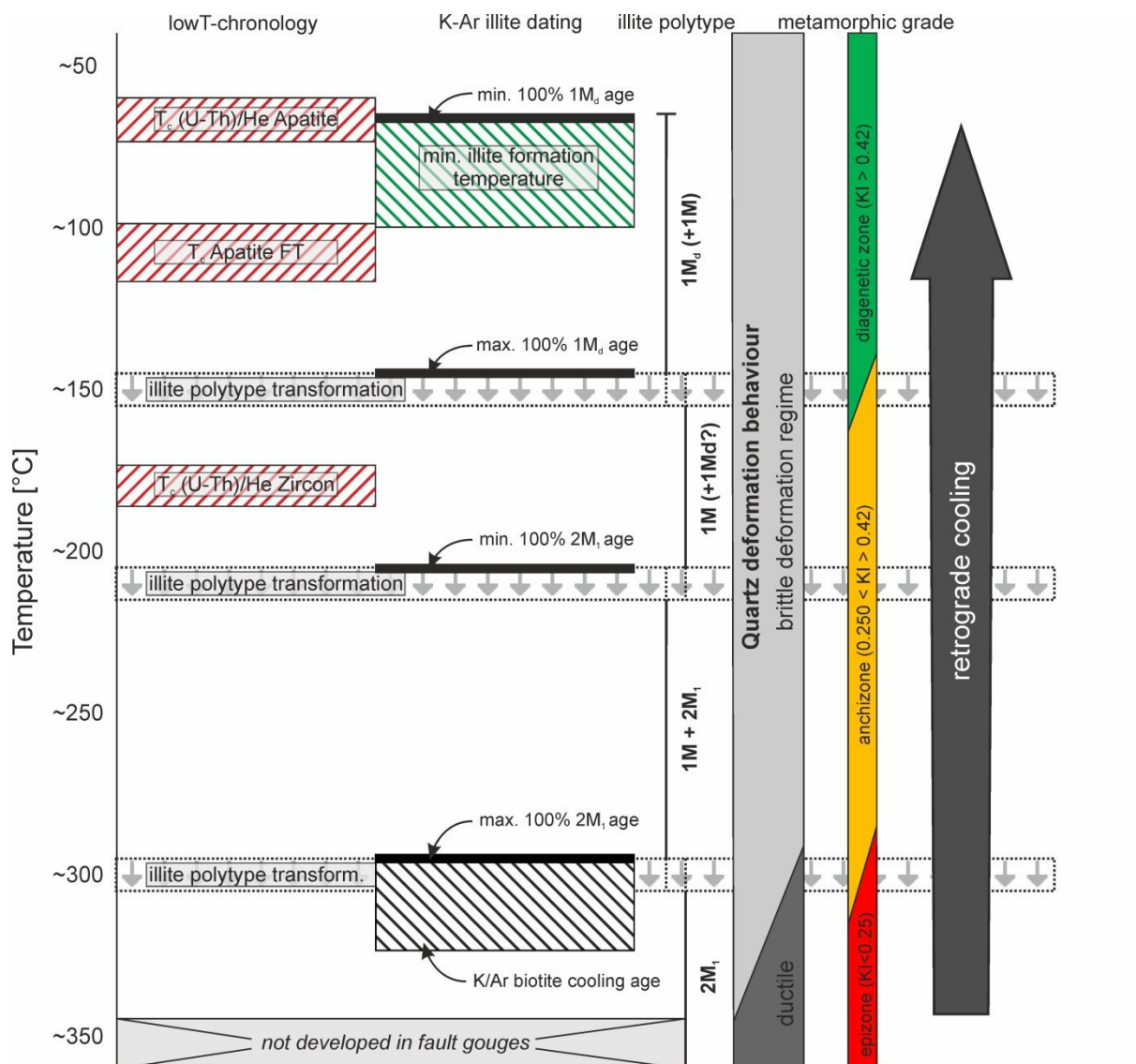


Fig. 4.4: Scheme for the interpretation of K-Ar illite fine fraction ages and polytype quantification data in combination with regional cooling data derived from (U-Th)/He, apatite fission track and K-Ar biotite method. The illite polytype transition zone marks the irreversible transition from one respective polytype to another under prograde conditions. Thus, under retrograde conditions there will always be a mixture of polytypes in the respective metamorphic zone. The temperatures for the transition between polytype- deformation- and metamorphic regimes have to be considered as continuously with not exact constrained temperature boundaries. The ages for the fault gouge fine-fraction (2-6 μm ; 2 μm and <0.2 μm) are not indicated in figure but would lie between the maximum 100% 2M₁ age and the minimum 100% 1M_d age (Please note that this scheme involve simplifications. Additionally scheme is mainly concerted on interpretation of non-sedimentary rocks; KI = Kübler Index; TC = effective closure temperature; temperatures for respective system see Reiners and Brandon (2006), approximated illite polytype transformation temperatures according to Hunziker et al. (1986), Yoder and Eugster (1955), Velde (1965), Weaver (1989) and Zoller and Brockamp (1997); temperature ranges of brittle and ductile deformation behavior of quartz taken from Passchier and Trouw (2005), KI values for diagenetic zone, anchi- and epizone according to Kübler (1967); closure temperature of K-Ar biotite system according to Purdy and Jäger (1976)).

Using XRD patterns derived from randomly oriented samples, it is possible to quantify the relative amounts of 2M₁, 1M and 1M_d illite. Randomly oriented samples are achieved by using a side-packing device as described by Moore and Reynolds (1997). A randomly oriented sample is essential for the polytype quantification because the polytype diagnostic peaks are non-(00l) indices and, therefore, absent in textured samples.

The randomness of orientation was checked by the ratio of the (002) and the (020) illite peak, which should be low for non-oriented samples and rise with an increase in orientation. Using a technique

proposed by Grathoff and Moore (1996), the concentration of the $2M_1$ and $1M$ polytype is determined by getting the ratio of either the area or the height of polytype-specific peaks to an area of a peak which is common to both polytypes (the 2.58\AA band; Grathoff and Moore (1996)). The amount of $1M_d$ illite is determined by assuming that the remaining illite is the $1M_d$ polytype.

We measured four fault-gouge samples taken from the Nogolí – Rio Grande transect (Fig. 4.2). For more details on the analytical procedure, the reader is referred to Wemmer (1991).

4.4.2 Thermochronology

Combining apatite fission-track dating with (U-Th)/He dating of zircon (ZHe) and apatite (AHe) allows the reconstruction of low-temperature exhumation and uplift history (e.g. Hurley 1954; Armstrong 1966; Wagner and van Den Haute 1992; Farley et al. 1996). According to Donelick et al. (1999), Ketcham et al. (1999) and others, the thermal sensitivity of the apatite fission track method, the so-called partial-annealing zone (PAZ; Gleadow and Fitzgerald 1987), ranges between $130\text{ }^{\circ}\text{C}$ and $60\text{ }^{\circ}\text{C}$. For the (U-Th)/He system of apatite and zircon, this temperature interval is referred to as the partial-retention zone (PRZ) and ranges between $65\text{ }^{\circ}\text{C}$ and $30\text{ }^{\circ}\text{C}$ and $185\text{ }^{\circ}\text{C}$ and $135\text{ }^{\circ}\text{C}$, respectively (e.g. Baldwin and Lister 1998; Wolf et al. 1998; Reiners and Brandon 2006).

Eight samples were collected along the San Luis transect (Figs. 4.2 and 4.3). Due to sample conditions and presence of suitable apatite and zircon crystals, six samples could be dated by all three methods, while one sample yielded no suitable zircon for ZHe dating and one sample lacked enough apatite grains for AFT dating (Tables 4.4 and 4.5).

According to Donelick et al. (1999), the AFT mounts were etched at 21°C for 20 s using 5.50 M nitric acid after grinding and polishing procedures in order to reveal spontaneous tracks within the apatite crystals. The external detector method described by Gleadow (1981) was used, while low-uranium muscovite sheets (Goodfellow mica) represented the external detector for induced tracks. For age determination, the zeta calibration approach was adopted (Hurford and Green 1983), and 25 good-quality grains per sample were randomly selected and dated. Zeta error was calculated using ZETAMEAN software (Brandon 1996; see Table 4). The fission track ages were calculated using the software TRACKKEY version 4.2 (Dunkl 2002). Furthermore, of all samples that had been dated, 10 Dpar measurements per grain were averaged to evaluate possible populations of different apatite compositions. Additionally, for track length analysis, approximately 50 horizontally confined tracks (Donelick et al. 1999) of each sample were measured.

4.5 Results

4.5.1 K-Ar Dating

Twelve K-Ar ages for the grain-size fractions of $<0.2\text{ }\mu\text{m}$, $<2\text{ }\mu\text{m}$ and $2\text{--}6\text{ }\mu\text{m}$ from four samples were obtained from the Nogolí – Rio Grande transect (Figs. 4.2 and 4.3). No outcrop could be found for the

major faults illustrated in the geological maps of the region (Figs 4.2 and 4.3). Thus, all samples were taken from associated small-scale faults in the middle part of the western hillslope (Fig. 4.3), where the best-exposed fault gouges were observed. Collected samples from small-scale faults yield well-developed clay gouges, in some locations with small grains of residual rock material. The monomineralic grains are only a few millimetres in diameter and consist almost exclusively of quartz. Polyminerallc rock fragments were not observed within sampled material. Gouge thicknesses range from several millimetres up to several centimetres, but mostly vary between 0.5 - 2 cm. Sampled gouges have monochrome brownish to reddish colours.

K-Ar ages range from Early Pennsylvanian to Early Jurassic times (315–178 Ma). The age-analysis plot of all analysed samples is depicted in Figure 4.5, and data are listed in Table 4.1. All samples show a time interval span between fractions, ranging from 18.7 Ma up to 84.7 Ma (Fig. 4.5). No overlapping ages could be observed within one sample.

Radiogenic ^{40}Ar content ranges from 80.3 % to 97.7 %, indicating reliable analytical conditions for all analyses. Potassium (K_2O) contents range from 1.26 % (APG 50-09, $<0.2\ \mu\text{m}$) to 6.17 % (APG 59-09, $26\ \mu\text{m}$).

XRD analyses of all samples confirm that illite, smectite and kaolinite are the major clay mineral components in the various fractions (Table 4.3 and Fig. 4.6). The presence of quartz is restricted to the fractions $<2\ \mu\text{m}$ and $2\text{--}6\ \mu\text{m}$, and none is found in the $<0.2\ \mu\text{m}$ fraction. In some samples, minor traces of potassium feldspar can be found, restricted to the $26\ \mu\text{m}$ fractions. These observations were confirmed by TEM analysis. Additionally, TEM analyses also reveal traces of halloysite (Table 4.2).

Glycolated XRD analyses were carried out to investigate the potential occurrence of expandable mixed-layers of illite and smectite. Major amounts of illite/smectite were found in all fractions of sample APG 50-09. For all other samples, considerable amounts of smectite could only be found in the $<0.2\ \mu\text{m}$ fraction. Except for sample APG 50-09, illite/smectite mixed-layers are nearly absent in the $2\text{--}6\ \mu\text{m}$ fractions (Table 4.1).

The KI of all analysed samples varies from $0.155\ \Delta^\circ 2\theta$ to $0.530\ \Delta^\circ 2\theta$ (Table 4.1). The KI values from the air-dried $<0.2\ \mu\text{m}$ fractions indicate that all but one developed under diagenetic conditions. In contrast, the fractions of $<2\ \mu\text{m}$ and $2\text{--}6\ \mu\text{m}$ yielded anchi- to epimetamorphic values. Variations in the $\Delta^\circ 2\theta$ between the glycolated and the air-dried measurements correspond to the presence of illite/smectite mixed-layers (Table 4.1). No systematic variation with respect to the sample location was observed.

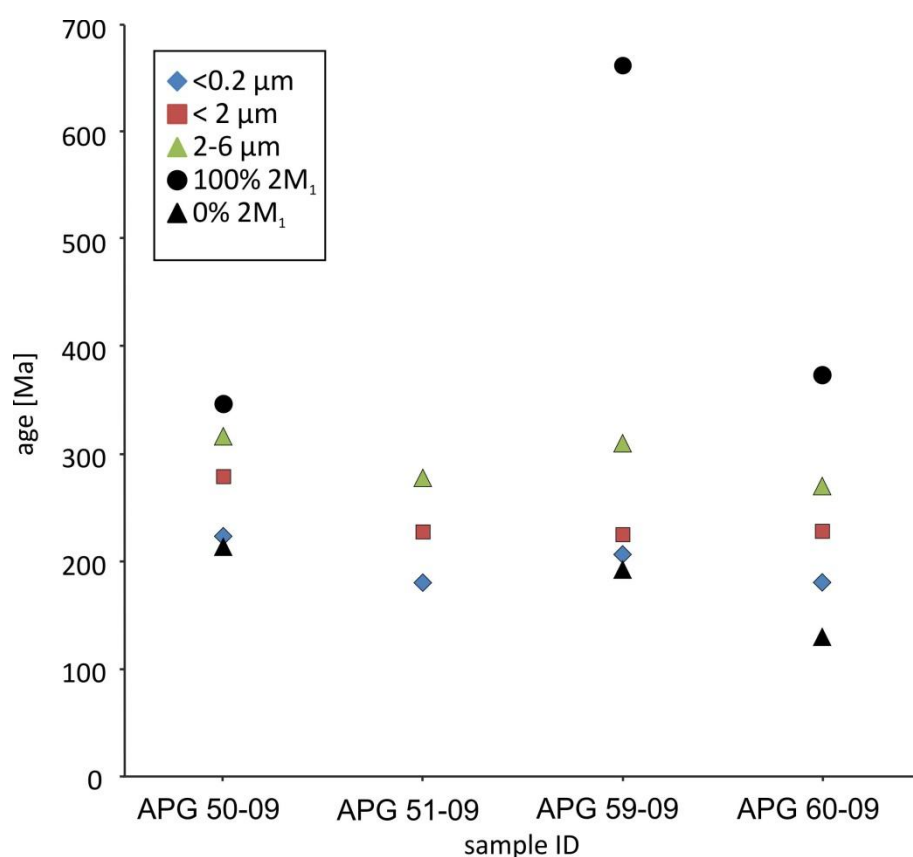


Fig. 4.5: K-Ar ages of all analyzed grain-size fractions and samples as well as extrapolated ages for the 2M₁ and 1Md polytypes. Radiogenic ⁴⁰Ar content ranges from 80.3 % to 97.7 %, indicating reliable analytical conditions for all analyses. Potassium (K₂O) contents range from 1.26 % (APG 50-09, <0.2 μm) to 6.17 % (APG 59-09, 26 μm).

Table 4.1: K-Ar ages, illite crystallinity and illite polytypism of the investigated mineral fractions

Sample	Grain fraction	K-Ar Data					Illite crystallinity		Illite polytypism 2M1, 1M, 1Md	Extrapolated age	
		K ₂ O [wt%]	⁴⁰ Ar*	⁴⁰ Ar*	Age [Ma]	±2σ- error [Ma]	air dry [Δ°2θ]	glycolated [Δ°2θ]		100 % 2M ₁	0 % 2M ₁
			[nl/g] STP	[%]							
50-09	< 0.2 μm	1,26	9,60	82,58	222,0	6,0	0,226	0,316	9%, 7%, 84%		
	< 2 μm	2,48	24,04	92,18	278,0	9,5	0,223	0,206	45%, 5%, 49%	346	212
	2-6 μm	4,21	46,80	92,61	315,4	7,0	0,162	0,158	79%, 5%, 15%		
51-09	< 0.2 μm	1,77	10,74	80,34	178,9	4,9	0,565	0,748	no polytype analysis performed		
	< 2 μm	2,70	21,02	91,47	226,5	5,0	0,425	0,496			
	2-6 μm	3,12	30,07	97,16	276,5	6,1	0,312	0,338			
59-09	< 0.2 μm	4,56	31,96	94,05	205,2	4,9	0,579	0,651	3%, 4%, 93%		
	< 2 μm	4,76	36,60	94,43	223,9	5,1	0,427	0,655	7%, 5%, 88%	661	191
	2-6 μm	6,17	66,98	97,27	308,7	6,5	0,256	0,173	25%, 5%, 70%		
60-09	< 0.2 μm	2,77	16,81	86,00	179,0	4,2	0,294	0,275	20%, 4%, 76%		
	< 2 μm	3,80	29,63	93,11	226,9	7,0	0,276	0,292	46%, 4%, 49%	372	128
	2-6 μm	5,30	49,55	97,70	268,8	5,5	0,195	0,218	53%, 4%, 43%		

Table 4.2: Results of X-ray diffraction analyses from the sample material fractions.

sample No.	grain size fraction							others ¹
		Illite	Chlorite	Kaolinite	Smectite	Quartz	Feldspar	
50-09	< 0.2 μm	+	-	-	++	-	-	Halloysit o/-
	< 2 μm	+	-	-	++	-	-	Halloysit o/-
	2-6 μm	o	-	-	+	-	-	Halloysit o/-
51-09	< 0.2 μm	+	-	+	+	-	-	
	< 2 μm	+	-	+	o	+	-	
	2-6 μm	+	-	+	-	++	o/-	
59-09	< 0.2 μm	++	-	++	o/-	-	-	
	< 2 μm	++	-	++	o/-	o/-	-	
	2-6 μm	++	-	++	-	o/-	o/-	
60-09	< 0.2 μm	++	-	-	++	-	-	Halloysit o/-
	< 2 μm	++	-	-	+	-	-	Halloysit o/-
	2-6 μm	+	-	-	o/-	+	o/-	Halloysit o/-

++ = dominant, + = abundant, o = less abundant, o/- = unclear, possibly traces, - none; ¹) identified by TEM.

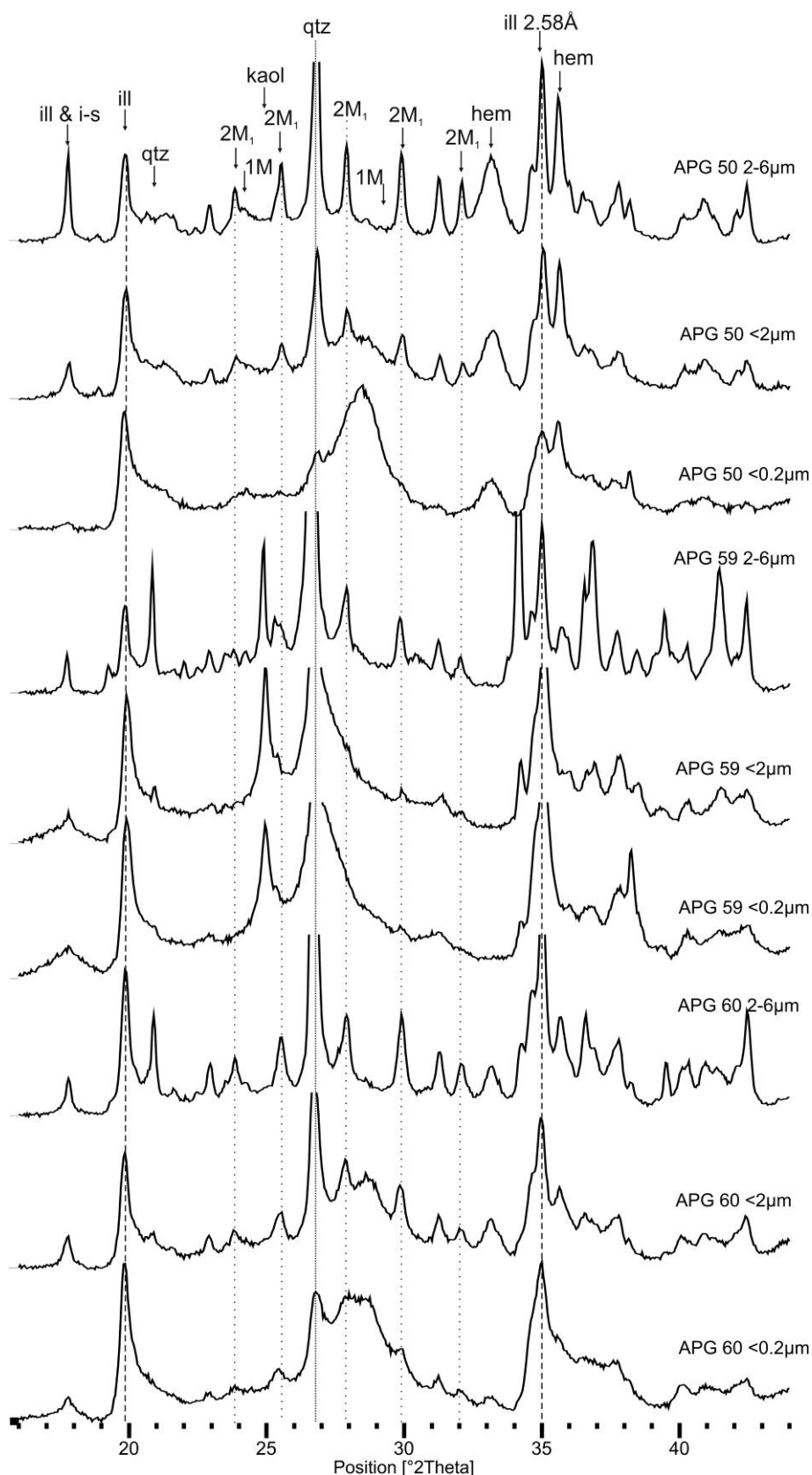


Fig. 4.6: XRD pattern derived from randomly oriented samples with indicated positions of 2M1 and 1M polytype specific peaks. Other phases are indicated as follows: illite (ill), Illite-Smectite (i-s), quartz (qtz), kaolinite (kaol) K-feldspar (kfs) and hematite (hem).

4.5.2 Illite Polytypism and Illite Crystallinity

All samples used for the illite polytype quantification show a random orientation expressed by a low (002)/(020) illite ratio as well as low (004) illite intensity. XRD tracings of random powders from all samples presented in this study contain a mixture of illite polytypes 2M₁, 1M and 1M_d. The analyzed

illite fractions are composed mainly of $1M_d$ and $2M_1$ polytypes. The $1M_d$ polytype is dominant in the $<0.2 \mu\text{m}$ fractions throughout all analyzed samples. In the $<2 \mu\text{m}$ fraction, the $1M_d$ as well as the $2M_1$ polytype are observed as the dominant phases. The $2-6 \mu\text{m}$ fractions are mostly made up of $2M_1$ illite. The $1M$ illite content is subordinate (maximum of 7 %) and more or less constant for all analyzed grain-size fractions and samples. Table 4.1 shows changes in percentage of polytypes with respect to the grain-size fraction of all analyzed samples. The content of different polytypes correlates with obtained KI values, showing smaller KI-values (better crystallinity) for samples with higher $2M_1$ content (Table 4.2).

In TEM and SAED analyses on sample APM 59-09, it was not possible to identify $1M$ illite, which might be attributed to the small TEM sample volume. However, other authors also describe being almost entirely unable to find the $1M$ polytype proposed by XRD studies during TEM analysis (e.g. Peacor et al. 2002; Solum et al. 2005).

4.5.3 Zircon (U-Th)/He Ages

Mean zircon (U-Th)/He ages range from the Late Carboniferous to Middle Triassic (313 Ma to 229 Ma). Ages show no clear correlation with elevation (Fig. 4.7, Table 4.5), which we attribute to younger tectonism along the transect (see above). Because of the scatter of individual ages, ZHe ages are not interpreted as event ages but are used as constraints for the modelling of the thermal history of individual samples (see below).

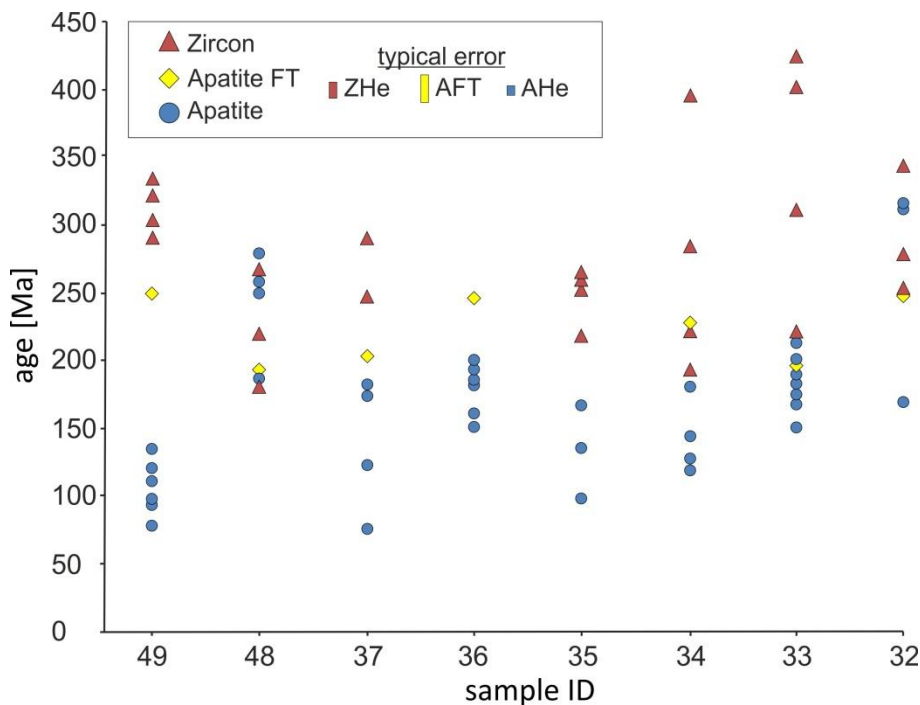


Fig. 4.7: compilation of (U-Th)/He and AFT ages for all analyzed samples.

4.5.4 Fission Track Ages

The seven analysed samples within the San Luis transect show apparent apatite fission track ages ranging from Early Triassic to Early Jurassic (Table 4.4 and Fig. 4.8). A correlation between age and

elevation as expected for undisturbed elevation profiles (Fitzgerald et al. 2006) exists neither on the western slope nor on the eastern slope, which we attribute to younger tectonism along the transect (see above). The youngest apparent ages (196 Ma and 192 Ma) can be found in the middle part of both slopes due to differential block faulting.

All investigated samples are characterized by distinct, shortened tracks. They show an unimodal track length distribution (Table 4.4 and Fig. 4.8) where the mean track length varies between 11.9 μm and 12.9 μm with standard deviations of 0.9-1.5 μm (Table 4.4). The mean etch-pit diameters (D_{par} values) of the seven samples are between 1.79 μm and 2.09 μm (Table 4.4).

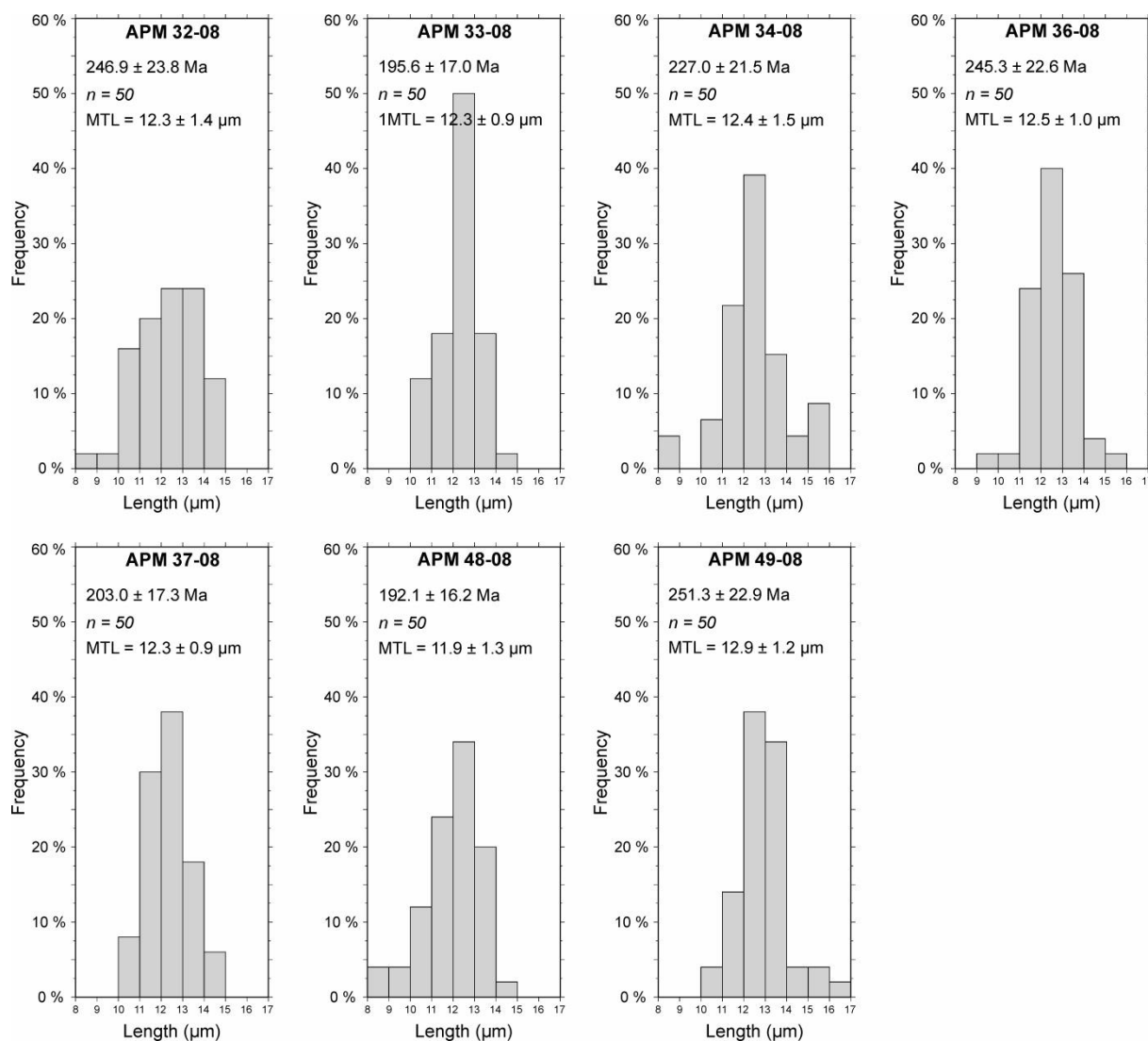


Fig. 4.8: Track length distribution of the investigated samples. The amount of measured confined tracks is given by n. The apparent age of each sample is shown in italic letters.

4.5.5 Apatite (U-Th)/He Ages

The mean apatite (U-Th)/He ages along the San Luis transect range between the Middle Triassic and the Middle Cretaceous (Table 4.5 and Fig. 4.7). There is no correlation between age and elevation on either the western slope or on the eastern flank (Fig. 4.2). The youngest sample is APM 49-08 at the base of the western slope, with an age of around 105 Ma.

Apatite (U-Th)/He ages of every sample, except for APM 48-08 and 32-08, are younger or overlap within their 1σ -error with their corresponding AFT-age (Table 4.4 and Fig. 4.7). Some single-grain ages of samples APM 48-08 and 32-08, show older (U-Th)/He age than the corresponding fission track age and, thus, contradict the normal age trend of AFT > AHe (Table 4.5 and Fig. 4.7).

4.6 Discussion

4.6.1 Brittle Fault Activity Constrained by K-Ar Ages

In this study, we used the different illite polytypes to decipher different illite-forming events, thus, the time span of the deformation history. In diagenetic to very low grade sedimentary rocks, $1M_d$ and $1M$ polytypes are considered authigenic products formed under diagenetic to anchimetamorphic, prograde conditions during subsequent burial (e.g. Grathoff and Moore 1996). In contrast, the $2M_1$ illite polytype is considered a detrital component due to its restriction to epizonal conditions.

However, at higher temperatures, even $2M_1$ illite could be developed in fault gouges, especially if the onset of brittle deformation and, thus, fault gouge development directly follows cooling to brittle deformation temperatures (about 300°C for quartz, e.g. Passchier and Trouw 2005 and references therein). The development of $2M_1$ illite polytypes in a brittle fault gouge is possible due to cooling and its passage through epizonal conditions during retrograde metamorphism of the host rock, contemporaneous to faulting (Fig. 4.4). Thus, in contrast to a sedimentary environment, the $2M_1$ illite must not be excluded from consideration but can be considered to record the onset of fault gouge formation.

Based on the calculated polytype compositions of the samples, we extrapolated the ‘end-member’ age of the $1M_d$ polytype and the $2M_1$ polytype (hypothetically samples which consist of 0% $2M_1$ illite and 100 % $2M_1$ illite, respectively) by plotting the age of each individual grain-size fraction of a fault gouge sample against the $2M_1$ illite content (Fig. 4.9 and Table 4.1). These plots show a coefficient of determination (R^2) always larger than 0.9, confirming a clear linear relationship between age and $2M_1$ polytype content. In this study, the $1M_d$ end-member age can be interpreted to best represent the age of the youngest movement because the age-increasing influence of the “older” $2M_1$ polytypes is eliminated, whereas the $2M_1$ end-member age representing a) the oldest generation of neoformed illite and/or b) the age of “detrital” muscovite, meaning crushed muscovite from the host rock. Contamination of mineral fine fractions (<2 μm , <0.2 μm) by cataclastically crushed muscovite from the host rock is very unlikely because of the very strong mechanical resistance of this mineral. Muscovite flakes are apt to rotate parallel to the faulting plane rather than being ground into extremely small particles (e.g. Wemmer 1991). If so, they could be identified by their excellent crystallinity (ca. 0.060 $\Delta^{\circ}2\theta$).

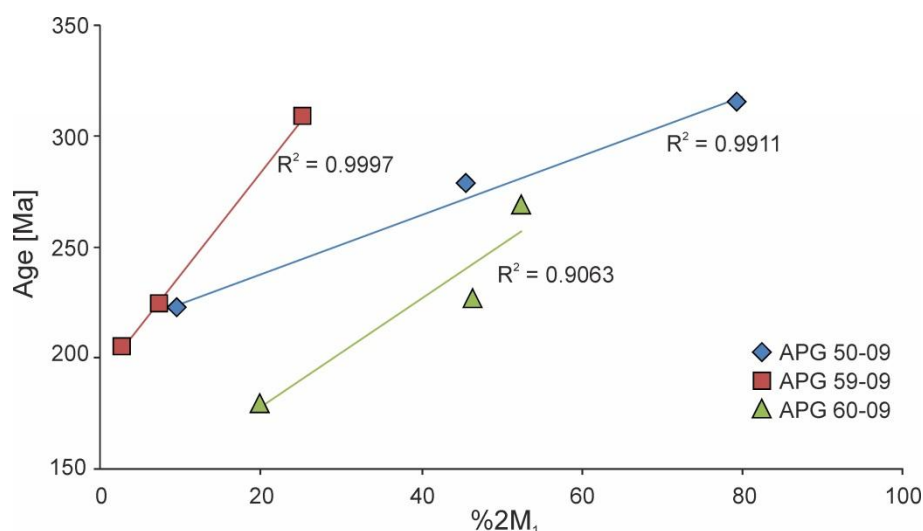


Fig. 4.9: K-Ar ages vs. % 2M₁ illite content for three analyzed samples.

Errors on polytype age determinations are largely dependent on the reliability of illite compositional analysis. Grathoff and Moore (1996) conservatively assume an error of 2-5% for the polytype quantification method. However, they performed polytype quantification on nearly pure illite samples (see Grathoff and Moore 1996). In this study, one of the main problems in polytype quantification was the abundance of kaolinite, as well as substantial amounts of smectite. Especially XRD reflections from smectite exhibit overlap with illite polytype specific reflections. As a consequence, the illite content might be overestimated in the case of superposition of smectite reflections on illite peaks. Polytype quantification obtained by this study could be quantified (Table 4.3) but is subjected to errors greater than those reported by Grathoff and Moore (1996). Thus, polytype quantification results can only be considered as rough estimations due to the abundance of interfering phases. As a consequence, extrapolated 100 % 2M₁ and 0 % 2M₁ illite ages are subjected to substantial error sources. Extrapolated ages are reported here (Table 4.1) but are excluded from interpretation. Nevertheless, polytype quantification is in very good accordance with other parameters, such as grain-size age, illite crystallinity and K-Ar age, indicating the consistency of the data set. Even most of the extrapolated polytype end-member ages (Table 4.3) are in good accordance with K-Ar mica cooling ages (see below).

Following the above-stated assumptions, we interpret all illite to be neoformed, i.e. to be fault-gouge related. However, non-deformational illite formation by fluid percolation cannot be excluded but is unlikely due to the consistency of the data set. The wide age span of the dated sample fractions documents a long-lasting fault activity from 315 Ma (Early Carboniferous) to 179 Ma (Early/Middle Jurassic), whereby the relationship of increasing K-Ar ages with increasing grain size (Table 4.1 and Fig. 4.5) is consistent with increasing content of the 2M₁ illite polytype, formed in the earlier fault history under higher temperatures. However, especially the larger grain-size fractions have to be considered as mixtures of illite formed at different times during different events and, thus, to show an age younger than the effectively oldest illite-forming event. Additionally, the youngest age

documented by fault gouge dating cannot be considered as the cessation of fault activity but to represent the last illite-forming event and, thus, the cooling below illite-forming temperatures (see Fig. 4.3 and discussion below).

When the $2M_1$ illite age represents the onset of brittle deformation, illite ages should always be younger than K-Ar biotite cooling ages (Fig. 4.4). Biotite shows a closure temperature around 350°C (Harrison et al. 2009) and can be interpreted to date the cooling of the basement from ductile to brittle deformation temperatures. Thus, biotite ages represent cooling ages before the first brittle deformation and formation of illite containing fault gouges (Fig. 4.4).

In the Nogolí region, K-Ar biotite ages document a basement cooling to epimetamorphic temperature conditions during the Middle Mississippian (Varela et al. 1994; Sims et al. 1998; González and Sato 2000; Sosa et al. 2002; Steenken et al. 2004; 2008). Further constraint is given by K-Ar and Ar-Ar muscovite ages (Sims et al. 1998; Steenken et al. 2008) taken from several mylonitic shear zones in this region, yielding ages of 380-350 Ma. These ages are interpreted as the last mylonitization event caused by the Achalian Orogenic Cycle before the final cooling of the basement to brittle deformation temperatures (below 300°C for quartz, e.g. Passchier and Trouw 2005 and references therein; see also Fig. 4.4).

In addition, the ages obtained by this study are consistent with epimetamorphic illites from the San Luis Formation (330-290 Ma; Wemmer et al. 2011). The latter are associated with the Toco orogeny (Bahlburg and Breitzkreuz 1991).

Whether our illite fine-fraction ages are influenced by this event or not is unclear. We think that Late Carboniferous ages from both locations can be better related to the last episode of the Chanic phase of the Famatina Orogeny, which reactivated several shear zones in the Sierras Pampeanas (e.g. Martino 2003).

Illite-generating fault gouge activity along the sampled faults is interpreted to have ceased between 222 Ma (APG 50-09 <0.2 μm) and 173 Ma (APG 59-09 100% 1Md), as shown by the majority of the <0.2 μm grain-size fractions as well as the calculated 100% 1Md illite fractions. Only sample APG 6009 shows a younger age for the 100% 1Md fraction of 119 Ma. Similar to the unusually high age of the calculated 100% $2M_1$ fraction of sample 59-09 discussed above, this comparatively young age might be related to an extrapolation error resulting from its – compared to the other samples – low 1Md illite content in the <0.2 μm fraction (see Table 4.1). The youngest age documented by fault gouge dating must not be considered to represent the cessation of fault activity but to represent the last illite-forming event and, thus, the cooling of the fault block below illite-forming temperatures (approximately between 75-110°C; e.g. Hamilton et al. 1992; see Fig. 4.4). Cooling below the illite-forming temperatures is constrained by AFT and AHe ages (Tables 4.4 and 4.5). The youngest illite must overlap with the apatite fission track ages (representing cooling below 110°C), whereas the AHe

ages (representing cooling below 60°C) must always be younger than the K-Ar illite ages (Fig. 4.4). This can indeed be observed for all analysed samples (Tables 4.4 and 4.5, Figs. 4.5 and 4.6)

4.6.2 Thermal Modeling

Fission track single grain ages and confined track length distributions are used along with the (U-Th)/He ages to numerically model possible t-T paths for individual samples. Eight samples along the transect were modelled following the approach of Ketcham (2005) using HeFTy 1.7.0 software. Several boundary conditions were set to the thermal models: (1) the age and temperature range of the K-Ar ages from brittle fault gouges constrains the beginning of transition from ductile to brittle temperatures and, thus, to <300°C due to the onset of brittle behaviour of quartz below this temperature (e.g. van Daalen et al. 1999; Passchier and Trouw 2005 and references therein); (2) the age of the pure 1Md illite fraction (Table 4.3) from fault gouge dating indicates cooling below the illite-forming temperatures (approx. 75-110°C), so reasonable models should show cooling below this temperature range before the youngest 1Md illite-forming event; (3) the annual mean surface temperature of 17 °C (Müller 1996) defines the end of the time-temperature path. The resulting cooling models are shown in Fig. 4.10.

Based on the individual cooling paths derived from HeFTy modelling (Fig. 4.10), a regional thermal history for the entire transect was compiled and is shown in Figure 4.11. This compilation highlights a similar thermal history for all samples within the transect. Within a margin of error, ages are similar for the passage of different temperature regimes for individual samples and respective dating systems. Based on the upper temperature boundary defined by the ZHe ages, cooling below the PRZ_z temperatures (≈175 °C) over the whole transect started in Latest Carboniferous to Middle Permian times. An exception of this is given by samples 49-08 and 34-08, which show initial cooling below the PRZ_z in Carboniferous times. This clear deviation from the trend shown by all other samples gives an indication of an older thermal history of these samples compared to the others. The temperature regime for the apatite fission track partial-annealing zone (PAZ_A ≈110-90 °C) was passed in Middle Permian to Early Triassic times. The lower temperature boundary recorded in our data (PRZ_A ≈65 °C) was reached in Late Permian to Jurassic times, and, for some samples, even Cretaceous times (Fig. 4.11). The span of this time interval is related to very slow cooling during this time, as is evident in all individual models (see Fig. 4.10). In combination with a long-lasting passage through the PRZ_z, PAZ_A and PRZ_A, this led to a broad scattering of helium and fission-track ages (see Fig. 4.7). The long-lasting passage through the PAZ_A is also evident in the broad, unimodal, fission track length distribution and distinct, shortened tracks (see Fig. 4.8). The very slow cooling rate formed suitable conditions for the development of erosional surfaces during one or several planation events.

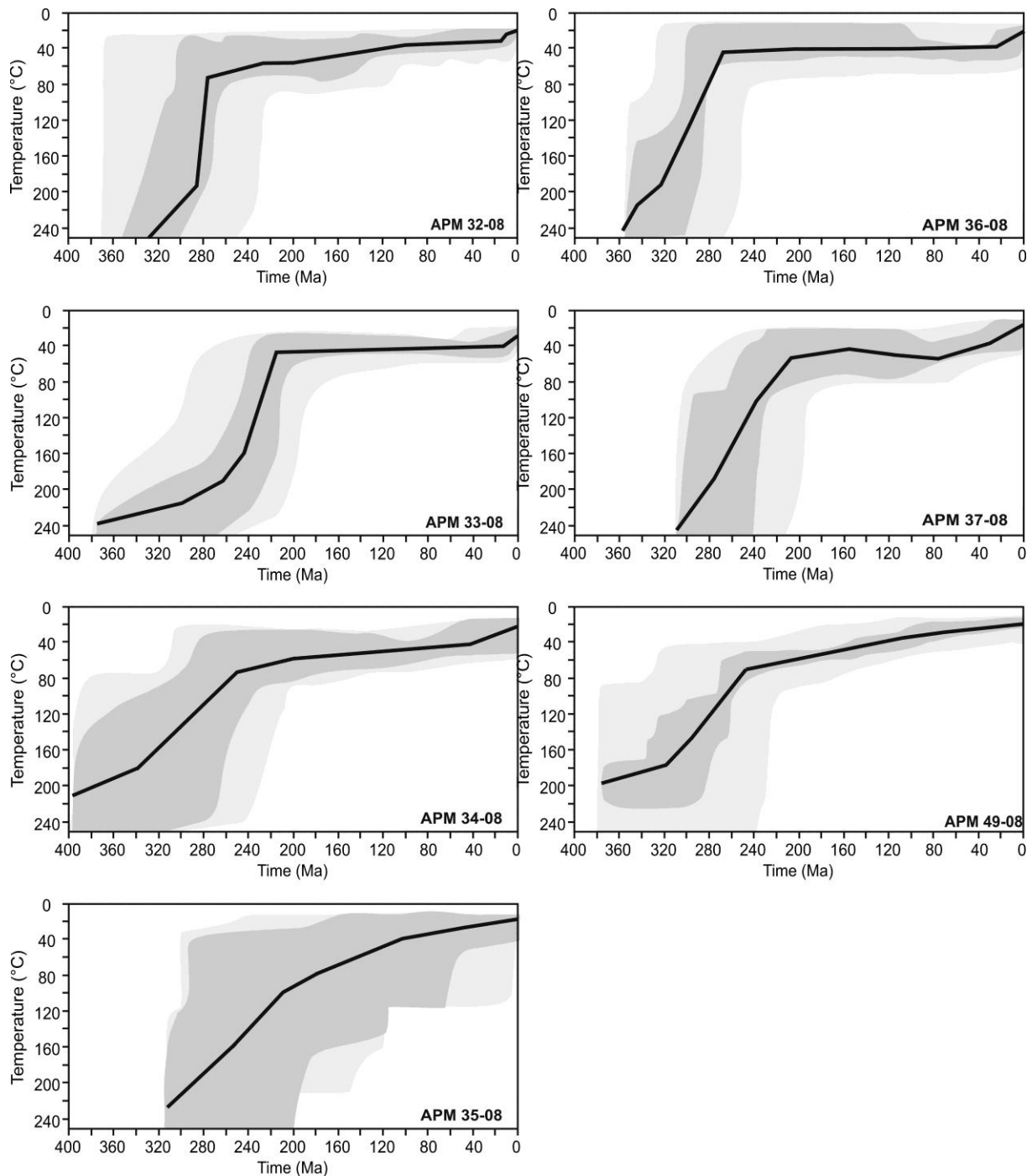


Fig. 4.10: possible t-T paths for individual samples based on Fission track single grain ages and the confined track length distribution as well as the (U-Th)/He ages of apatite and zircon; light grey paths: acceptable fit, dark grey: good fit, black line: best fitting path. With exception of APM 35-08 all models are based on (U-Th)/He data from zircon and apatite and Apatite Fission track data. Model 35-08 is only based on (U-Th)/He data.

Based on model data, conservative calculation of cooling rates to temperatures around 175°C (as illustrated in Figures 4.10 and 4.11) always yields rates below 5°C/Ma. For the temperature range of ca. 175°C (PRZ₂) to ca. 65°C (PRZ_A), rates vary from around 2°C/Ma to 10°C/Ma. An exception of slow to moderate cooling rates is given by samples APM 34-08 and 49-08, which yield rates of 0.5 to 1.5 °C/Ma. These very low cooling rates, with the observation of older ages for cooling to temperatures of ca. 175°C (see above), strongly indicate a different thermal history of samples 34-08 and 49-08 in comparison to all other samples, at least for the cooling above the PAZ_A (Fig. 4.11). Very

low cooling rates of $<0.5^{\circ}\text{C}/\text{Ma}$ (mostly even smaller) are calculated for all models in the temperature range of 65°C to around 30°C . Final cooling to the present day mean surface temperature of 17°C (Müller 1996) is difficult to define because model paths are less constrained in this temperature range. However, calculations based on modelling results demonstrate cooling rates in the range of 0.5 to $1.5^{\circ}\text{C}/\text{Ma}$ for the cooling to surface temperatures.

In summary, all models show slow cooling of less than $0.5^{\circ}\text{C}/\text{Ma}$ since at least 200 Ma (APM 37-08) and less than $0.15^{\circ}\text{C}/\text{Ma}$ since at least 165 Ma (APM 34-08). Although cooling to surface temperatures is methodically only poorly constrained, it is not unlikely to have occurred between 80 - 40 Ma (Fig. 4.10).

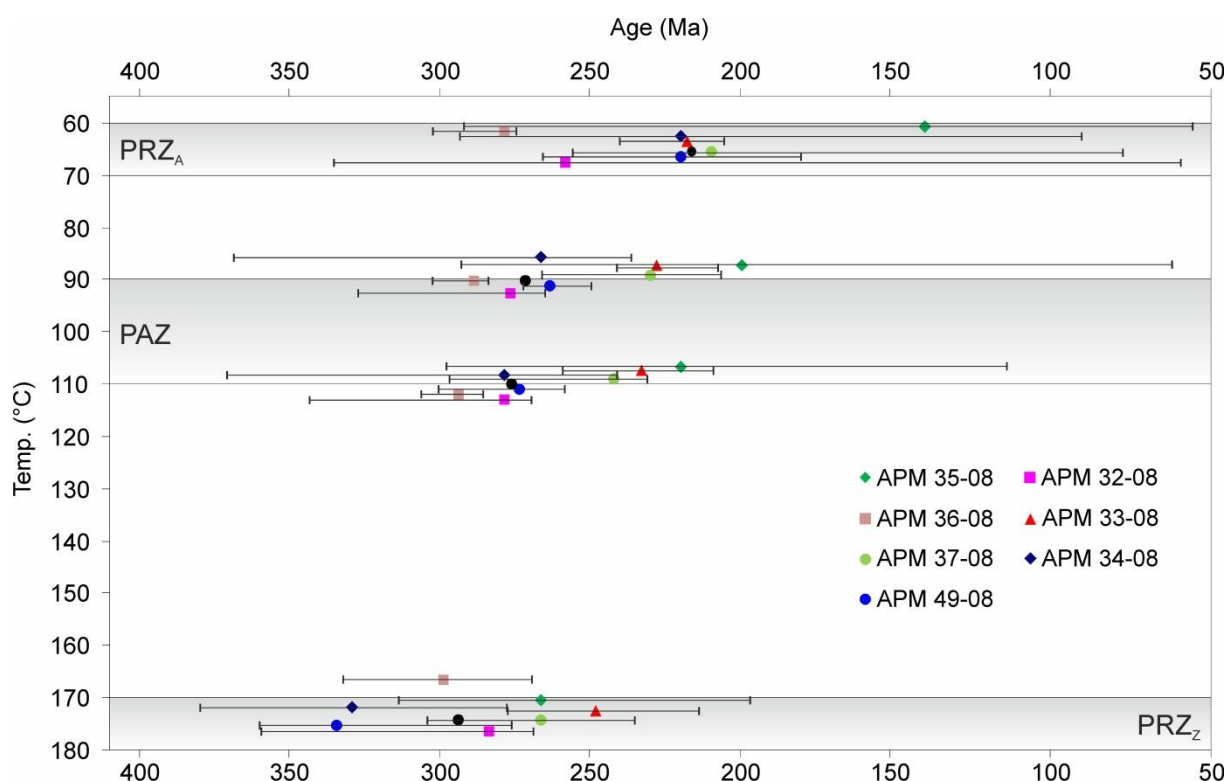


Fig. 4.11: Cooling history for the San Luis profile based on individual t-T paths presented in Fig. 4.10. Horizontal error bars decipher the range of good fits, the position of the marker represents position of best fit path (see Fig. 4.9). For a better illustration the individual samples are exhibited at slightly different temperatures. The approximate temperature ranges of the Partial Retention Zone for zircon (PRZZ), the Partial Annealing Zone for apatite (PAZA) as well as the Partial Retention Zone for apatite (PRZA) are shown as grey bars. The high age span of sample APM 35-08 is due to lack of Apatite Fission Track data (see Fig. 4.10).

4.6.3 Evolution Model

The following regional evolution model for the Sierra de San Luis (SSL) can be proposed. The topographic imprint of the SSL as a positive morpho-structural unit started during the Late Devonian to Early Carboniferous (Fig. 4.12a), as suggested by the onset of brittle deformation in the region of present-day SSL. Brittle deformation followed up the ductile to semi-brittle deformation associated with the Achaian orogenic cycle, which was mainly accommodated along some major shear zones (Rio Guzman, La Arenilla). Especially in the eastern part of SSL, it is likely that a mountainous landscape was developed during this time, after the cessation of magmatic activity.

During the Carboniferous to the Early Permian (Fig. 4.12b), a mountainous landscape developed, associated with the down-wearing of the Early Carboniferous surface (indicated by PTES in Fig. 4.12). Between mountain ranges, several intermountain basins developed, some of which trapped and preserved sedimentary records of this time period (as in the outcrops of Bajo de Véliz, Agua Dorada, La Estanzuela and Suco region; Hünicken and Penza; 1980; Hünicken et al. 1981; Limarino and Spalletti 2006). However, the extent and dimensions as well as possible interconnections of these basins are unknown. In the Bajo de Véliz area, a fluvial-lacustrine environment with typical Gondwanian flora and fauna was preserved in a fault-bounded depression, which is considered to represent the south-easternmost extent of the Paganzo basin (which was widely developed in NW Argentina; e.g. Salfity and Gorustovich 1983; Limarino and Spalletti 2006). A similar situation with a Carboniferous landscape that is carved into older rocks and covered or filled by fluvial sediments can be found in the Chepes range (La Rioja province; pers. comment C. Carignano).

In addition to sedimentation and erosion, brittle deformation continued on within the entire region, as evidenced by K-Ar fault gouge data. Thermochronological data give no clear evidence of whether exhumation of the sampled area above the PRZ_z temperatures took place during this time interval, but it is more likely that this happened during Permian times. It can be concluded that a mountainous landscape had prevailed by then in this region, suggesting that the main planation processes which led to the present-day erosional surfaces had not yet started.

Data suggest that the middle Permian to Jurassic epoch (Fig. 4.12c) is the main exhumation and regional planation phase that affected the sampled area, maybe accompanied by Early Cretaceous processes. In addition, the data give indication of a strong, east-west directed differential exhumation history in the SSL. During Permian times, the eastern part was exhumed to a surface or a near-surface position and interacted with surficial processes, as evidenced by the conservation of Gondwanian sediments in the Bajo de Véliz region. In contrast, the western part (sampled locations) were at least below the PAZ_A depths and, thus, still at several kilometres in depth, as shown by our data.

We interpret this differential exhumation to be caused by differential block faulting with significant vertical components along different fault zones throughout the SSL. The latter is constrained by long-lasting fault activity, as it is traced by our K-Ar illite ages from fault gouges (Table 4.1).

Our thermochronological data do not explicitly constrain the differential exhumation procedure. However, our data clearly document the onset of exhumation during the Permian. In addition, it gives indication that PAZ_A temperatures were reached by the Latest Permian / Early Triassic (Fig. 4.11). This event comprises the main exhumation concerning the difference in depth from the PRZ_z to the PAZ_A. Depending on the geothermal gradient, the latter may range from 1 km to 3km.

the ages obtained are highly synchronous to several compressional events in the region, although an explicit association with a regional orogenic event is not definitely clear. Old K-Ar ages are synchronous to the latest Chanic orogenic phase of the Famatinian Orogen (defined e.g. Martino 2003) as well as to the Achalian Orogeny (Miller and Söllner 2005), as well as to the Toco Orogeny (Bahlburg and Breitzkreuz 1991) in the NW-Argentina and N-Chile region. The Permian exhumation event is synchronous with the San Rafael Orogeny (e.g. Kleimann and Japas 2009) in the San Rafael region. However, until now, no link of the structural inventory in the Sierras de San Luis or the San Rafael Orogeny has been made.

Final exhumation to the surface level is less constrained by the data. However, thermal modelling (Fig. 4.11, Tables 4.4 and 4.5) indicates that exhumation above PAZ_A temperatures occurred in post-Permian times.

Concerning the time of development of planation surfaces, the Triassic epoch is not well suited for their regional development due to crustal rifting west of the SSL and the development of fault-bounded ranges and related half-graben basins. These processes have been well documented in southwestern San Luis and Mendoza province (Criado Roque et al. 1981; Ramos and Kay 1991; Kosłowski et al. 1993; Dellapé and Hegedus 1995). Evidence of these processes crop out at the Sierra de Varela area, 100 km to the south of the SSL (Costa et al. 1998). It is assumed that this prevailing tectonic unrest with a continuous base-level fall of the fluvial system did not favour the development of planation surfaces with regional significance. In addition, a Triassic emergence of the sampled area is not evidenced by AHe ages, which yield predominantly Jurassic and Cretaceous ages.

During Early Cretaceous times, rifting took place east and west of SSL. Rifting had probably already started in Late Jurassic times, as indicated by 150-160 Ma and 106 Ma old Ar-Ar ages of basalts in the Las Quijadas range, west of the SSL (González and Toselli 1973; Yrigoyen 1975). In addition to the Triassic epoch (see above), the time span from the Late Jurassic to Early Cretaceous is also less suited to development of regional planation surfaces because of the prevailing crustal tectonic activity.

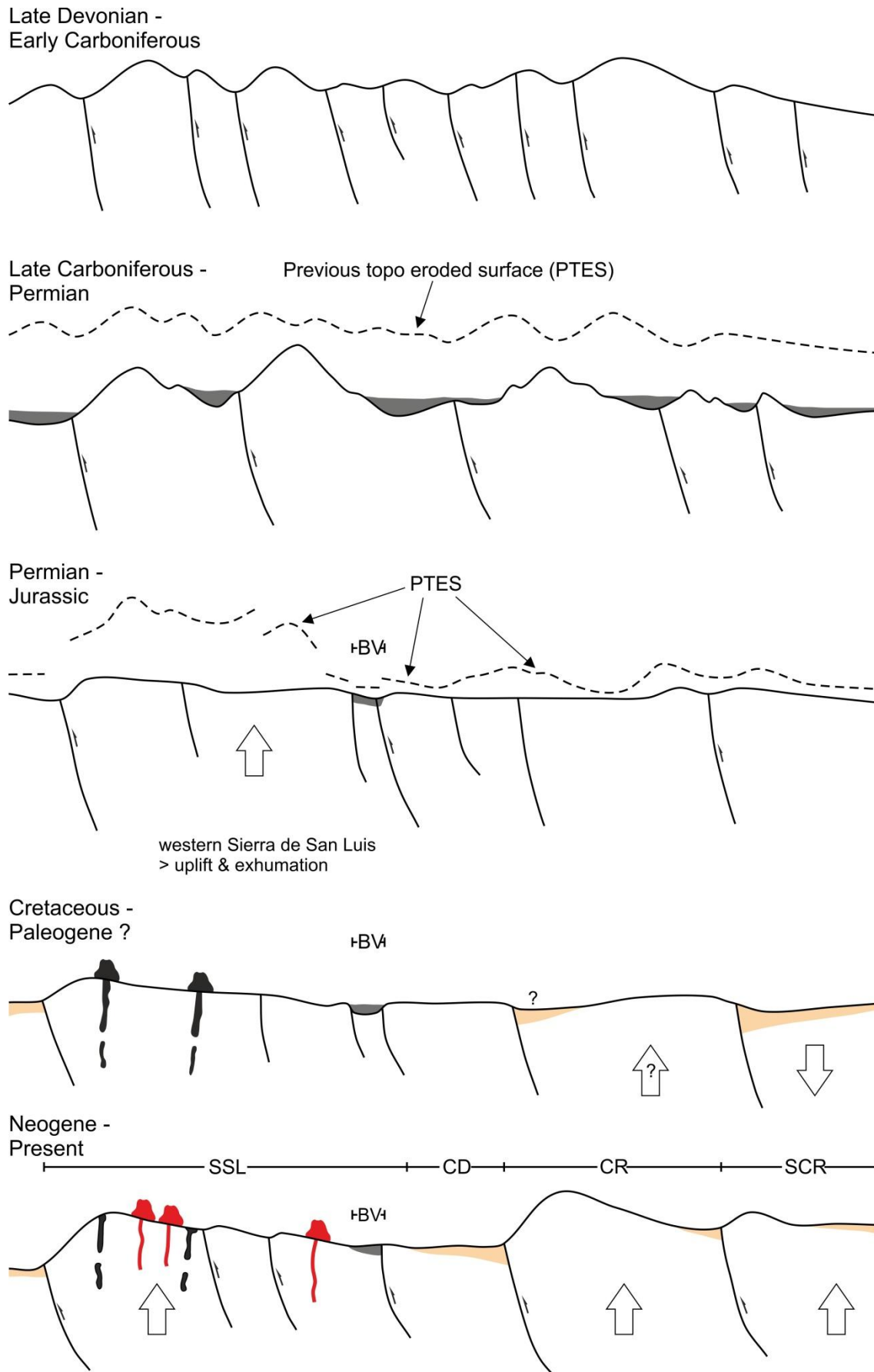


Fig. 4.12: Exhumation model for the Sierra de San Luis. See text for details (BV = Bajo de Véliz; PTES = Previous Topo-graphic Eroded Surface; SSL = Sierra de San Luis; CD = Conlara Depression; CR = Comechingones range; SCR = Sierra Chica Range; white arrow indicating area affected by uplift or subsidence). For further details on the Sierra de Comechingones see Löbens et al. 2011.

It can be concluded that the final exhumation of the sample region, as well as regional planation processes, took place either during the Early-Middle Jurassic and/or during the Late Cretaceous. This idea is supported by the absence of Jurassic deposits in the Sierras Pampeanas, while Jurassic basins did develop in surrounding regions (e.g. the Neuquén basin, Howell et al. 2005). Thus, we assume that the Pampeanas region, or at least the southeastern Sierra Pampeanas, were had positive topography affected by erosion during that time.

AHe ages indicate that both time intervals contributed to the exhumation of the sampled area. Samples from higher elevations show predominantly Jurassic ages and were probably also exhumed to surface conditions during this time. The lowermost sample, which represents the western footslope area of the SSL, passed through PRZ_A conditions in Middle Cretaceous times (AHe mean age 105 Ma, see Table 4.5). Whether or not emergence happened during this time cannot be concluded from our data. Further constraints may come from several basalts which were emplaced at higher altitudes in the SSL during the Cretaceous (Fig. 4.12d). Remnants of those basalts yield ages around 84 Ma (Pampa de La Invernada basalts; Solá 1981). If these basalts were emplaced atop the erosional surface, the emergence and formation of the erosional surface could be bracketed to be older than 84 Ma. This age is in contrast to AHe single grain ages of the lowermost sample from the western footslope (APM 49-08), which show a minimum age for passage through the PRZ_A of 72 Ma (Table 4.5), coinciding with a depth of about 2.4 km (considering a geothermal gradient of 25°C/km). This favours the idea of diachronous development of the erosional surfaces in this part of the SSL, with an older surface on top of the range (>84 Ma) and a younger erosional surface (<72 Ma) in the footslope area of the westernmost SSL. In any case, the effusive character of the dated basalts is unclear because no robust field evidence for effusion above erosional surface exists. Basaltic remnants might also correspond to a sill or dyke which has no relationship to the erosional surface and, thus, cannot be used as a marker for emergence beyond doubt.

The geomorphologic situation in the Comechingones range (Fig. 4.12d) is also enigmatic and is still a matter of ongoing debate (e.g. Löbens et al. 2011) – especially in terms of whether the region represents a positive morphostructural unit that acted as a sedimentary source for Cretaceous basins to the east or, in contrast, was affected by subsidence and Cretaceous sedimentation itself. Findings of large blocks composed of red conglomerates along some creeks (Morla, pers. comm.), favour the existence of a sedimentary cover overlying the present Comechingones ranges. Similar findings are documented in the nearby Sierra Chica (Gordillo and Lencinas 1979; Bonalumi 2005).

Cenozoic events (Fig. 4.12e) are not evident in the data presented here. Thus, any Cenozoic contribution to the exhumation of the SSL can be concluded to be of minor magnitude when considering that the minimum total exhumation along a transect through the SSL equals the topographic difference between topmost and lowermost parts. This value must be smaller than the

depth of the Paleo-PRZ (2.4 Km for a gradient of 25°C/km). If the total exhumation since the record of the youngest age (Cretaceous) exceeds this difference, the samples from the footslope area of the SSL must yield younger, reset ages. Additionally, this would be represented by a break in slope in the age-elevation plot (see Gleadow and Fitzgerald 1987).

The evaluation of any exhumation postdating the youngest AHe ages depends on the interpretation of the 84 Ma basalts. If the basalts represent surficial lava flows above a paleolandsurface, exhumation had already finished by this time. In this case, final exhumation of the present day top regions of the SSL to the surface happened between the Jurassic and Upper Cretaceous. If, in contrast, the basalts represent dykes with no relationship to a paleosurface, no further constraints on the final exhumation can be made. Regardless, even in the latter case, the characteristic volcanic texture of the basalts can hint to a persisting exhumation between the passage of the samples through the PRZ_A and the emplacement of the basalts. Considering an AHe age for the region of the Pampa de La Invernada between the age of nearest samples APM 3308 (188 Ma) and 3408 (142 Ma), the age of the basalts (84 Ma), the maximum depth for the development of volcanic texture (1-1.5 km), and the depth of the PRZA (2.4 km with a geothermal gradient of 25°C/km), exhumation would be about 1 km between PRZA-passage, and basalt emplacement would be about 60 Ma later.

Even though we cannot solve the final, post-Cretaceous exhumation and uplift history (Fig. 4.12e), there is no doubt that range uplift occurred after the Paleocene due to Andean shortening, giving an imprint to the present day landscape (Costa 1992; Ramos et al. 2002). For instance, Piedmont landform association as well as morphotectonic parameters suggest that the SSL is currently characterized by moderate to low Quaternary uplift rates (< 0.1 mm/a, according to Costa 1992). However, a significant change in the regional base level fall occurred from 6-4 Ma ago to present times. This is suggested by the behaviour of long-term neotectonic indicators and by the occurrence of Quaternary-active faulting on the main range bounding fault (Costa 1992; Costa et al. 1999; 2001).

4.6.4 Regional Constraints

4.6.4.1 Comparison of K-Ar Ages

K-Ar illite ages from fault gouges in the Sierra de Comechingones, east of the Sierra de San Luis (Fig. 4.1) show ages in the range of 340 Ma to 170 Ma (Löbens et al. 2011). In comparison, the oldest fault gouge ages in the Sierra de San Luis (SSL) are about 25 Ma younger (315-170 Ma, Table 4.1). Thus, onset of brittle deformation started slightly earlier in the Sierra de Comechingones than in the SSL. The youngest illite ages, interpreted to document cooling below illite formation temperatures (110°C - 75°C, e.g. Hamilton et al. 1992), are synchronous for both ranges.

4.6.4.2 Comparison of (U-Th)-He and AFT Thermochronological Data

Single grain ages, as well as modelled cooling paths, show differential cooling for the Nogolí region (SSL) and the Yacanto area (Sierra de Comechingones; Löbens et al. 2011). On the basis of ZHe data, we conclude that cooling started earlier in SSL than in the Sierra de Comechingones. Over time, cooling of both ranges became subsequently more synchronous, as shown by overlapping AFT, K-Ar illite and AHe ages, although AHe ages also indicate that final cooling below PRZ_A temperatures occurred earlier in the Nogolí area.

Additional thermochronological data from the Sierra de Ancasti (Fig. 4.1; Sobel and Strecker 2003) in combination with preliminary data from the Sierras Pie de Palo, Aconquija and Pocho (Fig. 4.1; Löbens et al. in review; Bense et al. in review B) document that the evolution of the Pampean ranges cannot be condensed in a chronologically or structurally uniform evolution, which would have been caused by a single event. Instead, a heterogeneous evolution must be considered to have been caused and affected by multiple events, resulting in distinct variations in cooling and exhumation history from north to south and east to west.

4.7 Conclusions

Based on the K-Ar illite fine-fraction ages and low-temperature thermochronological data presented in this study, as well as on the regional geologic evidence discussed, we draw the following conclusions:

Exhumation of the section of the Sierra de San Luis (SSL) studied here started during Permian times and is synchronous with an orogenic phase called San Rafael Orogeny further south. A direct link between this orogenic phase and the structural evolution of the SSL has not yet been developed. The coeval timing and the relative proximity of the proposed key area of the San Rafael Orogeny (San Rafael Massif, Mendoza province) should incite the idea of further studies to evaluate possible influences of this compressive phase for the San Luis region. In a more general framework, these exhumation processes might also record the tectonic imprint of a flat-slab subduction episode proposed at these latitudes (see e.g. Ramos and Folguera 2009).

These results point out that the lithologies currently exposed at the eastern and western parts of the SSL affected by regional Mesozoic planation processes have followed different exhumation paths. The eastern part was already in a near-surface position and constituted the substratum of the Bajo de Véliz basin during Late Carboniferous-Permian times, whereas the rocks of the cross section analysed here were still below the PAZ_A by then.

The main exhumation phase can be bracketed between Middle Permian and Jurassic times. It is characterized by a strong differential exhumation with low exhumation rates in the east and higher rates in the west, which is interpreted to be caused by differential block faulting. The period from

Jurassic to Cretaceous times is characterized by further exhumation but also considered to be the time period when most of the remaining erosional surfaces were developed. However, erosional processes had also evolved previously.

The development of a distinct mountainous landscape in the SSL region probably started during Late Devonian to Early Carboniferous times. During the Carboniferous to Early Permian, the positive relief underwent erosion and development of intermountain basins, as evidenced by relictic Gondwanian deposits (e.g. Bajo de Véliz area). Planation processes giving rise to erosional surfaces have not been ruled out, but it is understood that their regional significance was achieved during Mesozoic times.

Cooling below 175 °C started differentially in the transect of the SSL and the Sierras de Comechingones studied but became more synchronous over time. There are arguments that final cooling to surface temperatures in the section of the SSL studied started significantly earlier than in the Sierra de Comechingones.

Cooling rates varied from slow to intermediate over time. The highest rates are observed during the Permian and Triassic periods (2-10°C/Ma). Post-Triassic cooling yields lower rates of 0.5-1-5 °C/km.

Data on the regional high temperature thermal history indicate a cooling propagating from west to east. Our data show that this trend is reversed during further cooling ($T < 180^{\circ}\text{C}$), with cooling propagation from east to west. As a consequence, the Bajo de Véliz region (east) cooled before the Nogolí region (west).

Cenozoic shortening and flattening of the subduction angle of the Nazca Plate due to the collision of the Juan Fernandez Ridge in the Miocene might have contributed to the exhumation of the SSL. However, no Cenozoic event is evident in the presented data. Even if we cannot solve the post-Cretaceous uplift and exhumation story in full detail with our data, there is no doubt that shortening and range uplift took place after the Paleocene due to Andean shortening, which gives rise to neotectonic movement and uplift in the Sierras Pampeanas.

K-Ar illite fine-fraction dating on fault gouges revealed a long-lasting brittle deformation history for the SSL. Brittle deformation started during Carboniferous times in compliance with the ages of the regional cooling after the Achaian orogenic cycle. The youngest illite ages (ca. 130 Ma) represent cooling below illite formation temperatures but not the cessation of brittle deformation. This is in good accordance with the thermochronological data discussed here.

The oldest K-Ar ages are synchronous to an orogenic event defined as the Chanic Orogeny. If these ages have any connection to the Toco Orogeny, as is suggested for similar K-Ar fine-fraction ages from the San Luis Formation, it has not yet been clarified. However, a connection to the Toco Orogeny seems unrealistic due to the great distance between its key location and the study area.

As with the Sierras de Comechingones, the SSL also documents a long-lasting brittle deformation period. The onset of brittle deformation in the SSL started during the Carboniferous and is around 25 Ma younger than the onset of brittle deformation in the Sierra de Comechingones.

For the interpretation of K-Ar ages from fault gouge samples, we developed an interpretation scheme based on a number of constraints for cross-evaluating the data derived from K-Ar illite fine-fraction dating, illite polytype quantification and polytype age extrapolation with data derived from independent dating methods, such as K-Ar biotite and apatite fission track, as well as (U/Th)-He on apatite and zircon (Fig. 4.3). The schema developed combines and highlights concordant data sets derived from different data sources and eases the combination of all observations into a consistent regional evolution model.

Table 4.3: Fission track data.

Sample No. (rocktype)	Latitude Longitude	Altitude (m)	n	ρ_s	N_s	ρ_i	N_i	ρ_d	N_d	$P(\chi^2)$ (%)	Age (Ma)	$\pm 1\sigma$ (Ma)	MTL (μm)	SD (μm)	N (L)	Dpar (μm)
APM 32-08 (granite)	66°09,99' 33°02,66'	1811	25	15.9	1025	7.9	514	7.80	7368	42.1	246.9	23.1	12.3	1.4	50	1.79
APM 33-08 (granite)	66°11,29' 33°01,09'	1947	23	33.6	2051	21.4	1307	7.83	7368	58.7	195.6	17.0	12.3	0.9	50	1.85
APM 34-08 (granite)	66°12,22' 33°00,28'	2085	23	16.4	1167	8.6	616	7.54	7368	26.4	227.0	21.5	12.4	1.5	48	1.93
APM 36-08 (migm.)	66°12,83' 32°59,23'	1702	25	22.4	1907	11.1	950	7.63	7368	11.7	245.3	22.6	12.5	1.0	50	2.05
APM 37-08 (schist)	66°13,50' 32°58,76'	1503	25	34.3	2734	20.7	1647	7.69	7368	64.5	203.0	17.3	12.3	0.9	50	2.09
APM 48-08 (granite)	66°14,60' 32°58,58'	1269	24	32.1	3102	20.4	1972	7.67	7368	42.0	192.1	16.2	11.9	1.3	50	1.91
APM 49-08 (granite)	66°16,47' 32°56,28'	981	22	19.8	1745	9.8	863	7.87	7368	28.3	251.3	22.9	12.9	1.2	50	1.84

Presented ages are central ages $\pm 1\sigma$ (Galbraith and Laslett 1993); ages were calculated using zeta calibration method (Hurford and Green 1983); glass dosimeter CN-5, and zeta value of S.L. is $323.16 \pm 10.1 \text{ a cm}^{-2}$; zeta error was calculated using ZETAMEAN software (Brandon 1996); n , number of dated apatite crystals; ρ_s/ρ_i , spontaneous/induced track densities ($\times 10^5 \text{ tracks cm}^{-2}$); N_s/N_i , number of counted spontaneous/induced tracks; N_d , number of tracks counted on dosimeter; $P(\chi^2)$, probability obtaining chi-squared value (χ^2) for n degree of freedom (where n is the number of crystals – 1), MTL, mean track length; SD, standard deviation of track length distribution; N , number of tracks measured; Dpar, etch pit diameter.

Table 4.4: Zircon and apatite (U-Th)/He data of the samples from the Nogolí – Rio Grande profile

Sample	He [ncc]	s.e. [%]	U238 mass [ng]	s.e. %	Th232 mass [ng]	s.e. %	Th/U	Sm mass [ng]	s.e. %	Corr. Ft USED	Uncorr. [Ma]	Ft-Corr [Ma]	1s [Ma]	Sample weighted average age [Ma]
<u>Zircon</u>														
APM 32-08 (granite)	41.203	1.6	1.527	1.8	0.906	2.4	0.59	0.183	5.5	0.694	192.7	277.6	14.2	291.6
	20.928	1.6	0.582	1.8	0.247	2.4	0.42	0.036	6.1	0.770	264.4	343.3	14.2	
	12.423	1.6	0.547	1.8	0.192	2.4	0.35	0.032	6.1	0.679	171.0	251.8	13.44	
APM 33-08 (granite)	90.940	1.6	4.444	1.8	0.739	2.4	0.17	0.070	8.1	0.726	160.8	221.7	10.5	266.2
	11.792	1.6	0.431	1.8	0.241	2.4	0.56	0.023	11.1	0.633	196.8	310.8	18.52	
APM 34-08 (granite)	9.649	1.6	0.383	1.8	0.235	2.4	0.61	0.021	6.7	0.633	179.3	283.0	16.83	
	3.268	1.7	0.231	1.9	0.007	2.8	0.03	0.001	19.7	0.602	115.4	191.7	12.37	232.2
	4.462	1.7	0.266	1.8	0.023	2.5	0.09	0.010	7.7	0.607	134.7	222.0	14.15	

Sample	He [ncc]	s.e. [%]	U238 mass [ng]	s.e. %	Th232 mass [ng]	s.e. %	Th/U	Sm mass [ng]	s.e. %	Corr. Ft USED	Uncorr. [Ma]	Ft-Corr [Ma]	1s [Ma]	Sample weighted average age [Ma]
APM 35-08	53.820	1.6	2.308	1.8	0.605	2.4	0.26	0.343	5.8	0.818	178.9	218.8	7.84	
(gneiss)	26.703	1.6	1.068	1.8	0.292	2.4	0.27	0.115	6.5	0.753	191.2	253.9	11.1	
	69.049	1.6	2.352	1.8	1.759	2.4	0.75	0.421	5.5	0.772	202.9	262.7	10.72	
	29.805	1.6	1.142	1.8	0.712	2.4	0.62	0.164	6.5	0.696	185.4	266.2	13.53	253.6
APM 37-08	23.232	1.6	0.823	1.8	0.359	2.4	0.44	0.024	32.3	0.718	208.2	289.9	13.94	
(mica schist)	20.578	1.6	0.832	1.8	0.285	2.4	0.34	0.026	31.4	0.757	186.4	246.4	10.64	271.1
APM 48-08	29.467	1.6	1.229	1.8	0.487	2.4	0.4	0.109	5.2	0.713	178.7	250.6	12.22	
(granite)	205.521	1.6	7.045	1.8	1.868	2.4	0.27	0.372	5.5	0.835	222.9	266.9	9.03	
	512.118	1.6	25.276	1.8	5.105	2.4	0.2	1.210	5.2	0.877	158.0	180.2	5.36	
	110.013	1.6	4.842	1.8	1.055	2.4	0.22	0.480	5.1	0.805	176.2	218.9	8.19	
	119.681	1.6	5.978	1.8	1.517	2.4	0.25	0.475	5.4	0.856	154.3	180.2	5.7	228.6
APM 49-08	80.278	1.6	1.890	1.8	2.560	2.4	1.35	0.127	5.1	0.812	261.0	321.5	11.47	
(granite)	203.857	1.6	4.418	1.8	6.572	2.4	1.49	0.289	5.1	0.832	276.7	332.6	11.07	
	110.448	1.6	2.508	1.8	4.243	2.4	1.69	0.195	5.1	0.839	255.4	304.6	9.89	
	122.269	1.6	3.146	1.8	4.156	2.4	1.32	0.162	5.2	0.831	240.6	289.6	9.69	313.1
<u>Apatite</u>														
APM 32-08	0.263	2.1	0.003	21.2	0.014	3.7	5.32	0.244	6.1	0.852	265.8	311.9	24.07	
(granite)	0.323	2.1	0.014	4.1	0.021	3.3	1.52	0.195	6.1	0.784	132.3	168.7	8.06	
	1.533	1.7	0.014	4.1	0.127	2.5	8.98	0.250	5.9	0.864	271.7	314.6	10.59	285.6
APM 33-08	4.699	1.7	0.234	1.8	0.012	4	0.05	0.507	5.1	0.843	159.3	188.9	6.33	
(granite)	7.967	1.7	0.401	1.8	0.069	2.5	0.17	1.129	5.6	0.838	152.8	182.2	6.14	
	3.778	1.7	0.169	1.9	0.023	3.2	0.13	0.562	5.2	0.805	172.0	213.8	8.06	
	3.162	1.7	0.169	1.8	0.017	2.9	0.1	0.237	5.5	0.884	147.9	167.3	4.96	
	3.554	1.7	0.214	1.8	0.010	4.3	0.05	0.584	4.8	0.876	131.6	150.2	4.56	
	7.168	1.7	0.317	1.8	0.022	2.8	0.07	0.670	5.4	0.896	178.6	199.4	5.66	
	11.524	1.6	0.482	1.8	0.044	2.6	0.09	0.648	5.4	0.890	188.5	211.8	6.11	
	3.136	1.7	0.165	1.8	0.030	2.7	0.18	0.356	5.4	0.843	146.6	174.0	5.82	188.7
APM 34-08	1.654	1.8	0.080	1.9	0.003	6	0.04	0.326	5.7	0.898	161.5	179.9	5.27	
(granite)	0.230	2.1	0.007	9.7	0.019	3.4	2.7	0.972	4.7	0.831	98.6	118.5	6.06	
	0.109	2.8	0.006	9	0.002	7	0.39	0.019	9.8	0.876	125.8	143.5	12.15	
	0.609	1.9	0.044	2.1	0.005	4.7	0.1	0.096	6.6	0.855	109.2	127.7	4.48	142.4
APM 35-08	0.581	1.8	0.034	2.7	0.008	4.9	0.23	0.018	5.4	0.804	134.0	166.7	7.08	
(gneiss)	0.082	2.6	0.007	8.4	0.011	2.7	1.62	0.020	3	0.753	73.4	97.5	7.13	
	0.030	3.8	0.003	20.5	0.003	2.7	1.31	0.019	3.3	0.495	66.7	134.7	22.45	133.7
APM 36-08	1.735	1.7	0.084	1.9	0.004	7.5	0.04	0.663	6.4	0.871	157.5	180.7	5.65	
(migmatite)	2.896	1.7	0.147	1.8	0.004	4.5	0.03	0.408	4.5	0.812	156.5	192.7	7.13	
	0.980	1.8	0.051	2.1	0.003	8.7	0.06	0.281	6.3	0.799	147.7	184.8	7.35	
	1.768	1.7	0.080	1.9	0.003	5.2	0.04	0.393	4.5	0.859	171.9	200.1	6.46	
	0.555	1.9	0.029	2.3	0.002	7	0.06	0.293	4.6	0.891	142.7	160.2	5.19	
	0.511	1.8	0.030	2.3	0.003	5	0.11	0.198	4.7	0.862	129.9	150.7	5.18	
	4.793	1.7	0.208	1.8	0.013	3	0.06	0.775	4.6	0.926	179.8	194.1	5.07	181.8

Sample	He [ncc]	s.e. [%]	U238 mass [ng]	s.e. %	Th232 mass [ng]	s.e. %	Th/U	Sm mass [ng]	s.e. %	Corr. Ft USED	Uncorr. [Ma]	Ft-Corr [Ma]	1s [Ma]	Sample weighted average age [Ma]
APM 37-08	1.367	1.7	0.071	2.1	0.009	4.6	0.13	0.283	5.1	0.819	148.5	181.4	6.74	
(mica schist)	0.263	2	0.033	2.4	0.003	5.1	0.1	0.074	5.6	0.840	63.4	75.5	2.9	
	0.806	1.8	0.057	2	0.009	3.5	0.16	0.244	5.8	0.885	107.8	121.8	3.76	
	1.164	1.8	0.064	2	0.004	5	0.07	0.289	5.7	0.823	142.2	172.7	6.34	137.9
APM 48-08	2.203	1.7	0.081	2	0.011	4.2	0.13	0.714	4.8	0.799	201.6	252.2	9.77	
(granite)	2.467	1.7	0.113	1.9	0.012	3.2	0.1	0.633	5.3	0.894	166.9	186.7	5.38	
	4.698	1.7	0.165	1.9	0.017	3.5	0.1	1.128	4.9	0.856	214.6	250.7	8.02	
	5.598	1.7	0.172	1.8	0.022	2.8	0.13	0.898	5.4	0.884	246.3	278.7	8.16	
	7.677	1.7	0.255	1.8	0.023	2.7	0.09	1.180	5.3	0.892	230.7	258.6	7.38	245.4
APM 49-08	0.768	1.8	0.035	2.3	0.132	2.5	3.75	0.396	6.1	0.820	91.0	111.1	4.05	
(granite)	1.490	1.7	0.089	1.9	0.363	2.4	4.1	0.741	5.4	0.876	68.0	77.6	2.27	
	0.393	2	0.022	2.9	0.082	2.6	3.75	0.215	5.9	0.774	75.1	97.0	4.2	
	1.423	1.7	0.094	1.9	0.297	2.4	3.17	0.708	5.4	0.875	69.0	78.8	2.3	
	0.696	1.8	0.034	2.4	0.048	2.6	1.42	0.335	5.5	0.886	118.6	133.9	4.09	
	2.224	1.7	0.117	1.9	0.429	2.4	3.68	0.782	5.4	0.873	81.4	93.3	2.74	
	1.442	1.7	0.060	2	0.189	2.4	3.15	0.568	5.4	0.904	108.3	119.8	3.21	105.1

5 The Sierra de Pie de Palo

5.1 Introduction

Most recent geochronological studies of the western margin of the Sierras Pampeanas in western Argentina are concerned to terrane-related accretional history at the southwestern proto-Andean margin of Gondwana and the accompanying metamorphic evolution during the Paleozoic (e.g. Casquet et al. 2001; Morata et al. 2010; Mulcahy et al. 2007; Pankhurst and Rapela, 1998; Ramos et al. 1998; Varela and Dalla Salda, 1992; Varela et al. 2011; Vujovich et al. 2004). One of these terranes is represented by the Cuyania Terrane which is bounded by the Pampean Terrane to the east, the Chilenia Terrane in the west and the Famatinia Terrane to the north (Fig. 5.1; e.g. Ramos et al. 2002; Ramos and Vujovich, 2000). The origin and accretion of the Cuyania Terrane, which comprises the Western Sierras Pampeanas (*sensu* Caminos, 1979) including the Sierra de Pie de Palo, during the Ordovician is still controversially discussed in the literature (e.g. Aceñolanza and Toselli, 1988; Finney et al. 2003; Meira et al. 2012; Mulcahy et al. 2007; Ramos, 1988; Ramos et al. 1998; Ramos, 2004; Thomas and Astini, 2003; van Staal et al. 2011). On one hand, most authors agree that the exotic Cuyania, or Precordillera Terrane represents an allochthonous continental block derived from Laurentia and accreted to the southwestern proto-Andean margin of Gondwana during the Famatinian orogenic cycle in Middle Ordovician (e.g. Ramos, 1988; Ramos et al. 1998; Ramos, 2004; Thomas and Astini, 2003) or Silurian/Devonian times (e.g. Keller et al. 1998; Pankhurst and Rapela, 1998; Rapela et al. 1998). On the other hand, the Cuyania Terrane is considered to be of parautochthonous Gondwanan origin displaced along a strike-slip fault at the southern margin of West Gondwana (present situation, e.g. Aceñolanza and Toselli, 1988; Baldi et al. 1989; Finney et al. 2003).

The Cenozoic evolution of the most western basement uplifts of the Sierras Pampeanas, which is mainly associated with the Andean deformation (e.g. Ramos et al. 2002), was usually investigated using geophysical, structural, and lithological approaches (e.g. Jordan and Allmendinger, 1986; Ramos and Vujovich, 2000; Regnier et al. 1992). However, low-temperature thermochronological data, i.e. fission-track and (U-Th)/He dating of apatite, providing constraints on amount of cooling/erosion related to mountain building, crustal deformation, extensional tectonics as well as landscape evolution (e.g. Farley, 2002; Fitzgerald et al. 2006; Gallagher et al. 1998; Stockli et al. 2000) are still scarce within this region. Coughlin et al. (1998) reported apatite fission-track measurements for the Sierra de Valle Fértil, Sierra de La Maz, and Sierra Umango suggesting that deformation in the Sierras Pampeanas could be associated with uplift of the Puna Plateau during the Oligocene to Miocene and final flat-slab subduction-related exhumation (e.g. Jordan et al. 1983; Ramos et al. 2002; Yáñez et al. 2001) of the Pampean ranges commenced in Miocene-Pliocene times.

The aim of this study is to investigate the Cenozoic cooling exhumation and uplift (*sensu* England and Molnar, 1990) history of the Sierra de Pie de Palo and its relationship to the Andean deformation within the Western Sierras Pampeanas using geochronological methods. Therefore, we conducted apatite fission-track measurements, (U-Th)/He analysis of zircon and apatite of samples from the Sierra de Pie de Palo, and subsequent thermal modeling to get complete cooling paths from below approximately 200 °C to surface temperature.

5.2 Geologic Setting

The Sierra de Pie de Palo located between 67°30′-68°30′ W and 31°00′-32°00′ S is one of the westernmost ranges of the Argentine Sierras Pampeanas (Fig. 5.1). It represents a NNE trending elongated dome with an area of approximately 2400 km² and elevations of more than 3000 m. This fault bounded basement anticline (Perez and Martínez, 1990) is part of the Western Sierras Pampeanas (*sensu* Caminos, 1979; Pankhurst and Rapela, 1998) constituting the central part of a north-south trending belt, the Cuyania Terrane (Sato et al. 2000), which accreted along a major suture west of the Valle Fértil (e.g. Ramos et al. 2002) to the southwestern proto-Andean margin of Gondwana during the Late Paleozoic (e.g. Keller et al. 1998; Pankhurst and Rapela, 1998; Ramos, 1988; Ramos et al. 1998; Ramos, 2004; Rapela et al. 1998; Thomas and Astini, 2003). Sato et al. (2000), Ramos (2004), Sato et al. (2004), and others describe further morphological features farther to the north and south within this belt, i.e. the Sierra Toro Negro, Sierra Umango, Sierra Maz, and Sierra Espinal as well as the San Rafael and Las Matras blocks, respectively. These mountain ranges are mainly composed of Mesoproterozoic to Early Paleozoic rocks, which are considered being the basement of the Cuyania Terrane (Astini et al. 1995; Casquet et al. 2001; Sato et al. 2000; Sato et al. 2004).

Within the Sierra de Pie de Palo the basement is characterized by a nappe structure (e.g. Bollinger and Langer, 1988; Meira et al. 2012; Vujovich et al. 2004), which is related to an east-west compression and an orthogonal collision during the Famatinian orogenic cycle (e.g. Le Corre and Rossello, 1994; Martino, 2003; Simpson et al. 2003; van Staal et al. 2011). Additionally, this deformation-regime caused a top-to-the-west vergence expressed in the basement units and by the Early Paleozoic north-south trending thrust systems, e.g. the Las Pirquitas Thrust, controlling the contact between the different metamorphic sequences within the mountain range (Fig. 5.1b; Dalla Salda and Varela, 1984; Ramos et al. 1998; Ramos and Vujovich, 2000). These units are represented by *i*) the Neoproterozoic to Cambrian Caucete Group (e.g. Casquet et al. 2001; Naipauer et al. 2010; Ramos et al. 1996), consisting of metasedimentary sequences, i.e. low- to medium-grade quartzite and marble (e.g. Naipauer et al. 2010; Vujovich, 2003), which is assumed to be an equivalent of the Cambrian platform sequence of the Precordillera (Galindo et al. 2004; Naipauer et al. 2010; Ramos et al. 1998; Vujovich and Kay, 1998); *ii*) the Mesoproterozoic Pie de Palo Complex (e.g. Dalla Salda and

Varela, 1984; Ramos et al. 1998; Ramos and Vujovich, 2000; Vujovich and Kay, 1998), juxtaposed with the Caucete Group along the Las Pirquitas Thrust (Ramos et al. 1996) (Ramos et al. 1996), consists of ultramafic to mafic rocks and amphibolites in the area between the Las Pirquitas Thrust and the Duraznos Shear Zone (Fig. 5.1b), intermediate orthogneisses and qtz-fsp-ms-ep shists east of the Duraznos Shear Zone (Fig. 5.1b), and orthogneisses as well as shists in the eastern area of the Sierra de Pie de Palo (Fig. 5.1b; e.g. Ramos et al. 1998; Ramos and Vujovich, 2000; Varela et al. 2011); *iii*) the Difunta Correa Metasedimentary Sequence (Fig. 5.1b; Baldo et al. 1998), mainly composed of Ca-pelitic shists, quartzites, marbles, and less abundant amphibolites (Baldo et al. 1998), is considered being the Neoproterozoic sedimentary cover of the Pie de Palo Complex (Galindo et al. 2004); and *iv*) the Neoproterozoic Quebrada Derecha Orthogneiss described in detail by (Baldo et al. 2006).

Accretion and deformation in the Early Paleozoic was followed by orogenic collapse during the Late Paleozoic (Mpodozis and Ramos, 1989) leading to extensional reactivation of the former major sutures and the formation of the Paganzo Basin (e.g. Ramos et al. 2002). Main depocentres of this basin are associated and controlled by the crustal discontinuities inherited from the Early Paleozoic deformation (Fernandez Sevesco et al. 1993; Ramos et al. 2002). One of these depocentres is west of the Valle Fértil Fault containing Carboniferous deposits separating the Sierra de Pie de Palo from the mountain ranges further to the east (Ramos et al. 2002; Regnier et al. 1992). Sedimentary successions deposited on these Carboniferous sediments are mainly related to Mesozoic rifting and Andean compression in the Cenozoic (e.g. Ramos et al. 2002). During the latter the Mesozoic normal faults were inversely reactivated resulting in a diachronous uplift of the Sierras Pampeanas and uplift of the Precordillera (e.g. Jordan and Allmendinger, 1986; Jordan et al. 1989). According to (Ramos and Vujovich, 2000) synorogenic sediments derived from the latter covered the Sierra de Pie de Palo in the Late Pliocene.

Uplift and exhumation accompanied by deformation of the Sierra de Pie de Palo commenced at approximately 3 Ma and still continues showing an uplift rate of 1 mm/a and a shortening rate of 4 mm/a (Ramos et al. 2002; Ramos and Vujovich, 2000). According to the authors these processes are controlled by a mid-crustal basement wedge (Fig. 5.2), whereas (Vita Finzi, 2009) interprets the Sierra de Pie de Palo representing a cataclastic diapir, which is primarily uplifted and exhumed by lateral compressive forces and secondarily by density differences.

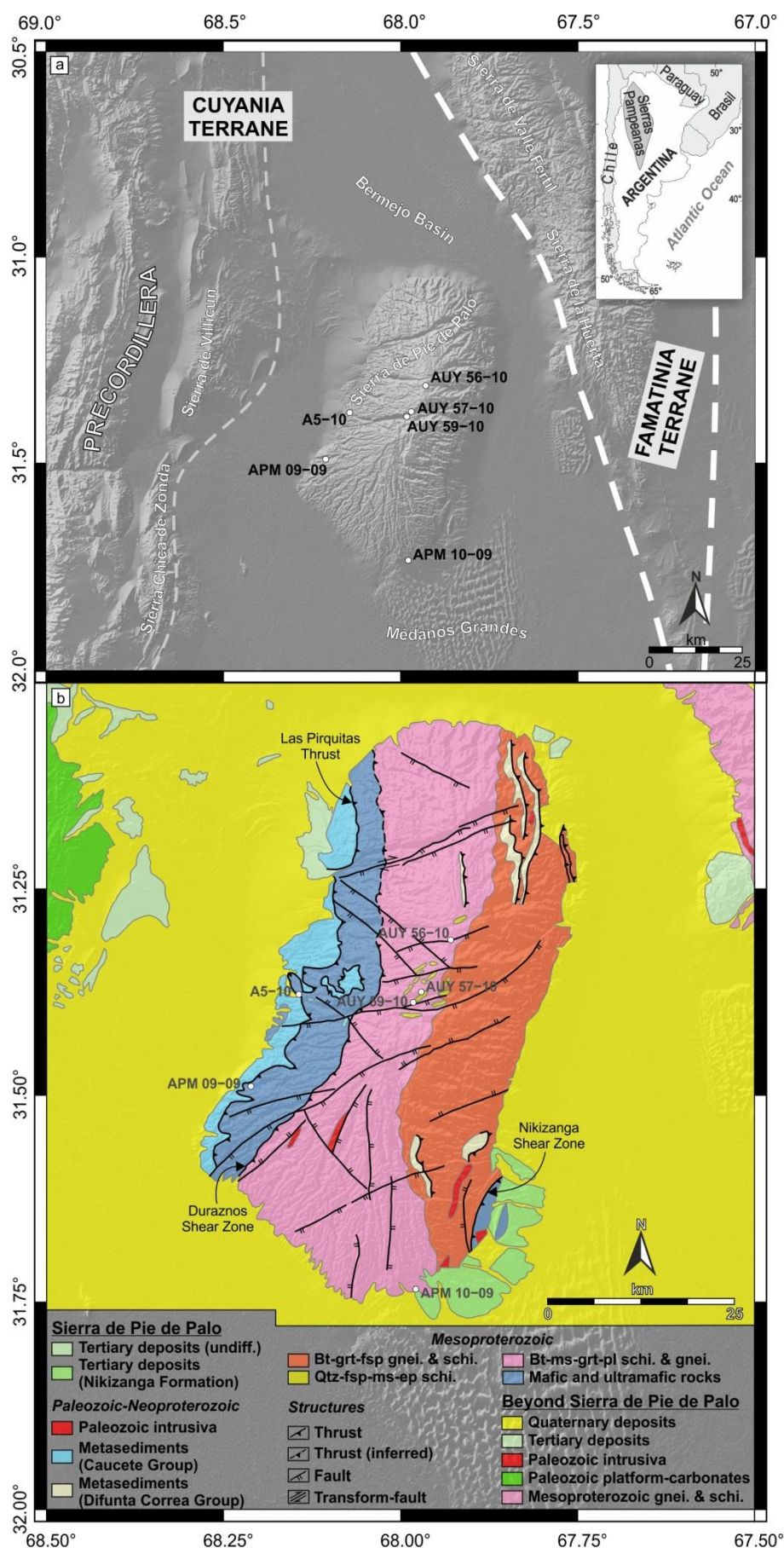


Fig. 5.1: Overview of the study area. a) SRTM-3 digital elevation model showing morphostructural features in the western part of the Argentine Sierras Pampeanas including the Sierra de Pie de Palo and the localities of samples. White dashed lines mark the boundary between different terranes accreted during the Paleozoic (from Ramos (2004)); grey dashed line defines the boundary between the Precordillera and the Western Sierras Pampeanas (from Giambiagi and Martinez (2008)). The schematic inset in upper right shows the study area on the South American continent. b) Simplified geological map of the Sierra de Pie de Palo according to the 1:250,000 geological maps of Ramos and Vujovich (2000) and Varela et al. (2011); schi. = schists, gnei. = gneisses.

5.3 Applied Methods

The combination of different temperature-dependent geochronometers, e.g. (U-Th)/He of zircon and apatite as well as apatite fission-track, is a suitable approach to reconstruct temperature-age relationships below 200 °C, thus the cooling/exhumation history of mountain ranges (e.g. Farley et al. 1996). These geochronological systems are thermally sensitive over geological times for temperature intervals, namely the partial-retention zone (PRZ_{Z/A}) for the zircon and apatite (U-Th)/He system (ZHe and AHe, respectively; e.g. Baldwin and Lister, 1998; Wolf et al. 1998) and the partial annealing zone (PAZ_A) for the apatite fission-track system (AFT; e.g. Gleadow and Fitzgerald, 1987). Depending on the retentivity of radiogenic He within the zircon and apatite crystals and the fission-tracks in the apatite crystals these intervals range between 200-160 °C, 80-55 °C, and 120-90 °C for the PRZ of zircon and apatite as well as the PAZ_A, respectively (e.g. Donelick et al. 1999; Farley, 2000; Laslett et al. 1987; Reiners et al. 2004). In turn, the retention behavior of the radiogenic He in the (U-Th)/He system and of the fission-tracks in the AFT system is mainly controlled by grain size, crystal morphology, alpha-damage density, and cooling rate (e.g. Ehlers and Farley, 2003; Reiners and Brandon, 2006; Wolf et al. 1996) as well as by cooling rate and kinetic parameter of track annealing, which is described by the etch pit diameter (Dpar) roughly representing an indication of the chemical composition (Donelick et al. 1999; Ketcham et al. 1999; Reiners and Brandon, 2006), respectively.

During this study, basement samples from an elevation profile in the Sierra de Pie de Palo as well as two samples from the western margin and the southern tip of the mountain range, respectively (Fig. 5.1a), were investigated using the AHe and ZHe method. Additionally, apatite fission-track dating was applied on the samples from the elevation profile (Fig. 5.1a). The sample treatment and preparation procedure are described in more detail by (Löbens et al. 2011).

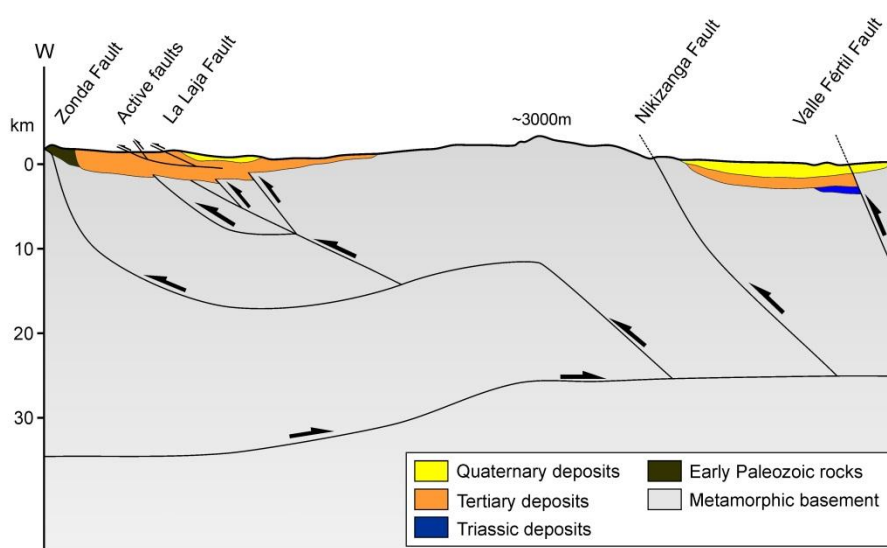


Fig. 5.2: The dominant structure of the crust beneath the Sierra de Pie de Palo is an east-vergent crustal basement wedge (modified from Ramos et al. (2002)).

5.4 Results

5.4.1 Zircon (U-Th)/He Ages

Mean zircon He ages range from 334 Ma (Carboniferous) to 252 Ma (Permian-Triassic). Three samples were taken along the elevation profile (A5-10, AUY 59-10, AUY 57-10). In general, the obtained ages correlate with elevation, showing youngest ages in lower elevated areas and increasing ages towards higher altitudes (Table 5.1, Fig. 5.3). Due to an insufficient amount of suitable zircon crystals, no age could be obtained from the topmost sample (AUY 56-10). The samples APM 09-09 and APM 10-09, which both represent amphibolite, from the western margin and the southern tip of the mountain range, respectively, yield ages of 287.3 ± 28.6 Ma (APM 09-09) and 252.4 ± 17.3 Ma (APM 10-09, Table 5.1, Fig. 5.3b).

5.4.2 Apatite Fission-Track Analyses

Central ages of the samples from the elevation profile within the Sierra de Pie de Palo (Fig. 5.1a) range between the Late Triassic and the Late Jurassic (Fig. 5.3, Table 5.2). There is a distinct correlation between age and elevation (Fig. 5.3) with an age of 207.0 ± 20.1 Ma (AUY 56-10) and 152.3 ± 20.5 Ma (A5-10) at the top and the bottom of the range, respectively (Fig. 3a). An exception of this trend is represented by sample AUY 57-10, which is situated at a relatively greater elevation than AUY 59-10 but is younger (173.9 ± 26.7 Ma) than the latter (204.6 ± 23.8 Ma, Figs. 5.3a, c, Table 5.2).

All samples are characterized by distinct shortened tracks (Fig. 5.3a). The mean track length varies from 12.68 ± 1.44 μm (AUY 56-10) to 13.57 ± 1.63 μm (AUY 57-10). For samples A5-10, AUY 56-10, and AUY 57-10 these lengths are bimodal distributed (Fig. 5.3a), but for A5-10 less distinct than for the latter two. Contrastingly, AUY 59-10 yields an unimodal track length distribution (Fig. 5.3a). The mean etch pit diameter of the four investigated samples ranges between 1.88 ± 0.09 μm and 2.24 ± 0.15 μm (Table 5.2).

5.4.3 Apatite (U-Th)/He Ages

The unweighted average ages of the five analyzed samples from the Sierra de Pie de Palo range between the Early Cretaceous and the Pliocene (Table 5.1). Samples A5-10, AUY 56-10, and AUY 59-10, situated along the elevation profile (Fig. 5.1a), show a distinct positive correlation between age and elevation (Fig. 5.3d). The lowest and the top most samples (A5-10 and AUY 56-10) yield ages of 46.1 ± 9.3 Ma and 131.3 ± 9.96 Ma, respectively (Table 5.1). APM 10-09, located at the southern tip of the mountain range, shows an age of 102.7 ± 6.5 Ma and APM 09-09 from the western margin of the range yields an age of 3.4 ± 1.5 Ma (Fig. 5.3d, Table 5.1).

Table 5.1: Zircon and apatite (U-Th)/He data of the samples from the Sierra de Pie de Palo.

Sample	aliqu.	He		²³⁸ U	²³² Th		Sm		Ejection correction (Ft)	Uncorr. [Ma]	Corr. [Ma]	2σ [Ma]	Mean age [Ma]	±2σ [Ma]	
		vol. [ncc]	1σ [%]	mass [ng]	1σ [%]	mass [ng]	1σ [%]	mass [ng]							1σ [%]
<i>Zircon</i>															
APM 09-09	z1	14.879	1.6	0.589	1.8	0.208	2.4	0.012	12	0.69	189.9	275.9	28.8		
	z2	18.648	1.6	0.710	1.8	0.196	2.4	0.020	11	0.69	200.7	290.9	30.3		
	z3	34.307	1.6	1.278	1.8	0.350	2.4	0.109	12	0.73	205.0	281.8	26.5		
	z4	16.259	1.6	0.572	1.8	0.167	2.4	0.021	12	0.72	216.2	300.4	28.9	287.3	28.6
APM 10-09	z1	21.470	1.6	0.868	1.8	0.604	2.4	0.359	7	0.76	172.9	226.5	19.1		
	z2	98.612	1.6	3.066	1.8	0.242	2.4	0.060	8	0.86	255.6	298.5	19.1		
	z3	315.484	1.6	10.862	1.8	1.825	2.4	2.303	8	0.86	226.5	264.9	16.9		
	z4	264.292	1.6	11.226	1.8	0.575	2.4	2.813	8	0.86	189.1	219.7	13.9	252.4	17.3
A 5- 10z1	z1	221.648	1.6	7.845	1.8	1.841	2.4	0.207	10	0.84	217.5	259.7	17.5		
	z3	248.267	1.6	7.600	1.8	2.321	2.4	0.126	10	0.83	247.0	298.0	20.6	278.8	19.1
AUY 57-10	z4	12.767	1.7	0.447	1.9	0.153	2.4	0.013	11	0.71	214.9	303.2	30.1	303.2	30.1
AUY 59-10	z5	12.252	1.7	0.403	1.9	0.133	2.4	0.018	11	0.70	229.1	325.9	32.8		
	z6	13.845	1.7	0.492	1.8	0.088	2.4	0.010	14	0.71	219.2	309.2	30.7		
	z7	21.697	1.7	0.613	1.8	0.239	2.4	0.015	11	0.71	262.5	368.7	36.2	334.6	33.2
<i>Apatite</i>															
A5-10	a1	0.044	5.5	0.003	29.1	0.007	3.9	0.611	7	0.87	38.4	43.9	9.4		
	a4	0.056	5.2	0.004	20.8	0.003	5.1	0.851	7	0.84	40.4	48.3	9.3	46.1	9.3
APM 09-09	a1	0.001	44.5	0.002	36.2	0.011	3.3	0.009	9	0.84	1.1	1.3	1.2		
	a3	0.002	16.9	0.003	17.7	0.013	3.1	0.009	8	0.82	2.8	3.5	1.3		
	a4	0.003	13.3	0.002	30.2	0.012	3.3	0.011	9	0.88	4.8	5.4	2.0	3.4	1.5
APM 10-09	a3	0.224	2.1	0.017	3.6	0.020	2.8	0.117	6	0.89	81.0	91.0	6.9		
	a4	0.981	1.8	0.055	2.1	0.078	2.5	0.407	7	0.91	104.4	114.3	6.2	102.6	6.5
AUY 56-10	a1	0.553	2.1	0.036	2.6	0.002	6.0	0.462	9	0.86	112.7	130.9	10.0		
	a2	0.689	2.1	0.045	2.3	0.006	4.1	0.459	9	0.86	113.6	131.7	9.5		
	a3	0.529	2.3	0.035	2.5	0.002	5.9	0.331	9	0.86	112.4	131.4	10.3	131.3	10.0
AUY 57-10	a1	no reliable data due to insufficient He-content													
	a2														
	a3														
AUY 59-10	a1	0.061	4.6	0.007	9.4	0.008	3.7	0.078	9	0.91	52.3	57.4	9.4		
	a2	0.062	4.8	0.006	11.6	0.012	3.2	0.079	9	0.93	55.5	59.7	10.2	58.6	9.9

Notes: aliqu. = aliquote, uncorr. = uncorrected age, and Ft-corr. = Ft-corrected age. Amount of He is given in nano-cubic-cm in standard temperature and pressure; amount of radioactive elements are given in nanograms; ejection correct. (Ft): correction factor for alpha-ejection (according to Farley et al. (1996) and Hourigan et al. (2005)); uncertainties of He and the radioactive element contents are given as 1 sigma, in relative error %; uncertainty of the single grain age is given as 2 sigma in Ma and it includes both the analytical uncertainty and the estimated uncertainty of the Ft; uncertainty of the sample average age is 2 standard error, as $(SD)/(n)^{1/2}$; where SD = standard deviation of the age replicates and n = number of age determinations. Four to six aliquots per sample were picked and analyzed. If the investigated age of a single grain deviates by more than 2σ from the mean age, the aliquot was rejected. These erroneous ages can be caused by several factors, such as zoning of alpha-emitting elements, micro inclusions, the limit of detection, or the bias of the ejection correction (smaller grains have larger errors).

Table 5.1: Apatite fission-track data of the samples from the elevation profile within the Sierra de Pie de Palo.

Sample (rocktype)	Longitude (W) Latitude (S)	Elevation [m]	n	ρ_s	N_s	ρ_i	N_i	ρ_d	N_d	$P(X^2)$ [%]	Age [Ma]	$\pm 1\sigma$ [Ma]	MTL [μm]	s.d. [μm]	$N(L)$	Dpar [μm]	s.d. [μm]
A5-10 (gneiss)	68°08'36" 31°22'40"	925	25	3.34	221	2.10	139	6.00	5409	100	152.3	20.5	12.9	1.5	50	1.9	0.14
AUY 56-10 (mylonite)	67°55'46" 31°18'43"	3133	25	13.14	872	7.58	503	7.51	5725	99.1	207.0	20.1	12.7	1.4	50	1.9	0.09
AUY 57-10 (gneiss)	67°58'14" 31°22'30"	2824	25	2.13	164	1.16	89	5.92	5409	100	173.9	26.7	13.6	1.6	35	2.2	0.15
AUY 59-10 (gneiss)	67°58'56" 31°23'15"	2177	25	3.82	390	2.13	217	7.16	5409	96.7	204.6	23.8	12.7	1.3	50	1.9	0.13

Notes: n , number of dated apatite crystals; ρ_s/ρ_i , spontaneous/induced track densities ($\times 10^5$ tracks cm^{-2}); N_s/N_i , number of counted spontaneous/induced tracks; N_d , number of tracks counted on dosimeter; $P(X^2)$, probability obtaining chi-squared value (X^2) for n degree of freedom (where n is the number of crystals - 1); age $\pm 1\sigma$ is central age ± 1 standard error (Galbraith and Laslett, 1993); ages were calculated using zeta calibration method (Hurford and Green, 1983); glass dosimeter CN-5, and zeta value of 323.2 ± 25.3 ; MTL, mean track length; s.d., standard deviation of track length distribution and Dpar measurements; N , number of tracks measured; Dpar, etch pit diameter.

5.5 Discussion

5.5.1 Thermal Modeling

The thermal history of six samples from the Sierra de Pie de Palo was modeled using the HeFTy software (Fig. 5.4; Ketcham, 2005). The input data for the modeling were the fission-track single grain ages, track length distribution, and Dpar data, as well as the corresponding apparent zircon and apatite (U-Th)/He ages. If all single grain ages of a sample show unusual ages concerning the U-Th/He system, i.e. AHe ages of AUY 57-10, which is probably related to small inclusions or to an insufficient He content, the affected system was not considered by thermal modeling. The starting- and end-point of the modeled time-temperature history were constrained by Ar-Ar data of muscovite (closure temperature of approx. 400 °C) reported by Mulcahy et al. (2011) and the mean annual surface temperature of 17 °C (Müller, 1996), respectively. Further constraints set are related to the measured ages of the different systems.

5.5.2 General Structural Evolution of the Sierra de Pie de Palo

The modeled time-temperature histories suggest that generally cooling below ~ 175 °C commenced between in the Late Paleozoic (Fig. 5.4). This cooling, hence exhumation is probably related to erosion affecting the rugged relief generated during the Famatinian Orogeny, which is associated with accretion of the Cuyania Terrane at the southwestern proto-Andean margin of Gondwana during the Paleozoic (Fig. 5.5a, e.g. Pankhurst and Rapela, 1998) (Fig. 5.5a, e.g. Pankhurst and Rapela 1998). Potentially, further exhumation of our samples from the PRZ_z into the PAZ_A (Figs. 5.4, 5a) during Permian and Triassic times was caused by a Permo-Triassic compressional phase described by Ramos and Folguera (2009) among others and the related tectonically triggered erosion (Fig. 5.5a).

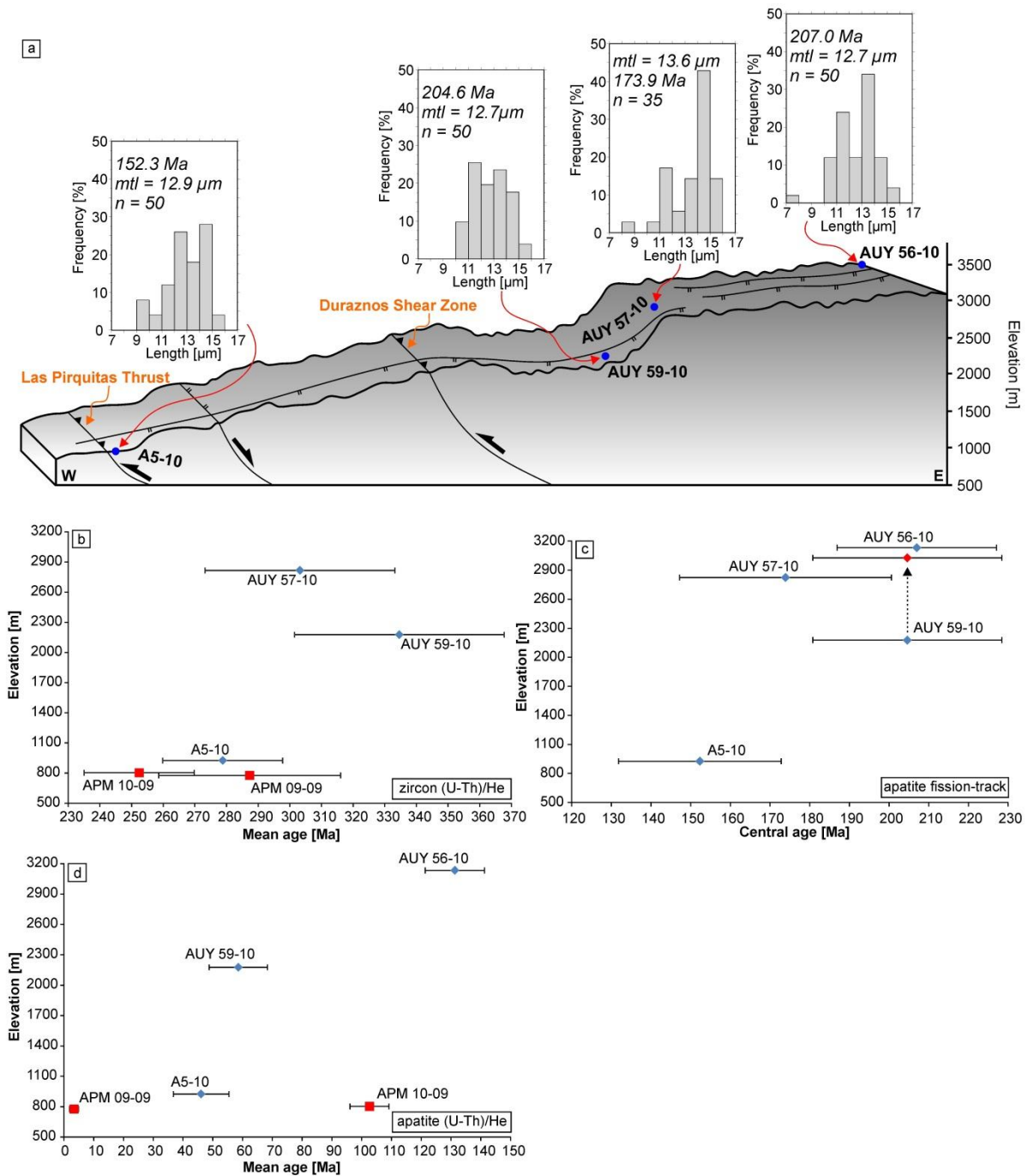


Fig. 5.3: Thermo-chronological results of the samples from the Sierra de Pie de Palo. a) Schematic profile across the mountain range along the investigated samples with the major structures (surface exposure of faults is just schematic). The apparent fission-track age, the corresponding track length distribution, the mean track length (mtl), and the number of confined tracks (n) measured for each sample are also shown. b), c) and d) Age-elevation plot for the ZHe-, AFT- and AHe-system, respectively. Samples, which are not collected along the profile are indicated by red squares in b) and d). Since AUY 59-10 is presumably relatively displaced to AUY 57-10 along a normal fault, the red point in b) would be the approximated projected elevation of the former sample in an undisturbed profile.

Although the inflection point for the AFT thermochronometer (Fig. 5.3c) is not well constrained the modeled cooling paths suggest that cooling below the lower thermal boundary of the PAZ_A occurred between the Late Triassic and the Jurassic (Fig. 5.4), possibly at around 170 Ma (Fig. 5.3c). This exhumation is presumably related to erosion controlled by extension, at least during the Triassic (e.g. Ramos et al. 2002). Associated Triassic rifting occurred along reactivated Paleozoic suture zones, i.e.

the master fault bounding the Sierra de Valle Fértil in the west. Since the area of the Sierra de Pie de Palo was *i)* still characterized by a positive topography and *ii)* situated on the footwall, erosion, which probably mainly occurred towards the east, caused the cooling and exhumation (Figs. 5.4, 5b). Subsequent cooling into the PRZ_A generally commenced during the Jurassic (Fig. 5.4). Since the area of the Sierra de Pie de Palo was presumably still characterized by a positive relief during that time, continuous erosion lead to exhumation of our samples to a temperature of approximately 65 °C (Figs. 5.4, 5.5c). Additionally, sub-humid conditions during that time, as described by Carignano et al. (1999), would facilitate enduring erosion. Variations of individual cooling paths from this general trend (Fig. 5.4) are referred to the fault-related internal structure of the mountain range.

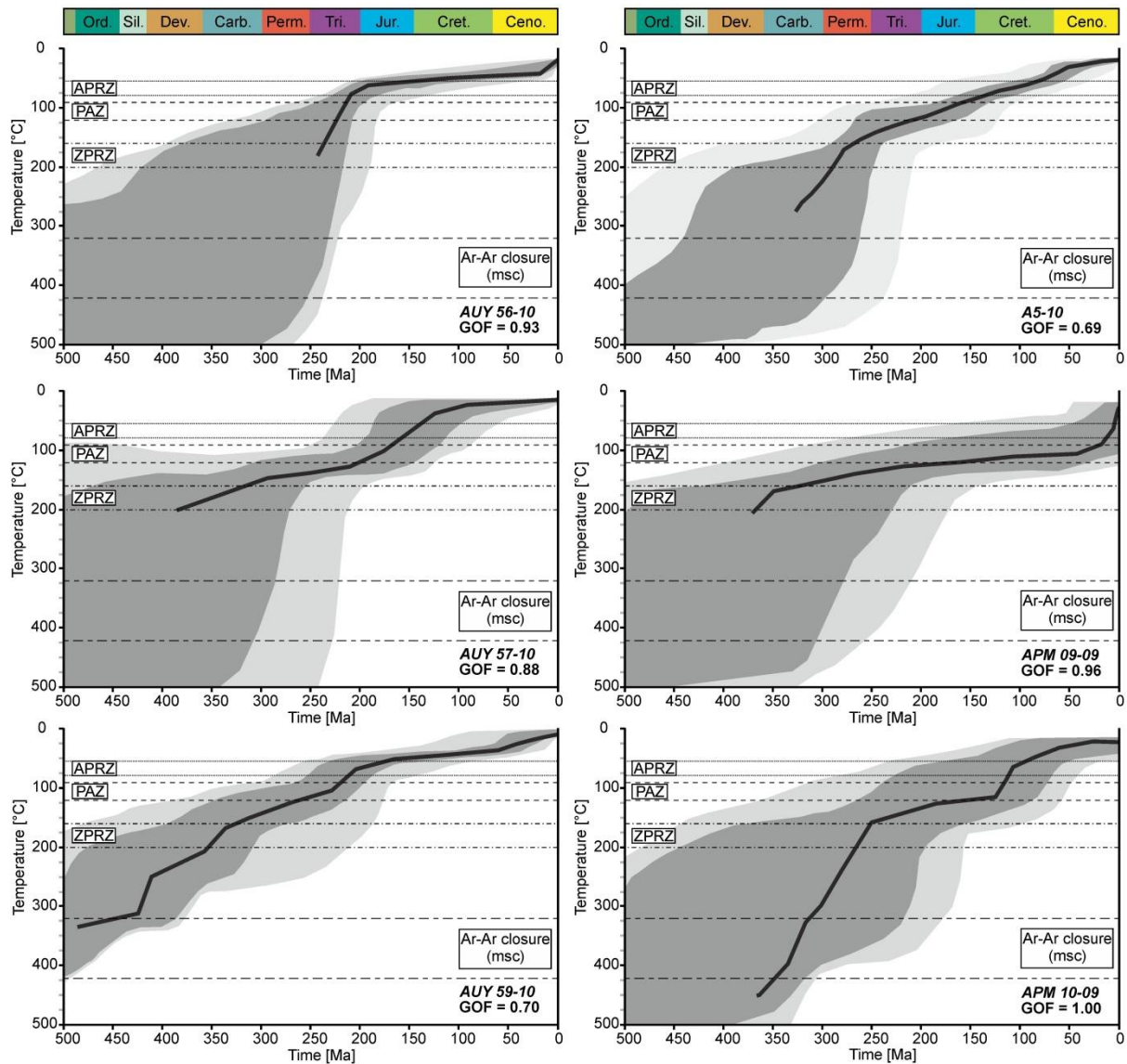


Fig. 5.4: Time-temperature history derived by thermal modeling including the ranges of the effective closure temperatures for the different dating systems, where APRZ/ZPRZ represents the partial-retention zone of apatite/zircon (called PRZA/PRZZ in the text), PAZ defines the partial annealing zone, and GOF the goodness of fit between the measured and modeled data averaged for all considered systems. The black curve indicates the average fit, good fits are shown in dark grey, and acceptable fits in light grey. Note that the individual average fits do not necessarily represent the overall cooling/exhumation path of the mountain range, meaning that the general cooling path could also lie within the range of good and acceptable fits of the individual samples. The starting constraint set (muscovite Ar-Ar closure temperature and related age obtained by Mulcahy et al. (2011) is also shown, but not to scale. Ord. = Ordovician, Sil. = Silurian, Dev. = Devonian, Carb. = Carboniferous, Perm. = Permian, Tri. = Triassic, Jur. = Jurassic, Cret. = Cretaceous, Cen. = Cenozoic.

However, final cooling below the lower temperature boundary of the PRZ_A, thus exhumation towards the surface generally commenced between the Cretaceous and the Paleogene (Fig. 5.4); possibly, although not well constrained, at around 60 Ma (Fig. 5.3d). Exhumation due to erosion within the Sierra de Pie de Palo during the time of Cretaceous rifting, which was generated by the opening of the South Atlantic during that time (e.g. Schmidt et al. 1995), cannot completely be excluded. But since Cretaceous deposits are generally absent in the adjacent intracontinental basins (e.g. Zapata, 1998) and this extension rather affected the eastern part of the Sierras Pampeanas than the western part (e.g. Ramos et al. 2002; Rossello and Mozetic, 1999), it is not very likely that cooling of our samples is referred to this event. Instead, exhumation in the area of the Sierra de Pie de Palo is presumably related to the ca. east-west compression during the early stage of the Andean deformation (Fig. 5.5d). The latter process generated movement along the right lateral transpressional Tucumán Transfer Zone (TTZ; e.g. de Urreiztieta et al. 1996; Roy et al. 2006). Deformation was probably accommodated by the north-south trending Paleozoic discontinuities in the area of the Sierra de Pie de Palo (Fig. 5.1, 3a), generating en-block uplift (see below) accompanied by erosion in this region as well as causing uplift of the early Puna Plateau further to the north (Fig. 5.5d; e.g. Carrapa et al. 2005; Löbens et al. 2013).

Based on our interpretations of the obtained thermal models two different hypotheses concerning the Cenozoic structural and thermal evolution of the Sierra de Pie de Palo can be considered; *i*) a positive relief since the Paleocene; possibly since ~60 Ma as indicated by the age-elevation relationship (Fig. 5.3d); and *ii*) an area acting as accommodation space for Pliocene sediments derived from the Precordillera before being uplifted in post-Pliocene times.

i) Due to the thermal modeling suggests continuous exhumation within the Sierra de Pie de Palo at least since the Late Mesozoic to Early Cenozoic, the area already had to be characterized by a positive relief (Fig. 5.5d). Further, the region could still be capped by a thin sedimentary cover, from that time until today (see below). If there would have been a flat topography and the area of the recent mountain range was entirely covered by a substantial amount of Pliocene sediments derived from the uplifted Precordillera until 3 Ma as proposed by Ramos et al. (2002), the time-temperature paths should indicate a re-heating or at least stagnation in cooling caused by burial beneath these deposits rather than cooling (Fig. 5.4). Therefore, we propose that there had to be some kind of topography in the vicinity of the Sierra de Pie de Palo before 3 Ma, otherwise there would not have been any erosion causing cooling/exhumation of our samples since the Late Cretaceous to Paleogene, as indicated by modeled t-T-paths (Figs. 5.4, 4.5d). Further, although our data and the related models do not illuminate the amount of uplift generated by the Andean deformation which is additionally characterized by the flat-slab subduction in the Late Cenozoic, uplift presumably was less

than the 3 km (present elevation) in the last 3 Ma as suggested by (Ramos et al. 2002) Ramos et al. (2002) because of the positive relief controlling continuous exhumation as mentioned above.

ii) Alternatively, exhumation below the PRZ_A was caused by erosion from the Late Cretaceous to the Late Miocene eliminating any topography and producing accommodation space in the Pie de Palo region filled by sediments derived from the Precordillera during the Pliocene (Ramos et al. 2002). Subsequently, continuous Andean deformation uplifts the Sierra de Pie de Palo to a present-day peak elevation of 3 km in the last 3 Ma (Ramos et al. 2002). Therefore, exhumation had to be more than 3 km because of the sedimentary Pliocene cover. Further, the thermal models do not suggest re-heating (Fig. 5.4), thus thickness of these sediments could be limited by the temperature of the PRZ_A. If the sedimentary thickness would cause burial re-heating to temperatures above the lower PRZ_A temperature, any age reset should be visible in the mean AHe ages. But since Tertiary deposits are up to 10 km thick in the Bermejo Basin east of the Sierra de Pie de Palo (Zapata, 1998), it is doubtful that there was no substantial sedimentary cover atop of the range, which would have caused re-heating at least to temperatures characteristic for the PRZ_A during the Cenozoic. Additionally, any sedimentation scenario contradicts this continuous exhumation since at least the Mesozoic as indicated by the time-temperature relationship (Fig. 5.4). Therefore, based on our data this Cenozoic evolution is rather questionable and we favor the first hypothesis.

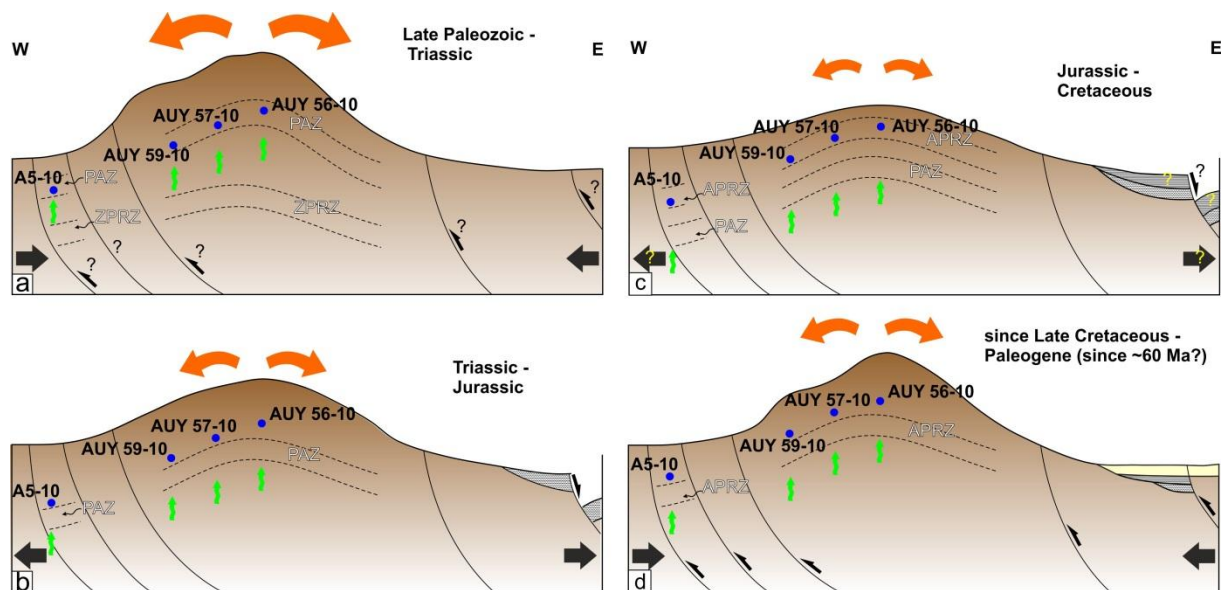


Fig. 5.5: Schematic sketch of the structural evolution of the Sierra de Pie de Palo through time (vertical exaggerated) based on the new thermochronological data and the modeled time-temperature history. APRZ/ZPRZ = partial-retention zone of apatite/zircon, PAZ = partial annealing zone, red arrows = relative mass and direction of erosion, green arrows = exhumation, bold black arrows = tectonic regime, black and yellow question marks = uncertainties about sedimentary sequence/tectonic regime and fault activity. Note that possible advection of isotherms is not considered. Further details are in the text.

5.5.3 Internal Structure and Related Exhumation

The internal structure of the Sierra de Pie de Palo is mainly controlled by Paleozoic north-south trending thrusts, e. g. the Las Pirquitas Thrust and the Duraznos Shear Zone, and ~east-west striking normal faults (Figs. 5.1b, 5.3a). Since Cenozoic movement along the Paleozoic discontinuities accompanied by erosion presumably caused en-block uplift of the mountain range commencing at around 60 Ma (Fig. 5.5, mentioned above), the ~east-west trending normal faults dominantly affect local differences in the thermochronological ages, especially the apatite fission-track ages (Fig. 5.3). Concerning this system the cross-section is disturbed by normal faulting between samples AUY 57-10 and AUY 59-10, as suggested by the geological map of the Sierra de Pie de Palo (Fig. 5.1b; Ramos and Vujovich, 2000), resulting in an older central age of the relatively lower sample AUY 59-10 (Fig. 5.3). Basing on the AFT ages a re-projection would lead this sample formerly being at an elevation between samples AUY 56-10 and AUY 57-10, hence between 3133 m (recent crestal elevation) and 2824 m, respectively (Fig. 5.3). But due to the apatite fission-track ages (central age and observed single grain ages) of AUY 59-10 are similar to those of AUY 56-10, initial elevation of the former presumably was closer to 3133 m than to 2824 m. Further, this re-projection results in *i)* a better constraint of the potential inflection point, which seems to be around 172 Ma (Fig. 5.3) and *ii)* in a maximal displacement of approximately 956 m (difference between the present elevation of AUY 59-10 and 3133 m) along the east-west trending normal fault affecting the investigated profile (Figs. 1b, 3). Since this fault probably also generated a displacement of sample A5-10 as suggested by its trace (Figs. 5.1b, 3) the latter also has to be re-projected by a maximum offset of 956 m resulting in an initial elevation of around 1881 m. Therefore, A5-10 is still relatively lower than AUY 57-10, thus the maximal offset is plausible. Furthermore, a time constraint of fault activity is just suggested by the AHe data. Since there is no fault-related disturbance of the AHe ages in the cross-section, movement along the normal fault probably occurred before 60 Ma, indicated by the possible, but not well constrained, inflection point (Fig. 5.3d). Although there is no AHe data of sample AUY 57-10 which would confirm this hypothesis, we propose that the significantly younger age of AUY 59-10 compared to AUY 56-10 implies an undisturbed profile regarding this certain fault since around 60 Ma. Otherwise, if faulting would also perturb the AHe ages within the profile, the age of AUY 59-10 probably would have been similar to that of AUY 56-10 like in the AFT system (Fig. 5.3).

However, although the two other basement samples lack AFT-data their cooling histories also suggest continuous exhumation at least since the Mesozoic (Fig. 5.4). Further, exhumation occurred earlier in the eastern part of the mountain range (Figs. 5.1, 5.4, APM 10-09) than at the western margin (APM 09-09), where it is presumably related to Neogene movement along the Las Pirquitas Thrust (Figs. 5.1b, 5.3a, 5.4, Table 5.1). Therefore, deformation and exhumation probably propagated towards the west as also proposed by Coughlin et al. (1998) for at least the Sierra Famatina. But these authors restrict westward propagation to Miocene-Pliocene times, whereas our data suggest

that deformation in the most eastern area of the Sierra de Pie de Palo already occurred in the Late Mesozoic. Therefore, final cooling and exhumation of the region below the lower temperature boundary of the PRZ_A is presumably closely related to commencement of movement along the TTZ during the Late Mesozoic-Cenozoic induced by the Andean deformation (e.g. de Urreiztieta et al. 1996; Roy et al. 2006).

5.5.4 Cenozoic Thermal Evolution and Amount of Exhumation

Since a perturbation of the geothermal gradient by advection through volcanic activity can be excluded in the area of the Sierra de Pie de Palo during the Early Cenozoic, an extrapolation of 20-26 °C/km assumed by Sobel and Strecker (2003) and Löbens et al. (2013) for the Northern Sierras Pampeanas and by Löbens et al. (2011) for the Eastern Sierras Pampeanas to the Western Sierras Pampeanas is suitable. Based on this geothermal gradient and assuming an effective closure temperature (T_c) of around 60 °C for the AHe-system as well as a paleo-surface temperature of 17 °C, there had to be an exhumation between 2.2 km (20 °C/km) and 1.7 km (26 °C/km) during the Cenozoic bringing samples to the surface. Therefore, average exhumation rate, which is mainly controlled by erosion, would be around 0.04-0.03 mm/a since 60 Ma, when cooling below approximately 60 °C occurred (Fig. 5.4, 5.5d). Further, since the adjacent Bermejo Basin is characterized by 5-10 km thick Tertiary deposits (Zapata, 1998) a rock column of up to ~2 km above our samples, which had to be eroded since 60 Ma in order to allow this exhumation, is plausible. Furthermore, since the top sample (AUY 56-10) is at an elevation of 3 km today vertical rock uplift had to be between 3.7 km and 4.2 km during the Cenozoic.

However, if the Sierra de Pie de Palo was completely covered by Pliocene deposits as proposed by Ramos and Vujovich (2000) and Ramos et al. (2002), these sediments could not be thicker than approximately 3 km (as mentioned above), which is equivalent to 60 °C for a geothermal gradient of 20 °C/km, because the modeled cooling path do not indicate a re-heating/burial in the Late Cenozoic (Fig. 5.4). Therefore, the maximum exhumation rate would be around 1 mm/a being equivalent to the surface uplift rate proposed by Ramos et al. (2002). But since there is rather a continuous exhumation for the whole Cenozoic, as suggested by the modeled time-temperature histories (Fig. 5.4) and as mentioned above, than an increase of the exhumation rate in the Late Cenozoic, the hypothesis that uplift of peak level commenced in the Pliocene is arguable. Instead, this process was presumably generated earlier, possibly also between the Late Cretaceous and Paleocene, otherwise there could not have been continuous erosion, thus exhumation, as suggested by the time-temperature histories (Fig. 5.4). But our data do not illuminate the onset more precisely.

5.6 Conclusions

- 1) Cooling and exhumation below ca. 175 °C in the Sierra de Pie de Palo is mainly controlled by erosion affecting a rugged relief generated during the Famatinian Orogeny.
- 2) Exhumation of our samples from the PRZ_Z into the PAZ_A occurred during Permian and Triassic times and is related to erosion controlled by a Permo-Triassic compressional phase.
- 3) During the Mesozoic further cooling and exhumation in the area of the Sierra de Pie de Palo is related to erosion affecting a positive relief being occasionally controlled by an extensional tectonic setting.
- 4) Final cooling and exhumation of the Sierra de Pie de Palo commenced between the Cretaceous and the Paleogene, possibly at around 60 Ma, being related to ~east-west compression during the early stage of the Andean deformation, which generated en-block uplift accompanied by tectonically controlled erosion in that region.
- 5) Westward propagation of deformation and exhumation in the Western Sierras Pampeanas, at least in the Sierra de Pie de Palo, has probably been occurred since the Late Mesozoic to Paleogene.
- 6) Overall 3.7-4.2 km vertical rock uplift occurred in the Sierra de Pie de Palo since ~60 Ma, and the exhumation was between 2.2 km and 1.7 km resulting in an average exhumation rate of 0.04-0.03 mm/a since that time.
- 7) Peak level uplift of the Sierra de Pie de Palo probably also commenced at around 60 Ma in order to allow continuous erosion since that time; thus Pliocene surface uplift, previously assumed being around 3 km, is presumably overestimated.

6 Fault Gouge Analyses

6.1 Introduction

In brittle near-surface faults, rocks are broken and crushed by tectonic movements. In these localized zones, the increased surfaces create high chemical reactivity, allowing retrograde processes to produce fault gouges which are composed of authigenic hydrosilicates, such as illite. During formation of illite, K is fixed within the crystal lattice. The radioactive decay product Ar is retained within the lattice, allowing the illite system to act as a radiometric dating system. Thus, formation time of the authigenic illite in a fault gouge can be correlated with periods of motion along a fault (e.g. Lyons and Snellenberg 1971; Kralik et al. 1987). In addition to faulting and thrusting (e.g. Solum et al. 2005, Schleicher et al. 2006, Haines and van der Pluijm 2008, Zwingmann et al. 2010, Surace et al. 2011, Wolf et al. 2011, Löbens et al. 2011), K-Ar illite dating has been used to constrain the age of hydrothermal fluid migration as well as oil and gas migration (e.g. Hoffman et al. 1976, Aronson and Burtner 1983, Lee et al. 1985, Hay et al. 1988, Hamilton et al. 1989, Pevear et al. 1997, Pevear 1999, Grathoff et al. 2001, van der Pluijm et al. 2001). In addition to K-Ar ages, constraining the timing of fault activity, illite crystallinity and illite polytypism can be used to illuminate the path during retrograde metamorphic conditions.

The Sierras Pampeanas in northwest Argentina have been affected by brittle deformation processes since Carboniferous times. Deformation is accommodated by numerous faults, of which most exhibit well-developed clay gouges. The large number of gouge-bearing fault zones, as well as good exposure conditions, make the area an excellent testing ground for evaluating the tectonic significance of fault-gouge analysis data, i.e. to date events like fault formation and activity.

Gouge-bearing fault zones were systematically sampled throughout the Eastern Sierras Pampeanas and several grain-size fractions were dated by the K-Ar illite method. Mineralogical classification of gouges was done by X-ray diffraction and fluorescence methods, cation-exchange capacity determination, infrared spectroscopy, differential thermal analyses and transmission electron microscopy. The path of retrograde metamorphism during gouge formation was characterized by examining illite crystallinity and polytypism. K-Ar illite ages derived from polytype mixtures were concluded to have end-member ages through the illite age extrapolation technique.

In order to constrain the "deformation path" of the Sierras Pampeanas, the data obtained are correlated with low-temperature thermochronological data (apatite and zircon (U-Th)/He and apatite fission track), as well as high-temperature cooling ages (K-Ar muscovite and biotite). The information derived is used to elucidate regional tectonic influences and is discussed in context with established assumptions about the regional evolution of the Sierras Pampeanas.

6.2 Geological Setting

The basement complex of the Sierras Pampeanas is formed by the accretion of different allochthonous and parautochthonous terranes during the sequel of the Pampean, Famatinian and Achalian Orogenies in the Late Proterozoic and Early Paleozoic (e.g. Ramos 1988; Ramos et al. 2002; Steenken et al. 2004; Miller and Söllner 2005; Ramos 2008). The proposed sutures indicate the margins of adjacent cratons and terranes, e.g. Río del la Plata Craton, Pampia terrane and Cuyania terrane (Fig. 6.1; Ramos (2004). The tectonometamorphic evolution and associated ductile deformation of the basement is considered to have been completed in Early Carboniferous times.

During the Mesozoic, the area of the present-day Sierras Pampeanas was affected by several extensional deformation events, i.e. during the Late Triassic to the Early Jurassic and the Early Cretaceous (e.g. Ramos et al. 2002). The latter period is related to the opening of the South Atlantic Ocean at these latitudes (Rossello and Mozetic 1999). These Mesozoic events led to an extensional reactivation of the terrane sutures and crustal discontinuities formed during terrane accretion (see Fig 6.1; Criado Roque et al. 1981; Schmidt et al. 1995; Ramos et al. 2002). The latter resulted in the development of continental basins which are usually characterized by a half-graben structure and mainly contain Early Cretaceous deposits (Schmidt et al. 1995). These extensional fault systems on their part are considered to have been reactivated and inverted during the Cenozoic Andean compression caused by the subduction of the Nazca Plate beneath the South American plate. The geometry of these reverse faults and thrusts is mainly dictated by the orientation of the older structures, resulting in a dominance of east-dipping structures. This preferred orientation is also expressed on the surface by a distinct morphologic asymmetry of the basement blocks comprising the Pampean mountain ranges. Generally, the ranges show a steep slope on the fault-facing side (mostly the western side) in contrast to a gently dipping slope on the fault-averted side (mostly the eastern side; see e.g. González Bonorino 1950; Gordillo and Lencinas 1979; González Díaz 1981; Jordan and Allmendinger 1986; Introcaso et al. 1987; Costa and Vita Finzi 1996, Ramos et al. 2002).

During Miocene times (18-11 Ma) the Juan Fernández ridge was incorporated into the subduction of the Nazca plate (e.g. Yañez et al. 2001; Ramos et al. 2002). The collateral shortening and flattening of the Nazca plate subduction angle (Stauder 1973; Barazanghi and Isacks 1976; Pilger 1984) is interpreted to have led to uplift and deformation of the Pampean basement blocks (González Bonorino 1950; Gordillo and Lencinas 1979; Criado Roque et al. 1981; González Díaz 1981; Jordan and Allmendinger 1986; Introcaso et al. 1987; Massabie 1987; Costa and Vita Finzi 1996 Ramos et al. 2002), resulting in the uplift of the Sierra de San Luis and Sierra de Comechingones during Quaternary times (Costa 1992, Ramos et al. 2002).

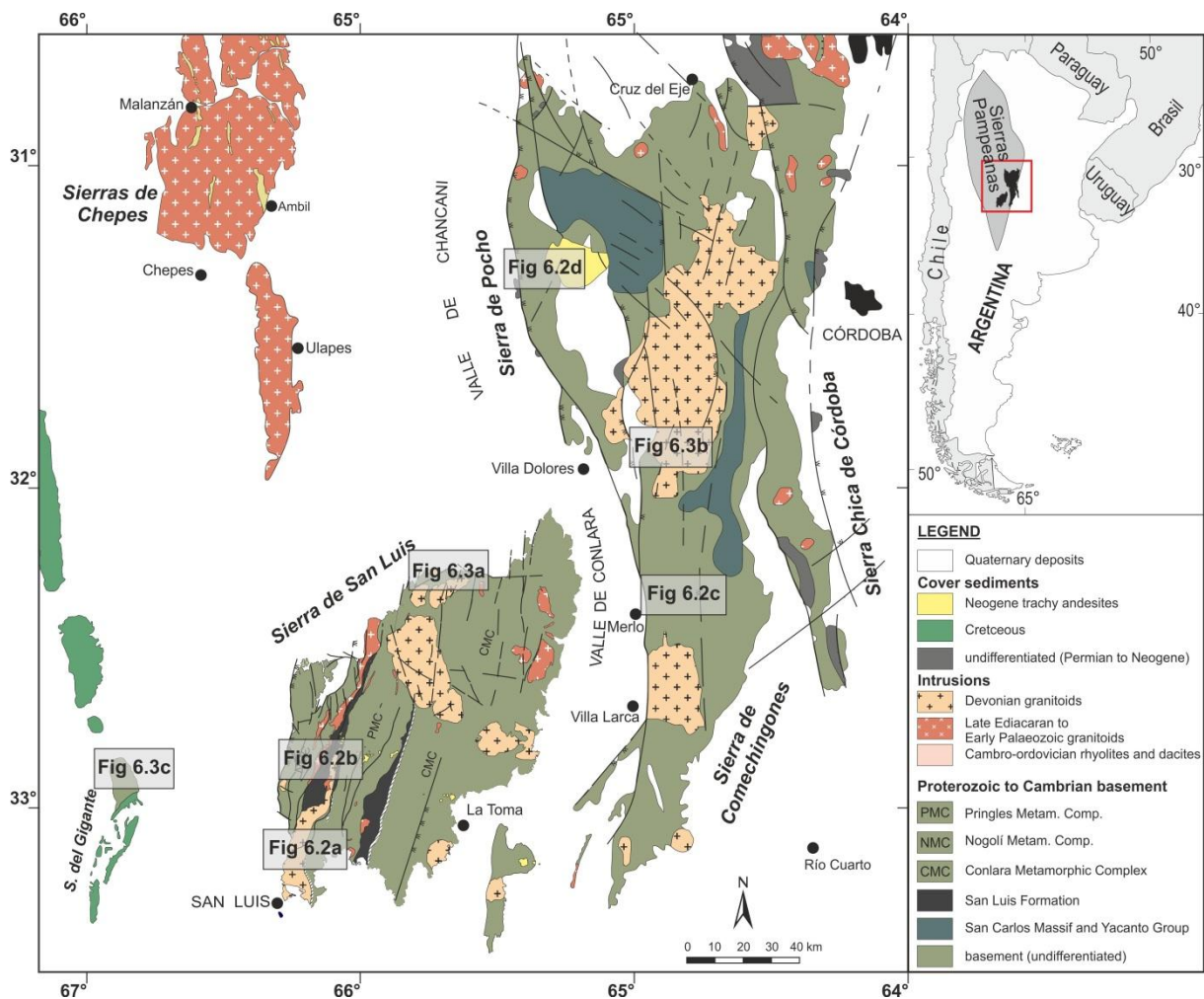


Fig. 6.1: Simplified geological map of study area. Detailed figures of sample locations are highlighted by rectangles with respective figure number.

The majority of faults with suspected or proven compressional Quaternary activity strike north-south with an eastward dip between 20 - 65°, e.g. the San Luis fault (Costa 1992), the Sierra Chica fault (Lencinas and Timonieri 1968), the Carlos Paz fault (Massabie and Szlafsztain 1991) and the Santa Rosa fault (Massabie 1976). Only a few faults strike northwest or show dipping to the west (Sierra Baja de San Marcos fault; Massabie 1976), Potrero de Garay fault (Schlagintweit 1954), Nono fault (Kraemer et al. 1993). Only one fault with Quaternary activity, located in the southernmost Sierra de San Luis, shows normal displacement (Costa and Cortés 1993). Models of fault geometry based on the uplifted blocks' topographic asymmetry favor a listric fault shape (e.g. González Bonorino 1950, Jordan and Allmendinger 1986, Costa and Vita-Finzi 1996, Intracoso et al. 1987, Richardson et al. 2012), but planar fault geometries have also been proposed (e.g. Martino et al. 1995). In contrast to these findings of Quaternary movement along some of the larger, range-bounding faults, Richardson et al. (2012) found little seismicity occurring along these east-dipping faults. Whether these faults are no longer active or accumulating stress instead of slipping has not yet been clarified.

Nonetheless, many open questions remain. For example, the evolutionary path of these ranges as well as the significance of the different tectonic regimes that have prevailed since the Gondwana

break-up in terms of uplift and exhumation is not well understood. Additionally, little is known of to what extent the current structural relief of the Pampean blocks is related to the Andean compression. For example, (U-Th)/He dating and Apatite Fission Track ages indicate exhumation and development of a positive relief in the Sierras de Comechingones and San Luis prior to the Cenozoic Andean compression (Löbens et al. 2011, Bense et al. in review A). Hence, exhumation and uplift of the Sierras driven by Andean compression might be of minor contribution than formerly expected in comparison to the total exhumation of the Sierras Pampeanas.

6.3 Methodology

6.3.1 Sample Preparation

A total of 31 samples were collected from surface outcrops. Each sampled fault gouge consists of approximately 250-1000 g of fresh material. After careful selection, about 200 g of clay material was dispersed in distilled water and sieved <63 μm . The grain size fractions <2 μm and 2-6 μm are gained from <63 μm fraction by differential settling in distilled water (Atterberg method following Stoke's law). Enrichment of the grain-size fraction <0.2 μm was accelerated by ultra-centrifugation. For details the reader is referred to Wemmer (1991).

6.3.2 Analytical Methods and Procedures

Mineral identification was done by XRD analysis on random oriented sample powders as well as oriented (textured) compounds using a Phillips PW 1800 X-ray diffractometer in a step scan mode ($0.020^\circ 2\theta$) in the range from $4 - 70^\circ 2\theta$. Preparation, sample treatment and mineral identification followed the methods described by Moore and Reynolds (1997). In order to support the identification of clay minerals, samples were measured in different conditions, e.g. under air-dry and ethylene glycol solvated conditions. For more details the reader is referred to Wemmer (1991). In order to further characterise mineralogical composition as well as to calibrate and check mineral identification done by XRD analyses. Samples which show complex mineralogical compositions were further analysed by transmission electron microscopy and electron diffraction (TEM), X-ray fluorescence (XRF), cation exchange capacity (CEC), differential thermal analyses (DTA) as well as infrared spectroscopy (IR spectroscopy). In the course of mineral identification the percentage of smectite interlayered in illite/smectite minerals was determined by using the $\Delta 2\theta$ -methode (Środoń 1980), determining the differences in 2θ position of the $(002_{\text{illite}}/003_{\text{smectite}})$ peak and the $(001_{\text{illite}}/002_{\text{smectite}})$ peak under ethylene glycolated conditions.

The metamorphic grade of the samples has been inferred from the illite crystallinity (IC), derived from the peak width at half height of the 10 Å illite peak (Kübler 1967). The values for the illite crystallinity are expressed by the Kübler index (KI; Kübler 1967) which may range from 0.060 $\Delta 2\theta$ (ideally ordered muscovite) to 1 $\Delta 2\theta$ (illite/smectite mixed layers). Kübler (1967) used boundary

values of $0.420^\circ 2\theta$ and $0.250^\circ 2\theta$ to divide the zones of the very low grade metamorphism. Those are, from lower to higher grade, the diagenetic zone ($KI > 0.420^\circ 2\theta$), the anchizone ($0.420^\circ 2\theta < KI < 0.250^\circ 2\theta$) and the epizone ($KI < 0.250^\circ 2\theta$). Corresponding temperatures for the two boundaries are around 150°C and 300°C respectively. Determination of IC was done using “IDEX” software developed at the University of Göttingen by Friedrich (1991). IC measurements were performed on thin, oriented (textured) samples prepared according to Weber (1972). Samples were analysed by XRD in step scan mode in a range of $7 - 10^\circ 2\theta$, using a scan step of $0.01^\circ 2\theta$ (300 points) with an integration time of 4 s per step. The presence of mixed layer clays that may obliterate the 10 \AA peak has been tested by determination of the material under air-dry (AD) and ethylene-glycolated (EG) conditions. To evaluate a potential machine drift as well as possible evaporation of EG each sample were measured twice under AD and EG conditions.

Using XRD patterns derived from randomly oriented samples it is possible to identify and quantify the relative amounts of illite polytypes, i.e. $2M_1$, $1M$ and $1M_d$ illite. After a technique proposed by Grathoff and Moore (1996) the concentration of the $2M_1$ and $1M$ polytype is determined by getting the ratio of either the area or the height of polytype specific peaks with the area of a peak which is common to both polytypes (the 2.58 \AA band; Grathoff and Moore (1996)). The amount of $1M_d$ illite is determined by assuming that the remaining illite is the $1M_d$ polytype. A randomly oriented sample is essential for the polytype quantification because the polytype diagnostic peaks are non-(00l) indices, which are suppressed in textured samples. Randomly oriented samples are achieved by using a side packing device as recommended by Grathoff and Moore (1996) and described by Moore and Reynolds (1997). The randomness of orientation was checked by the ratio of the (002)/(020) illite peaks, which should be low for non-oriented samples. To determine the polytypism of illite, powder compounds were prepared and scanned in 561 steps in a range of $16 - 44^\circ 2\theta$, using a scan step of $0.05^\circ 2\theta$ and an integration time of 30 s per step to amplify polytype specific reflections. The allocation of peaks to the corresponding polytypes was done as suggested by Grathoff and Moore (1996) and Grathoff et al. (1998). Obtained polytype percentages were cross-checked by comparison of sample XRD tracings with XRD patterns from physical mixtures of different illite polytype contents as well as modelled XRD patterns.

K-Ar illite ages were determined by two different procedures. The argon isotopic composition was measured in a Pyrex glass extraction and purification vacuum line serviced with an on line ^{38}Ar spike pipette and coupled to a VG 1200 C noble gas mass spectrometer operating in static mode. Samples were pre-heated under vacuum at 120°C for 24 h to reduce the amount of atmospheric Argon adsorbed onto the mineral surfaces during sample preparation. Argon was extracted from the mineral fractions by fusing samples using a Mo-crucible within the pyrex glass extraction and purification line.

The amount of radiogenic ^{40}Ar was determined by isotope dilution method using a highly enriched ^{38}Ar spike (Schumacher 1975), which was calibrated against the biotite standard HD-B1 (Fuhrmann et al. 1987, Hess and Lippolt 1994). The released gases were subjected to a two-stage purification procedure via Ti-getters and SORB-ACs getters. Blanks for the extraction line and mass spectrometer were systematically determined and the mass discrimination factor was monitored by airshots. The overall error of the Argon analysis is below 1.00%. Potassium was determined in duplicate by flame photometry using an Eppendorf Elex 63/61. The samples were dissolved in a mixture of HF and HNO_3 . The pooled error of duplicate potassium determination on samples and standards is better than 1%. The K-Ar age were calculated based on the ^{40}K abundance and decay constants recommended by the IUGS quoted in Steiger and Jäger (1977). The analytical error for the K-Ar age calculations is given at a 95% confidence level (2σ). Analytical results are presented in Table 6.1. Details of argon and potassium analyses for the laboratory in Göttingen are given in Wemmer (1991).

6.4 Results

6.4.1 Gouge-Bearing Faults Systems

Along sampled locations (Figs. 6.1-6.3) the characteristics and orientation of gouge bearing faults, fault surfaces and fault zones were examined. Due to outcrop conditions, most of the observations were restricted to road ravines. Approximately 1200 faults were examined.

Almost all observed faults show a well-developed clay gouge on the fault surface. Some gouges show small lenses of residual rock material within a clay matrix, consisting of either polymineralic rock-fragments or monomineralic grains (Fig. 6.4). Polymineralic fragments show diameters of several millimetres to a few centimetres, consisting of host-rock material. The monomineralic grains are only a few millimeters in diameter and consist almost exclusively of quartz. Gouge thicknesses vary from several millimetres up to several decimetres, but mostly are between 1-5 cm. Most gouges have monochrome brownish, reddish, white or ochre-yellow colours but multi-coloured gouges with colours alternating in a centimetre-scale are also observed (Fig. 6.4).

The transition from the host-rock to the fault gouge is developed in several forms. In a mesoscopic scale some locations show a gradual transition from the undeformed host-rock to a damage zone (partially ultracataclastic) and fault-gouge zone (see Chester and Logan 1986). In other locations the fault gouge is bounded directly by the undeformed host-rock (Fig. 6.4).

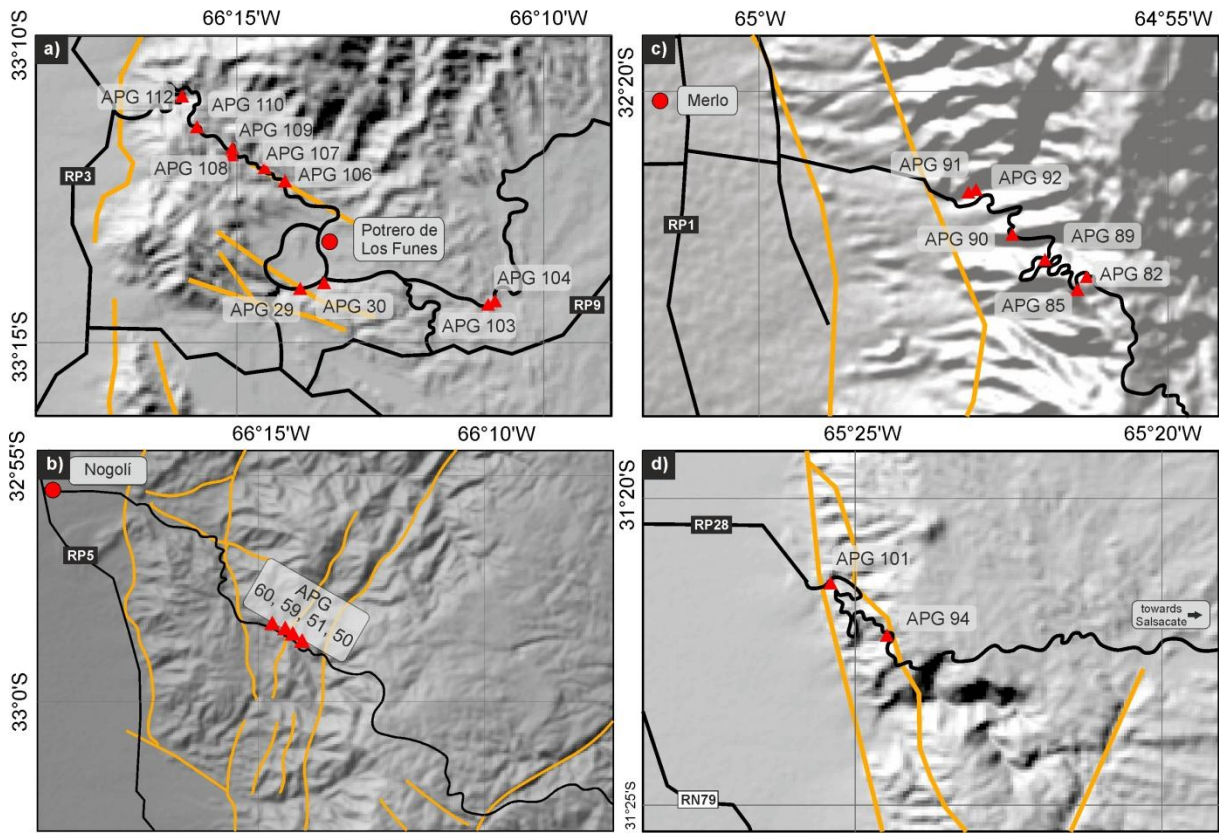


Fig. 6.2: Simplified map of sample locations: a) Potrero de Los Funes; b) Nogolí; c) Merlo; d) Los Tuneles. RP = Ruta Provincial; RN = Ruta Nacional; red triangles = fault-gouge sample location; orange lines = faults.

In the study area, kinematic indicators on fault surfaces are mainly developed in form of slickensides. Most of them are built up by fibrous crystallites, consisting of quartz, calcite, chlorite as well as iron-oxides and iron-hydroxides. Mineral lineation and slickenlines are generally well developed but almost exclusively lacking fault kinematic indicators (e.g. Doblas 1998) constraining the sense of movement along the lineation. Thus, collected data give only a bivalent sense of movement. Cross-cutting relationships of slickensides elucidating the temporal succession of slickenside development are only merely developed, prohibiting the decomposition of orientations in terms of a timely variation of movement directions.

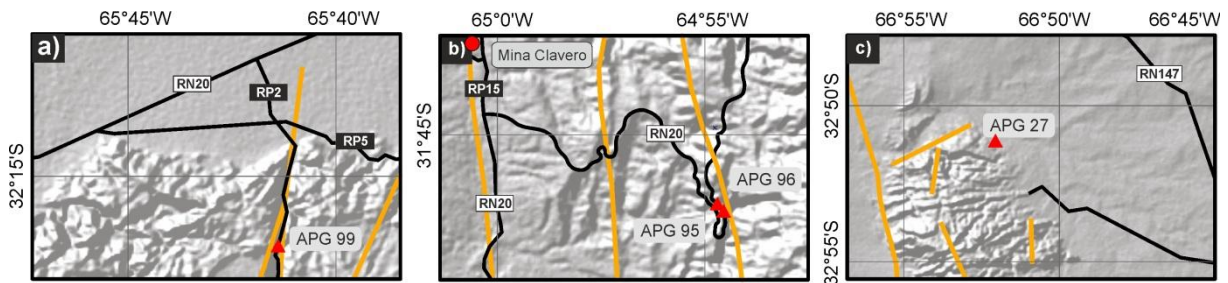


Fig. 6.3: Simplified map of sample locations; a) Quines; b) Achala; c) Sierra de Los Gigantes. RP = Ruta Provincial; RN = Ruta Nacional; red triangles = fault-gouge sample location; orange lines = faults.

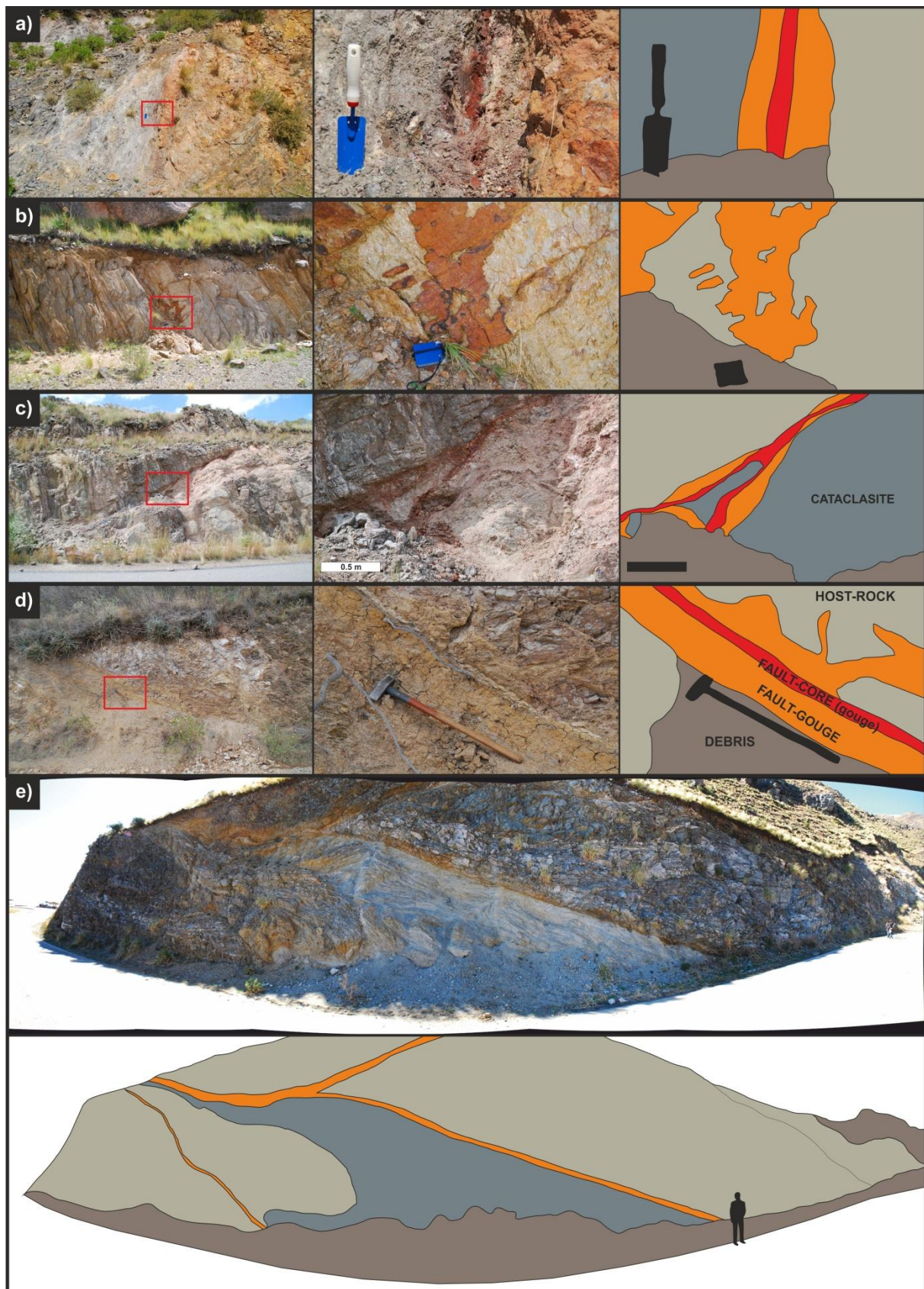


Fig. 6.4: Examples of gouge bearing faults zones from the study area; a-c) Nogolí (Sierra de San Luis); d) Los Tuneles (Sierra de Pocho); e) Merlo (Sierra de Comechingones). Left picture = overview, middle picture = detail of fault-gouge, right picture = sketch of fault-zone setting.

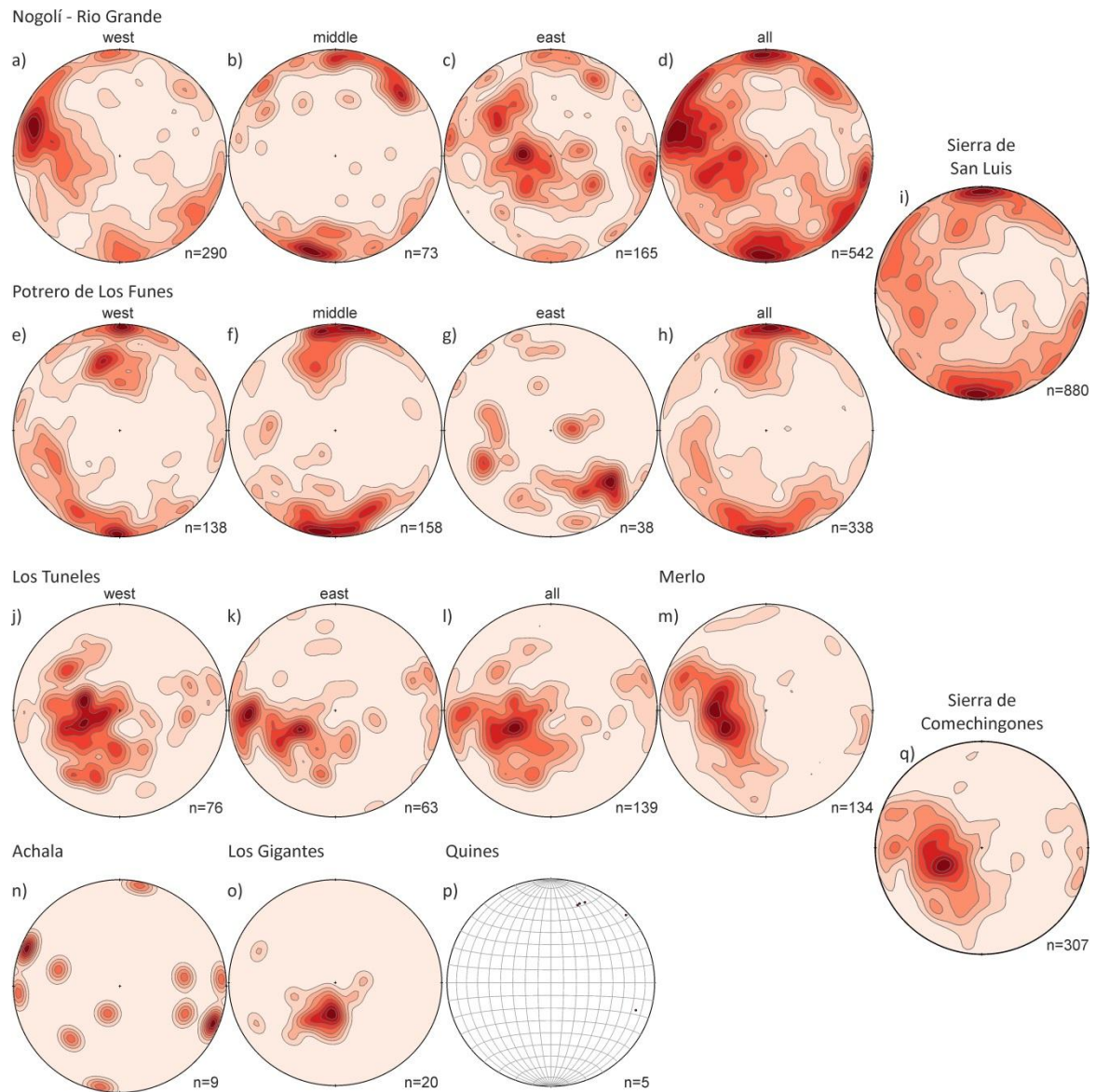


Fig. 6.5: Fault plane orientation data; Nogolí transect (a-d), Potrero de Los Funes (e-h) and compilation of all data from the Sierra de San Luis range (i). Sierra de Comechingones transects; Los Tuneles (j-l) and Merlo (m), compilation of all fault orientation data from the Comechingones ranges (q), additional locations; Achala (n), Los Gigantes (o), Quines (p). Contour interval show multiples ($n=1, 2, 3, \dots$) of normal distribution. Plots drawn with OpenStereo.

Nogolí

A total of 542 fault plane orientations (Fig. 6.5 a-d) were measured along the transect from Nogolí to Rio Grande (Fig. 6.2a). Based on the fault plane orientations, the data set can be divided into five domains: 1) steep N or S dipping fault planes with mean fault planes dipping 165/85 and 003/79, respectively, 2) steep NW or SE dipping fault planes with mean planes dipping 306/79 and 137/84, 3) intermediate-to-steep ESE-WSW dipping with mean poles of 106/75 and 280/84, 4) steep SW dipping with a mean plane dipping 216/73 and 5) flat-to-intermediate ENE to dipping with a mean plane at 066/33.

Generally, the orientations of the fault planes show significant variation from the western to the eastern side of the transect. The western profile is dominated by steep SSE as well as SE dipping systems; associated NNW and NW dipping systems are only weakly developed (Fig. 6.5 a). Dip shows

mainly steep, partially intermediate dip angles. In the central part of the profile (Fig. 6.5 b), the predominant SE dipping orientation of the faults change to more complex patterns with occasionally strong populations of steeply SW dipping planes, as well as an overall flattening of dip angles towards the easternmost parts in the area of the Rio Grande dam. Additionally, the distinct east-west striking fault system can be observed in the middle (La Escalerilla batholith) and the easternmost part (Fig. 6.5 c).

Potrero de Los Funes

A total of 338 fault planes were measured along the Potrero de Los Funes transect (Fig. 6.2b). Based on the orientation, four populations can be recognized: 1) steep N or S dipping with mean orientations of 004/86 and 181/86, 2) intermediate NNE dipping fault planes with a mean orientation of 066/59, 3) intermediate-to-steep SSE dipping population with a mean direction of 165/57 and 4) intermediate to steep NNW dipping population with a mean orientation of 026/70.

Some variation can be identified along the transect. The N and S dipping fault planes are present throughout the entire transect, except for the easternmost part (Fig. 6.5 e-h). The intermediate-to-steep SSE dipping population is not so dominant in the easternmost transect either. Observed dip angles in the Potrero de Los Funes region are almost exclusively intermediate to steep, and only occasional flat-lying faults were observed (Fig. 6.5 e-h). Interestingly, the strong NW-SE and ESE-WSW dipping systems in the Nogolí system are not developed in the Potrero area.

Los Tuneles A total of 139 faults were measured along the Los Tuneles transect (Fig. 6.2c). Fault plane orientation can be grouped into two major and several minor domains. NE dipping is predominant (Fig. 6.5 j-l): 1) intermediate ENE dipping faults, showing some scattering around a mean orientation of 065/30, 2) steep E dipping with a mean orientation of 088/70, 3) steep WSW dipping with a mean orientation of 249/72, 4) intermediate SE to ESE with a mean orientation of 126/53, 5) intermediate NNE dipping with a mean orientation of 017/50 and 6) intermediate NNE dipping with a mean orientation of 009/30.

From west to east, minor variations in the fault plane orientations are observed (Fig. 6.5 j-l). In the western section, intermediate SE and NNE populations can be found (Fig. 6.5 j), whereas the steep E dipping population is only observed in the eastern parts of the transect (Fig. 6.5 k). The dominant E-ENE dipping populations are found through the entire transect (Fig. 6.5 j-l).

Merlo

A total of 134 fault orientations were measured along the Merlo transect (Fig. 6.2d) with dip directions trending from ESE to NNE (Fig. 6.5m). Orientation data can be divided into two groups comprising intermediate E-ENE and steep ESE dipping faults. Mean orientations for the populations are 113/27 for the ESE-dipping population and 086/35 for the ENE-to-E-dipping population. No significant variation in fault orientation along the profile was observed.

Other Locations

Due to restricted outcrop conditions, only a minor amount of data ($n \leq 20$) could be collected in the area of the Sierra de Los Gigantes, San Martin and Achala (Fig. 6.1 and 6.3). Although the amount of measurements is not statistically significant, data fit with trends observed in the other transects. The Achala region shows a general north-south striking orientation (Fig. 6.5 n), as observed in the other Comechingones regions (Fig. 6.5 j-m). In the San Martin area, a general east-west striking is present (Fig. 6.5p), as is observed in the rest of the Sierra de San Luis (Fig. 6.5 i). Faults observed near La Calera in the northern part of the Sierra de Los Gigantes also show a general east-west striking trend with gentle-to-intermediate northward dipping (Fig. 6.5 o).

6.4.2 Fault Gouge Analyses

The following chapter discusses the results of fault-gouge analyses from 31 samples (Fig. 6.2+3; Table 6.1) with three grain-size fractions each. Data for 21 samples are presented here for the first time, while data from 10 samples are reviewed from previous publications by Löbens et al. (2011) and Bense et al. (in review A). To give the reader a complete overview as well as to ease the traceability of the following discussion, data from both publications are integrated here (Fig. 6.2+3; Table 6.1). Data published by Löbens et al. (2011) and Bense et al. (in review A) comprise K-Ar age, mineralogy, illite crystallinity and illite polytypism from six samples from the Merlo area (APG 82-09, 85-09, 89-09, 90-09, 91-09 and 92-09; Löbens et al. 2011) and four samples from the Nogolí area (APG 50-09, 51-09, 59-09 and 60-09; Bense et al. in review A). In addition to the data by Löbens et al. (2011), detailed polytype quantification as well as I/S quantification for the Merlo samples is presented in this study. Data from Bense et al. (in review A) are completed by I/S quantification presented in this study.

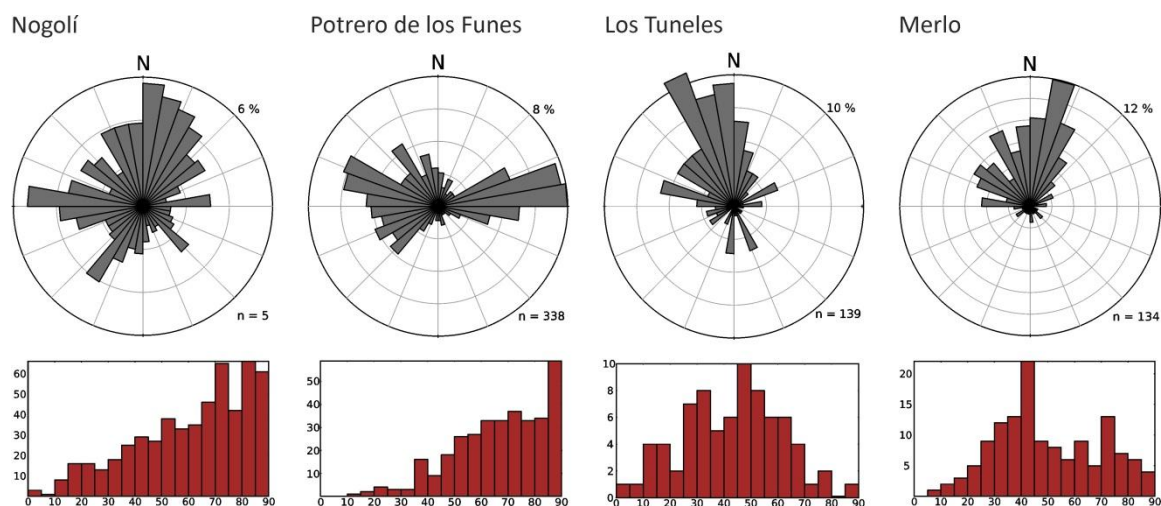


Fig. 6.6: Summarised orientation data; rose diagrams showing strike direction. Histograms show dip angle. Plots were drawn with OpenStereo.

Mineralogy

Mineralogical analyses by XRD and TEM (Figs. 6.7 and 6.8), and checked by IR, CEC and DTA. Data show illite and smectite as most abundant clay mineral phases in all samples (Table 6.1, Fig. 6.7 and 6.8). Furthermore chlorite and kaolinite are frequent. Occasionally traces of halloysite (Fig. 6.8) are identified by TEM, XRD and IR analyses. In some 2-6 μm fractions, XRD observations reveal traces of quartz, K-feldspar and plagioclase, while smaller fractions (<2 μm) sporadically contain traces of quartz but are almost exclusively free of K-feldspar and plagioclase. The smallest grain-size fractions (<0.2 μm) consist of clay mineral mixtures with variable amounts of illite, smectite, chlorite and kaolinite. In some cases traces of quartz were found, but no feldspar was detected. Detection limits to quantify the amount of quartz, K-feldspar and plagioclase by XRD are around 5 %. Assuming a moderate K_2O in K-feldspar of 12%, non-detected feldspar can contribute to the K_2O content of illite by approx. 0.6%, introducing error to the age determination (see above). However, TEM observations show no trace of feldspar contamination of fractions which are indicated feldspar-free by XRD analyses. In addition TEM show no contamination of fractions with particles greater than the respective grain-size fraction limits, confirming an accurate grain-size separation technique.

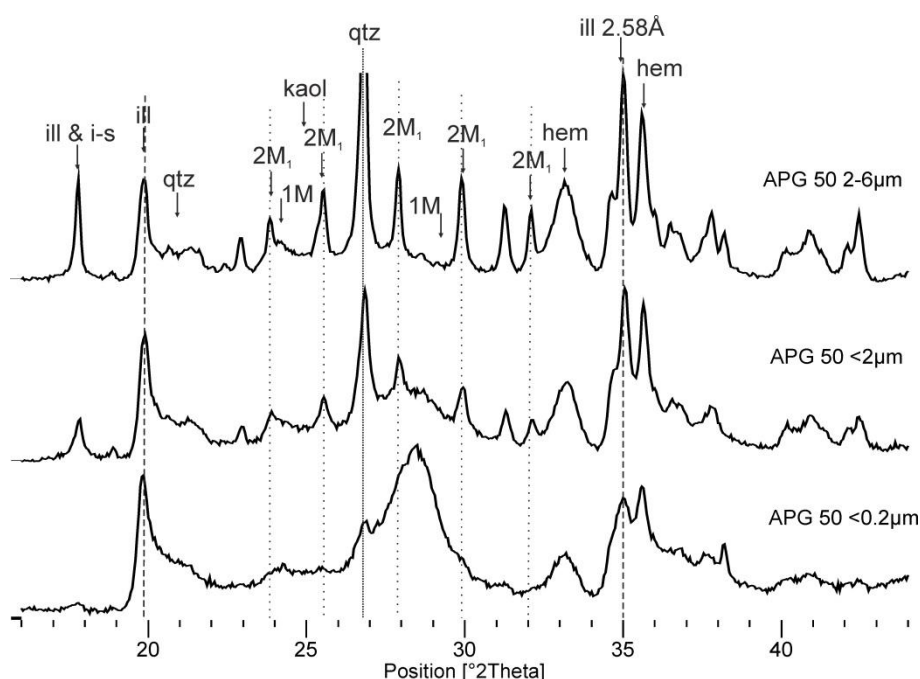


Fig. 6.7: XRD pattern derived from randomly oriented samples with indicated positions of 2M1 and 1M polytype specific peaks. Other phases are indicated as follows: illite (ill), Illite–Smectite (i–s), quartz (qtz), kaolinite (kaol) K-feldspar (kfs) and hematite (hem).

Grain-size fractions bearing illite and smectite show variable amounts of irregular I/S mixed layers. The occurrence of I/S mixed layers is mainly restricted to the fraction <2 μm and <0.2 μm . The percentage of illite in illite-smectite mixed layers range from <10 % to around 50 %, giving R0 (i.e. unordered; e.g. Moore and Reynolds 1997) illite(0.1)/smectite to R0 illite(0.5)/smectite minerals. In addition to the illite in I/S mixed layers, almost all samples contain discrete illite (Table 6.1). No other mixed layer clays were found.

CEC values ranging from 8 meq/100g to 80 meq/100g indicate smectite contents of up to 35 % in the 2-6 μm fraction and between 32 % and 84% in the smaller grain-size fractions, assuming normal layer charge density. Combined observations by CEC, DTA and XRF reveal the presence of several smectite member e.g. trans-vacant low-Fe montmorillonite, cis-vacant smectite as well as Fe-rich smectite.

Illite Crystallinity

The illite crystallinity (IC) expressed by the Kübler indices (KI values), range from $0.157 \Delta^{\circ}2\theta$ to $0.920 \Delta^{\circ}2\theta$. Extreme values of $1.288 \Delta^{\circ}2\theta$ and $1.433 \Delta^{\circ}2\theta$ were measured (Table 6.1). The KI-values obtained represent diagenetic and anchizonal, as well as epizonal conditions. In general, KI-values increase with decreasing grain-size, reflecting mostly diagenetic conditions for the $<0.2 \mu\text{m}$ fraction as well as the $<2 \mu\text{m}$ fraction. Anchizonal conditions are mostly represented by KI-values from the $<2 \mu\text{m}$ fraction but have also been obtained for the 2-6 μm and $<0.2 \mu\text{m}$ fractions. Epizonal conditions are mostly represented by KI-values from the 2-6 μm fractions but can be occasionally found in the other fractions.

Illite Polytypism

All 78 analysed powder samples show a low (002)/(020) peak ratio, documenting randomness in clay mineral orientation is assured. All analysed samples contain a mixture of polytypes with variable proportions in the respective grain-size fractions (Table 6.1). The dominating polytype (polytype content of $>50\%$) vary between fractions and correlates with grain-size, showing decreasing $2M_1$ content (increasing $1M_d$ content) with decreasing grain-size. The 2-6 μm fraction is mostly dominated by $2M_1$ illite (20 of 26 fractions) only a small number of samples show predominance of the $1M_d$ polytype (Table 6.1.). The majority of the $<2 \mu\text{m}$ fraction is controlled by $1M_d$ illite (24 of 27 fractions) only very few samples show $2M_1$ content of $>50\%$ in this grain-size fraction. The $<0.2 \mu\text{m}$ fraction is exclusively dominated by the $1M_d$ polytype (25 fractions). In general, the $<2 \mu\text{m}$ fraction represents the most variable fraction analysed showing the highest variability in percental polytype composition, whereas the $<0.2 \mu\text{m}$ fraction is the most invariable fraction in terms of polytype composition. The $2M_1$ and $1M_d$ polytypes can be found in almost all analysed fractions but there occurrence show opposites trends in relation to grain size. $2M_1$ illite is lesser frequent in the smaller fractions, the $1M_d$ polytype lesser frequent in the coarse grain-size fractions. The $1M$ polytype is less frequent and mainly linked to the fraction 2-6 μm and $<2 \mu\text{m}$ (Table 6.1).

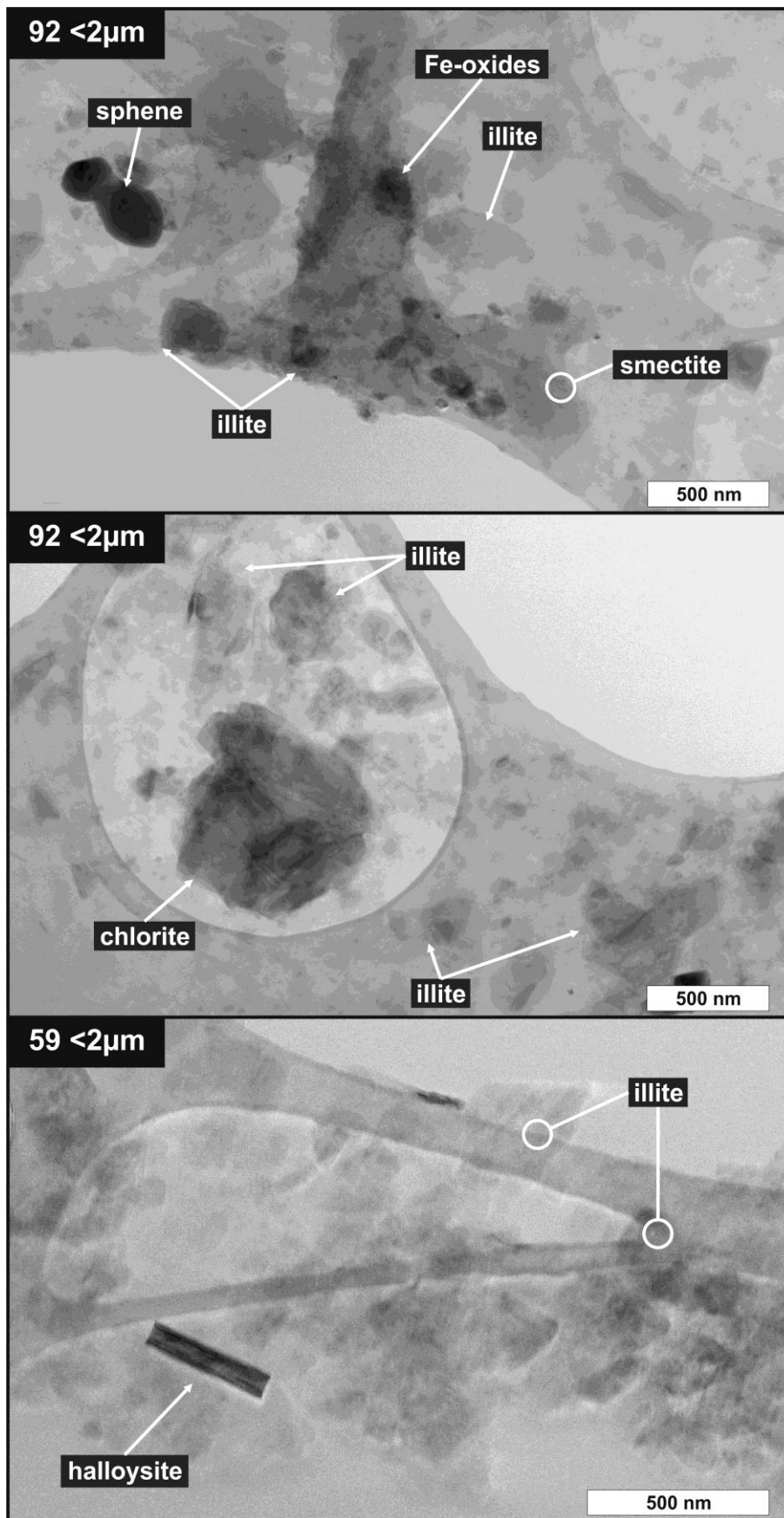


Fig. 6.8: TEM images of samples APG 92-09 and 59-09, showing common clay mineral phases as well as accessory minerals found in the clay fractions of fault-gouge samples.

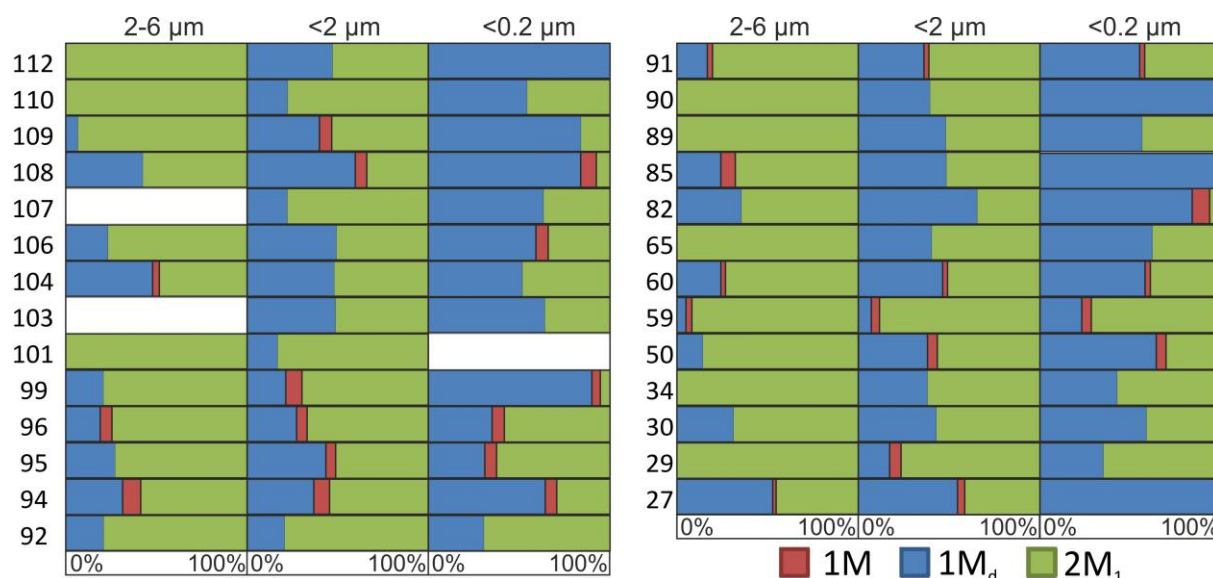


Fig. 6.9: Distribution of illite polytypes 2M₁, 1M and 1M_d in analyses samples and grain-size fractions.

K-Ar Age

A total of 88 K-Ar ages from 31 samples were obtained (Table 6.1, Fig. 6.9). Ages range from 382.1 Ma (Late Devonian) to 106.5 Ma (Middle Cretaceous). In general, ages increase with increasing grain-size fraction, whereby ages from fractions range between 297.6-106.5 Ma (<0.2 μm), 336.3-127.8 Ma (<2 μm) and 382.1 -193.7 Ma (2-6 μm; Fig. 6.9).

High content in radiogenic ⁴⁰Ar, ranging from 80 % to 99.6 %, confirm reliable analytical conditions for almost all analyses. Only 4 samples show ⁴⁰Ar contents between 60 % and 80 % (Table 6.1). Potassium (K₂O) content is less than 1 % for one samples, but ranges from 1.03 % to 8.41 % for the others (Table 6.1).

Considering the regional extend of the sampled fault gouges, significant differences in age can be observed. Generally, the samples from Nogolí, Potrero de los Funes and San Martin show younger ages, while the Achala, Los Tuneles and El Gigante and Merlo area reveal older ages.

Based on the age and calculated polytype compositions of the different grain-size fraction, we extrapolated the 'end-member' age of the 1M_d polytype and the 2M₁ polytype by plotting the age of each individual grain-size fraction of a fault gouge sample against the 2M₁ illite content and linear extrapolation (see also Grathoff and Moore 1999; Grathoff et al. 2001). Extrapolated ages represent hypothetical samples consisting of 0% 2M₁ illite and 100 % 2M₁ illite (Table 6.1) respectively. Extrapolations show a coefficient of determination (R²) better than 0.9 for most of the samples. Six samples show an R² below 0.7. These values correspond to samples showing different attributes complicating the age extrapolation: (1) insignificant differences in age and/or (2) insignificant differences in 2M₁ polytype content between two fractions and/or (3) an increase in grain-size which is not correlated with an increase in age (see Discussion; Table 6.1). However, in most cases, the high values for R² confirm a clear relationship between age and 2M₁ polytype content (Table 6.1). A

discussion of assumptions under which these calculation can give geological meaningful ages is given below.

6.5 Discussion

6.5.1 Fault Zones Orientations and Paleostress

Generally, major basement structures strike NNE in the Sierra de San Luis, NNE in the Sierra de Los Gigantes and NNW in the Sierra de Córdoba (Fig. 6.1, e.g. Schmidt et al. 1995, Lucero Michaut et al. 1995, Costa et al. 2001). Fault orientations measured in course of this study clearly display a more complex picture although those general trends are also represented by our data (Figs. 6.5 and 6.6). To what extend the observed deviation in fault orientation from main tectonic trends can be attributed to conjugated fault systems and/or reactivation short cut relationships (e.g. Simpson et al. 2001) is beyond the scope of this study. However, conjugated fault systems were identified in the study area.

Observed paleostress indicators are scares and often are in contradiction to the Mohr-Coulomb criterion, e.g. by giving reverse movement along high-angle near-surface faults. However, according to Simpson et al. (2001) these findings can be attributed to the existence of small scale faults in a short-cut orientation, give evidence for a reactivation of less suitable oriented faults.

In conclusion of the above elucidated data there is a main difference in small scale fault orientation between the Sierra de Córdoba and Sierra de San Luis. The San Luis area (Nogolí, Potrero de los Funes and San Martín area) shows, in addition to the overall observed N-S to NNE-SSW striking faults, a strong E-W striking fault population (Fig. 6.5). This orientation is not observed in the Sierra de Córdoba area (Los Tuneles, Merlo and Achala).

Additionally, the Sierra de Córdoba and Sierra de San Luis show significant differences in dip angles of small scale faults (Fig. 6.6). The Sierra de San Luis shows a left skewed distribution with maximum at high dip angles. In contrast, the Sierra de Córdoba shows a bimodal distribution with maxima between 20-30° and 50° (Los Tuneles) and 70-80° (Merlo). The first population matches the mean shear fracture angle of the Mohr-Coulomb criterion (Fig. 6.6). Whether this imply that a higher proportion of faults are reactivated in the Sierra de San Luis than in the Sierra de Córdoba or this is linked to pre-existing discontinuities (like fractures or foliations) cannot be concluded from our data.

No correlation between the age and the fault orientation could be established.

The observed localisation of faults throughout the entire width of the Pampean ranges illustrate that deformation was distributed throughout the entire mountain ranges since the beginning of brittle deformation.

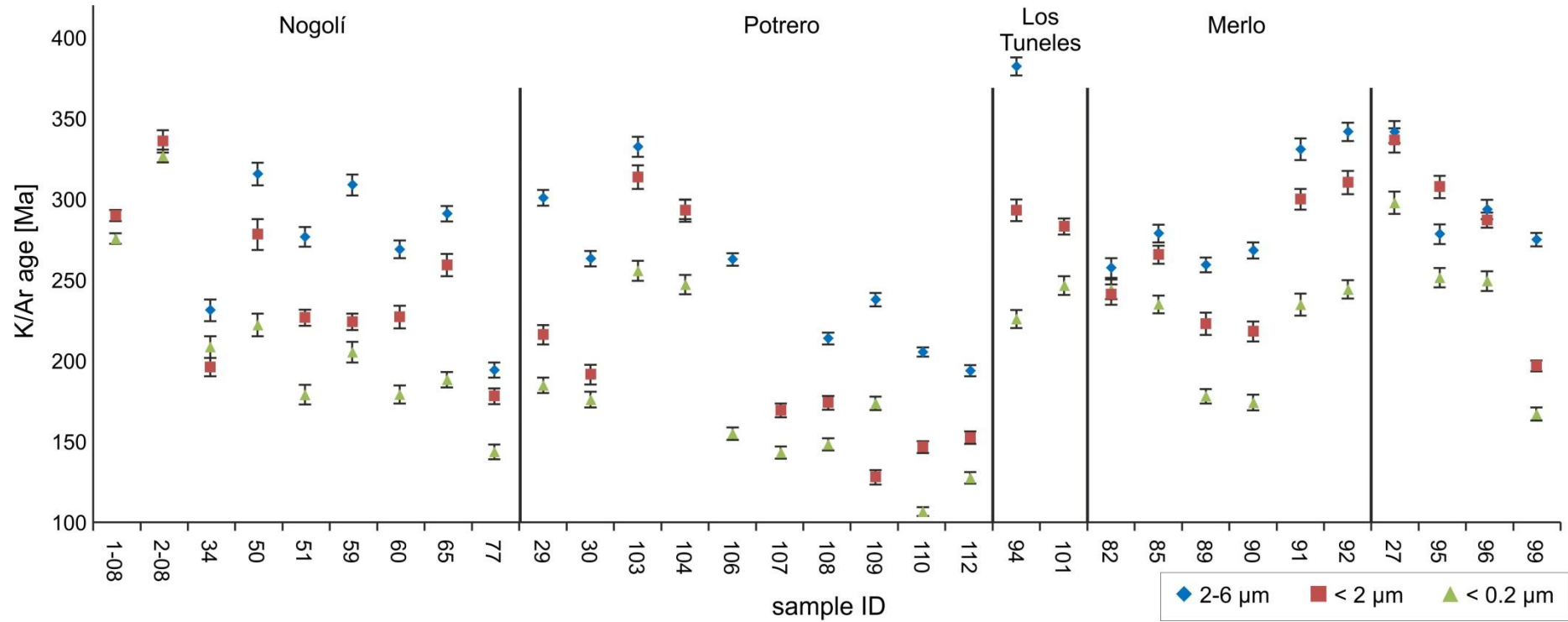


Fig. 6.10: K-Ar illite fine fraction ages for all analyzed samples and grain-size fractions.

In some locations in the Sierra de San Luis brittle faults are observed which are along mylonitic or pseudotachylitic zones, suggesting that brittle faulting reactivated those discontinuities and weakness zones. The same phenomenon is also reported by Northrup et al. 1998 and Simpson et al. (2001) for the Sierra de Córdoba.

The orientation of dated fault gouges is displayed in Fig. 6.5. Although the above mentioned preferred fault orientation are resembled by the dated gouge samples, no correlation between fault orientation and K-Ar illite age could be observed. Therefore, a decomposition of ages in terms of a timely variation in the orientation of active faults (and thus paleostress directions) is not possible.

Although the eastern Sierras Pampeanas are located in an apparently compressive regime, Richardson et al. (2012) found dominantly normal displacement with small components of strike-slip. The authors analysed focal mechanisms of the recent seismic activity in the Eastern Sierras Pampeanas. The normal displacement is interpreted to represent a period of seismic cycle during which stresses from concentration are released by small-magnitude events (Richardson et al. 2012). However, orientation of P-axes from focal mechanisms, although scattering, show a general E-W trend, correlating with the convergence direction of the Nazca plate (Brooks et al. 2003; Kendrick et al. 2006; Vigny et al. 2009).

6.5.2 Mineralogical Observations

Based on the qualitative clay-mineral composition (Table 6.1) of individual grain-size fractions the mineral content of each sample were classified by assigning all recognized combination of dominant clay mineral phases to eight compositional groups (Table 6.1). With respect to two samples the classification shows illite as one of the dominant clay mineral phases. Most samples (13) are dominated by illite in combination with kaolinite, only few samples show more than two dominant clay mineral phases (Table 6.1).

Except for illite, no correlation could be observed between the abundance of one or more dominant clay mineral phases and the IC or the K-Ar age (Table 6.1). It can be concluded that the amount of illite for dating is sufficient for all samples and that the collected fault gouge data is independent from mineral phases other than illite. Additionally no regional dependency on the clay-mineral abundance or composition could be observed.

The almost exclusive occurrence of Illite/smectite mixed layers in the smaller grain-size fractions is in agreement with the expected progression of illite development under retrograde conditions, starting with pure illite and 2M₁-rich, I/S-poor material and ending with 1M_d and I/S-rich material, representing the last formed illite phases. No other mixed layer clays were found.

6.5.3 K-Ar Fault Gouge Dating

One of the most important assumptions involved in the interpretation of K-Ar ages is a closed system behaviour, thus no gain or loss of either ^{40}K or ^{40}Ar after illite formation. A loss of Ar might be possible due to thermal diffusion effects or exchange reactions with hydrothermal fluids (e.g. Villa 1998). Concerning thermal diffusion, the effective diffusion radius has a major effect on the closure temperature for the Ar-system as it has been demonstrated throughout a large number of publications (e.g. Dahl 1996, Villa 1998, Hodges 2003). However, these publications are focused on the examination of white micas with grain sizes $>200\text{ }\mu\text{m}$. Concerning illite fine-fractions (grain-sizes $<2\text{ }\mu\text{m}$), available information is sparse. Hunziker et al. (1986) reported a closure temperature interval (end of significant diffusion of Ar) for mica fractions $<2\text{ }\mu\text{m}$ of $260\pm30\text{ }^{\circ}\text{C}$, whereas Wemmer and Ahrendt (1997) found indication that fine-grained white micas (sericite $<2\text{ }\mu\text{m}$) did not behave as open systems, even at temperatures of $275\text{ }^{\circ}\text{C}$. Therefore, the closure temperature of fine grained mica has to be estimated somewhere between $275\text{-}350^{\circ}\text{C}$ (Wemmer and Ahrendt 1997). Furthermore, errors in the acquisition of accurate K-Ar ages can arise from contamination by other K-bearing phases, e.g. K-feldspar. K-feldspar, even being very much older than the illite, can rejuvenate the age of the illite fine-fraction due to its low closure temperature of about $150\text{ }^{\circ}\text{C}$ (e.g. Fitz-Gerald and Harrison 1993). Another problem which must be considered is the possible mixture of illite formed by different events at different times. In general, for authigenic, neocrystallized illite, the finest illite fraction should represent the most recently grown illite, whereas coarser grain-size fraction should yield older ages, representing earlier illite forming events (e.g. Clauer et al. 2012). Nevertheless, even the smallest grain-size fraction can contain illite of different age. Thus, the age of this fraction could predate the last illite forming event because youngest illite population is mixed with older illite (see also 4.3).

6.5.4 Illite Crystallinity

On the basis of the obtained KI-values, the areas studied can be tentatively divided into four groups (Table 6.1); the grouping is mainly focused on the smaller grain-size fractions. The four groups are defined as:

- Group 1, very high crystallinity (very low KI), characterized by samples with exclusively epizonal conditions or epizonal conditions for the $2\text{-}6\text{ }\mu\text{m}$ and $<2\text{ }\mu\text{m}$ fractions and anchizonal conditions for the $<0.2\text{ }\mu\text{m}$ fraction.
- Group 2, high crystallinity, characterized by samples showing epizonal or anchizonal conditions in the $2\text{-}6\text{ }\mu\text{m}$ fractions and exclusively anchizonal conditions in the finer fractions.

- Group 3, low-to-intermediate crystallinity, especially samples showing epizonal or anchizonal conditions in the 2-6 μm fractions, anchizonal conditions for the $<2 \mu\text{m}$ fraction and diagenetic conditions for the $<0.2 \mu\text{m}$ fraction.
- Group 4, samples with very-low-to-low crystallinity, characterized by diagenetic conditions in the grain-size fractions $<2 \mu\text{m}$ and $<0.2 \mu\text{m}$.

Most of the analyzed samples lie in the groups 3 (10 samples) and 4 (13 samples). The regions Potrero (8 of 8), Nogolí (6 of 9), Los Tuneles (2 of 2), San Martin and Achala (2 of 2) especially show considerably low IC values. Only eight samples show high IC values, which are mostly samples from El Volcan (2 of 2), while individual samples from Merlo, Achala and Nogolí also show high IC values. In general, IC-groups demonstrate good correlation with the K-Ar illite ages obtained (Table 6.1).

It has to be kept in mind that the analyzed samples represent mixtures of illite of different ages and polytypism. In this case, IC as an indicator for temperature experienced by the fault gouge does not work because samples give mixed IC-values and, thus, inexplicit results. However, the KI values of authigenic fault-gouge illite, even in mixtures, can be used to estimate the minimum temperature experienced by the fault-gouge sample (Table 6.1). Additionally, the predominant distribution of gouge samples in the IC groups 3 and 4 is considered to express a polyphase deformation history resulting in strong polytype mixture and, as a function of that, IC-mixture (see below).

6.5.5 Illite Polytypism and Interpretation of $2M_1$ Illite

Polytypism (Bailey et al. 1977; Guinier et al. 1984) is a common phenomenon for layered silicate minerals such as mica, chlorite and kaolinite. For illite the most common polytypes are the $1M_d$, $1M$ and $2M_1$ (e.g. Reynolds and Thomson 1993), although Peacor et al. (2002) note that the $1M$ polytype stacking is possibly driven by compositional anomalies in the sample and thus not a polytype *sensu strictu*.

The determination of illite polytypism can be of major importance for the integrative interpretation because the presence of specific illite polytypes can be linked with temperature conditions during illite formation. With raising temperature, illite shows irreversible polytype transformation of $1M_d \rightarrow 1M \rightarrow 2M_1$ (Hunziker et al. 1986). Yoder and Eugster (1955), Velde (1965) as well as Weaver (1989) got indications from experiments that the transition from $1M_d$ and $1M$ to $2M_1$ appears between temperatures of approximately 210°C to 350°C. Contrasting, Lonker and Fitz Gerald (1990) and Zoller and Brockamp (1997) found apparently cogenetic $1M_d$, $1M$ and $2M_1$ illite in samples from hydrothermal systems, active at temperatures of approximately 270°C to 330°C (Lonker and Fitz Gerald 1990). Nevertheless, the $1M$ and $1M_d$ polytypes are thought to form at temperatures of below 200-210°C, whereas the $2M_1$ illite is thought to form above around 280°C.

Thus, the sequence of $1M_d \rightarrow 1M \rightarrow 2M_1$ indicate an increase of temperature and pressure whereby illite has $1M_d$ and $1M$ polytypes in a diagenetic zone ($<150^\circ\text{C}$), a mixture of $1M$ and $2M_1$ polytypes in the anchizone (ca. 150°C to $<300^\circ\text{C}$) and more or less sole $2M_1$ polytypes in the epizone ($>300^\circ\text{C}$) representing the onset of low-temperature metamorphism (Yoder and Eugster 1955, Velde 1965, Baile 1966; Środoń and Eberl 1984).

In contrast to the above stated, well studied continuous illite formation reactions under prograde conditions during burial diagenesis or hydrothermal environment, the behaviour of illite polytypes during retrograde conditions (cooling) is not well investigated (e.g. Zhao et al. 1999; Abad et al. 2003; Bense et al., in review A, in press). Most studies on illite polytypism (e.g. Pevear 1992, Grathoff and Moore 1996, Środoń 1999, Ylagan et al. 2000, Środoń et al. 2000, Środoń et al. 2002) focus on diagenetic to very low grade sedimentary rocks. It is known that illite in shale represents a mixture of detrital mica, mica weathering products as well as authigenic illite grown during burial diagenesis (Bailey et al., 1962). Additionally, it has been recognized that the K-Ar age of a shale decreases systematically with grain size (Hower et al. 1963; Velde and Hower 1963; Clauer et al. 1997) and that the abundance of the $2M_1$ polytype relative to the $1M$ and $1M_d$ polytypes also decreases systematically with grain size (Pevear 1992; Grathoff et al. 1998). These observations led to the widely accepted interpretation that the $1M_d$ and $1M$ polytypes represent authigenic products formed under diagenetic to anchimetamorphic, prograde conditions during subsequent burial, whereas the $2M_1$ illite polytype represents detrital components, due to its restriction to epizonal conditions. This distinction between illite polytypes ('authigenic' and 'detrital') was applied to fault gouges derived from non-sedimentary host rocks by assuming that the $2M_1$ component is inherited material derived from the wall rock (i.e. crushed muscovite) whereas the $1M$ and $1M_d$ components represent authigenic material formed in the fault zone in correspondence to fault slip (e.g. Haines and van der Pluijm 2008).

However, at higher temperatures, even $2M_1$ illite could be developed in fault gouges, especially if the onset of brittle deformation and thus fault gouge development directly follows cooling to brittle deformation temperatures (around 300°C for quartz, e.g. Passchier and Trouw 2005 and references therein). Thus, the development of $2M_1$ illite polytypes in a brittle fault gouge is possible due to cooling and its passage through epizonal conditions during retrograde metamorphism of the host rock, contemporaneous to faulting. This is particularly true for a slowly cooling basement (Bense et al. in press). The problem of possible inherited $2M_1$ component mixed with the authigenic (neoformed) $2M_1$ illite remains if the host rock of the gouge is sedimentary. In contrast, if the host rock is igneous or metamorphic, a contamination of fault-gouge mineral fine-fractions by cataclastically crushed muscovite of the host rock is very unlikely because of the very strong mechanical resistance of this mineral. This is especially true for faults with only minor displacement.

Muscovite flakes would rather rotate parallel to the faulting plane than being grinded to extremely small particles (e.g. Wemmer 1991). If so, they could be identified by their excellent crystallinity (ca. $0.060 \Delta^{\circ}2\theta$).

Pevear (1992) and Grathoff and Moore (1996) introduced a method to estimate the end-member ages of the different illite polytypes in sediments i.e. 'detrital' and 'diagenetic' illite. The method is based on a quantitative determination of the end-member proportions in different grain-size fractions (normally three or more) by XRD analyses and the K-Ar age for each grain-size fraction. The obtained percentages of illite polytypes are normalized to 100 % and the $2M_1$ illite content is plotted against the K-Ar age. The end-member ages for a hypothetical 0 % and 100 % $2M_1$ composition are calculated by linear extrapolation.

According to Pevear (1992) and Grathoff and Moore (1996) the extrapolated 'detrital' illite (100 % $2M_1$ illite) age represents the inherited muscovite component in the sediment. The 'diagenetic' age (0 % $2M_1$ illite) is interpreted as an integrated age for the time interval in which illite grew. The latter could be an instantaneous event like contact metamorphism (e.g. Aronson and Lee 1986), a hydrothermal event (e.g. Lonker and Fitz Gerald 1990) or a burial event (e.g. Grathoff and Moore 1996). Previous studies which dated fault-gouge illite from a sedimentary environment has encountered several difficulties. While the extrapolated age of the authigenic component (0 % $2M_1$ illite) could be related to the age of the gouge-developing faulting event, the extrapolated age of the detrital component was difficult to interpret in a geological way, because frequently the illite age varies considerably from the depositional age of the host rock.

Anyway, in contrast to such a sedimentary environment, the here presented illite data originates from fault gouges which developed under retrograde conditions from high-grade metamorphic and igneous host rocks. Thus, development of $2M_1$ illite polytypes in a brittle fault gouge is possible due to the subsequent cooling of the host rock and its passage through epizonal conditions contemporaneously to faulting and retrograde metamorphism. In contrast to a sedimentary environment, the extrapolated 100 % $2M_1$ illite age must not be excluded from consideration in terms of a geological event but can be considered to record the onset of brittle deformation (Bense et al. in review A).

Thus, based on the issues discussed above, we interpret the extrapolated 100 % $2M_1$ illite age to represent the onset of brittle deformation, while the 100% $1M_d$ age represents the last illite formation event (see below).

In this study, one of the main problems in polytype quantification was the abundance of smectite as well as kaolinite. Especially XRD reflections from smectite show overlap with illite polytype specific reflections (e.g. Grathoff and Moore 1996). Especially the $1M_d$ illite content might be overestimated in case of superposition of smectite reflections on illite peaks. Polytype composition could be

quantified (Table 6.1) but must be considered as rough estimations due to the partially considerable smectite content (as revealed by CEC). Nevertheless, polytype quantification is in very good agreement with other parameters such as grain-size age, illite crystallinity and K-Ar age indicating consistency of the dataset (see Table 6.1). As a consequence to errors involved in polytype quantification, extrapolation to the polytype end-member ages (100 % $2M_1$ and 0 % $2M_1$) is subjected by the same error sources. However, extrapolated end-member ages are reported here (Table 6.1) and discussed in terms of reliability, e.g. by comparison to K-Ar muscovite cooling ages (see below), but excluded from essential interpretation.

6.5.6 Age Constraints on Brittle Deformation in the Sierras Pampeanas

Nogolí

K-Ar illite ages are between 336 Ma (Early Carboniferous) and 144 Ma (Early Cretaceous), comprising a time span of 192 Ma (Table 6.1).

$2M_1$ polytype content is low in comparison to samples from other regions. Illite content is 25 % to 80 % in the 2-6 μm fraction, around 40 % in the <2 μm fraction and <10 % in the <0.2 μm fraction. Generally, the $2M_1$ illite content decreases with decreasing grain-size and correlates well with the IC values (Table 6.1). Extrapolated 100 % $2M_1$ ages are around 340 Ma - 280 Ma and 230 Ma (Table 6.1). One extrapolation gives a 100% $2M_1$ age of 732 Ma which is erroneous. Extrapolation error is attributed to the similar polytype composition of the grain-size fraction (as discussed above; see Table 6.1). If contamination of the analysed grain-size fraction by host-rock muscovite would have taken place, extrapolated ages would be in the range of the K-Ar and Ar/Ar muscovite cooling ages from host rock. Muscovite cooling ages taken from several mylonitic shear zones in this region yield ages in the range of 360 - 350 Ma (Fig. 6.10, Sims et al. 1998; Steenken et al. 2008), whereas muscovite from non-deformed host rock give muscovite cooling ages of 400 Ma to 380 Ma (Steenken et al. 2008). The former ages must be interpreted as the last mylonitisation event before the cooling of the basement below ductile deformation temperatures. This interpretation is supported by K-Ar ages taken from biotite by Steenken et al. (2008), documenting the cooling of the basement to temperature in the range of the brittle/ductile transition (>300°C, e.g. Passchier and Trouw 2005) during the Early Carboniferous (Fig. 6.10). Thus it can be concluded that the range in K-Ar illite ages of 192 Ma document a long lasting brittle faulting history, which started directly after cooling to brittle deformation temperatures.

Taking into account available (U-Th)/He ages from apatite and zircon as well as apatite fission track data from the region (Bense et al. in review A), the illite evolution can be further constrained. Zircon helium ages (Bense et al. in review A) show a wide range of ages due to slow cooling and a resulting long lasting passage through partial retention zone (PRZ) conditions, which certainly have led to variation in ages due to thermal diffusion of helium. Nevertheless, mean zircon helium ages show a

range of approximately 350 Ma to 228 Ma (Fig. 6.10) representing cooling below an effective closure temperature (T_c) of approx. 175°C to 140°C (e.g. Reiners and Brandon 2006). Thus before 228 Ma parts of the basement were at temperature conditions $> T_c$ of the zircon helium system which are sufficient for the development of $2M_1$ illite.

Although the youngest K-Ar illite age from the Nogolí transect yield 143 Ma (Table 6.1), this age cannot be considered as cessation of faulting activity. In fact, the area around Nogolí give evidence for recent, neotectonic compressional activity along clay gouge bearing faults by showing Precambrian rocks thrust above Tertiary to Quaternary deposits. This visible evidence of younger fault activity cannot be seen within the K-Ar fault gouge data. Instead, youngest K-Ar ages has to be considered to represent the last illite forming event and thus cooling below illite forming temperatures which lie approximately between 110°C - 75°C (e.g. Hamilton et al. 1992).

This interpretation is constrained by apatite fission track (AFT) and apatite (U-Th)/He (AHe) ages (Bense et al. in review A). Although effected by partial annealing (PAZ) and partial retention (PRZ), apatite fission track ages (representing cooling below PAZ-temperatures of approx. 110°C - 75°C) should overlap with K-Ar ages of illite formed at temperature of 110°C - 75°C (minimum illite formation temperature) whereas the youngest apatite helium ages (representing cooling below PRZ-temperatures of approx.. 90°C - 50°C) should be younger than the K-Ar illite ages. This can be observed for all analysed samples (Fig. 6.10, see also Bense et al. in review A).

Potrero de Los Funes and El Volcán

The Potrero de Los Funes transect represents the second profile across the Sierra de San Luis with continuous exposures from the western to the eastern side, lying approximately 25 km south of the Nogolí transect.

K-Ar illite ages range from 332 Ma (Early Carboniferous) to 107 Ma (Middle Cretaceous), with a range of 194 Ma (Table 6.1). $2M_1$ polytype content is variable throughout the analysed samples, ranging from 100 % - 35 % in the 2-6 μ m fractions. Smaller fractions show contents of 60 % to 17 % ($< 2 \mu$ m) and 42 % to 0% ($< 0.2 \mu$ m). Generally, the $2M_1$ illite content decreases with decreasing grain-size and show good correlation with IC values. Extrapolated 100 % $2M_1$ ages give ages around 390 Ma, 290 Ma - 240 Ma and 170 Ma (Table 6.1). One extrapolation gives a 100% $2M_1$ age of 507 Ma which is considered incorrect. Extrapolation error is attributed to the small amount of $2M_1$ illite polytype content in this sample (see Chapter 4). Extrapolated 100% $1M_d$ ages vary from 67 Ma to 175 Ma (Table 6.1).

As in the Nogolí transect, the comparison of K-Ar illite ages with muscovite and biotite K-Ar cooling ages from the vicinity around Potrero document a good compliance of K-Ar ages in regards to the end of mylonitic deformation, regional cooling and the onset of brittle deformation (Fig. 6.10; see also Nogolí discussion). No low temperature thermochronological data is available for the Potrero de

los Funes transect. Due to the close vicinity of the two transects we compared the K-Ar illite ages from Potrero with low temperature thermochronological data from the Nogolí transect (Bense et al. in review A). As with the illite ages from Nogolí, the Potrero gouge data overlap with ZHe and AFT ages, whereas AHe ages overlap (within error) or show younger ages than the K-Ar illite dating (Fig. 6.10). Thus, based on extrapolated 100 % $1M_d$ ages, cooling of the basement below illite forming temperatures in the Potrero region can be estimated at about 100 Ma - 67 Ma (Table 6.1). By comparing the minimum and maximum fine-fraction ages from Nogolí and Potrero, as well the extrapolated 100% $1M_d$ ages, it become apparent that samples from the Potrero transect are consistently 40-30 Ma younger than ages obtained along the Nogolí transect. Nonetheless both regions show the same time span of (illite forming) fault activity of about 190 Ma.

Los Tunels

The Los Tuneles transect in the Sierra de Pocho represents the northernmost transect in the Sierras de Córdoba (Figs. 6.1 and 6.2).

K-Ar illite fine-fraction ages vary from 382 Ma (Late Devonian) to 226 Ma (Late Triassic), with a range of 156 Ma (Table 6.1).

$2M_1$ illite content decreases with decreasing grain-size. Contents are 64 % for the 2-6 μm fraction, 37 % and 17 % in the <2 μm fractions and 31 % and 0 % in the <0.2 μm fractions. Polytype composition shows a good correlation with obtained IC-values. Extrapolated 100 % $2M_1$ ages give ages of 537 Ma and 439 Ma. The 537 Ma age is erroneously high which is attribute to the similar polytype composition of the smaller grain-size fractions (Table 6.1) multiplying the error of age extrapolation.

Muscovite and biotite K-Ar cooling ages from the direct surroundings of the fault-gouge samples show ages of 433-430 Ma. These ages are interpreted to date the latest phase of mylonitisation in this region (Steenken et al. 2010). This interpretations is confirmed by K-Ar muscovite fine-fractions ages from non-faulted rocks (La Mermela succession), yielding ages of 440 and 419 Ma for fractions <2 μm (Steenken et al. 2010). The latter indicates that deformation became more heterogeneous distributed at lower temperatures . K-Ar dating on muscovite from non-deformed host rock gives ages of 486 Ma and 484 Ma (Steenken et al. 2010). Thus the 100 % $2M_1$ age of 439 Ma is likely to represent the first illite development due to brittle faulting during the transition of ductile to brittle deformation.

According to low-temperature thermochronological data of the Los Tuneles region from Bense et al. (in review B), mean ZHe ages show a range from 327 Ma to 280 Ma (Fig. 6.11). Ages show that parts of the basement were at temperature conditions of 175°C to 140°C during this time, overlapping with the 2M₁ illite stability field and are, thus, in total accordance with illite fine-fraction ages and illite polytype composition. A further constraint to the illite age interpretation can be set by AFT and AHe ages from Bense et al. (in review B). AFT ages overlap with illite ages, while apatite He ages, ranging from 217 Ma to 174 Ma, are younger than the K-Ar illite ages (Fig. 6.11). As the ZHe data show, these ages align perfectly with the interpretation of K-Ar illite ages.

The end of illite-forming fault activity is not well defined by the 100 % 1M_d ages (Table 6.1) but, in accordance with AHe ages, it is likely to have occurred between the youngest AHe age (174 Ma) and the youngest K-Ar illite age (246 Ma).

Merlo

The Merlo transect in the Sierra de Comechingones represents the southern profile in the Sierra de Córdoba (Figs. 6.1 and 6.2).

K-Ar dating of illite fine fractions comprise ages from 342 Ma (Early Carboniferous) to 174 Ma (Middle Jurassic), with a range of 168 Ma (Table 6.1). 2M₁ illite content vary from 100 % to 31 % in the 2-6 µm fraction, 65 % to 21 % and 35 % to 0 % in the <2 µm and <0.2 µm fractions respectively. The decrease in grain-size correlates with 2M₁ content IC-values (Table 6.1). Extrapolated 100 % 2M₁ illite ages give 302 Ma – 257 Ma. Two 100 % 2M₁ ages of 788 Ma and 449 Ma were neglected from consideration because of high extrapolation errors due to similar polytype composition throughout analysed grain-size fractions (Table 6.1).

K-Ar muscovite-booklet cooling ages (T_c approx. 430-500°C; Kirschner et al. 1996, Villa 1998) from the non-deformed basement rocks in the Merlo area ages of 498 Ma and 474 Ma are reported (Steenken et al. 2010). For the basement effected by the ductile Guacha Corral shear zone Steenken et al. (2009) obtained two groups of K-Ar muscovite ages. An older group, taken from muscovite booklets, show Early Ordovician ages of 487 Ma and 486 Ma. These are interpreted to coincide with Early Ordovician shearing. The second group comprise ages taken from smaller muscovite grains of the same mylonitic rock, which yield early Silurian K-Ar ages of 440 Ma and 438 Ma. These ages are interpreted to represent an Early Silurian reactivation of the shear zone. Younger ages of 435 to 430 Ma ages are considered to post-date the last mylonitisation phase which is assigned to the late Famatinian cycle, i.e. the Ocloyic phase resulting from the final docking of the Cuyania terrane (Steenken et al. 2010). This interpretation is constrained by K-Ar biotite ages between 426 Ma and 420 Ma (Late Silurian; Steenken et al. 2010) from non-mylonitic metamorphic basement of the southern Sierra de Comechingones which document cooling of the basement to temperatures of approx. 300°C. The considerable older K-Ar muscovite ages as well as the proven cooling of the

basement to brittle deformation temperatures at Silurian times support our interpretation of the 100 % $2M_1$ (Table 6.1) to represent the oldest illite formation event due to brittle faulting.

Low temperature thermochronological data of Löbens et al. (2011) from the Yacanto area (approx. 30 km north of Merlo; see Fig. 6.1) as well as AHe data from the Merlo area (Bense et al., in review B) also support our interpretation. ZHe ages ranging between 264 Ma and 199 Ma as well as AFT ages (Löbens et al. 2011) overlap with the K-Ar illite ages. Ages from the AHe system, ranging from 120 Ma to 57 Ma for the Yacanto area and 86 Ma to 40 Ma in Merlo are invariably younger than obtained K-Ar illite ages (Fig. 6.10). This demonstrates the consistency of the dataset. Ages of the 100 % $1M_d$ fraction between 233 Ma and 116 Ma (Table 6.1), interpreted to mark the end of illite forming fault activity by cooling below 110 °C - 75 °C are also consistent with available AHe data.

Sierra de los Gigantes

The K-Ar illite ages from the Sierra de Los Gigantes range from 341 Ma (Early Carboniferous) to 281 Ma (Early Permian). Ages from the fractions $<2 \mu\text{m}$ and $<0.2 \mu\text{m}$ are oldest ages for those grain-sizes measured in this study (Table 6.1). The $2M_1$ illite content vary between 100 % (2-6 μm fraction) to 53 % ($<0.2 \mu\text{m}$ fraction), correlating with age and IC-values. Extrapolation to 100 % $2M_1$ and 0% $2M_1$ illite content give ages of 342 Ma and 281 Ma respectively. Preliminary low temperature thermochronological data from the Sierra de Los Gigantes (Bense et al., in review B) yield mean ZHe ages of 293 Ma - 250 Ma and mean AHe ages of 59 Ma - 21 Ma. Ages only overlap for the ZHe and K-Ar illite systems (Fig. 6.10), but are in good agreement considering the high amount of $2M_1$ illite in the different grain-size fractions (see chapter 4). Although high temperature cooling ages from K-Ar biotite and muscovite dating is missing, the data indicate onset of brittle deformation considerably earlier than in the more eastern areas (see Bense et al. in review B).

San Martin

K-Ar illite ages from this location vary from 275 Ma (Early Permian) to 167 Ma (Middle Jurassic). $2M_1$ illite content in grain-size fraction range from 90 % (2-6 μm) to 21 % ($<0.2 \mu\text{m}$) and correlate with IC-values and age. Extrapolated illite ages give 283 Ma for the 100% $2M_1$ fraction and 137 Ma for the 100 % $1M_d$ fraction, overlapping mostly with ages from the Nogolí transect. In the vicinity of San Martin only two K-Ar muscovite-booklet ages from pegmatites are available, yielding ages of 438 and 422 Ma (Steenken et al. 2008). These ages clearly predate the illite, indicating a non-contaminated system.

Achala

We took two samples from the Achala area, which yield ages between 294 Ma (Early Permian) and 251 Ma (Early Triassic). Fine fraction ages are comparatively close together, giving a range of only 45 Ma. This is attributed to a cogenetic evolution of both faults, resulting in similar polytype composition and age (Table 6.1). Illite age extrapolation gives unreasonable ages for the 100 % $2M_1$

due to extrapolation errors resulting in the similar polytype concentration throughout grain-size fractions. No thermochronological data is available from the close vicinity of the samples, but illite ages are in the range of ages obtained for the Merlo profile, thus can be considered reasonable. K-Ar fault gouge ages from the Achala granite in the Pampa de Achala area overlap with ages from Los Tuneles and Merlo. However, these younger ages might be in relation to the Devonian emplacement of the Achala batholith (e.g. Demange et al. 1996).

6.5.7 Implications on Regional Cooling, Deformation History and Tectonic Significance

Obtained K-Ar illite ages for the Sierra de Córdoba suggest that brittle deformation started in the northern part of the Sierra (Los Tuneles) at around 380 Ma. With time, deformation propagated further south, reaching the Merlo area at ca. 342 Ma (Fig. 6.10). The same trend of southward advancing cooling in the Sierra de Córdoba is clearly expressed by high temperature cooling data reported by Steenken et al. (2009), confirming our data. Additionally, this implicate that cooling rate does not changed dramatically during the time span recorded by both methods.

In accordance to the observation that brittle deformation started 41 Ma earlier in the Sierra de Pocho than in the Sierra de Comechingones, the cooling below illite forming temperatures took place about 50 Ma later in the Sierra de Comechingones (Fig. 6.10; Table 6.1). The similarity in these differences might be indicative for a uniform cooling in the Sierra de Córdoba, propagating from north to south. The observation of a south propagating cooling is also supported by low temperature thermochronological data from the Sierra de Pocho (Löbens et al. in review) and Sierra de Comechingones (Löbens et al. 2011) documenting a similar situation on basis of zircon and apatite helium data (Bense et al. in review B). However, no clear conclusion can be drawn concerning an east-west propagation of cooling.

As in the Sierra de Córdoba, a clear north-south variation in the onset of brittle deformation is developed in the Sierra de San Luis. In the Nogolí area, brittle deformation started at around 336 Ma (Table 6.1), about 35 Ma earlier than in the Potrero de Los Funes area. Illite crystallisation lasted about 37 Ma longer than in Nogolí. As in the Sierra de Córdoba, the similarities in time difference between onset and cessation of illite formation is indicative for a uniform cooling.

On basis of K-Ar cooling ages from hornblende and micas (Varela et al. 1994, Sims et al. 1998, González and Sato 2000, Sosa et al. 2002, Steenken et al. 2004, 2008) it was suggested that high temperature cooling commenced in the western part of the Sierra de San Luis (Nogolí Metamorphic Complex; Fig. 6.1) from where it migrated to the east Steenken et al. (2008). However, differences in ages from west to east are only small, wherefore this trend is not developed explicitly.

In contrast our data suggest west-advancing cooling of the basement. At best this can be seen in the Potrero de los Funes area where K-Ar illite ages becomes subsequently older towards the east (El

Volcán area; Fig. 6.1). In the Nogolí dataset, this trend is not as clear because samples locations show a much wider range in elevation, which requires to evaluate ages also in terms of cooling due to elevation differences between samples.

Because data from the Valle de Conlara area is sparse due to lacking outcrops, our data does not shed light on cooling differences between the Sierra de Córdoba and Sierra de San Luis. Thus, our data does not give much information on any longitudinal differences in cooling history or a coupled exhumation of the Sierras. Nevertheless, it is clear that any E-W difference in cooling is not as strong developed as in N-S directions, especially when taking into account available low-temperature thermochronological data (see Fig. 6.10; Bense et al. in press, Bense et al. in review B)

K-Ar illite fault gouge ages obtained by this study cover a huge time span, ranging from Devonian to Cretaceous times (Table 6.1). Evidently, due to the documented long lasting fault activity, the analysed faults were affected by numerous tectonic events. Especially ages >320 Ma are synchronous with a period of intra-Carboniferous compressional tectonism, e.g. the Chanic phase of the Famatinian Orogeny (e.g. Martino 2003) or the Achalian orogeny (e.g. Sims et al. 1998). In contrast, Wemmer et al. (2011) report K-Ar ages from epimetamorphic illites of the San Luis Formation between 330 Ma - 290 Ma which they attribute to the Toco orogeny, which is defined by Bahlburg and Breitzkreuz (1991) for NW-Argentina and N Chile. The tectonic of this Upper Mississippian event is poorly understood. A relationship to the accretion of a terrane has been proposed (Ramos et al. 1986; Gohrband 1992; Davis et al. 1999; Ramos 2001), but this contradicts the hypothesis of an Early Devonian docking of the Chilenia terrane (Achalian orogenic cycle) to the southwestern margin of Gondwana (Sims et al. 1998; Siegesmund et al. 2004).

However, because of the limited extend of the Toco Orogeny and its location far away from the study area, we think that those ages could also be better related to the end of Famatinian (Chanic) or Achalian orogeny.

Anyway, this Carboniferous time period can be considered to document the end of ductile deformation in this region (Bense et al. in review A).

Löbens et al. (2011) and Bense et al. (in review A) report that the low-temperature cooling and exhumation of the Sierra de Córdoba and Sierra de San Luis started during Permian to Permian-Triassic times. Because basement already cooled to temperatures <300°C during Carboniferous times, exhumation is accompanied by brittle deformation, represented by Permian-Triassic K-Ar ages found by this study. The exhumation and cooling in this part of the Sierras Pampeanas is synchronous with an orogenic phase defined as the San Rafael orogeny in the San Rafael Massif (Mendoza province; Kleiman and Japas 2009). Additionally, Permian ages are contemporaneous to a flat-slab subduction episode of the Farallon plate beneath the South American plate, interpreted to cause subsequent compression at these latitudes during the Early-Middle Permian (Ramos and Folguera 2009). In

addition, this time interval was a period of important magmatic expansion related to the San Rafael phase which also was linked to the San Rafael orogeny (Kleiman and Japas 2009). However, a direct link between this orogenic phase and the structural evolution of the study area has not been developed yet, but the coeval timing and the relative proximity of the proposed key area of San Rafael orogeny suggest an imprint in the studied region (Bense et al. in review A). Also differences in fault orientation between the Sierra de San Luis and Sierra de Córdoba favour the idea of a different tectonic imprint in both Sierras (see above).

Additionally, a Late Triassic – Early Jurassic as well as an Early Cretaceous extensional phase affected the studied region by extensional reactivation of older structures (e.g. Ramos et al. 2002). The latter event, which comprise an important period of normal faulting in the Eastern Sierras Pampeanas, is contemporaneous with the youngest measured K-Ar illite ages (Fig. 6.10), marking the end of illite formation in fault gouges. Low-temperature thermochronological data support this, by indicating that wide regions of the study area were already cooled to temperatures prohibiting illite formation (see also Bense et al. in review A).

One of the youngest tectonics events affecting the studied region is the flattening of the Nazca plate subduction angle due to the incorporation of the Juan Fernandez ridge into the subduction process (e.g. Pilger 1981, 1984, Von Huene et al. 1997). The ridge collision and accompanied flat-slab subduction starting at about 18 Ma Yañez et al. (2001) and is considered to have produced significant deformation and uplift in the Sierras Pampeanas (Ramos et al. 2002). Any imprint of this event in this region, is not recorded by our K-Ar illite fault gouge ages. However, this is only attributed to the end of illite formation along fault zones due to basement cooling below illite formation temperatures. Although there is evidence that this subduction related event affecting the studied region, e.g. by the eastward propagation of volcanic activity along the San Luis volcanic belt (e.g. Kay et al. 1991), or neotectonic thrusting (e.g. Schlagintweit 1954, Lencinas and Timonieri 1968, Massabie 1976, Massabie and Szlafsztajn 1991, Costa and Cortés 1993, Kraemer et al. 1993, Costa et al. 2001, see also Fig. 6.4) and recent seismicity (Richardson et al. 2012) new thermochronological data (Löbens et al. 2011, Bense et al. in review A, Bense et al. in review B, Löbens et al. in review) indicate that this event might have had only less significance for the eastern Sierras Pampeanas in terms of exhumation and low-temperature cooling (see also Bense et al. in review A).

6.6 Conclusions

Concerning fault-gouge analyses, the following methodological conclusions can be drawn:

- Illite age extrapolation can give valuable information for evaluating the obtained fine-fraction ages in terms of possible contamination with older muscovite phases. However, the extrapolation is often effected by numerous error sources, complicating the extrapolation.

-
- On the basis of data discussed, we could show that the interpretation of illite polytypism used here is geologically meaningful. Thus, illite from clay gouges of a non-sedimentary environment can be interpreted in terms of a subsequent development of 2M₁, 1M and 1M_d polytype during successive regional cooling. High- and low-temperature thermochronological data prove that conditions are sufficient for the development of the 2M₁ illite polytype within a fault gouge. This is especially true for regions affected by long-lasting brittle deformation and/or in slowly cooling regimes.
 - The method presented here of detailed interpretation of K-Ar illite fine-fraction ages of fault gouges from non-sedimentary host rocks by cross-evaluation of K-Ar illite ages with different, independent parameters (e.g. illite crystallinity, illite polytype quantification, grain size), mineralogical observations, K-Ar muscovite and biotite host-rock cooling ages and low-temperature thermochronological data (AFT, AHe, ZHe) can provide a powerful tool for evaluating the cooling and deformation history of a region. A combination of data sets derived from the aforementioned methods allows the user a cross-correlation and evaluation of the data set's integrity, greatly enhancing the reliability of the data. In combination with paleostress analyses, this method can become even more meaningful for the evaluation of complex geodynamic histories.
 - Apart from the deformation history, the tectonic significance of fault-gouge data strongly depends on the cooling history. In a rapidly-cooled region, K-Ar illite ages from fault gouges can be of great value when interpreting the timing of different deformation events. In contrast, in a slowly-cooled regime, interpretation of ages in terms of single deformation events is impossible. The Sierras Pampeanas encountered a long-lasting brittle-fault history with multiple deformation events under different tectonic regimes. For instance, multiple changes in stress regime (from extension and normal faulting to compression and thrusting), accompanied by reactivation of older structures in combination with a slow regional cooling and exhumation, detract the value of illite ages as a source for structural information. In contrast, the information which can be concluded in terms of the cooling history becomes more important than ever.

Based on the data presented here, the following regional conclusions can be drawn:

- The K-Ar illite fine-fraction ages provided by clay gouge document the onset of brittle deformation in the Eastern Sierras Pampeanas in Carboniferous times, directly after the cooling of the basement to temperatures of about 300°C. The oldest ages coincide with the basement cooling to brittle-deformation temperatures and are in perfect alignment with available high- and low-temperature thermochronological data, predating a distinct Permian-to-Permotriassic exhumation event. Younger illite ages cover the time span of low-temperature cooling and exhumation history as revealed by AHe, ZHe and AFT ages from the literature. The youngest illite ages represent the basement cooling below illite-formation temperatures as constrained by AHe ages, but not the end of brittle deformation.
- The pattern of obtained K-Ar ages, which document a long-lasting brittle fault activity, can be split in four different episodes. We relate ages >320 Ma to the end of the Famatinian Orogeny. Our data show that this event represents the ductile/brittle transition in this region. Early and Middle Permian ages can be related to a flat-slab subduction episode of the Farallon plate beneath the South American plate. Middle to Late Permian until Triassic ages correlate with a major extensional events, while Jurassic to Early Cretaceous ages are contemporaneous to a period of substantial normal faulting in the studied region.
- Data reveal a strong north-south variation in ages, indicating distinct southward propagation of cooling in the Sierra de Córdoba and Sierra de San Luis. Additionally, an eastward propagation of cooling is evident in the Sierra de San Luis.
- Differences in K-Ar ages indicate a partly different cooling history in the Sierra de San Luis compared to the Sierra de Córdoba. Those observations are in accordance with indications derived from low-temperature thermochronological modeling. A link to any tectonic event in this region cannot be established on the basis of the available data, but observations are indicative of a tectonic event only affecting the Sierra de San Luis, e.g. shown by structural observations of a strong east-west striking fault system in the Sierra de San Luis which is lacking in the Sierra de Córdoba.

Table 6.1: K-Ar ages, illite crystallinity and illite polytypism of the investigated mineral fractions

Location	Sample	Grain fraction [μm]	K-Ar Data					Illite crystallinity			Illite polytypism			Mineralogy								
			K2O [wt%]	40Ar* [nl/g] STP	40Ar* [%]	Age [Ma]	2σ [Ma]	air dry [Δ°2θ]	glycolated [Δ°2θ]	group	2M ₁ , 1M, 1M _d	extrapolated age		I	Q	C	K	S	K-Fsp	P	other	group
												100% 1M _d	100% 2M ₁									
Nogolí	1-08	2-6 μm						D - 0,523			no polytype analysis performed			+	+	-	+		o	-	-	IK
		< 2 μm	3,84	38,92	96,36	289,7	3,4	D - 0,544	D - 0,497	4		-	-	+	o	-	+		-	-	-	
		< 0.2 μm	4,29	41,18	93,64	275,5	3,3	D - 0,491	D - 0,457					+	-	-	+		-	-	-	
	2-08	2-6 μm						A - 0,396			no polytype analysis performed			+	+	-	-		-	o	-	I
		< 2 μm	7,22	85,90	97,39	335,7	7,0	A - 0,299	E - 0,244	2		-	-	+	o/-	-	-		-	o/-	-	
		< 0.2 μm	6,75	77,94	97,39	326,6	3,9	E - 0,201	A - 0,317					+	o/-	-	-	+	-	-	-	
	34-09	2-6 μm	1,33	9,48	66,06	231,1	6,7	E - 0,205	E - 0,198	3	43%, 0%, 57%			+	++	+	-	o/-	+	-	-	ICS
		< 2 μm	1,95	13,01	81,52	195,9	5,7	A - 0,337	A - 0,348		38%, 0%, 62%	206	226	+	o	++	-	+	o	-	-	
		< 0.2 μm	2,80	22,26	94,12	208,4	3,5	D - 0,431	A - 0,311		0%, 0%, 100%			+	-	+	-	+	-	-	-	
	50-09 ³	2-6 μm	4,21	46,80	92,61	315,4	7,0	E - 0,158	E - 0,162	1	79%, 5%, 15%			o	-	-	-	+	-	-	H o/-	IS
		< 2 μm	2,48	24,04	92,18	278,0	9,5	E - 0,206	E - 0,223		45%, 5%, 49%	201	385	+	-	-	-	+	-	-	H o/-	
		< 0.2 μm	1,26	9,60	82,58	222,0	6,0	A - 0,316	E - 0,226		9%, 7%, 84%			+	-	-	-	+	-	-	H o/-	
	51-09 ³	2-6 μm	3,12	30,07	97,16	276,5	6,1	A - 0,338	A - 0,312	4	no polytype analysis performed			+	+	-	+	-	o/-	-	-	IK
		< 2 μm	2,70	21,02	91,47	226,5	5,0	D - 0,496	D - 0,425			-	-	+	o	-	+	o	-	-	-	
		< 0.2 μm	1,77	10,74	80,34	178,9	4,9	D - 0,748	D - 0,565					+	-	-	+	+	-	-	-	
	59-09 ³	2-6 μm	6,17	66,98	97,27	308,7	6,5	E - 0,173	A - 0,256	4	25%, 5%, 70%			+	o/-	-	+	-	o/-	-	-	IK
		< 2 μm	4,76	36,60	94,43	223,9	5,1	D - 0,655	D - 0,427		7%, 5%, 88%	164	(732)	+	o/-	-	+	o/-	-	-	-	
		< 0.2 μm	4,56	31,96	94,05	205,2	4,9	D - 0,651	D - 0,579		3%, 4%, 93%			+	-	-	+	o/-	-	-	-	
	60-09 ³	2-6 μm	5,30	49,55	97,70	268,8	5,5	E - 0,218	E - 0,195	2	53%, 4%, 43%			+	o/-	-	-	o/-	o/-	-	H o/-	IS
		< 2 μm	3,80	29,63	93,11	226,9	7,0	A - 0,292	A - 0,276		46%, 4%, 49%	138	343	+	-	-	-	+	-	-	H o/-	
		< 0.2 μm	2,77	16,81	86,00	179,0	4,2	A - 0,275	A - 0,294		20%, 4%, 76%			+	-	-	-	+	-	-	H o/-	
	65-09	2-6 μm	2,16	13,82	86,60	290,9	4,8	A - 0,257	E - 0,239	3	62%, 0%, 38%			+	+	-	-	+	o	-	-	IS
		< 2 μm	3,08	27,68	84,79	259,1	7	A - 0,381	A - 0,382		40%, 0%, 60%	189	356	+	-	-	o/-	+	-	-	-	
		< 0.2 μm	3,72	37,87	96,81	188,2	4,4	D - 0,442	D - 0,519		0%, 0%, 100%			+	-	-	o/-	+	-	-	-	
	77-09	2-6 μm	0,66	3,18	66,32	194,1	4,6	D - 0,437	E - 0,322	4	no polytype analysis performed			o	o	-	-	+	-	-	-	S
		< 2 μm	0,84	5,07	70,95	177,9	4,9	D - 0,517	D - 0,665			-	-	o	-	-	-	+	-	-	-	
		< 0.2 μm	1,47	9,71	85,29	143,5	6,1	D - 0,452	D - 0,478					o	-	-	-	+	-	-	-	

Location	Sample	Grain fraction [μm]	K-Ar Data					Illite crystallinity			Illite polytypism			Mineralogy								
			K2O [wt%]	40Ar* [nl/g] STP	40Ar* [%]	Age [Ma]	2σ [Ma]	air dry [Δ°2θ]	glycolated [Δ°2θ]	group	2M ₁ , 1M, 1M _d	extrapolated age		I	Q	C	K	S	K-Fsp	P	other	group
												100% 1M _d	100% 2M ₁									
Potrero	29-09	2-6 μm	4,19	26,27	84,83	300,7	4,8	A - 0,268	A - 0,251		35%, 0%, 65%			+	++	-	+	-	o	-	-	IKS
		< 2 μm	4,02	30,17	88,90	215,9	6,0	A - 0,383	A - 0,348	3	17%, 6%, 76%	175	(507)	+	+	-	+	+	-	-	-	
		< 0.2 μm	2,71	28,60	94,79	184,6	4,6	D - 0,920	D - 0,546		0%, 0%, 100%			+	o	-	+	+	-	-	-	
	30-09	2-6 μm	3,11	18,53	80,10	263,0	4,8	E - 0,238			59%, 0%, 41%			+	+	o/-	+	-	o	-	-	IKS
		< 2 μm	3,69	24,02	83,02	191,3	6,1	D - 0,439	A - 0,268	4	43%, 0%, 57%	67	390	+	+	o/-	+	+	-	-	-	
		< 0.2 μm	4,56	41,65	95,33	175,8	4,0	D - 0,799	D - 0,475		31%, 0%, 69%			+	o	o/-	+	+	-	-	-	
	103-09	2-6 μm	4,89	43,30	93,24	332,3	6,2	E - 0,214	E - 0,199		64%, 0%, 36%			+	o	-	o/-	o	-	o	-	I
		< 2 μm	7,02	77,50	97,50	313,5	7,3	A - 0,271	A - 0,274	2	49%, 0%, 51%	254	376	+	-	-	o/-	o	-	o/-	-	
		< 0.2 μm	8,41	98,95	99,00	255,6	7,6	A - 0,385	A - 0,401		-			+	-	-	o/-	+	-	-	-	
	104-09	2-6 μm	5,73	48,92	93,41	293,5	5,9	E - 0,230	E - 0,214		52%, 0%, 48%			+	+	-	+	o	o	-	-	IK
		< 2 μm	6,49	66,57	96,56	292,9	6,9	A - 0,278	A - 0,272	2	48%, 0%, 52%	548	(593)	+	o	-	+	o	-	-	-	
		< 0.2 μm	3,67	37,72	97,74	247,0	6,8	A - 0,381	A - 0,399		48%, 4%, 48%			+	o	-	+	+	-	-	-	
	106-09	2-6 μm	3,73	19,44	87,71	262,6	3,9	A - 0,405	A - 0,392		59%, 7%, 34%			o	+	-	+	o	o	o	-	IK
		< 2 μm	-	-	-	-	-	A - 0,393	A - 0,374	3	49%, 0%, 51%	96	385								-	
		< 0.2 μm	5,47	49,86	95,28	154,8	6,2	D - 0,432	D - 0,430		23%, 0%, 77%			+	-	-	+	o	-	-	-	
	107-09	2-6 μm	4,78	22,96	83,75		3,8	-	E - 0,184		63%, 0%, 37%			o	+	-	o	-	-	o	-	IK
		< 2 μm	5,26	30,07	88,34	169,1	4,3	D - 0,471	D - 0,498	4	22%, 0%, 78%	169	169					o			-	
		< 0.2 μm	-	-	-	143,1	-	D - 0,586	D - 0,484		-			+	-	-	+	o	-	-	-	
	108-09	2-6 μm	5,32	26,49	89,01	213,7	3,7	A - 0,335	A - 0,363		84%, 9%, 8%			o	+	-	-	o	o	+	-	IK
		< 2 μm	5,63	33,13	92,03	173,8	4,2	D - 0,480	D - 0,478	4	60%, 6%, 34%	91	239								-	
		< 0.2 μm	5,47	40,01	96,65	148,2	5,0	D - 0,488	D - 0,447		42%, 0%, 58%			+	-	-	-	o/-	-	-	-	
	109-09	2-6 μm	5,62	33,01	92,47	237,7	4,2	A - 0,294	A - 0,288		84%, 0%, 16%			o	+	-	+	-	+	o	-	IK
		< 2 μm	6,04	-	60,86	127,8	4,4	D - 0,501	D - 0,476	4	40%, 7%, 53%	143	232	+	o	-	+	-	o/-	-	-	
		< 0.2 μm	5,84	47,85	98,61	173,5	5,5	D - 0,564	D - 0,547		7%, 0%, 93%			+	o/-	-	+	-	-	-	-	
	110-09	2-6 μm	6,10	21,59	83,90	205,3	2,8	A - 0,419	A - 0,397		54%, 0%, 46%			o	+	-	o	o/-	o/-	o	-	IK
		< 2 μm	6,23	30,65	89,84	146,5	3,6	D - 0,569	D - 0,556	4	22%, 0%, 78%	106	288	+	o/-	-	+	o/-	-	-	-	
		< 0.2 μm	7,46	52,31	96,78	106,5	4,8	D - 0,774	D - 0,747		0%, 0%, 100%			++	-	-	+	-	-	-	-	
	112-09	2-6 μm	2,90	12,35	78,51	193,7	3,5	A - 0,255	A - 0,331		100%, 0%, 0%			o	o	-	+	+	o	o	-	IKS
		< 2 μm	3,50	17,93	87,56	152,2	3,9	D - 1,288	A - 0,327	4	47%, 0%, 53%	125	192	+	-	-	+	+	-	-	-	
		< 0.2 μm	6,47	42,67	98,17	127,4	4,5	D - 1,433	D - 1,695		0%, 0%, 100%			+	-	-	+	o	-	-	-	

Location	Sample	Grain fraction [μm]	K-Ar Data					Illite crystallinity			Illite polytypism			Mineralogy									
			K2O [wt%]	40Ar* [nl/g] STP	40Ar* [%]	Age [Ma]	2σ [Ma]	air dry [Δ°2θ]	glycolated [Δ°2θ]	group	2M ₁ , 1M , 1M _d	extrapolated age		I	Q	C	K	S	K-Fsp	P	other	group	
												100% 1M _d	100% 2M ₁										
Los Tuneles	94-09	2-6 μm	4,92	38,14	89,80	382,1	5,6	E - 0,181	E - 0,180	4	64%, 6%, 29%	(54)	(537)	+	o	+	-	-	o	-	-	IC	
		< 2 μm	6,07	62,29	95,22	293,0	6,7	A - 0,399	A - 0,380		37%, 9%, 55%			+	-	+	-	-	-	-	-		
		< 0.2 μm	6,92	94,97	98,94	225,7	8,8	D - 0,539	D - 0,458		31%, 10%, 59%			++	-	+	-	+	-	-	-		
	101-09	2-6 μm	3,02	25,71	94,79		5,9	-	-	4	-	246	463	+	o/-	+	-	o/-	-	-	-	IC	
		< 2 μm	2,63	25,97	95,04	282,9	5,0	D - 0,565	D - 0,492		17%, 0%, 83%			+	-	++	-	o/-?	-	-	-		
		< 0.2 μm	-	-	-	246,4	-	D - 0,618	D - 0,648		0%, 0%, 100%			+	-	++	-	o/-?	-	-	-		
Merlo	82-09 ¹	2-6 μm	1,03	8,68	89,80	257,3	6,1	E - 0,180	E - 0,211	2	84%, 10%, 6% ²	233	257	+	-	+	o/-	o	o/-	-	-	ICS	
		< 2 μm	1,69	14,04	84,69	240,9	6,3	A - 0,282	A - 0,275		65%, 0%, 35% ²			+	-	+	o/-	+	o/-	-	-		
		< 0.2 μm	4,90	43,71	91,79	244,0	5,6	A - 0,281	E - 0,244		35%, 0%, 65% ²			+	o	+	o/-	+	o/-	-	-		
	85-09 ¹	2-6 μm	2,33	18,84	89,63	278,6	5,5	E - 0,161	E - 0,164	3	98%, 0%, 2% ²	226	283	+	+	-	o/-	o	o/-	-	-	IKS	
		< 2 μm	3,32	30,62	95,52	265,5	5,7	A - 0,296	A - 0,272		48%, 0%, 52% ²			+	o	o	+	+	-	-	-		
		< 0.2 μm	5,88	57,14	94,81	234,8	5,9	D - 0,491	A - 0,373		24%, 8%, 68% ²			+	o	-	+	+	-	-	-		
	89-09 ¹	2-6 μm	1,44	8,68	87,39	259,2	4,5	E - 0,163	E - 0,155	3	56%, 0%, 44% ²	176	302	o	o	+	+	-	o/-	-	-	ICS	
		< 2 μm	2,58	19,73	96,69	222,7	7,0	A - 0,273	E - 0,234		48%, 0%, 52% ²			+	o	+	+	+	-	-	-		
		< 0.2 μm	5,37	48,27	98,17	177,9	5,5	D - 0,428	A - 0,377		0%, 0%, 100% ²			+	-	+	o	+	-	-	-		
	90-09 ¹	2-6 μm	1,62	9,54	81,01	268,1	4,9	E - 0,171	E - 0,173	3	100%, 0%, 0% ²	177	270	o	+	o	+	-	o	-	-	IK	
		< 2 μm	2,33	17,41	91,56	218,0	6,1	A - 0,400	A - 0,313		39%, 0%, 61% ²			+	o	o	+	o	-	-	-		
		< 0.2 μm	3,61	33,65	97,03	174,0	5,7	D - 0,530	A - 0,332		0%, 0%, 100% ²			+	-	-	+	+	-	-	-		
	91-09 ¹	2-6 μm	2,11	17,05	93,43	330,7	6,7	E - 0,187	E - 0,179	2	55%, 3%, 42% ²	191	(449)	+	+	+	+	-	o	o	-	IC	
		< 2 μm	3,39	35,67	97,11	299,9	6,4	A - 0,299	A - 0,266		36%, 3%, 61% ²			+	o	+	+	o	-	-	-		
		< 0.2 μm	4,17	48,81	98,55	234,6	7,1	A - 0,417	A - 0,358		17%, 3%, 80% ²			+	-	+	-	+	-	-	-		
	92-09 ¹	2-6 μm	2,21	18,62	95,07	341,6	5,7	E - 0,168	E - 0,170	3	31%, 0%, 69% ²	116	(788)	+	+	++	o	-	o/-	o/-	-	C	
		< 2 μm	3,57	38,97	98,65	310,2	7,2	A - 0,260	E - 0,247		21%, 0%, 79% ²			+	-	+	o/-	o	-	-	-		
		< 0.2 μm	3,81	46,21	98,44	244,0	7,9	D - 0,441	A - 0,331		21%, 0%, 79% ²			o	-	+	o	+	-	-	-		
Gigante	27-09	2-6 μm	6,09	63,55	99,03	341,4	6,8	E - 0,157	E - 0,156	1	100%, 0%, 0%	281	342	++	o	-	+	-	o/-	-	-	IK	
		< 2 μm	6,18	73,67	98,26	336,3	7,5	E - 0,250	A - 0,251		55%, 4%, 41%			+	o	-	+	-	-	-	-		
		< 0.2 μm	6,52	79,04	99,60	297,6	7,8	E - 0,204	E - 0,222		53%, 2%, 45%			+	o	-	+	-	-	-	-		

Location	Sample	Grain fraction [μm]	K-Ar Data					Illite crystallinity			Illite polytypism			Mineralogy								
			K2O [wt%]	40Ar* [nl/g] STP	40Ar* [%]	Age [Ma]	2σ [Ma]	air dry [Δ°2θ]	glycolated [Δ°2θ]	group	2M ₁ , 1M, 1M _d	extrapolated age		I	Q	C	K	S	K-Fsp	P	other	group
												100% 1M _d	100% 2M ₁									
Achala	95-09	2-6 μm	4,29	37,31	94,26	278,2	6,0	E - 0,185	E - 0,180		31%, 6%, 62%			+	+	-	+	-	o	o	-	IK
		< 2 μm	5,32	57,52	96,79	307,5	6,9	D - 0,485	D - 0,468	3	43%, 5%, 51%	181	(491)	+	o	-	+	o	-	-	-	
		< 0.2 μm	7,10	68,87	98,84	251,4	6,4	A - 0,389	D - 0,486		27%, 0%, 73%			++	-	-	+	+	-	-	-	
	96-09	2-6 μm	4,88	42,05	92,34	293,5	6,1	E - 0,189	E - 0,183		35%, 7%, 58%			+	+	-	o	-	o	o	-	I
		< 2 μm	5,08	50,95	95,37	286,9	4,7	A - 0,373	A - 0,363	3	27%, 6%, 67%	188	(478)	+	o	-	+	o	-	-	-	
		< 0.2 μm	4,32	44,41	98,32	249,2	4,4	D - 0,483	D - 0,451		19%, 6%, 75%			+	-	-	o	+	-	-	-	
Quines	99-09	2-6 μm	5,23	29,50	89,79	274,9	4,1	A - 0,273	A - 0,264		90%, 5%, 5%			-/o	+	-	o	-	o	-	-	IK
		< 2 μm	4,89	32,78	90,09	196,7	3,4	D - 0,536	D - 0,500	4	21%, 9%, 70%	137	283	+	o	-	+	o	-	-	-	
		< 0.2 μm	3,65	34,96	98,62	166,9	6,3	D - 0,575	D - 0,541		21%, 0%, 79%			++	-	-	+	o	-	-	-	

D = diagenetic zone, A = anchizone, E = epizone I = illite, Q = quartz, C = chlorite, K = kaolinite, S = smectite, K-Fsp = potassium feldspar, P = plagioclase, H = halloysit. ¹: data taken from Löbens et al. (2011), ²: new data for samples from Löbens et al. (2011), ³: data from Bense et al. (in review A).

7 Synthesis of Thermochronological Data

7.1 Introduction

Thermochronological dating methods such as apatite fission-track (AFT) as well as (U-Th)/He zircon and apatite dating (ZHe & AHe) are appropriate for investigating the thermal evolution of the upper crust below ~200 °C (e.g. Farley and Wolf 1996). Integration of this thermal evolution of basement blocks with information from the sedimentary record of the surroundings can be used to constrain the thermal and tectonic evolution of the shallow crust (e.g. Gallagher et al. 1998, Farley 2002, Ehlers and Farley 2003, Löbens et al. 2011).

The Sierras Pampeanas in central and northwestern Argentina constitute a morphotectonic region of several roughly north-south trending mountain ranges (Fig. 7.1) separated by inter-mountain basins (e.g. González Bonorino 1950, Caminos 1979, Jordan and Allmendinger 1986, Ramos et al. 2002). The study area is composed of twelve major Pampean basement blocks (Fig. 7.1) consisting of Neoproterozoic to Early Paleozoic igneous and metamorphic rocks (e.g. González Bonorino 1950, Caminos 1979, Gordillo and Lencinas 1979). Those ranges were affected by Early Cenozoic crustal shortening (e.g. Benjamin et al. 1987, Noble et al. 1990, Carrapa et al. 2011) related to the westward subduction of the Nazca Plate beneath the South American Plate. Deformation results in a thick-skinned thrust belt (Jordan and Allmendinger 1986), characterized by i) the uplift of the eastern margin of the Puna Plateau in the northern part of the Pampean ranges (Isacks 1988, Jordan and Alonso 1987) and ii) presumably the uplift of the Sierra de Pie de Palo in the Western Sierras Pampeanas (Löbens et al. in review) at that time. During the Neogene, the incorporation of the aseismic Juan Fernández Ridge into the subduction generated a flattening of the subduction angle in the area of 27-33 °S (e.g. Barazangi and Isacks 1976, Pilger 1981, Jordan et al. 1983, Yañez et al. 2001). This flat-slab subduction is interpreted to have caused the exhumation and uplift of the individual Pampean mountain ranges as well as to have determined the type of deformation within the Sierras Pampeanas by reactivating and inverting major Late Proterozoic and Early Paleozoic crustal discontinuities during Andean deformation (e.g. Jordan et al. 1983, Yañez et al. 2001).

Exhumation processes can be qualitatively and quantitatively constrained by integrated cooling paths, which enable the development of time-dependent structural and surficial evolutionary models for a region. So far, those models exist either for individual mountain ranges within the Sierras Pampeanas (e.g. Sobel and Strecker 2003, Mortimer et al. 2007, Löbens et al. 2011), or they are only based on thermochronological data lacking modeled time-temperature paths (Jordan et al. 1989). Therefore, the aim of this paper is to combine those evolutionary models of basement ranges from the Eastern, Western, and Northern Sierras Pampeanas with new apatite fission-track and zircon and

apatite (U-Th)/He cooling ages, in order to develop a time-dependent cooling model for the whole Sierras Pampeanas.

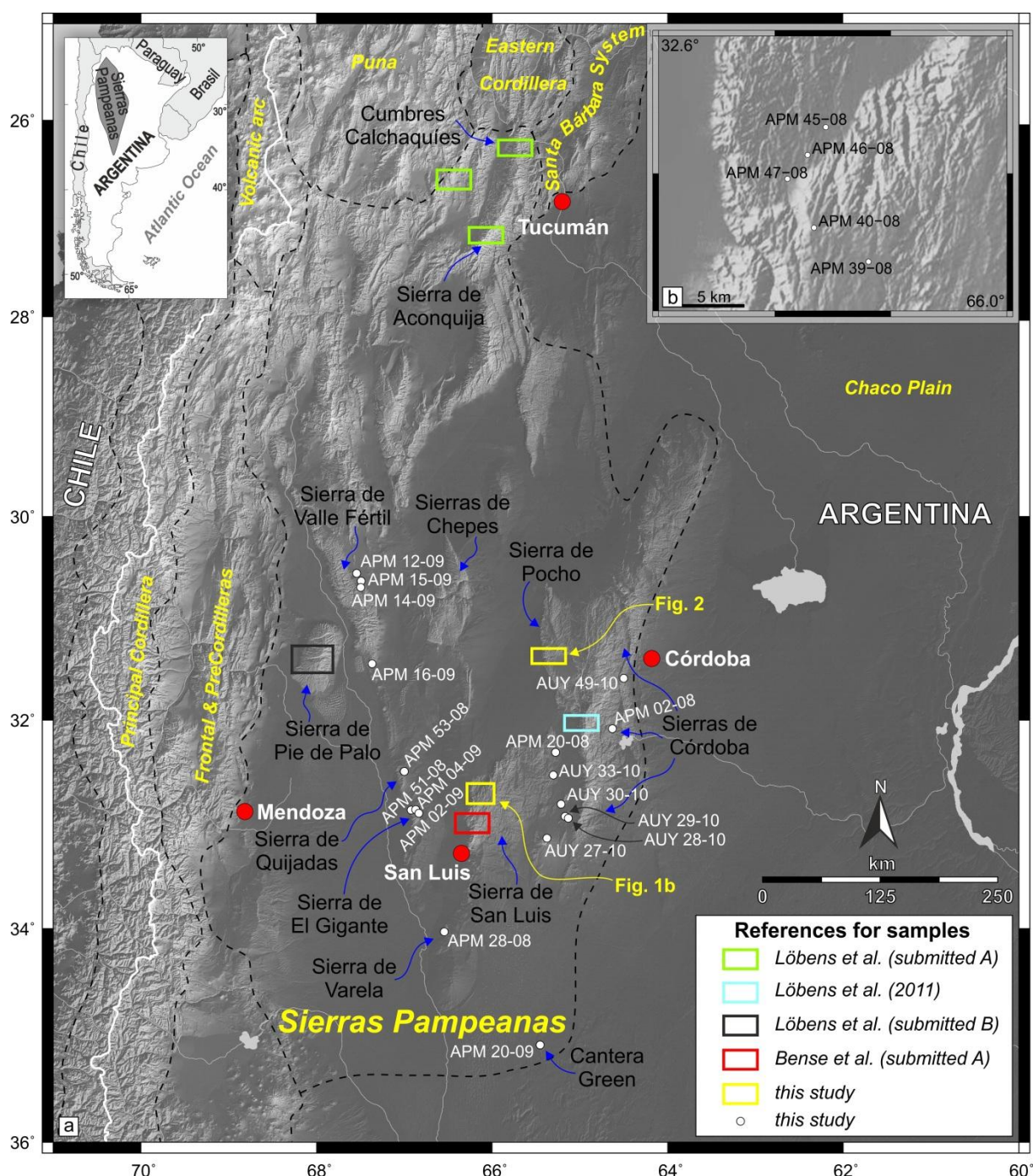


Fig. 7.1: a) SRTM3 digital elevation model of the Sierras Pampeanas showing location of sample discussed in this study; b) magnification of the San Francisco del Monte de Oro area. Black dashed lines mark boundaries of tectonic provinces according to (Hilley and Coutand 2010).

7.2 Regional Geology of the Sierras Pampeanas

The Sierras Pampeanas in central and northwestern Argentina constitute several mountain ranges representing individual tectonic blocks of crystalline basement. Basement is mainly characterized by metamorphic and granitic rocks, e.g. low-to-medium-grade schists, amphiboles, and gneisses (e.g. González Bonorino 1950, Caminos 1979, Gordillo and Lencinas 1979), formed during the accretion of

different allochthonous and parautochthonous terranes during the Pampean, Famatinian, and Achalian Orogeny in Late Proterozoic to Middle Paleozoic times. The tectonometamorphic evolution and associated ductile deformation of the basement is considered to have been completed by Early Carboniferous times (e.g. Ramos 1988, Ramos et al. 2002, Steenken et al. 2004, Miller and Söllner 2005, Ramos 2008).

During Late Paleozoic to Mesozoic times, the deposition of non-marine strata occurred. The Upper Paleozoic to Lower Mesozoic strata of the Paganzo basin (e.g. Gonzalez and Aceñolaza 1972), which formed due to extension during the orogenic collapse following the Early Paleozoic orogenic mountain building (Mpodozis and Ramos 1989, Ramos et al. 2002), is mainly restricted to the southwestern parts of the Sierras Pampeanas (Salfity and Gorustovich 1983). During the Mesozoic, two rift events affected the basement of the Sierras Pampeanas and reactivated older crustal discontinuities, leading to an irregular cover of non-marine sediments atop the basement with variable but, locally, up to 5000m thickness (e.g. Jordan et al. 1983, Schmidt et al. 1995). The first extensional event occurred during Late Triassic to Early Jurassic times. It led to the deposition of non-marine sediments in localized depocenters. They were mainly located along a NNW-trending series of basins, i.e. along the Valle Fértil fault in the western part of the Sierras Pampeanas, e.g. the Ischigualasto, Marayes, Las Salinas, and Beazley basins (Fig. 7.6; Criado Roque et al. 1981, Aceñolaza and Toselli 1988, Ramos et al. 2002).

The second extensional event occurred during Early Cretaceous times, associated with the opening of the South Atlantic Ocean at these latitudes (Schmidt et al. 1995, Rossello and Mozetic 1999). Major but narrow rift basins developed along the eastern and western borders of the Pampia terrane, e.g. along the western side of the Sierra Chica de Córdoba and Valle Fértil. These basins contain accumulated sediment thicknesses of up to 2000-2500m (e.g. Santa Cruz 1979, Gordillo and Lencinas 1979, Criado Roque et al. 1981, Battaglia 1982, Jordan et al. 1983, Schmidt et al. 1995, Gardini et al. 1996, Gardini et al. 1999, Costa et al. 2000, Costa et al. 2001, Ramos et al. 2001, Ramos et al. 2002). Due to subsequent erosion, the original extent of those Mesozoic depocenters is not well known (Furque 1968, Gonzalez and Aceñolaza 1972, Lucero Michaut and Olsacher 1981, Ramos 1982, Salfity and Gorustovich 1983, Jordan et al. 1983). However, the quite asymmetrical patterns of Mesozoic cover sediments indicate that large areas of the Central and Eastern Sierras Pampeanas had little or no sedimentary cover (e.g. Jordan et al. 1983, Schmidt et al. 1995, Löbens et al. 2011).

During Miocene times (18-11 Ma), the Juan Fernández Ridge was incorporated into this subduction of the Nazca Plate beneath the South American Plate (e.g. Gutscher et al. 2000, Yañez et al. 2001). The collateral shortening and flattening of the subduction angle (Stauder 1973, Barazangi and Isacks 1976, Pilger 1984) is interpreted to have led to a reactivation and inversion of the Mesozoic extensional fault systems, causing uplift and deformation of the Pampean basement blocks. The

geometry of these reverse faults and thrusts is mainly determined by the orientation of the older Late Proterozoic to Paleozoic structures, resulting in a dominance of east-dipping structures. The preferred fault orientation is also morphologically expressed by the distinct asymmetry of the Pampean basement blocks. Generally, the ranges show a steeply dipping, fault-facing western slope in contrast to a gently dipping slope on the fault-averted eastern side (González Bonorino 1950, Gordillo and Lencinas 1979, Criado Roque et al. 1981, Gonzalez Diaz 1981, Jordan and Allmendinger 1986, Introcaso et al. 1987, Massabie 1987, Costa and Vita-Finzi 1996, Ramos et al. 2002).

7.3 Methodology

Utilizing a combination of several thermochronometers, i.e. apatite fission-track (AFT) and (U-Th)/He dating of zircon and apatite (ZHe and AHe, respectively), is an effective approach to reconstructing the thermal history of the upper crust below 200 °C, which is equivalent to a depth of approximately 10-8 km, assuming a geothermal gradient between 20 ° and 26 °C/km (e.g. Farley and Wolf 1996). The temperature interval of the AFT system is sensitive for the so-called “partial annealing zone” (PAZ, e.g. Gleadow and Fitzgerald 1987), which ranges from 110 °C to 60 °C for typical apatite affected by moderate cooling rates (e.g. Ketcham et al. 1999, Laslett et al. 1987). The comparable temperature range for the (U-Th)/He systems, the “partial retention zone” (PRZ, e.g. Baldwin and Lister 1998, Wolf et al. 1998), is 200-160 °C for zircon (PRZ_Z) and 80-55 °C for apatite (PRZ_A; Farley 2000, Reiners et al. 2004). Since these temperature intervals strongly depend on the retentivity of radiogenic He and fission-tracks in the zircon and apatite crystals, the grain size, crystal morphology, effective uranium content, and cooling rate, retention behavior directly affects these temperature ranges (e.g. Ehlers and Farley 2003, Reiners and Brandon 2006, Wolf et al. 1996). For the AFT, the kinetic parameter, usually expressed by the chlorine content or by the etch-pit diameter (Dpar) of fission-tracks, controls the retention behavior (Donelick et al. 1999, Ketcham et al. 1999).

In this study, basement samples from the Sierra de Pocho, the Conlara Valley (including the Sierra del Morro), the Sierras de Córdoba, the Sierra del Gigante, the Sierra de Varela, Cantera Green, the Sierra de Valle Fértil, and the Sierra de la Huerta (Fig. 7.1) were analyzed using the ZHe and AHe dating systems. Corresponding apatite fission-track data was obtained from samples from the Sierra de Pocho, the Conlara Valley, the Sierra del Morro, the Sierras de Córdoba, the Sierra del Gigante, the Sierra de Varela, and Cantera Green (Fig. 7.1). The mineral separation and analytical procedures applied are described in detail by Löbens et al. (2011).

7.4 Results

7.4.1 Zircon (U-Th)/He Ages

ZHe ages from twenty samples were obtained during this study. Sample locations are shown in Figure 7.1; analytical results are displayed in Table 7.1. Ages of samples from the Sierra de Valle Fértil

vary between Early Carboniferous (353 Ma; APM 15-09) and Early Triassic (245 Ma; APM 12-09), becoming progressively younger from north to south. Three samples from the Sierra del Gigante yield ages ranging from Early Permian (293 Ma; APM 51-08) in the west to Middle Cretaceous (105 Ma; APM 02-09) in the east. Samples from the southernmost expressions of the Sierras Pampeanas, i.e. the Sierra de Varela and Cantera Green area, yield Late Triassic ages (212 Ma; APM 28-08 and 202 Ma; APM 20-09). Samples from the Conlara Valley region between the Sierras de San Luis and Comechingones range from the Late Carboniferous (307 Ma; AUY 27-10) to the Late Triassic (206 Ma; AUY 30-10). Samples collected along an elevation profile in Sierra de Pocho (Fig. 7.2) yield Late Carboniferous (308 Ma; APM 55-08) to Early Permian (281 Ma; APM 59-08) ages.

The five samples from the San Francisco del Monte de Oro profile yield ages from the Late Carboniferous (304 Ma; APM 45-08) to the Middle Triassic (237 Ma; APM 39-08). Individual samples from the Sierra de Comechingones (APM 02-08, AUY 49-10) show Middle to Late Triassic ages (223 Ma; APM 2-08 and 234 Ma; AUY 49-10).

7.4.2 Apatite (U-Th)/He Ages

Overall, 24 samples were analyzed using the AHe dating method (Fig. 7.1, Table 7.1). In general, the mean AHe age of every sample is younger or coincides with its corresponding fission-track age within the 2σ -error. The average AHe ages of the samples from the elevation profile in the Sierra de Pocho (Fig. 7.2) vary between the Middle Triassic (230 Ma; APM 55-08) and the Middle Cretaceous (112 Ma; AUY 38-10). Within this cross-section, there is a distinct age-elevation correlation (Fig. 7.2). Four basement samples from small ranges within the Conlara Valley region were analyzed, yielding average AHe ages between the Late Jurassic (156 Ma; AUY 28-10) and the Late Cretaceous (78 Ma; AUY 33-10). Two samples were taken from the Sierras de Córdoba, showing Early Cretaceous (140 Ma; APM 02-08) and Late Paleocene ages (57 Ma; AUY 49-10). Mean AHe ages of basement samples from the Sierra del Gigante show Paleocene (59 Ma; APM 02-09) to Early Miocene ages (22 Ma; APM 51-08). Three samples from the eastern side of the Sierra de Valle Fértil were dated. AHe ages span from the Early Permian (294 Ma; APM 15-09) to the Cenozoic (63 Ma; APM 12-09 and 5 Ma; APM 16-09) in the Sierra de la Huerta, the southernmost extension of the Valle Fértil range (Fig. 7.1). The five mean AHe ages of samples from the San Francisco del Monte de Oro area range from the Middle Triassic (238 Ma; APM 47-08) to the Middle Cretaceous (96 Ma; APM 40-08). Samples from the southernmost ranges of the Sierras Pampeanas, i.e. the Sierra de Varela and Cantera Green, show Middle Cretaceous (97 Ma; APM 28-08) and Early Jurassic ages (177 Ma; APM 20-09), respectively.

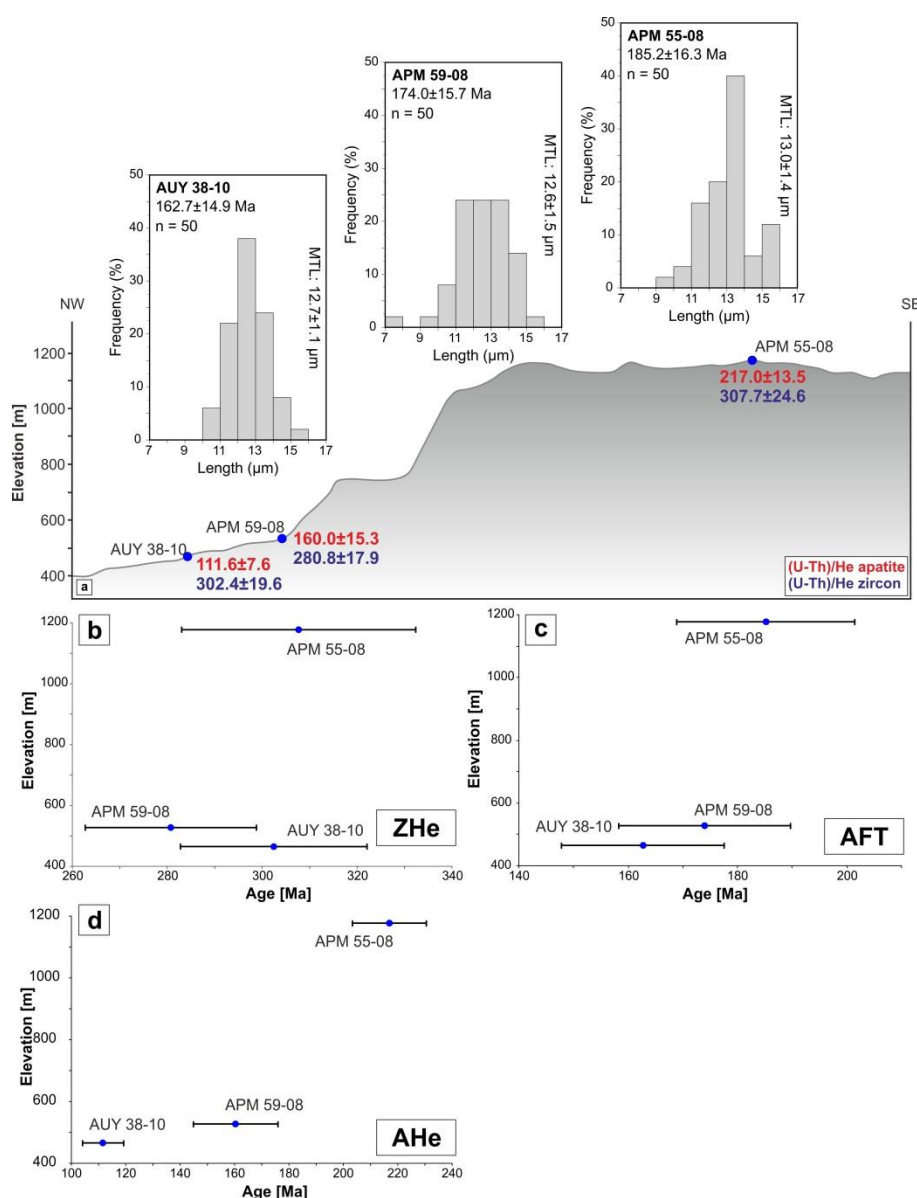
7.4.3 Apatite Fission-Track Ages

Thirteen basement samples from the Eastern Sierras Pampeanas were dated using the AFT method, i.e. the Sierra de Pocho, the Conlara Valley (including the Sierra del Morro), the Sierras de Córdoba,

the Sierra de Varela, the Sierra del Gigante, and Cantera Green, the most southern exposure of the Pampean ranges (Figs. 7.1 and 7.3, Table 7.2). All investigated samples passed the chi-squared test.

Three samples from the Sierra de Pocho were analyzed from a ~700 m elevation profile on the western side of the mountain range. The central ages range from 185.2 ± 16.3 Ma to 162.7 ± 14.9 Ma, correlating positively with elevation (Fig. 7.2). Track-length distributions are generally unimodal and moderately reduced with a mean of 12.8 ± 1.3 μm (Fig. 7.2). Dpar values vary from 1.9 ± 0.1 μm to 2.4 ± 0.3 μm .

Five basement samples were analyzed from the Conlara Valley, including the Sierra del Morro (Fig. 7.1). The four samples collected directly from the former (AUY 28-10, 29-10, 30-10, 33-10) yield central ages between 270 Ma and 189 Ma. All these samples are characterized by moderately reduced track lengths with a mean of 12.5 ± 1.6 μm . Furthermore, the track lengths are unimodally distributed for AUY 28-10 and AUY 33-10, whereas samples AUY 29-10 and AUY 30-10 show a distinct bimodal track-length distribution (Fig. 7.3). A bimodal track-length distribution is also characteristic of the moderately reduced track lengths of sample AUY 27-10 from the Sierra del Morro, which has a central age of 223 Ma. Dpar values of all five samples are similar, ranging between 1.8 ± 0.1 μm and 1.9 ± 0.1 μm (Fig. 7.3).



The samples from the Sierra de Varela (APM 28-08), south of the Sierra de San Luis, and Cantera Green (APM 20-09) yield central AFT ages of 230 Ma and 186 Ma, respectively (Table 7.2). Their track lengths are moderately reduced with a mean of $12.5 \pm 1.2 \mu\text{m}$ and $12.2 \pm 1.4 \mu\text{m}$ and show unimodal distributions (Fig. 7.3). The Dpar value of APM 28-08 is $2.1 \pm 0.1 \mu\text{m}$, whereas the Dpar of APM 20-09 is distinctly shorter, showing a value of $1.7 \pm 0.1 \mu\text{m}$.

Two, samples were analyzed from the eastern side of the Sierra de Comechingones (APM 02-08, AUY 49-10) and one from the eastern side of the Sierra del Gigante (APM 51-08). The former yields central ages between 178 Ma and 152 Ma. Both are characterized by distinctly shortened track lengths with a mean of $12.2 \pm 1.7 \mu\text{m}$, which are unimodally distributed (Fig. 7.3). Dpar values of both samples are $1.9 \pm 0.2 \mu\text{m}$. The sample from the Sierra del Gigante has a central AFT age of 237 Ma. The track lengths are moderately reduced with a mean of $13.4 \pm 1.2 \mu\text{m}$ and also show a unimodal distribution (Fig. 7.3), whereas the Dpar value of $2.0 \pm 0.1 \mu\text{m}$ is slightly increased compared to that of the samples from the Sierras de Córdoba.

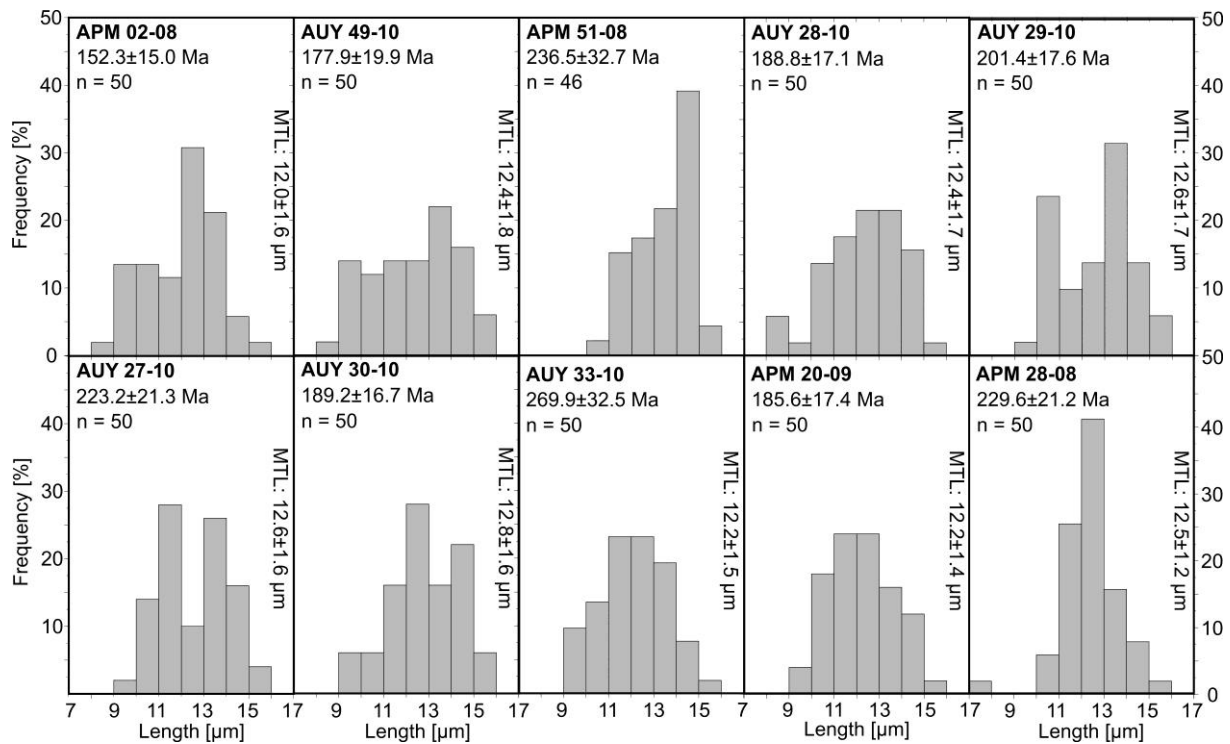


Fig. 7.3: AFT age and track length distribution for all analyzed samples. AFT data for the Sierra de Pocho is displayed in Fig. 7.2; n = number of confined tracks measured, MTL = mean track length.

7.5 Discussion

7.5.1 Thermal Modeling

The thermal history of 22 samples from the Eastern and Western Sierras Pampeanas was modeled following the approach of Ketcham (2005), utilizing the HeFTy software (Fig. 7.4). The input data for the modeling of 13 samples were the apatite fission-track single grain ages, track-length distribution, and Dpar data, as well as the corresponding (U-Th)/He ages of zircon and apatite. For nine samples, the models were only based on the zircon and apatite (U-Th)/He data. Two boundary conditions were imposed on each thermal model in order to obtain geologically reasonable cooling histories: *i*) the starting-point of the modeled time-temperature history is constrained by the zircon (U-Th)/He data (effective closure temperature of approximately 175 °C), and *ii*) the end is confined by the mean annual surface temperature of 17 °C (Müller 1996). Further constraints are related to the measured ages of the other thermochronometers used.

Analyses of the time-temperature paths obtained also allow the calculation of cooling rates. However, any rate calculated here has to be considered as a long-term mean cooling rate based on the average best-fit model path, defined by the temperature boundary conditions of the PRZ_Z, PAZ_A, and PRZ_A.

Table 7.1: Zircon and apatite (U-Th)/He data.

Location	Sample ID (Lithology)	coordinates [DD.dd]	altitude [m]	He [ncc]	s.e. [%]	U238 mass [ng]	s.e. [%]	Th232 mass [ng]	s.e. [%]	Th/U	Sm mass [ng]	s.e. [%]	used Ft- Corr.	uncorr. age [Ma]	Ft- Corr. Age [Ma]	2s [Ma]	mean age [Ma]
Zircon																	
Sierra de Córdoba Santa Rosa de Calamuchita	APM 02-08 (migmatite)	-64.63000 -32.08067	805	15.023	1.7	0.666	1.8	0.125	2.4	0.19	0.029	22	0.76	176.2	176.2	8.3	
				80.195	1.6	2.411	1.8	0.862	2.4	0.36	0.276	21	0.82	248.4	248.4	11.4	
				32.439	1.6	0.998	1.8	0.345	2.4	0.35	0.059	22	0.84	243.6	243.6	11.3	222.7
Conlara Valley Santa Rosa del Conlara	APM 20-08 (gneiss)	-65.276500 -32.310166	631	143.775	1.6	5.01	1.8	1.191	2.4	0.24	0.246	10	0.79	220.83	278.74	21.67	
				66.673	1.6	3.04	1.8	0.790	2.4	0.26	0.161	10	0.76	168.58	222.23	19.12	
				37.967	1.6	1.25	1.8	0.485	2.4	0.39	0.030	10	0.79	226.21	284.54	21.86	
				67.277	1.6	2.60	1.8	0.342	2.4	0.13	0.040	10	0.75	203.81	271.54	24.01	264.2
Sierra de Varela	APM 28-08 (gneiss)	-66.54650 -34.03100	548	82.134	1.6	2.899	1.8	0.628	2.4	0.22	0.217	6	0.79	218.9	276.4	21.5	
				39.851	1.6	2.185	1.8	0.187	2.4	0.09	0.152	20	0.74	146.1	197.7	18.1	
				62.310	1.6	4.025	1.8	0.549	2.4	0.14	0.530	20	0.74	122.8	164.9	14.8	
				166.147	1.6	7.633	1.8	1.017	2.4	0.13	0.869	5	0.83	172.0	208.2	14.6	211.8
Sierra de San Luis San Francisco del Monte de Oro	APM 39-08 (granitoid)	-66.11933 -32.76417	1745	61.172	1.6	2.62	1.8	0.885	2.4	0.34	0.386	5	0.73	176.0	241.7	22.6	
				53.190	1.6	2.08	1.8	1.123	2.4	0.54	0.349	5	0.77	185.1	238.9	19.4	
				81.004	1.6	3.30	1.8	1.629	2.4	0.49	0.294	5	0.78	179.4	231.3	18.8	237.3
	APM 40-08 (granitoid)	-66.16617 -32.73950	1775	55.491	1.6	1.92	1.8	1.013	2.4	0.53	0.113	8	0.79	209.5	266.8	21.0	
				132.291	1.6	4.19	1.8	1.971	2.4	0.47	0.725	7	0.81	230.4	283.1	20.4	
				54.942	1.6	1.88	1.8	0.815	2.4	0.43	0.170	7	0.78	215.8	277.5	22.4	
	APM 45-08 (migmatite)	-66.15600 -32.66633	966	46.785	1.6	1.63	1.8	0.731	2.4	0.45	0.090	8	0.75	210.5	281.5	24.9	277.2
				172.097	1.6	5.87	1.8	0.829	2.4	0.14	0.263	5	0.82	230.2	280.9	20.1	
				492.653	1.6	13.84	1.8	4.443	2.4	0.32	1.211	5	0.83	267.6	320.9	21.8	
				289.397	1.6	7.34	1.8	3.359	2.4	0.46	0.781	5	0.84	287.3	343.9	23.1	
				192.049	1.6	6.77	1.8	1.498	2.4	0.22	0.278	5	0.84	218.9	260.0	17.3	
	APM 46-08 (granitoid)	-66.17167 -32.68650	1008	322.685	1.6	9.06	1.8	2.902	2.4	0.32	1.425	5	0.85	267.6	315.5	20.4	304.2
				88.295	1.6	3.75	1.8	1.336	2.4	0.36	0.133	6	0.83	177.1	213.4	14.6	
				307.452	1.6	7.88	1.8	3.498	2.4	0.44	1.030	6	0.87	285.2	326.3	19.3	
	APM 47-08 (migmatite)	-66.18900 -32.70400	1077	558.316	1.6	25.90	1.8	9.674	2.4	0.37	4.385	6	0.89	161.6	182.1	10.4	240.6
				81.732	1.6	2.69	1.8	0.771	2.4	0.29	0.222	5	0.84	230.9	275.8	18.5	
				196.059	1.6	7.00	1.8	1.325	2.4	0.19	0.501	5	0.84	217.7	260.6	17.7	
Sierra de El Gigante	APM 51-08 (schist)	-66.92200 -32.86667	638	50.975	1.6	2.08	1.8	1.641	2.4	0.79	0.428	5	0.82	168.4	205.2	14.3	247.2
				85.106	1.6	3.323	1.8	0.658	2.4	0.20	0.242	5	0.79	199.0	250.6	19.4	
				25.001	1.6	0.817	1.8	0.257	2.4	0.31	0.020	21	0.76	231.3	304.4	26.1	
				18.856	1.6	0.576	1.8	0.219	2.4	0.38	0.068	22	0.75	243.6	324.0	28.4	292.9

Location	Sample ID (Lithology)	coordinates [DD.dd]	altitude [m]	He [ncc]	s.e. [%]	U238 mass [ng]	s.e. [%]	Th232 mass [ng]	s.e. [%]	Th/U	Sm mass [ng]	s.e. [%]	used Ft- Corr.	uncorr. age [Ma]	Ft- Corr. Age [Ma]	2s [Ma]	mean age [Ma]
Sierra de Pocho Los Tuneles	APM 55-08 (granitoid)	-65.37667 -31.37400	1177	22.789	1.6	0.826	1.8	0.221	2.4	0.27	0.108	9	0.74	210.9	283.9	25.6	307.7
				52.236	1.6	1.791	1.8	0.244	2.4	0.14	0.042	9	0.79	229.3	289.3	22.6	
				95.552	1.6	2.653	1.8	0.232	2.4	0.09	0.021	10	0.83	284.9	344.0	24.1	
				41.810	1.6	1.319	1.8	0.062	2.4	0.05	0.022	10	0.80	253.8	318.9	24.7	
				29.961	1.6	1.026	1.8	0.123	2.4	0.12	0.036	10	0.76	230.4	302.3	25.9	
	APM 59-08 (phyllite)	-65.42600 -31.35883	527	84.593	1.6	2.338	1.8	1.296	2.4	0.55	0.112	5	0.86	259.1	302.4	18.9	280.8
63.232	1.6	2.150	1.8	0.835	2.4	0.39	0.130	6	0.84	218.9	259.1	16.9					
Sierra de Valle Fértil	APM 12-09 (gneiss)	-67.54256 -30.56240	908	442.594	1.6	11.09	1.8	4.300	2.4	0.39	0.466	10	0.88	295.0	334.2	19.3	336.5
				139.404	1.6	3.82	1.8	1.546	2.4	0.40	0.142	10	0.84	269.5	322.3	21.6	
				371.670	1.6	9.18	1.8	3.340	2.4	0.36	0.327	11	0.86	300.6	348.7	21.6	
				138.088	1.6	3.48	1.8	1.626	2.4	0.47	0.082	11	0.85	288.5	340.9	22.1	
	APM 15-09 (granitoid)	-67.49066 -30.63729	882	1132.818	1.6	24.17	1.8	14.847	2.4	0.61	0.452	14	0.89	329.6	369.2	20.4	352.8
				412.561	1.6	10.63	1.8	5.372	2.4	0.51	2.932	14	0.84	279.9	331.4	21.6	
				229.753	1.6	5.52	1.8	2.433	2.4	0.44	0.130	8	0.84	304.3	364.3	24.5	
				272.565	1.6	6.66	1.8	3.543	2.4	0.53	0.169	8	0.85	293.7	346.3	22.3	
	APM 16-09 (amphibolite)	-67.36539 -31.44892	636	142.101	1.6	4.98	1.8	2.891	2.4	0.58	0.047	9	0.83	204.4	247.3	17.1	244.5
				138.499	1.6	4.74	1.8	2.367	2.4	0.50	0.064	9	0.82	212.4	259.4	18.4	
24.655				1.6	0.81	1.8	0.469	2.4	0.58	0.003	15	0.83	218.0	264.0	18.2		
42.817				1.6	1.88	1.8	0.900	2.4	0.48	0.027	10	0.81	167.0	207.4	15.4		
Cantera Green	APM 20-09 (granitoid)	-65.45101 -35.09387	369	628.190	1.6	27.28	1.8	0.854	2.4	0.03	0.161	9	0.76	186.2	244.0	20.9	202.2
				246.579	1.6	19.76	1.8	0.177	2.4	0.01	0.163	9	0.63	102.3	161.7	19.4	
				403.830	1.6	24.36	1.8	1.121	2.4	0.05	0.336	9	0.78	134.2	172.8	14.2	
				293.964	1.6	12.99	1.8	0.227	2.4	0.02	0.211	9	0.80	183.7	230.2	17.8	
Conlara valley	AUY 27-10 (granitoid)	-65.37598 -33.13835	1171	80.868	1.6	2.232	1.8	0.463	2.4	0.21	0.012	12	0.84	279.1	333.4	22.5	306.8
				94.625	1.6	3.142	1.8	0.178	2.4	0.06	0.038	10	0.86	240.9	280.2	17.8	
	AUY 29-10 (migmatite)	-65.16814 -32.92813	904	18.994	1.7	0.700	1.8	0.235	2.4	0.34	0.012	12	0.74	204.4	275.7	24.9	275.7
				AUY 30-10 (granitoid)	-65.21731 -32.81117	810	15.594	1.66	0.403	1.88	1.796	2.41	4.45	2.59	9.68	0.86	150.5
230.192	1.64	8.802	1.81				3.868	2.41	0.44	0.82	9.70	0.87	192.9	221.8	13.3		
Sierra de Pocho Los Tuneles	AUY 38-10 (phyllite)	-65.43324 -31.35132	465	173.921	1.64	7.206	1.81	1.775	2.41	0.25	0.66	9.71	0.84	185.8	220.1	14.5	
				123.488	1.64	4.106	1.81	1.565	2.41	0.38	0.12	9.87	0.80	224.1	279.7	21.1	302.4
				223.804	1.64	6.268	1.81	1.392	2.41	0.22	0.21	10.52	0.82	274.2	334.9	24.0	
Sierra de Córdoba Falda del Carmen	AUY 49-10 (gneiss)	-64.50304 -31.59147	538	33.163	1.65	0.863	1.81	0.218	2.41	0.25	0.02	22.92	1.00	292.7	292.7	13.7	
				40.918	1.64	1.408	1.81	0.908	2.41	0.64	0.01	8.92	0.80	205.3	257.3	19.4	234.3
				32.739	1.64	1.071	1.81	0.393	2.41	0.37	0.02	9.24	0.81	228.4	282.7	20.9	
7.283	1.69	0.411	1.84	0.140	2.42	0.34	0.02	8.28	0.82	134.3	162.9	11.5					

Location	Sample ID (Lithology)	coordinates [DD.dd]	altitude [m]	He [ncc]	s.e. [%]	U238 mass [ng]	s.e. [%]	Th232 mass [ng]	s.e. [%]	Th/U	Sm mass [ng]	s.e. [%]	used Ft- Corr.	uncorr. age [Ma]	Ft- Corr. Age [Ma]	2s [Ma]	mean age [Ma]
Apatite																	
Santa Rosa de Calamuchita	APM 02-08 (migmatite)	-64.63000	805	7.910	1.67	0.53	1.82	0.010	3.75	0.02	1.11	2.10	0.83	119.4	144.3	10.2	
		-32.08067		1.200	1.91	0.08	1.97	0.000	186.61	0.00	0.57	2.28	0.85	115.1	135.0	9.3	139.7
Conlara valley Santa Rosa de Conlara	APM 20-08 (gneiss)	-65.276500	631	2.716	1.73	0.12	1.89	0.01	3.42	0.08	0.54	2.07	0.91	179.21	197.00	10.99	
		-32.310166		1.881	1.78	0.10	1.91	0.01	3.87	0.06	1.01	1.94	0.93	139.70	150.47	8.05	
				1.319	1.85	0.06	2.12	0.01	4.15	0.09	0.42	1.98	0.93	179.45	193.31	11.02	180.3
Santa Rosa del Conlara	APM 28-08 (gneiss)	-66.54650	548	0.445	1.88	0.038	2.57	0.003	8.36	0.09	1.12	5.00	0.80	76.9	96.6	8.1	
		-34.03100		0.328	2.00	0.028	2.93	0.006	5.79	0.20	0.64	5.23	0.80	78.1	97.8	8.5	97.2
Sierra de Varela	APM 39-08 (granitoid)	-66.11933	1745	0.985	1.73	0.04	2.12	0.018	2.84	0.43	0.45	15.26	0.82	160.0	194.2	14.7	
		-32.76417		0.930	1.74	0.04	2.19	0.018	2.86	0.46	0.43	16.30	0.83	164.6	198.5	15.0	196.3
Sierra de San Luis San Francisco del Monte de Oro	APM 40-08 (granitoid)	-66.16617	1775	0.389	2.33	0.03	3.78	0.009	3.57	0.35	0.38	11.27	0.93	99.8	106.9	8.8	
		-32.73950		0.224	2.72	0.02	3.91	0.004	4.42	0.16	0.20	12.26	0.84	70.9	84.8	8.6	95.9
	APM 45-08 (migmatite)	-66.15600 -32.66633	966	0.575	1.79	0.10	1.89	0.012	3.16	0.12	0.18	12.26	0.80	47.2	59.0	4.6	
				4.936	1.66	0.39	1.82	0.009	3.47	0.02	0.65	12.82	0.85	102.4	120.7	8.0	
				5.239	1.65	0.19	1.83	0.008	3.51	0.04	0.48	12.12	0.81	217.2	267.7	19.8	
				12.296	1.64	0.53	1.81	0.015	2.94	0.03	1.33	12.06	0.80	184.0	231.2	17.9	169.6
APM 46-08 (granitoid)	-66.17167	1008	1.920	1.68	0.12	1.86	0.015	2.97	0.12	0.31	17.48	0.89	120.4	135.5	8.0		
	-32.68650		5.587	1.65	0.36	1.82	0.010	3.36	0.03	0.20	18.20	0.83	124.5	150.3	10.6	142.9	
APM 47-08 (migmatite)	-66.18900	1077	3.432	1.67	0.12	1.86	0.012	3.19	0.09	1.14	48.61	0.88	206.7	234.3	21.0		
	-32.70400		2.022	1.69	0.07	1.94	0.009	3.46	0.12	0.73	52.16	0.83	199.0	240.8	25.0	237.5	
APM 51-08 (schist)	-66.92200	638	0.012	6.06	0.005	13.78	0.003	9.92	0.51	0.05	5.08	0.83	16.8	20.2	5.2		
	-32.86667		0.015	5.85	0.005	12.57	0.003	8.67	0.62	0.04	5.22	0.87	20.5	23.6	5.5	21.9	
Sierra de El Gigante	APM 55-08 (granitoid)	-65.37667	1177	20.476	1.64	0.84	1.81	0.011	3.21	0.01	1.09	23.74	0.88	196.52	224.11	13.54	
		-31.37400		4.364	1.66	0.19	1.83	0.012	3.16	0.06	0.27	24.72	0.86	179.67	209.84	13.55	216.9
Sierra de Pocho	APM 59-08	-65.42600	527	0.895	1.73	0.02	3.02	0.210	2.44	10.72	0.36	12.07	0.72	101.91	142.29	14.17	
Los Tuneles	(phyllite)	-31.35883		1.092	1.71	0.06	2.01	0.045	2.56	0.79	0.09	12.14	0.74	130.63	177.63	16.45	159.9
Sierra de El Gigante	APM 02-09 (schist)	-66.83339	689	0.061	2.87	0.01	11.56	0.009	3.16	1.09	0.12	5.61	0.84	44.4	52.8	9.4	
		-32.89684		0.077	2.46	0.01	11.59	0.011	2.90	1.40	0.16	5.45	0.84	55.1	65.4	10.7	59.1
	APM 04-09 (schist)	-66.87234	692	0.042	3.46	0.00	11.48	0.013	3.08	2.76	0.05	32.53	0.85	42.5	50.3	7.9	
		-32.86408		0.000	4.14	0.01	9.44	0.014	3.00	2.54	0.08	35.11	0.79	32.2	40.8	6.4	45.5

Location	Sample ID (Lithology)	coordinates [DD.dd]	altitude [m]	He [ncc]	s.e. [%]	U238 mass [ng]	s.e. [%]	Th232 mass [ng]	s.e. [%]	Th/U	Sm mass [ng]	s.e. [%]	used Ft- Corr.	uncorr. age [Ma]	Ft- Corr. Age [Ma]	2s [Ma]	mean age [Ma]
Sierra de Valle Fértil	APM 12-09 (gneiss)	-67.54256 -30.56240	908	0.437	1.85	0.12	1.87	0.031	2.48	0.26	0.57	3.51	0.45	27.5	61.1	10.5	62.9
				0.256	2.07	0.06	2.07	0.019	2.58	0.31	0.37	3.45	0.47	30.4	64.8	10.9	
	APM 15-09 (granitoid)	-67.49066 -30.63729	882	1.543	1.70	0.07	2.04	0.081	2.42	1.12	0.23	2.89	0.46	135.9	296.7	50.2	293.5
				3.226	1.67	0.13	1.87	0.143	2.41	1.06	0.36	3.23	0.49	154.1	313.8	49.9	
				2.857	1.67	0.11	1.90	0.130	2.41	1.22	0.39	2.90	0.62	166.3	270.0	33.4	
	APM 16-09 (amphibolite)	-67.36539 -31.44892	636	0.103	2.34	0.11	1.91	0.268	2.41	2.40	1.54	3.58	0.73	4.5	6.2	0.6	5.1
				0.052	3.00	0.07	2.05	0.135	2.41	1.83	0.60	5.04	0.88	3.9	4.4	0.3	
				0.019	4.55	0.03	3.09	0.050	2.45	1.76	0.46	4.66	0.72	3.6	4.9	0.6	
Cantera Green	APM 20-09 (gneiss)	-65.45101 -35.09387	369	3.750	1.66	0.20	1.83	0.014	2.99	0.07	0.29	25.69	0.85	146.5	172.1	11.3	177.9
				1.172	1.72	0.07	1.96	0.009	3.43	0.13	0.07	26.78	0.75	137.8	183.7	16.6	
Conlara Valley	AUY 27-10 (granitoid)	-65.37598 -33.13835	1171	0.832	2.07	0.043	2.34	0.002	5.77	0.05	0.74	5.25	0.89	136.7	154.3	10.4	131.4
				0.683	2.12	0.042	2.36	0.001	12.86	0.02	0.74	5.21	0.89	117.3	131.4	8.9	
				0.404	2.49	0.029	3.01	0.005	4.41	0.17	0.46	5.29	0.90	97.3	108.4	8.4	
	AUY 28-10 (granitoid)	-65.13318 -32.94683	922	0.391	2.54	0.021	3.64	0.004	4.82	0.19	0.19	5.50	0.91	138.2	151.1	12.8	156.2
				2.360	1.80	0.136	1.88	0.011	3.36	0.08	0.10	5.84	0.86	138.9	161.3	10.6	
	AUY 29-10 (migmatite)	-65.16814 -32.92813	904	0.483	2.38	0.047	2.26	0.006	4.10	0.13	0.30	5.56	0.82	77.9	94.4	7.7	94.4
				0.792	2.08	0.081	1.99	0.003	5.31	0.04	0.46	5.62	0.81	76.7	94.3	7.4	
	AUY 30-10 (granitoid)	-65.21731 -32.81117	810	2.543	1.78	0.185	1.85	0.042	2.60	0.23	3.48	5.46	0.89	93.5	104.9	6.1	105.9
				0.408	2.44	0.032	2.75	0.009	3.57	0.28	0.66	5.42	0.80	85.4	107.0	9.7	
Sierra de Pocho Los Tuneles	AUY 33-10 (pegmatite)	-65.30370 -32.52856	705	0.054	5.34	0.005	15.35	0.005	4.44	0.98	0.20	5.72	0.90	59.0	65.3	14.4	77.9
				0.090	4.39	0.005	15.18	0.005	4.25	1.13	0.42	5.54	0.86	78.2	90.5	16.3	
				0.458	2.16	0.018	3.98	0.112	2.47	6.21	0.06	6.61	0.82	84.1	102.1	8.2	
	AUY 38-10 (phyllite)	-65.43324 -31.35132	465	1.232	1.89	0.051	2.24	0.162	2.45	3.19	0.61	5.72	0.87	107.8	123.9	7.7	111.7
				2.724	1.74	0.193	1.85	0.176	2.45	0.91	0.44	5.62	0.86	94.1	109.0	6.7	
				0.142	2.79	0.014	4.91	0.005	4.27	0.34	0.60	2.20	0.86	59.8	69.6	6.7	
	AUY 49-10 (gneiss)	-64.50304 -31.59147	538	0.275	2.31	0.039	2.39	0.008	3.61	0.20	0.23	2.35	0.89	53.3	59.9	4.2	56.8
				0.027	6.00	0.005	11.12	0.002	5.38	0.45	0.12	2.61	0.79	31.7	39.9	8.6	
				0.059	4.23	0.009	7.13	0.003	4.84	0.37	0.13	2.45	0.81	46.7	57.8	8.8	

Notes: DD.dd = Latitude and Longitude in decimal degree, uncorr. = uncorrected age, and Ft-corr. = Ft-corrected age. Amount of He is given in nano-cubic-cm in standard temperature and pressure; amount of radioactive elements are given in nanograms; ejection correct. (Ft): correction factor for alpha-ejection (according to Farley and Wolff (1996) and Hourigan et al. (2005); uncertainties of He and the radioactive element contents are given as 1 sigma, in relative error %; uncertainty of the single grain age is given as 2 sigma in Ma and it includes both the analytical uncertainty and the estimated uncertainty of the Ft; uncertainty of the sample average age is 2 standard error, as (SD)/(n)1/2; where SD = standard deviation of the age replicates and n = number of age determinations. Four to six aliquots per sample were picked and analyzed. If the investigated age of a single grain deviates by more than 2σ from the mean age, the aliquot was rejected. These erroneous ages can be caused by several factors, such as zoning of alpha-emitting elements, micro inclusions, the limit of detection, or the bias of the ejection correction (smaller grains have larger errors).

Table 7.2: Apatite fission-track data.

Sample	Longitude (W)	Latitude (S)	Elevation [m]	n	ρ_s	N_s	ρ_i	N_i	ρ_d	N_d	$P(X^2)$ [%]	Age [Ma]	$\pm 1\sigma$ [Ma]	MTL [μm]	s.d. [μm]	Dpar [μm]	s.d. [μm]
APM 20-09	65°27'04"	35°05'38"	369	25	21.19	1429	12.06	813	6.54	6342	41.9	185.6	17.4	12.2	1.4	1.7	0.09
AUY 49-10	64°30'11"	31°35'29"	538	25	9.01	438	5.21	253	6.45	5725	100.0	177.9	19.9	12.4	1.8	1.9	0.15
APM 51-08	66°55'19"	32°52'00"	638	25	1.97	226	1.04	119	7.85	7368	100.0	236.5	32.7	13.4	1.2	2.0	0.11
AUY 28-10	65°07'59"	32°56'49"	922	25	18.51	1669	9.39	847	6.00	5725	32.3	188.8	17.1	12.4	1.7	1.9	0.09
AUY 29-10	65°10'05"	32°55'41"	904	25	24.53	2058	14.40	1208	7.43	5725	66.2	201.4	17.6	12.6	1.7	1.9	0.10
AUY 30-10	65°13'02"	32°48'40"	810	25	18.33	2026	9.64	1066	6.25	5409	47.1	189.2	16.7	12.8	1.6	1.8	0.09
AUY 33-10	65°18'13"	32°31'43"	705	25	10.85	691	4.68	298	6.75	5409	9.4	269.9	32.5	12.2	1.5	1.8	0.11
AUY 27-10	65°22'34"	33°08'18"	1171	25	15.72	1562	7.70	765	6.71	5725	8.2	223.2	21.3	12.6	1.6	1.9	0.10
APM 02-08	64°37'48"	32°04'50"	805	21	21.66	781	13.42	484	5.91	5725	78.5	152.3	15.0	12.0	1.6	1.9	0.16
APM 55-08	65°22'36"	31°22'26"	1177	25	36.25	2426	19.36	1296	6.21	6086	9.3	185.2	16.3	13.0	1.4	2.1	0.12
APM 59-08	65°25'34"	31°21'32"	527	25	18.26	1951	10.93	1167	6.42	6086	14.1	174.0	15.7	12.6	1.5	2.4	0.27
AUY 38-10	65°26'00"	31°21'05"	465	25	23.41	1413	13.24	799	5.75	5409	56.9	162.7	14.9	12.7	1.1	1.9	0.12
APM 28-08	66°32'47"	34°01'52"	548	25	16.61	1265	8.71	663	7.58	7368	97.8	229.6	21.2	12.5	1.2	2.1	0.13

Notes: n , number of dated apatite crystals; ρ_s/ρ_i , spontaneous/induced track densities ($\times 10^5$ tracks cm^{-2}); N_s/N_i , number of counted spontaneous/induced tracks; N_d , number of tracks counted on dosimeter; $P(X^2)$, probability obtaining chi-squared value (X^2) for n degree of freedom (where n is the number of crystals - 1); age $\pm 1\sigma$ is central age ± 1 standard error Galbraith and Laslett (1993); ages were calculated using zeta calibration method Hurford and Green (1983); glass dosimeter CN-5, and zeta value of SL is 323.16 ± 10.1 ; MTL, mean track length; s.d., standard deviation of track length distribution and Dpar measurements; N , number of tracks measured; Dpar, etch pit diameter.

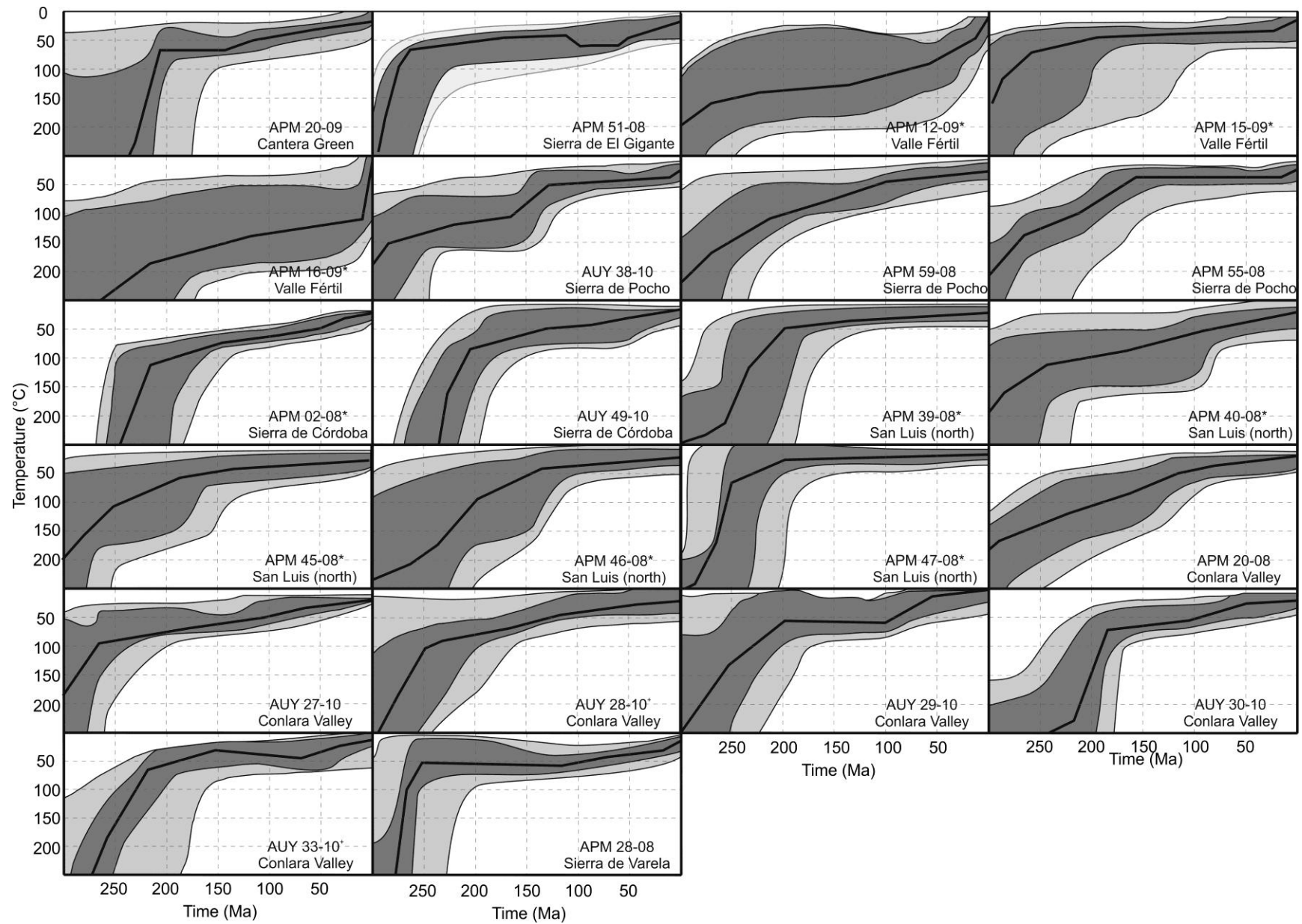


Fig. 7.4: Modeled time-temperature paths based on ZHe, AFT and AHe data, * indicate models without AFT data, + indicate model without ZHe data.

7.5.2 Thermal Evolution of the Basement Ranges

Due to the thermal histories obtained, as well as to the distribution of the apparent ages of the individual methods, the area of the Sierras Pampeanas has been divided into two “regions”: an eastern one, including the Sierras de Córdoba, Pocho, and San Luis, as well as a western one, containing the Sierras Pie de Palo, Valle Fétil, El Gigante, Varela, and the Cantera Green area (Fig. 7.1).

7.5.2.1 *Western and Southernmost Sierras Pampeanas*

Based on the thermochronological data, we propose the following evolution model for the western region, lasting from the post-orogenic phase of the Famatinian Orogeny to today. In general, moderate-to-rapid cooling from the PRZ_Z into the PRZ_A occurred in the northern part of the western region, i.e. the Sierra Valle Fétil, during the Late Paleozoic (Figs. 7.4 and 7.5), which is similar to the Sierra de Pie de Palo and the Sierra de San Luis in the Eastern Sierras Pampeanas. Although cooling based on AFT data is not well constrained in the Sierra Valle Fétil, because the modeled time-temperature history lacks track-length distributions, the cooling path obtained for sample APM 15-09 seems to best represent the overall cooling trend. Variations of the other models (APM 12-09 and APM 16-09) are interpreted to be fault-related, e.g. ~E-W trending discontinuities, within the mountain range. Therefore, we suggest that exhumation in the region of the Sierra Valle Fétil is presumably related to erosion affecting the pronounced relief of the mountain range, which was generated during the Famatinian Orogeny. Later, during the Permo-Triassic compressional phase (see above), erosion was mainly tectonically triggered. Further cooling and exhumation below the lower thermal boundary of the PRZ_A occurred during the Triassic (Figs. 7.4 and 7.5). This is probably due to erosion during Triassic rifting, as indicated by syn-rift deposits at the western margin of the range (e.g. Ramos et al. 2002). Followed by very low exhumation from the Jurassic until the Late Cretaceous, exhumation to near-surface temperatures commenced in the Paleogene, similar to the exhumation of the Sierra de Pie de Palo, but slightly delayed (Figs. 7.4 and 7.5). The very low exhumation is presumably related to a period of tectonic quiescence during that time, thus a very slow erosion. In both areas, this exhumation to near-surface temperatures is probably associated with the early Andean deformation, characterized by ~E-W compression and tectonically-triggered erosion. Therefore, the general structural evolution of the latter range is similar to that of the Sierra Valle Fétil. Both mountain ranges are potentially characterized by a positive relief since the Late Paleozoic. Evolutionary differences only existed during the Mesozoic. Since there was considerable cooling and exhumation in the area of the Sierra de Pie de Palo, the Sierra Valle Fétil was just affected by very slow exhumation (Fig. 7.5). This could be because the topography of the latter range was less pronounced, i.e. the mountain range was characterized by a lower surface elevation, compared to the Sierra de Pie de Palo. Presumably, a relatively lower elevation could be related to

rift-related subsidence of the whole range during the Triassic, or the Sierra de Pie de Palo in the west possibly represented an orographic barrier, causing only slow erosion within the region of the Sierra Valle Fértil during that time. However, final exhumation to near-surface temperatures occurred more or less synchronously, as mentioned above.

In the middle part of the western belt, i.e. the Sierra del Gigante, the onset of cooling and exhumation from PRZ_Z-to-PAZ_A-related temperatures occurred during Permian and Triassic times (Figs. 7.4 and 7.5), potentially related to the Permo-Triassic compressional phase (see above). Presumably, this produced minor relief, which was affected by erosion afterwards, resulting in further exhumation of our samples (Figs. 7.4 and 7.5). Furthermore, this topography was probably nearly eroded by Early to Middle Cretaceous times. Subsequently, Early Cretaceous rifting, linked to the opening of the South Atlantic at these latitudes (e.g. Schmidt et al. 1995, Rossello and Mozetic 1999), triggered the development of an intracontinental rift basin, i.e. the Beazley Basin (Fig. 7.6; e.g. Schmidt et al. 1995), in the region of the Sierra del Gigante. Since the latter is situated within this basin, it is very likely that the observed Cretaceous re-heating of the El Gigante samples (Figs. 7.4 and 7.5) was caused by burial beneath sediments derived from the surrounding heights. The maximum re-heating temperature was around 55 °C, equivalent to a maximum thickness of 2.1-2.8 km (assuming a geothermal gradient of 20-26 °C/km) for the overlying sedimentary succession, which agrees well with the ~2 km of cumulative thickness of the Cretaceous strata in this region (Yrigoyen 1975). Following this burial, re-exhumation to near-surface temperatures occurred during the Late Paleocene to Neogene (Figs. 7.4 and 7.5). Exhumation is potentially related to the Andean deformation, accompanied by erosion stripping off the Cretaceous sediments and leading to exposure of the metamorphic basement. Furthermore, the increasing AHe ages from west to east within this mountain range (Figs. 7.4 and 7.5, Table 7.1) *i)* indicate Neogene activity of the western main boundary fault as proposed by (Schmidt et al. 1995) and *ii)* suggest a similar thermal evolution as described by Bense et al. (in review A, in press) for the Sierra de San Luis.

Within the most southern exposures of the Sierras Pampeanas, i.e. the Sierra de Varela and Cantera Green, rapid cooling from the PRZ_Z into the PRZ_A occurred between Permian and Triassic times (Figs. 7.4 and 7.5). This rapid exhumation of both mountain ranges was presumably generated by tectonism accompanied by erosion during the Permo-Triassic compressional phase (see above). Furthermore, the time-temperature histories suggest a younger exhumation of Cantera Green than of the Sierra de Varela (Figs. 7.4 and 7.5). Presumably, deformation first affected the western area of the Sierras Pampeanas and propagated towards the east, as also suggested by comparison of the cooling paths from the latter ranges with those from the Sierra Valle Fértil (Figs. 7.4 and 7.5). Thus, onset of exhumation as well as exhumation into PRZ_A temperatures occurred relatively earlier in the Sierra de Varela because it is located farther in the west than Cantera Green (Figs. 7.4 and 7.5).

Disposition of our samples from the Cantera Green within this temperature interval lasted until the Early Cretaceous (Figs. 7.4 and 7.5), potentially due to tectonic quiescence and very low erosion in this area. The phase of tectonic quiescence is followed by onset of exhumation out of the PRZ_A to near-surface temperatures during the Early Cretaceous (Figs. 7.4 and 7.5). Rift-related erosion probably caused this exhumation, which, in turn, is associated with the Atlantic rifting that affected the area at these latitudes during the Cretaceous (e.g. Schmidt et al. 1995). In contrast, our sample from the Sierra de Varela remained within the temperature interval of the PRZ_A until the Late Cretaceous (Figs. 7.4 and 7.5). Due to tectonic quiescence, there was probably very slow erosion, hence very low exhumation in this region during the Jurassic, similar to the area of Cantera Green. However, more or less stagnation within the PRZ_A during the Cretaceous is presumably related to the geographical position of the Sierra de Varela compared to Cantera Green. The latter range was situated beyond the extension of the Cretaceous Beazley Basin (Fig. 7.6) proposed by Jordan et al. (1989) and Schmidt et al. (1995), whereas the Sierra de Varela was located at the eastern margin of this basin (Fig. 7.1). Therefore, sediments derived from the surrounding heights were presumably deposited in the vicinity of the Sierra de Varela. However, it is noteworthy that the AHe ages are not reset within this mountain range, in contrast to the Sierra del Gigante (Figs. 7.4 and 7.5). Therefore, cooling paths do not suggest Cretaceous burial re-heating in the Sierra de Varela, which is probably related to different geographical positions of this mountain range and the Sierra del Gigante (present situation) within the Beazley Basin (Fig. 7.6). Since the latter was located near the inferred rift axis and the main depocenters (Schmidt et al. 1995), the mountain range was affected by burial re-heating (as mentioned above), whereas, in the vicinity of the Sierra de Varela, the maximum sedimentary thickness was probably less than 500 m (Jordan et al. 1983), which was insufficient to reset the AHe ages. However, the subsequent cooling and exhumation of this mountain range during the Late Cretaceous is probably related to cessation of rifting and onset of the slow erosion of Cretaceous sediments in this region. Continuous cooling and exhumation of the Sierras Varela and Cantera Green during the Cenozoic (Figs. 7.4 and 7.5) was caused by deformation accompanied by erosion during the Andean Orogeny.

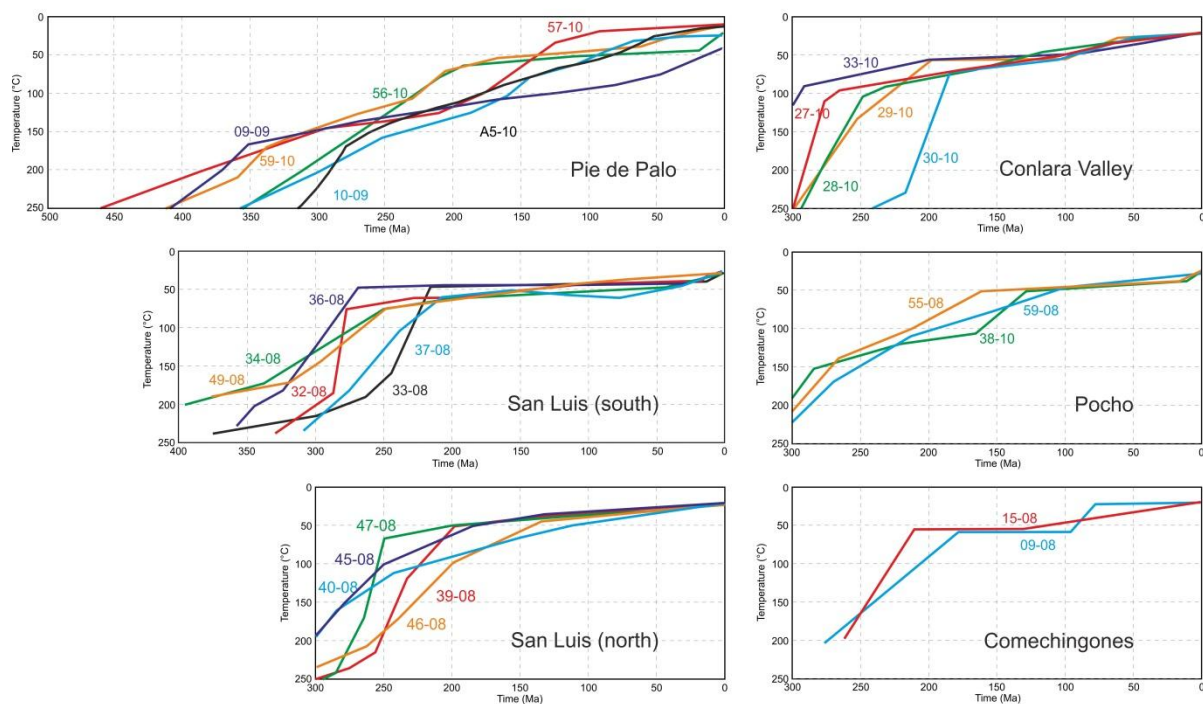


Fig. 7.5: Comparison of mean average cooling paths from the entire Sierras Pampeanas. Data for the Sierras de Pie de Palo, Comechingones and southern San Luis are taken from (Löbens et al. 2011), (Bense et al. in review A) and (Löbens et al. 2013). Abbreviated sample ID; -08 is APM, -09 is APM, -10 is AUY. Different colours mark different samples.

7.5.2.2 South-Eastern Sierras Pampeanas

Thermal modeling of samples from the Nogolí area in the southern Sierra de San Luis show that samples passed through PRZ_Z and PAZ_A temperature conditions during Permian to Middle Triassic times (Figs. 7.4 and 7.5). Cooling through PRZ_A temperature conditions is not well constrained for all samples, but models indicate a Triassic to Middle Cretaceous age. Subsequent cooling to surface temperatures commenced in post-Permian times, most probably between the Cretaceous and the Paleogene (Fig. 7.5). From the Sierra de San Luis, cooling rates of <5°C/Ma for the passage through the PRZ_Z and PAZ_A and <1°C/Ma for PRZ_A temperature and below are reported (Bense et al. in press). Modeled time-temperature paths based on data from the San Francisco del Monte de Oro area in the northern Sierra de San Luis document cooling through PRZ_Z temperatures in Late Carboniferous to Permian times (Figs. 7.4 and 7.5). No AFT data is available, so cooling through PAZ_A temperature conditions is not well constrained. However, cooling through PRZ_A temperatures occurred in Middle Triassic to Cretaceous times (Figs. 7.4 and 7.5). Subsequent cooling to surface temperatures is likely to have occurred during Cretaceous time, also it is less constrained by the modeled thermal history. In general, time-temperature conditions from the northern and southern Sierra de San Luis indicate a quite similar thermal history for both regions (Fig. 7.5).

Several samples were collected from smaller mountain ranges in the Conlara Valley region, between the Sierra de San Luis and Sierras de Córdoba (Fig. 7.1). The thermal modeling based on AFT and AHe data shows that PAZ_A temperatures had already been reached in Early Permian times. Passage

through PRZ_A temperatures occurred during the Cretaceous. Subsequent cooling to surface temperatures is indicated to have occurred in Cretaceous to Paleogene times.

Thermal modeling indicates that samples from the eastern and southern parts of Conlara Valley, i.e. AUY 28-10 and AUY 29-10 as well as AUY 27-10, cooled through PRZ_Z temperatures during Permian times. Subsequent cooling through PRZ_Z and PAZ_A temperatures occurred in Permian to Triassic times, which is very similar to those findings from the Sierra de San Luis (see above); it was followed by decelerated cooling, as suggested by thermal models (Figs. 7.4 and 7.5). Cooling through temperatures of the PRZ_A is indicated to have happened synchronously for all Conlara Valley samples during Jurassic to Cretaceous times (Figs. 7.4 and 7.5), whereupon surface temperature conditions were probably reached in Late Cretaceous to Paleogene times. Nevertheless, there are minor differences between individual time-temperature paths. Sample AUY 27-10 from the El Morro range in the southern Conlara Valley shows a slightly older thermal history than AUY 28-10 and AUY 29-10. However, one sample (AUY 30-10) shows a significantly younger history than the other samples from the Conlara Valley (Figs. 7.4 and 7.5). Instead of Permian PRZ_Z-cooling ages, AUY 30-10 shows Late Triassic ages. PAZ_A and PRZ_A temperatures were passed in Jurassic to Cretaceous times. We attribute those differences to an association of the smaller mountain ranges with different basement blocks. El Morro (AUY 27-10) constitutes an individual range, AUY 33-10 belongs to the Sierra de San Luis, and AUY 28-10 and AUY 29-10 are associated with the Sierra de Comechingones. In contrast, AUY 30-10 represents a solitary block within the Conlara Valley with unclear structural affiliation with one of the nearby mountain ranges. Thermal models for the Conlara Valley samples indicate that cooling through the PRZ_Z and PAZ_A temperature regime coincides with moderate cooling rates between 2.5 and 4.5°C/Ma, whereas passage through PRZ_A and post-PRZ_A temperatures is characterized by slower cooling rates, approximately 0.3-1°C/Ma.

Time-temperature paths for the Los Tuneles area in the Sierra de Pocho generally show slow cooling. Exhumation through PRZ_Z temperatures occurred in Permian times. PAZ_A temperatures were passed in Triassic to Jurassic times. Subsequent cooling through the PRZ_A took place in Late Triassic to Early Cretaceous times. Cooling to surface temperature potentially occurred in Cenozoic times (Figs. 7.4 and 7.5).

Modeled time-temperature paths for the Sierra de Pocho suggest cooling rates of around 1-2°C/Ma for the temperature range between PRZ_Z and PAZ_A and below 1°C/Ma for the PRZ_A temperature range and below.

Samples collected in the western Sierras de Córdoba, between the Sierra de Pocho and the Yacanto area (Fig. 7.1), indicate Triassic cooling through PRZ_Z and PAZ_A temperature conditions. PRZ_A temperature conditions were passed in Early to Late Cretaceous times, whereby surface temperatures were probably reached in Cretaceous to Cenozoic times (Figs. 7.4 and 7.5).

Thermal modeling by Löbens et al. (2011) in the southern Sierra de Comechingones reveals Late Permian ages for cooling through PRZ_Z temperatures. PAZ_A temperature conditions were reached during Late Triassic to Jurassic times. Cooling from PAZ_A to PRZ_A temperatures was slow, as indicated by thermal models, reaching PRZ_A temperatures in Middle Cretaceous times (Fig. 7.5). Cooling to surface temperatures occurred in Late Cretaceous to Paleogene times (Löbens et al. 2011). The thermal history of the Sierra de Comechingones indicates rates between 1.5 and 4°C/Ma for cooling through PRZ_Z and PAZ_A temperatures and <1°C/Ma for the PRZ_A and post PRZ_A temperatures, as reported by Löbens et al. (2011).

The thermal history observed in this part of the Sierras Pampeanas can be linked to several geological and geodynamic processes. The oldest cooling event occurred in the Carboniferous (Figs. 7.4 and 7.5). We relate this to the erosion of existing topography which was built up during previous orogenic phases. Additionally, the Late Carboniferous is characterized by a period of orogenic collapse (Mpodozis and Ramos 1989), supporting the idea of pronounced cooling during this time period.

As discussed above, the majority of samples passed the PRZ_Z and PAZ_A in Permian to Triassic times (Fig. 7.5). This Permo-Triassic time interval is synchronous with an inferred flat-slab subduction episode of the Nazca Plate beneath the South American Plate (Ramos and Folguera 2009). This event might have led to considerable compression, thus to exhumation and cooling at these latitudes (Bense et al. in press). The flat-slab segment was also linked to an orogenic phase in the San Rafael Massif in the province of Mendoza, defined as the San Rafael Orogeny by Kleiman and Japas (2009). Although a direct link between this orogenic phase and the study area has not been developed yet, those findings discussed above show the importance of this, until now, not well understood Permian to Triassic event for the thermal history of the entire Southern Sierras Pampeanas (see below).

However, further cooling in post-Triassic times is generally characterized by comparatively low cooling rates in the entire Southeastern Sierras Pampeanas. We interpret this to be related to low erosional rates as a consequence of relatively stable tectonic conditions within the sampled mountain ranges without substantial uplift or burial events (see below, Fig. 7.5). Although the Cenozoic compression that followed probably contributed to the final cooling of samples to temperatures below 50°C, its extent is not constrained by modeled time-temperature histories; however, it is presumably lower than previously proposed (e.g. González Bonorino 1950).

7.5.3 Spatial and Temporal Variability of Cooling

Based on the findings discussed above, we conclude that cooling during Permian times in the western regions of the Southern Sierras Pampeanas and its subsequent eastward propagation until Early to Middle Triassic times (Figs. 7.6 and 7.7) is spatially and temporally related to a period of flat-slab subduction at these latitudes. This flat-slab subduction event was initially defined for Late

Carboniferous to Early Permian times in the Southern Central Andes (Martínez et al. 2006, Ramos et al. 1986), but, based on our data, it also shows a clear imprint in the Southern Sierras Pampeanas. An imprint of this event in the study area is also indicated by a distinct eastward propagation of Late Paleozoic calc-alkaline magmatism from the Southern Central Andes to the Southwestern Sierras Pampeanas (Sierra de Valle Fértil and Sierra de La Huerta, Fig. 7.1) during Permian to Early Triassic times (see Caminos 1979, Ramos 1988, Mpodozis and Ramos 1989, Mpodozis and Kay 1990, Varela et al. 1993, Ramos and Folguera 2009, and references therein). Inversely to its onset, cooling ceased first in the southeastern parts of the region studied and propagated westwards during Late Triassic times (Figs. 7.5 and 7.6). Whether or not Triassic rifting along terrane boundaries and crustal unconformities (see Ramos et al. 2002) and subsequent stagnation in cooling is related to the end of flat-slab subduction cannot be solved here. However, a hypothetical re-steepening of the subduction angle following the end of flat-slab subduction could have led to tensional forces in the crust, supporting crustal extension in the Late Triassic to Early Jurassic.

In contrast, the Sierras de Pie de Palo and Pocho show notably slower but more continuous cooling compared to other modeled time-temperature paths. Additionally, both ranges (in particular, Pie de Palo) show prolongation of cooling, even during periods marked by an extensional tectonic setting (see Figs. 7.5, 7.6, and 7.7). A possible explanation for this is that both ranges formed topographic heights, subjected by ongoing erosion, unaffected by extensional events. This interpretation is supported by spatial distribution of rift-related sediments in the region studied, showing that neither the Sierra de Pie de Palo boundary faults nor the Sierra de Pocho main boundary fault were significantly extensionally reactivated during rift events (e.g. Jordan et al. 1983, Schmidt et al. 1995, Ramos et al. 2002). Additionally, the position of the Sierra de Pie de Palo on the footwall of the Valle Fértil fault presumably did not allow any burial re-heating of the Pie de Palo samples due to rifting along this fault (Fig. 7.6). Thus, both regions are considered to be relatively unaffected by Late Triassic to Early Jurassic as well as Early Cretaceous rifting.

Another exception is given by sample AUY 30-10 which is in conflict with findings from the surrounding samples. For instance, AUY 30-10 displays accelerated cooling during Late Triassic to Early Jurassic extensional settings. A possible explanation might be related to the complex arrangement of different faults in the Conlara Valley (e.g. Miró and Martos 1999), leading to some kind of step-over or push-up structure (see van der Pluijm and Marshak 2004). However, since the structural affiliation of this basement block with the surrounding ranges is unclear due to the sedimentary cover of the basement blocks in the Conlara Valley, the thermal history of this minor basement block remains enigmatic.

Finally, thermal modeling indicates that the cooling to near-surface temperatures in the different parts of the Sierras Pampeanas, as far as has been traced by the AHe thermochronometer, occurred

between the Latest Cretaceous and the Paleogene (Figs. 7.5, 7.6, and 7.7). Although it is geologically evident that the Neogene flat-slab subduction period led to the uplift of the present-day Sierras Pampeanas (e.g. Ramos et al. 2002), the new thermochronological results discussed here strongly indicate that a positive topography already existed before the Paleogene. Thus, we conclude that previous models (e.g. Ramos et al. 2002) overestimated the amount of uplift attributed to this event. Instead, it might be considered that the Andean compression led to an accentuation of a pre-existing relief in the Southern Sierras Pampeanas.

7.5.4 Paleosurfaces and Denudation Rates

The Sierras Pampeanas uplifts are defined as a broken foreland during the Andean Orogeny and, at least in their recent structural configuration, as distinctive surficial characteristics of the Pampean flat-slab segment of the subducting Nazca Plate (Jordan et al. 1983, Jordan and Allmendinger 1986, Ramos et al. 2002). However, the age and the pre-Andean morphotectonic evolution of those planation surfaces, which are mainly developed on the eastern side of the ranges, have not yet been completely clarified (e.g. Jordan et al. 1983, Carignano 1999, Rabassa et al. 2010). Since almost no pre-Quaternary sedimentary cover is preserved atop the ranges for constraining the post-Paleozoic relief, the erosional surfaces themselves have to be envisaged as a key geometric marker for this purpose.

Ideas about the geomorphological evolution of the Sierras Pampeanas have already been described and controversially discussed in early works (e.g. Stelzner 1885, Brackebusch 1891, Bodenbender 1890, Bodenbender 1895, Bodenbender 1911, Gross 1948, González Bonorino 1950; see also Rabassa et al. 2010 for a recent review). The Evolution has been discussed in two ways:

Gonzalez Diaz (1981) and Criado Roque et al. (1981), based on the ideas of Bodenbender (1905) and Bodenbender (1911), suggested that planation surfaces represent a continuous and essentially synchronous surface, which was uplifted and disrupted during the Andean Orogeny.

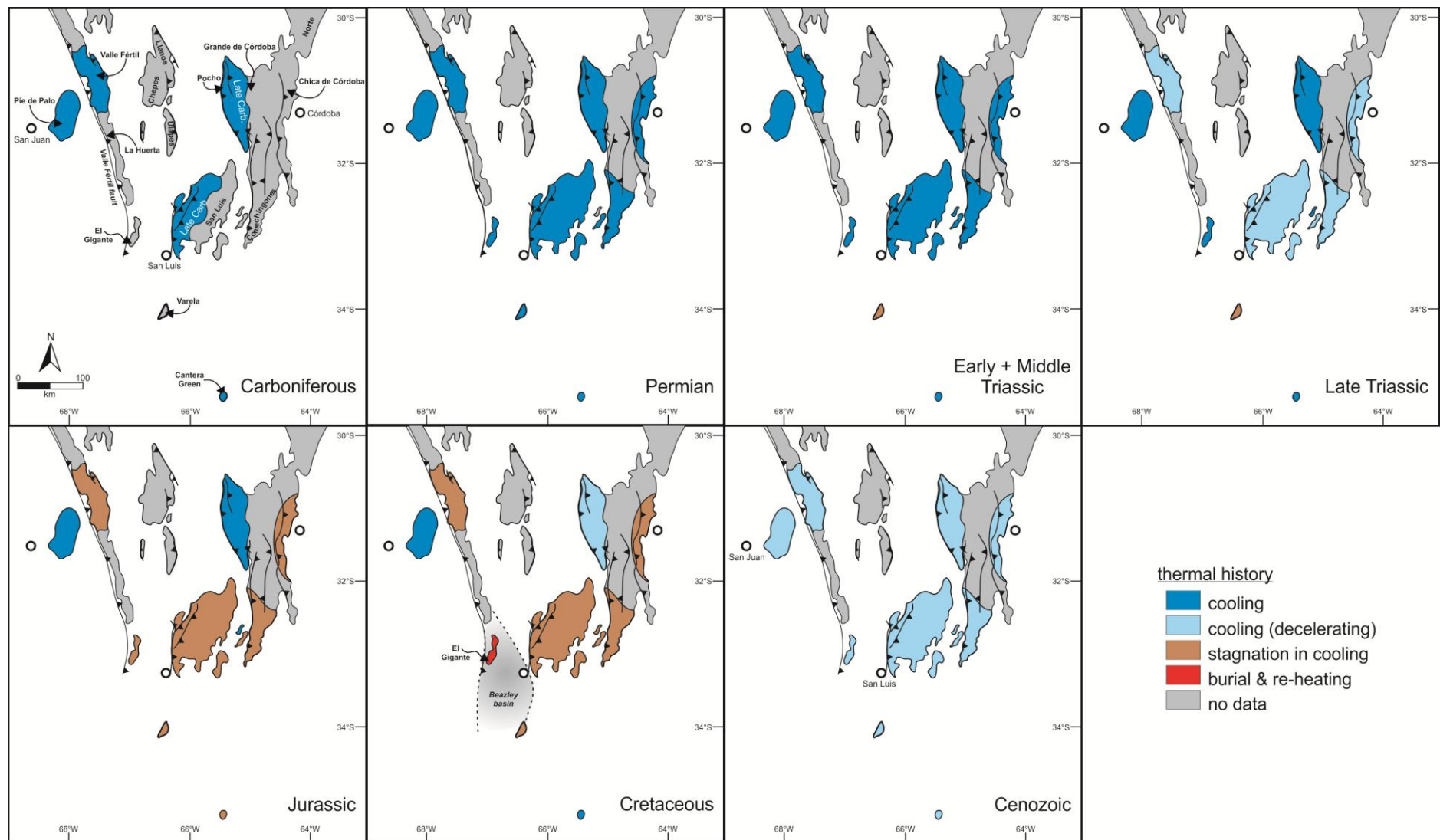


Fig. 7.6: Map highlighting areas of cooling, stagnation in cooling as well as burial and re-heating within the Sierras Pampeanas from Carboniferous to Cenozoic times, based on thermal modeling. Fault locations according to González Bonorino (1950) and Jordan and Allmendinger (1986). Further details are discussed in the text.

Alternatively, Rovereto (1911) first introduced the idea of a diachronous development of the erosional surfaces in the Sierras Pampeanas and considered Paleozoic to Mesozoic ages. The idea of diachronous development was later picked up by other authors (e.g. Jordan et al. 1983, Carignano et al. 1999, Carignano et al. 1999), who suggested that topographic scarps between distinct surfaces were the result of juxtaposition of several, individual surfaces with diachronous ages ranging from the Late Paleozoic to the Paleogene.

Although initially not intended to date paleo-land-surfaces or erosional surfaces, recent thermochronological data for the Sierra de Comechingones, Sierra de San Luis, Sierra de Aconquija and Cumbres Calchaquies, and the Sierra Pie de Palo (see Figs. 7.4 and 7.5) support the idea of a diachronous development of erosional surfaces in Jurassic to Cretaceous times.

Especially AHe ages, as well as the calculated denudation rates of the Sierras de San Luis and Comechingones (see above), fit with the suggested formation age of the erosional surfaces proposed by Carignano (1999). However, AHe ages can only be used as an indirect age constraint for erosional surfaces, because exact denudation rates, which led to exhumation of the samples from the PRZ_A to surface temperatures, are unknown. This is especially important for areas where numerous faults of unknown age are penetrating the basement, as observed in the Southern Sierras Pampeanas (e.g. Simpson et al. 2001, Bense et al. (in review A, in press).

Thermochronological data presented in this study (Figs. 7.4 and 7.5), as well as data published by Löbens et al. (2011), indicate slow denudation rates of the basement during Mesozoic and Cenozoic times. Assuming a geothermal gradient of around 25 °C/km (Sobel and Strecker 2003, Löbens et al. 2011) and the effective closure temperature of the AHe system (approximately 60°C), the upper thermal boundary of the paleo-PRZ_A would have been located at 2300 m depth. A Mesozoic sedimentary cover can be excluded for basement samples taken in the Sierras de San Luis and Comechingones (Löbens et al. 2011), as well as for most samples presented in this study. Thus, the age of passage through the PRZ_A of those basement samples allow the calculation of very rough denudation rates for the Pampean basement. These rates vary between 0.010 and 0.024 km/Ma, which is close to those of Jordan et al. (1989) and Löbens et al. (2011). Those rates are considerably small (see Ahnert 1970); therefore, we consider quite stable conditions within the Sierras Pampeanas since samples passed through the PRZ_A in Jurassic to Cretaceous times.

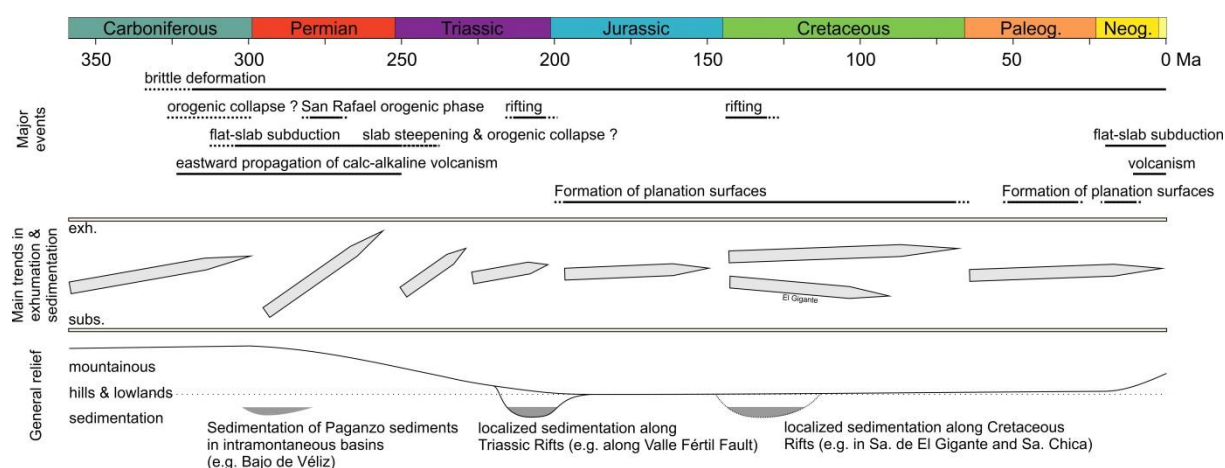


Fig. 7.7: Summary of the major geological events, sedimentation periods, mean trends in exhumation or subsidence (see also Fig. 7.6) and the deduced relief evolution of the southern Sierras Pampeanas. Details are described in the text.

7.5.5 Comparison of the Northern and Southern Pampean Ranges

The thermochronological data from the Eastern and Western Sierras Pampeanas and the new data presented in this study (Figs. 7.4 and 7.5) suggest similarities as well as important differences concerning the thermal and structural evolution of these regions compared to that of the northern Pampean ranges (e.g. Sobel and Strecker 2003, Mortimer et al. 2007).

Within both areas, onset of the thermochronological record happened during the Late Paleozoic. In the northern Pampean ranges, cooling and exhumation within the temperature interval of approximately 200 °C is probably related to erosion affecting a pronounced relief generated during former orogenic phases in the Paleozoic (e.g. Löbens et al. 2013), similar to the most westerly mountain ranges of the Western Sierras Pampeanas, i.e. the Sierra de Pie de Palo and the Sierra Valle Fértil, as well as the Sierra de Pocho in the Eastern Sierras Pampeanas. The onset of cooling concerning the temperature interval of the ranges farther in the south of the Sierras Pampeanas, i.e. the Sierra de Comechingones, the Sierra de San Luis, the Sierra del Gigante, the Sierra de Varela, and Cantera Green, is presumably caused by a Permo-Triassic compressional event (see above). This process probably also affected the region of the Sierra de Pie de Palo and the Sierra Valle Fértil, leading to further cooling and exhumation within these areas. Whether it also had an effect on the northern Pampean ranges cannot be excluded, but it is not very likely. Furthermore, this compressional phase is potentially related to a Permo-Triassic flat-slab subduction, as suggested by the decreasing ages of arc-related volcanism towards the east, shown by Ramos and Folguera (2009), which is analogous to the Andean flat-slab subduction (e.g. Barazangi and Isacks 1976, Pardo Casas and Molnar 1987, Smalley and Isacks 1990, Cahill and Isacks 1992, Löbens et al. 2011). However, since the north-south extension of this flat-slab segment was presumably restricted to the more southern parts of the recent Sierras Pampeanas, i.e. the Eastern and Western Pampean ranges, the most northern mountain ranges, e.g. the Sierra de Aconquija and the Cumbres Calchaquíes, were not affected.

The Mesozoic cooling and exhumation or burial re-heating in the northern and southern parts of the Sierras Pampeanas are mainly linked to rift events and the position of the individual ranges relative to the related rift basins. The Triassic rifting mainly affected the Western Sierras Pampeanas, and the thermochronological record also suggests considerable cooling activity, especially for the mountain ranges proximal to the rift; The Eastern Sierras Pampeanas and the northern Pampean ranges can be characterized by a period of more or less thermal stability during that time. In contrast, Cretaceous rifting generally affected the more easterly part of the Sierras Pampeanas (e.g. Rossello and Mozetic 1999, Ramos et al. 2002), which also includes the Sierra de Aconquija and the Cumbres Calchaquies in the north. Therefore, there was particular cooling and exhumation or burial re-heating in these regions, i.e. Sierra de Aconquija (Sobel and Strecker 2003) and the Sierra del Gigante, respectively, during that time, whereas the westernmost exposures of the Sierras Pampeanas were less affected.

The most important differences between the northern Pampean ranges and the Western and Eastern Sierras Pampeanas concern the thermal evolution during the Paleogene and the Neogene. The basement in the former region was partly affected by burial re-heating during the Paleogene, which was presumably related to the early uplift of the Puna Plateau, accompanied by sedimentation into foreland basins (e.g. Mortimer et al. 2007). Subsequently, the development of the modern topography, i.e. exhumation and uplift of the recent mountain ranges, dominantly occurred during the Neogene (e.g. Coughlin et al. 1998, Sobel and Strecker 2003, Carrapa et al. 2005, Mortimer et al. 2007). Whether this is related to the Miocene flat-slab subduction of the Nazca Plate beneath the South American Plate (e.g. Barazangi and Isacks 1976, Pilger 1981, Jordan and Allmendinger 1986), as previously generally proposed in the literature (e.g. González Bonorino 1950, Ramos et al. 2002), is not constrained by thermochronological data. Therefore, it could be possible that there is a correlation between the uplift of the northern Pampean ranges and the shallowing of the Nazca Plate, but there is no clear thermochronological indication.

In contrast, thermochronological data and related cooling models suggest that the regions of the Eastern and Western Sierras Pampeanas have generally been characterized by cooling and exhumation to near-surface temperatures since the Late Cretaceous to Paleogene, and locally even earlier than Late Cretaceous (i.e. Sierra de Pocho). Thus, exhumation occurred considerably earlier than in the northern Pampean ranges. To what extent the Andean deformation during the Neogene contributed to the overall exhumation and uplift within these regions and whether these processes are linked to the Miocene flat-slab subduction is not clearly illuminated by the thermochronological data. Nevertheless, the proposed Neogene influence, including the flattening of the subduction angle of the Nazca Plate, has obviously been overestimated so far.

7.6 Conclusions

- Locally, the oldest cooling event occurred during the Carboniferous, which we relate to a period of orogenic collapse.
- New thermochronological data show pronounced cooling during Permian to Triassic times. We attribute this to a period of flat-slab subduction at these latitudes, which clearly shows a distinct propagation of cooling activity from the Southwestern Sierras Pampeanas to the east in Early to Middle Triassic times. Additional evidence comes from an eastward propagation of Late Paleozoic calc-alkaline magmatism from the Southern Central Andes to the Southwestern Sierras Pampeanas during that period.
- Cooling decelerated or stagnated during the Late Triassic until the Early Cretaceous. This is contemporaneous with two rift events affecting the Sierras Pampeanas. Burial re-heating and the reset of AHe ages is only observed in the Sierra del Gigante, which is related to Cretaceous sedimentary cover of the basement. This indicates that substantial sedimentary thicknesses were only accumulated along the narrow and spatially restricted Cretaceous rift basins, as well as the existence of topography during this time.
- Published and new thermochronological data from the Sierras Pampeanas indicate that cooling to near-surface temperatures occurred between the Late Cretaceous and the Paleogene. This strongly supports the idea that a positive topography already existed before Neogene flat-slab subduction. We conclude that the amount of uplift attributed to this event is overestimated by previous models. Instead, we suggest that the Andean flat-slab subduction just accentuated the pre-existing relief.
- AHe ages and denudation rates of the Sierras de San Luis and Comechingones, although initially not intended to date paleo-land-surfaces, support the formation age of erosional surfaces suggested by geomorphological studies. Denudation rates are considerably small, varying between 0.010 and 0.024 km/Ma; hence, we consider quite stable conditions since samples passed through the PRZ_A in Jurassic to Cretaceous times.
- Since the extent of the Permo-Triassic flat-slab is not well known, an effect on the northern Pampean ranges cannot be excluded, but, based on thermochronological data, it is not very likely. The Western and Eastern Sierras Pampeanas have generally been affected by exhumation to near-surface temperatures since Late Cretaceous to Paleogene times. In contrast, final cooling in the northern Pampean ranges, at least in the Sierra de Aconquija and Cumbres Calchaquies, occurred during the Neogene.

8 General Conclusions

In relation to the aims of this thesis (see Chapter 1.1), the following chapter summarizes the main conclusions on the thermochronological and morphotectonic evolution of the Eastern and Western Sierras Pampeanas. In addition to the results presented in this study, this conclusion incorporates findings from Löbens et al. (2013); see also Löbens (2012).

(1) The time-space disaggregation of the Late Paleozoic to Paleogene post-accretional cooling history of the Eastern and Western Sierras Pampeanas.

Our thermochronological data trace the time-temperature evolution of the Pampean basement blocks since their cooling below ca. 180°C (zircon He system) and their passage through the uppermost kilometres of the crust, allow us to extend the high-temperature cooling path of the Eastern Sierras Pampeanas of Steenken et al. (2008) down to surface temperatures (Fig. 8.1).

Based on our thermochronological findings, the main cooling episodes in the Eastern and Western Sierras Pampeanas can be identified as Carboniferous orogenic collapse, Permo-Triassic flat-slab subduction and Neogene flat-slab subduction (see below), although our data illustrate that the contribution of the latter is certainly smaller than previously thought. The effect of Permo-Triassic flat-slab subduction to the Sierras Pampeanas is postulated here for the first time. Generally, Jurassic and Carboniferous rift events are represented by stagnating temperature conditions and, thus, can be considered to be of minor importance to the cooling of the present-day Eastern and Western Pampean basement blocks.

In general, the following five major time increments can be deciphered from our data and related to regional geodynamic events (see Chapter 7.5):

Carboniferous: The oldest ages record a period of accelerated cooling during Carboniferous times, which we attribute to a geodynamic setting dominated by orogenic collapse subsequent to the Middle Paleozoic, multi-terrane accretion along the western margin of Gondwana (see Fig. 7.6, 7.7 and 8.2).

Permian to Early Triassic: Carboniferous cooling persisted in some Pampean ranges. In particular, the southern ranges of the Western Sierras Pampeanas experienced accelerated cooling during Permian times. Our data clearly show that this intensification in cooling propagated towards the eastern Pampean ranges until the Early to Middle Triassic. Based on our thermochronological data as well as on regional geological findings, we postulate that this distinct shift of cooling activity occurred in relation to a period of eastwardly-directed flat-slab subduction of a Farallon plate segment beneath the present-day South American plate at these latitudes (see Fig. 7.6, 7.7 and 8.2). Although indications of Late Paleozoic flat-slab subduction has already been recognized in the Central

Cordillera region (Martinez et al. 2006, Ramos and Folguera 2009), our data offer the first geological evidence for this event in the Sierras Pampeanas. In relation to total exhumation, the Permo-Triassic cooling comprises the main exhumation event concerning the difference overcome in depth from the PRZ_Z to the PAZ_A and PRZ_A, respectively. Depending on geothermal gradient, the latter is in a range of up to 6 km.

Late Triassic to Early Jurassic: Generally, the Late Triassic and Early Jurassic are characterized by stagnation in cooling related to rifting along Late Proterozoic-Middle Paleozoic terrane boundaries. Inverse to the onset of flat-slab-related cooling, cooling first ceased in the Eastern Pampean regions and propagated westwards until Late Triassic times (see Fig. 7.6, 7.7 and 8.2). Although re-steepening of the subduction angle of the flat-slab segment may have led to tensional forces in the crust, supporting crustal extension and stagnation in cooling in the Late Triassic to Early Jurassic, a causal consequence between both cannot be concluded from our data.

Late Jurassic to Early Cretaceous: Stagnation in cooling related to rifting and crustal extension persisted during this period. Burial re-heating and reset of AHe ages due to Cretaceous sedimentary basement cover is only observed in a single sample, located within a Cretaceous rift basin (Sierra de El Gigante). It follows that sedimentary thicknesses, substantial enough to have led to the reset of AHe cooling ages, were only accumulated along narrow and spatially-restricted Cretaceous rift basins, while the surrounding area certainly maintained a positive topography during this time span (see Fig. 7.6, 7.7 and 8.2).

Late Cretaceous to Paleogene: Cooling to near surface temperatures, as far as traced by the apatite He thermochronometer, occurred between the Latest Cretaceous and Early Paleogene times. This strongly supports the idea that a positive topography already existed before Neogene flat-slab subduction. Based on our data, we conclude that the amount of exhumation and uplift attributed to this event is overestimated by previous models. Instead, we suggest that the Andean flat-slab subduction only accentuated the pre-existing relief (see Fig. 7.6, 7.7 and 8.2).

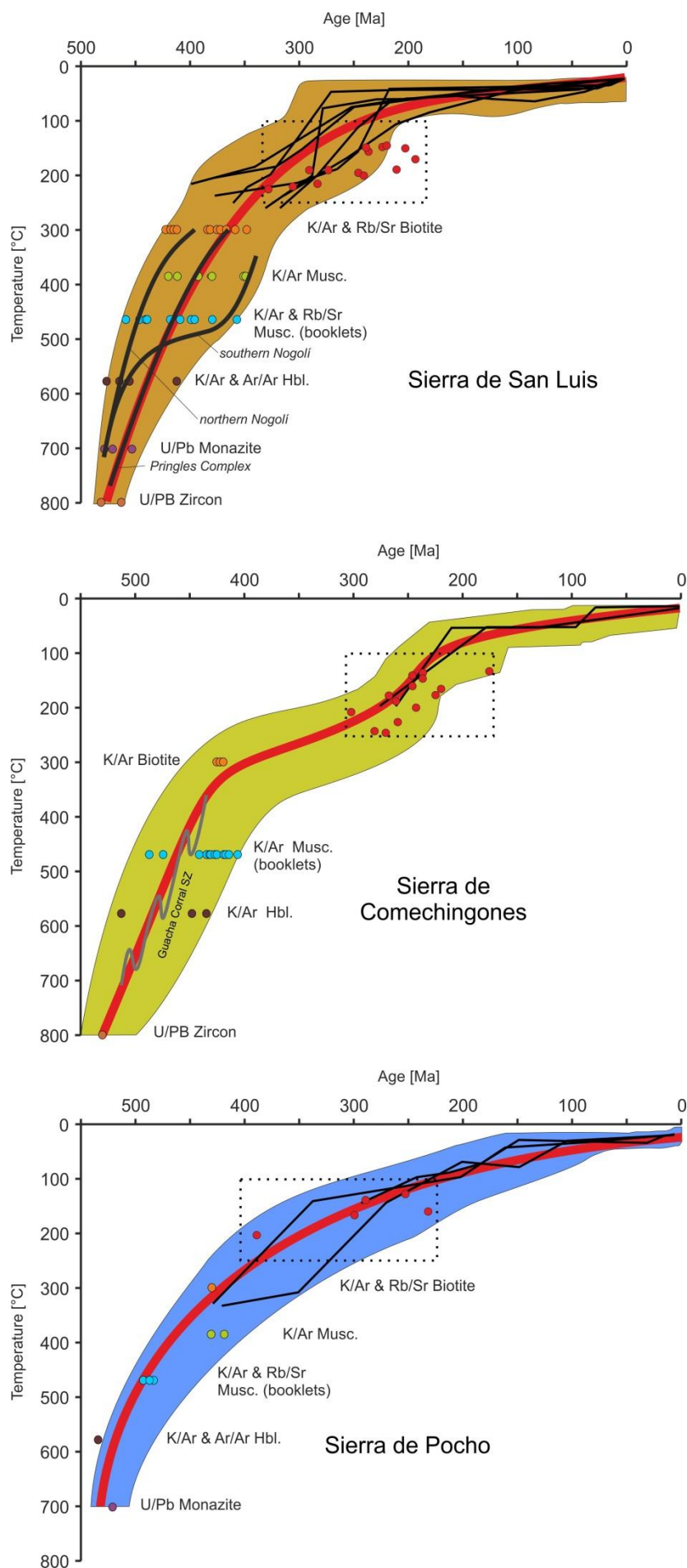


Fig. 8.1: Compilation of high- and low temperature thermochronological data from the Eastern Sierras Pampeanas (Sierras de San Luis, Comechingones and Pocho) in a single time-temperature path. High-temperature data were extracted from Rapela et al. (1998), Escayola et al. (2007), Steenken et al. (2006, 2008, 2010). Colored circles indicate age of respective thermochronometer; thick red line mark the averaged cooling path; black line indicate modelled time-temperature history based on our low-temperature thermochronological data; dotted rectangle give range of K-Ar illite fault-gouge ages; illite ages are displayed at different position along y-axes for a better view.

(2) *The identification of a potential modification in the exhumation and uplift history since Neogene times.*

In Neogene times, the Juan-Férrandez Ridge was incorporated into the subduction of the Nazca plate beneath the South American Plate. To identify any modification in exhumation and uplift history of the Pampean ranges since the onset of flat-slab subduction, we collected thermochronological samples from above the inferred flat-slab segment, as well as from adjacent areas to the north and south, where normal subduction persisted. Evaluation of data obtained from both locations provides no trace of substantial Neogene uplift, which contradicts the well-established hypothesis that the exhumation and uplift of the Sierras Pampeanas are almost entirely related to Neogene flat-slab subduction. In contrast, we can show that the main exhumation event in the Eastern and Western Sierras Pampean occurred from Permian to Triassic times due to a flat-slab subduction segment of the Farallon plate (see above). The latter comprises around 40-50 % of the total exhumation traced by the thermochronological methods used.

Although our data show no explicit evidence for any Cenozoic exhumation and uplift, aspects from regional geology indicate that range uplift occurred after the Paleocene (e.g. Costa 1992; Costa et al. 1999; Ramos et al. 2002). In addition, neotectonic deformation is evident. For instance, according to Costa 1992, the Sierra de San Luis is currently characterized by moderate-to-low Quaternary uplift rates of < 0.1 mm/a. Considering the geothermal gradient, depth of the Paleo-PRZ and Paleo-PAZ, peak elevation of mountain ranges and altitude differences between samples, we can constrain the exhumation in the Sierras de Comechingones and San Luis to approximately 450-550 m since Late Cretaceous times, which corresponds to a maximum of 20 % of the total exhumation recorded by our data. Similar values are considered for the other mountain ranges of the Eastern and Western Sierras Pampeanas.

We can conclude that in relation to the exhumation of the Sierras Pampeanas in pre-Cenozoic times, the amount of exhumation attributed to Cenozoic compression and Neogene flat-slab subduction is of minor importance and overestimated by previous models (e.g. Ramos et al. 2002). In contrast to those, we consider the Cenozoic compression as simply accentuating a pre-existing relief (Fig. 8.2).

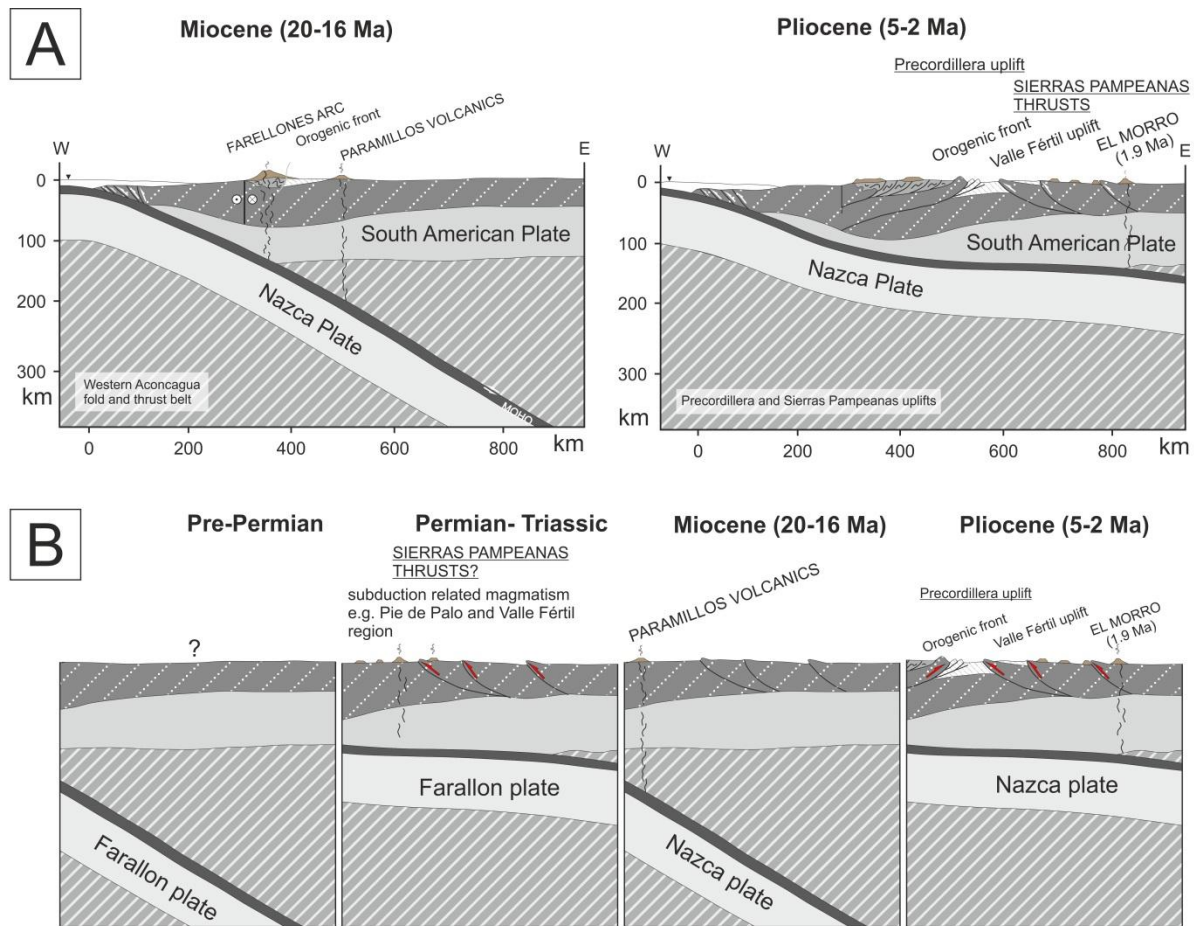


Fig. 8.2: A) The generally accepted exhumation and uplift scenario for the Sierras Pampeanas according to Ramos et al. (2002). Late Cenozoic stage of Pampean evolution associated with the shallowing of the Nazca plate subduction angle. The two cross-section in A) show normal subduction prior to Juan Fernandez Ridge collision (left) and last arc magmatic activity prior to the present-day cessation of magmatism in the Sierras Pampeanas. In comparison, in B) we propose a modification of this evolution model based on thermochronological data. Data show that substantial uplift occurred in Permian to Triassic times which can be related to a flat-slab subduction event. For more details see text above and Chapter 7.5. Cross-sections modified from Ramos et al. (2002).

(3) *Improving knowledge of the formation time of erosional surfaces in the Pampean ranges as well as confining the existence of a pronounced positive relief in the eastern Sierras Pampeanas in pre-Neogene times.*

The Eastern and Western Pampean ranges show several planation surfaces at different altitudes. Those surfaces are especially well-developed in the Eastern Sierras Pampeanas (i.e. Sierra de Comechingones and San Luis). The evolution of those surfaces and, thus, the geomorphological evolution of the Pampean ranges has generally been discussed in two ways: (1) all present-day planation surfaces represent remnants of continuous and essentially synchronous surfaces, which were uplifted and juxtaposed during the Andean Orogeny (e.g. Criado Roque et al. (1981) and (2) planation surfaces are diachronous in age, representing individual surfaces which have developed as a consequence of different events from Late Paleozoic to Paleogene times (see Rabassa 2010). In any case, the ages of the pre-Andean planation surfaces have not completely been clarified yet. Since almost no pre-Quaternary sedimentary cover is preserved atop the ranges for constraining the post-

Paleozoic relief, the erosional surfaces themselves have to be envisaged as a key geometric marker to constrain their formation age.

Taking into account aspects from regional geology, the Triassic and Late Jurassic to Early Cretaceous epochs are not well suited for the regional development of extensive planation surfaces in the Eastern and Western Sierras Pampeanas due to the prevalence of crustal tectonics. As a consequence, regional planation processes most likely took place either during the Early-Middle Jurassic and/or during the Late Cretaceous. This idea is supported by the heterogeneous and discontinuous deposition of terrigenous sediments since Late Carboniferous times and the absence of Jurassic deposits, suggesting the existence of a pronounced positive morphology in the Sierras Pampeanas.

Our apatite He cooling ages as well as the calculated denudation rates of the Sierras de San Luis and Comechingones (see below) fit with the suggested formation age of the erosional surfaces proposed by Carignano et al. (1999) (Fig. 8.3). However, apatite He ages can only be used as an indirect age constraint for erosional surfaces, because exact denudation rates, which led to exhumation of the samples from the PRZ_A to surface temperatures, are unknown. This is especially important for areas where numerous faults of unknown age penetrate the basement, as documented for all eastern Pampean mountain ranges by our K-Ar illite fault-gouge data (see below). Thus, although initially not intended to date paleolandscapes, our thermochronological data support the idea of a diachronous development of planation surfaces in Jurassic to Cretaceous times.

Denudation Rates

Considering a range of reasonable geothermal gradients and the depth of apatite Paleo-PRZ, our thermochronological data allow the calculation of very rough denudation rates for the Eastern and Western Pampean basement. The calculated rates are considerably small, varying between 0.010 to 0.024 km/Ma. Based on that, we conclude that quiet stable conditions persisted in the Sierras Pampeanas, since samples passed through the PRZ_A, which occurred predominantly in Jurassic to Cretaceous times (Fig. 8.1).

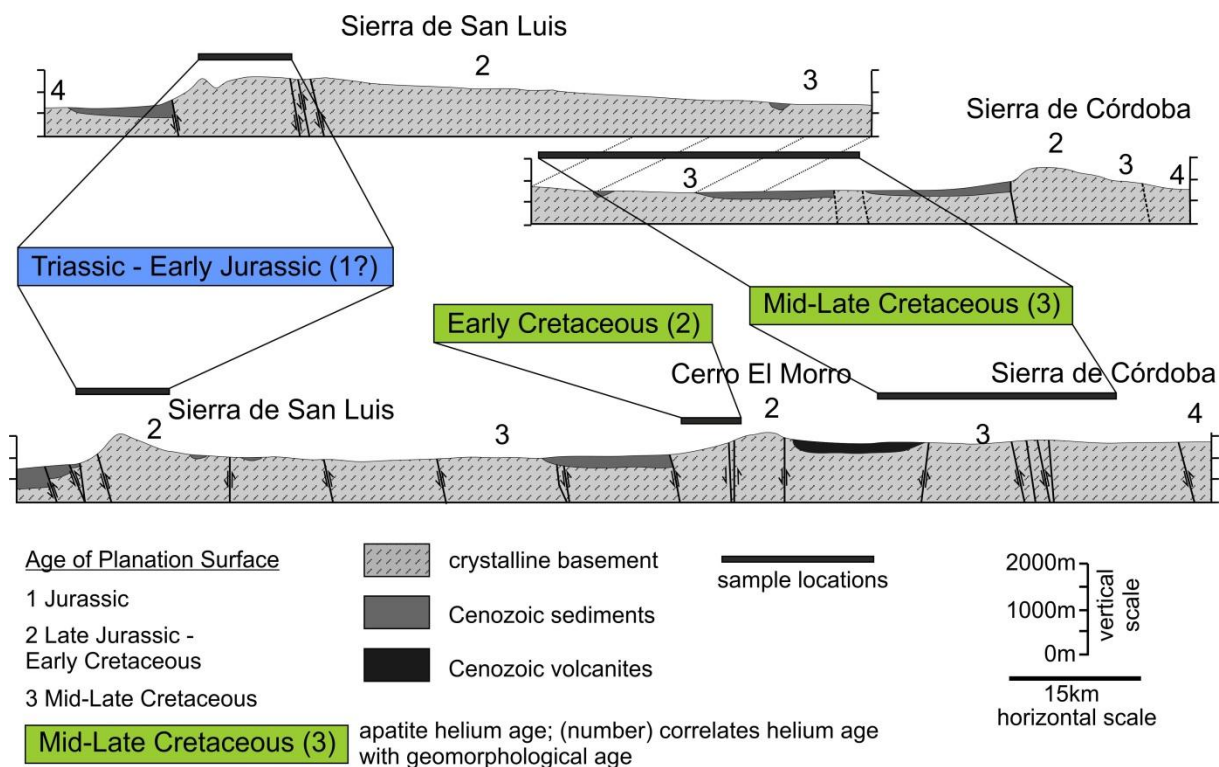


Fig. 8.3: Correlation of proposed formation age of erosional surfaces in Eastern Sierras Pampeanas with apatite helium data presented in this study. In general ages from geomorphological considerations and low-temperature thermochronologie are in good agreement. For the Sierra de San Luis our data propose an even older erosional surface. However, differences may arise from fault activity along numerous fault zones along the profile and/or low denudation rates (see Chapter 0). Geomorphological profile modified from Carignano et al. (1999).

(4) Analysis of gouge-bearing fault systems and the evaluation of the brittle deformation activity in the Eastern Sierras Pampeanas as revealed by K-Ar illite fine-fraction dating on clay gouges.

The K-Ar illite fine-fraction ages provided by clay gouge document the onset of brittle deformation in the Eastern Sierras Pampeanas in Carboniferous times, directly after the cooling of the basement to temperatures of about 300°C. The oldest ages coincide with basement cooling to brittle deformation temperatures, while younger illite ages cover the time span of low-temperature cooling and exhumation history, as revealed by our thermochronological data. It was shown that the youngest illite ages represent the cooling of the basement below illite formation temperatures but not the end of brittle deformation (see Chapters 4.6.1 and 6.5).

The age pattern derived from K-Ar fault-gouge dating documents long-lasting brittle fault activity. Generally, the age pattern can be split into four different episodes. We relate ages <320 Ma to the end of the Chanic phase of the Famatinian Orogeny, which can be shown to be synchronous with the transition from ductile to brittle deformation behavior in the Eastern Sierras Pampeanas. Early and Middle Permian ages can be related to a flat-slab subduction episode of the Farallon plate beneath the South American plate. Middle-to-Late Permian until the Triassic ages correlate with major extensional events, while Jurassic-to-Early Cretaceous ages are contemporaneous to a period of substantially normal faulting in the study region.

Additionally, our data reveal a strong north-south variation in fault-gouge ages in the Eastern Sierras Pampeanas, which we interpret to represent a distinct southward propagation of cooling below 300°C. Those observations are in perfect accordance with our thermochronological data as well as high temperature cooling ages for this region (see Chapters 4.6.1 and 6.5).

(5) Development of concepts to constrain K-Ar illite fine-fraction ages by integrating results from clay mineralogy, thermochronology and geochronology, as well as the evaluation of its tectonic significance in terms of gouge formation and fault activity.

In order to evaluate the tectonic significance of the K-Ar fault-gouge dating technique as well as to constrain the "deformation path" of the Sierras Pampeanas (see above), we cross-evaluated K-Ar illite fine-fraction ages from brittle fault gouges with several independent parameters, i.e. illite crystallinity, illite polytype quantification, grain-size, mineralogical observations, K-Ar muscovite and biotite host-rock cooling ages, as well as low-temperature thermochronological data (see Chapters 4.6 and 6.5).

We were able to show that the development of illite in clay gouges from non-sedimentary rocks during successive regional cooling can be interpreted as a subsequent formation of 2M₁, 1M and 1M_d illite polytypes. High- and low-temperature thermochronological data prove that conditions were sufficient for the development of the 2M₁ illite polytype within a fault gouge. This is especially true for regions affected by long-lasting brittle deformation and/or in slowly cooling regimes. Additionally, we found that Illite age extrapolation, although effected by several methodological issues, can provide valuable information, e.g. deciphering a possible contamination of illite fine-fractions with host-rock muscovite phases as well as dating the last illite forming event, which may coincide with cooling below illite formation temperatures or the end of brittle deformation activity (see Chapters 0 and 0).

In general, we were able to show that the approach presented here (see Fig. 4.4) to interpret K-Ar illite fine-fraction ages of fault gouges from non-sedimentary host rocks provides a powerful tool for evaluating the cooling and deformation history of a region. The combination of results from different independent methods allows the user to evaluate the integrity of the data set, which may significantly enhance the reliability of interpretations made. In combination with paleostress analysis, this method can become even more meaningful in the evaluation of complex geodynamic histories.

(6) Comparison between Northern and Southern Sierras Pampeanas

The following chapter highlights the most important differences in thermal evolution between the northern and southern Pampean ranges. For more details, the reader is referred to Löbens 2012 (see also Löbens et al. 2013), who investigated the thermochronologic and morphotectonic evolution of the northern Sierras Pampeanas in detail.

Generally, within both the northern and southern Pampean regions, the thermochronological evolution recorded by zircon He dating started during the Late Paleozoic. In the northern Pampean ranges, this can be related to the latest stage of the Famatinian Orogeny from Devonian to Carboniferous times.

The first significant differences in the cooling history occurred during the Mesozoic. While the eastern and western Sierras Pampeanas are generally characterized by almost stagnant cooling, the northern Pampean ranges are partially affected by distinct cooling and exhumation, especially in Late Cretaceous to Early Jurassic times.

The most important differences between both regions can be observed in the Cenozoic thermal evolution. Our thermochronological data show that the regions of the southern Pampean ranges were generally exhumed to near-surface temperatures until the Late Cretaceous / Early Paleogene (see above), while the northern Pampean ranges were still affected by substantial burial and re-heating during the Paleogene, which was caused by sediments derived from the early Puna Plateau to the west. Furthermore, our thermochronological data show that the main exhumation and uplift episode of the northern mountain ranges occurred during the Neogene. We estimate the maximum amount of exhumation in the northern Sierras Pampeanas to have been upwards of 6-8 km since the Late Cenozoic, while the southern Pampean ranges are generally characterized by significantly smaller values, perhaps even as small as 0.5 km since the Cenozoic. Whether exhumation and uplift in the northern Pampean ranges is related to the Neogene flat-slab subduction of the Nazca Plate (see above) ultimately cannot be clarified, but no obvious indication of this event is evident in our data.

9 Outlook

- The studies and methodological approaches presented in this thesis offer starting points for future research in the following fields:
- Field studies should further focus on paleostress analyses. Paleostress data may be used in combination with fault gouge analyses data to decipher fault activity and reactivation in relation to the stress field.
- Dating rock exposure ages with cosmogenic nuclide dating (e.g. ^{26}Al , ^{36}Cl) may constrain calculated denudation rates and give further insight into the timing of planation surface formation.
- (U-Th)/He dating on epidote may provide further insight into the low temperature branch in the cooling history of the Sierras Pampeanas. First indications suggest a relatively low closure temperature for this phase, certainly below the AHe closure temperature, which may even trace any Cenozoic exhumation in the Eastern and Western Sierras Pampeanas.
- Ar-Ar dating of K-Feldspar can provide a continuous time-temperature cooling path (multi diffusion domain model), which may further constrain the thermal evolution of the Sierras Pampeanas.
- Further evaluate the closure temperature of K-Ar illite system by laboratory experiments and a detailed review of data from field studies.
- Further studies should assess the diffusion behavior of Ar in illite in relation to time and temperature conditions, analogue to the PAZ/PRZ model for the He and AFT dating systems.
- Theoretical and experimental studies should further assess the temperature range under which illite may be formed, especially in different geotectonic regimes such as prograde sedimentary environment, retrograde environment like the fault zones investigated in this study, as well as hydrothermal systems.
- Theoretical and experimental studies should address possibilities to mechanically separate different illite generations and/or illite polytypes, e.g. by magnetic separation.

10 References

- Abad I, Nieto F, Peacor DR, Velilla N (2003) Prograde and retrograde diagenetic and metamorphic evolution in metapelitic rocks of Sierra Espuna (Spain). *Clay Minerals* 38(1):1–23. doi:10.1180/0009855033810074
- Aceñolaza G, Toselli AJ (1988) El Sistema de Famatina, Argentina: su interpretación como orógeno de margen continental activo. In: V° Congreso Geológico Chileno, vol 1, pp A55–67
- Ahnert F (1970) Functional relationships between denudation, relief, and uplift in large, mid-latitude drainage basins. *American Journal of Science* 268(3):243–263. doi:10.2475/ajs.268.3.243
- Armstrong RL (1966) K-Ar dating of plutonic and volcanic rocks in orogenic belts. In: Schaeffer OA, Zähringer J (eds) *Potassium-Argon Dating*. Springer, Berlin, pp 117–133
- Aronson JL, Burtner RL (1983) K-Ar dating of illitic clays in Jurassic Nugget Sandstone and timing of petroleum migration in Wyoming Overthrust Belt. *AAPG Bulletin* 67(3):414. doi:10.1306/03B5AD6D-16D1-11D7-8645000102C1865D
- Aronson JL, Lee M (1986) K-Ar Systematics of Bentonite and Shale in a Contact Metamorphic Zone, Cerrillos, New Mexico. *Clays and Clay Minerals* 34(4):483–487. doi:10.1346/CCMN.1986.0340415
- Astini RA, Benedetto J, Vaccari N (1995) The early Paleozoic evolution of the Argentine Precordillera as a Laurentian rifted, drifted, and collided terrane: A geodynamic model. *Geological Society of America Bulletin* 107(3):253–273
- Azcuy CL, Carrizo H, Caminos R (1999) Carbonífero y Pérmico de las Sierras Pampeanas, Famatina, Precordillera, Cordillera Frontal y Bloque de San Rafael. *Instituto de Geología y Recursos Minerales Geología Argentina* 29:779–784
- Bahlburg H, Breitkreuz C (1991) Paleozoic evolution of active margin basins in the southern Central Andes (northwestern Argentina and northern Chile). *Journal of South American Earth Sciences* 4(3):171–188
- Bähr R, Lippolt HJ, Wernicke R (1994) Temperature-induced ^4He degassing of specularite and botryoidal hematite: A ^4He retentivity study. *Journal of Geophysical Research* 99:17695–17707
- Bailey SW (1966) The status of clay mineral structures. *Proceedings of the 14th National Conference on Clays and Clay Minerals*:1–23
- Bailey SW, Frank-Kamenetskii VA, Goldshtaub S, Kato A, Pabst A, Schulz H, Taylor HFW, Fleischer M, Wilson AJC (1977) Report of the International Mineralogical Association (IMA)-International Union of Crystallography (IUCr) Joint Committee on Nomenclature. *Acta Crystallographica Section A Foundations of Crystallography* 33(4):681–684. doi:10.1107/S0567739477001703
- Bailey SW, Hurley PM, Fairbairn HW, Pinson WH, Jr. (1962) K-Ar dating of sedimentary illite polytypes. *Geological Society of America Bulletin* 73(9):1167–1170
- Baldis B, Peralta S, Villegas R (1989) Esquematisaciones de una posible transcurriencia del terrane de Precordillera como fragmento continental procedente de areas pampeano-bonaerenses. *Correlaciones Geológicas*. *Correlaciones Geológicas*(5):81–100
- Baldo E, Casquet C, Galindo C (1998) Datos preliminares sobre el metamorfismo de la Sierra de Pie de Palo, Sierras Pampeanas Occidentales (Argentina). *Geogaceta*(24):39–42
- Baldo E, Casquet C, Pankhurst RJ, Galindo C, Rapela CW, Fanning C, Dahlquist J, Murra J (2006) Neoproterozoic A-type magmatism in the Western Sierras Pampeanas (Argentina): evidence for Rodinia break-up along a proto-lapetus rift? *Terra Nova* 18(6):388–394
- Baldwin SL, Lister GS (1998) Thermochronology of the South Cyclades Shear Zone, Ios, Greece: effects of ductile shear in the argon partial-retention zone. *Journal of Geophysical Research*(103):7315–7336. doi:10.1029/97JB03106
- Barazangi M, Isacks BL (1976) Spatial distribution of earthquakes and subduction of the Nasca plate beneath South America. *Geology* 4:686–692
- Barbarand J, Carter A, Hurford T (2003) Variation in apatite fission-track length measurement: implications for thermal history modeling. *Chemical Geology* 198:77–106
- Battaglia AAC (1982) Descripción Geológica de las Hojas 13f, Río Hondo; 13g, Santiago del estero; 14g, El Alto; 14h, Villa San Martín; 15g, Frias (Provincias de Santiago del estero, Catamarca y Tucumán). *Boletín*, vol 186, Buenos Aires

- Benjamin MT, Johnson NM, Naeser CW (1987) Recent rapid uplift in the Bolivian Andes; evidence from fission-track dating. *Geology Boulder* 15(7):680–683
- Bense FA, Löbens S, Dunkl I, Wemmer K, Costa CH, Siegesmund S (in review A) Exhumation history and landscape evolution of the southeastern Sierras Pampeanas, Argentina – a low-temperature multichronometer approach. *International Journal of Earth Sciences*
- Bense FA, Wemmer K, Löbens S, Siegesmund S (in press) Fault gouge analyses: K-Ar illite dating, clay mineralogy and tectonic significance – A study from the Sierras Pampeanas, Argentina. *International Journal of Earth Sciences*
- Bense FA, Löbens S, Dunkl I, Wemmer K, Siegesmund S (in review B) Is the exhumation of the Sierras Pampeanas just related to Neogene flat-slab subduction? Implications from a multi-thermochronological approach. Submitted to the *Journal of South American Earth Sciences*
- Bodenbender G (1890) La cuenca del valle del Río Primero en Córdoba. Descripción geológica del Río Primero desde la Sierra de Córdoba hasta la Mar Chiquita. *Boletín de la Academia Nacional de Ciencias*(12):5–55
- Bodenbender G (1895) Devónico y Gondwana en la República Argentina. *Boletín de la Academia Nacional de Ciencias* 15(2-3):201-252
- Bodenbender G (1905) La Sierra de Córdoba. Construcción geológica y productos minerales de aplicación. *Anales del Ministerio de Agricultura de la Nación, Sección Geología* 1(2):1–146
- Bodenbender G (1911) Constitución geológica de la parte meridional de la provincia de La Rioja y regiones limítrofes. República Argentina. *Boletín de la Academia Nacional de Ciencias* 19(1):2-211
- Bollinger G, Langer C (1988) Development of a velocity model for locating aftershocks in the Sierra Pie de Palo region of western Argentina. *Bulletin of the U.S. Geological Survey*(1795):1–16
- Bonalumi A, Martino RD, Sfragulla J, Carignano C, Tauber A (2005) Hoja Geológica 3363-I. Villa Maria. Provincia de Córdoba. Servicio Geológico Minero Argentino Bulletin 347
- Brackebusch L (1891) Mapa geológico del interior de la República Argentina. Escala 1:1.000.000. Academia Nacional de Ciencias, Córdoba
- Brooks BA, Bevis M, Smalley RF, Jr., Kendrick E, Manceda R, Lauría E, Maturana R, Araujo M (2003) Crustal motion in the Southern Andes (26°–36°S): Do the Andes behave like a microplate? *Geochemistry Geophysics Geosystems* 4(10). doi:10.1029/2003GC000505
- Burtner RL, Nigrini A, Donelick RA (1994) Thermochronology of Lower Cretaceous source rocks in the Idaho-Wyoming thrust belt. *Bulletin* 78:1613–1636
- Cahill T, Isacks BL (1992) Seismicity and shape of the subducted Nazca Plate. *J. Geophys. Res.* 97(B12):17503. doi:10.1029/92JB00493
- Caillière S, Henin S, Rautureau M (1982) *Minéralogie des Argiles*. Masson, Paris
- Caminos R (1972) Sierras Pampeanas de Catamarca, Tucumán, La Rioja y San Juan. In: Leanza AF (ed) *Geología Regional Argentina*, Córdoba, pp 41–47
- Carignano C (1999) Late Pleistocene to recent climate change in Córdoba Province, Argentina: Geomorphological evidence. *Quaternary International* 57-58(1):117-134. doi:10.1016/S1040-6182(98)00054-8
- Carignano C, Cioccale M, Rabassa J (1999) Landscape Antiquity of the Central-Eastern Sierras Pampeanas (Argentina): Geomorphological Evolution since Gondwanic Times. *Zeitschrift für Geomorphologie* 118:245–268
- Carrapa B, Adelmann D, Hilley GE, Mortimer E, Sobel ER (2005) Oligocene range uplift and development of plateau morphology in the southern Central Andes. *Tectonics* 24(4)
- Carrapa B, Trimble JD, Stockli DF (2011) Patterns and timing of exhumation and deformation in the Eastern Cordillera of NW Argentina revealed by (U-Th)/He thermochronology. *Tectonics* 30(3):Citation TC3003
- Casquet C, Baldo E, Pankhurst RJ, Rapela CW, Galindo C, Fanning C, Saavedra J (2001) Involvement of the Argentine Precordillera terrane in the Famatinian mobile belt: U-Pb SHRIMP and metamorphic evidence from the Sierra de Pie de Palo. *Geology* 29(8):703–706. doi:10.1130/0091-7613(2001)029<0703:IOTAPT>2.0.CO;2
- Clauer N, Chaudhuri S (1998) *Isotopic dating of very low grade metasedimentary and metavolcanic rocks: techniques and methods*. Blackwell Science, Cambridge

- Clauer N, Liewig N, Zwingmann H (2012a) Time-constrained illitization in gas-bearing Rotliegende (Permian) sandstones from northern Germany by illite potassium-argon dating. *Bulletin* 96(3):519–543. doi:10.1306/07131111003
- Clauer N, Środoń J, Francu J, Sucha V (1997) K-Ar Dating of Illite Fundamental Particles Separated from Illite-Smectite. *Clay Minerals* 32(2):181-196. doi:10.1180/claymin.1997.032.2.02
- Clauer N, Zwingmann H, Liewig N, Wendling R (2012b) Comparative $^{40}\text{Ar}/^{39}\text{Ar}$ and K–Ar dating of illite-type clay minerals: A tentative explanation for age identities and differences. *Earth-Science Reviews* 115(1–2):76–96. doi:10.1016/j.earscirev.2012.07.003
- Cordani U, Milani EJ, Thomaz Filho A, Campos DA (eds) (2001) *Tectonic Evolution of South America*, Rio de Janeiro
- Costa CH (1987) Neotectónica de la sierra de San Luis: Resultados preliminares. In: 10° Congreso Geológico Argentino, Actas 1, Actas 1, pp 255–258
- Costa CH (1992) Neotectónica del sur de la Sierra de San Luis. PhD thesis, Universidad Nacional de San Luis
- Costa CH (1996) Análisis neotectónico en la sierra de San Luis y Comechingones: problemas y métodos. In: 13° Congreso Geológico Argentino, pp 285–300
- Costa CH (1999) Tectonica cuaternaria en las Sierras Pampeanas. *Anales Direccion Nacional del Servicio Geologico Report* 29:779-784
- Costa CH, Audemard M, Bezerra F, Lavenu A, Machette MN, Paris G (2006) An Overview of the Main Quaternary Deformation of South America. *Revista de la Asociación Geológica Argentina* 61(4):461–479
- Costa CH, Cortés JM (1993) Tectónica extensional en el extremo sur de la Sierra de San Luis. In: 12° Congreso Geológico Argentino, vol 3, pp 113–118
- Costa CH, Gardini CE, Ortiz Suárez A, Chiesa J, Ojeda G, Rivarola D, Strasser E, Morla P, Ulaco J, Tognelli G, Carugno Durán A, Vinciguerra H, Salas D (2001a) Hoja Geológica 3366-I San Francisco del Monte de Oro. *Servicio Geológico Minero Argentino Bulletin* 278:82
- Costa CH, Gardini CE, Schmidt CJ (1998) Dataciones $^{40}\text{Ar}/^{39}\text{Ar}$ y rasgos estructurales de la Formación Cerro Varela (Triásico), provincia de San Luis. *Revista de la Asociación Geológica Argentina* 53(2):282-285
- Costa CH, Giaccardi AD, Díaz EFG (1999) Palaeolandsurfaces and neotectonic analysis in the southern Sierras Pampeanas, Argentina. *Geological Society, London, Special Publications*(162):229-238. doi:10.1144/GSL.SP.1999.162.01.18
- Costa CH, Machette MN, Dart R, Bastías H, Paredes J, Perucca L, Tello G, Haller K (2000) Map and Database of Quaternary Faults and Folds in Argentina. In: *International Lithosphere Program, USGS. Open-file report* 00-0108, p 81
- Costa CH, Murillo VM, Sagripanti GL, Gardini CE (2001b) Quaternary intraplate deformation in the southeastern Sierras Pampeanas, Argentina. *Journal of Seismology* 5:399-409
- Costa CH, Vita-Finzi C (1996) Late Holocene Faulting in the southeast Sierras Pampeanas of Argentina. *Geology* 24:1127-1130
- Coughlin TJ, O'Sullivan PB, Kohn B., Holcombe RJ (1998) Apatite fission-track thermochronology of the Sierras Pampeanas, central western Argentina; implications for the mechanism of plateau uplift in the Andes. *Geology Boulder* 26(11):999–1002
- Criado Roque P, Mombrú C, Ramos VA, Yrigoyen MR (1981) Estructura e interpretación tectónica. In: 8° Congreso Geológico Argentino, vol 155, pp 155-192
- Cristallini EO, Comínguez AH, Ramos VA, Mercerat ED, McClay K (2004) Basement double-wedge thrusting in the northern Sierras Pampeanas of Argentina (27° S)-Constraints from deep seismic reflection. In: McClay K (ed) *Thrust tectonics and hydrocarbon systems*. AAPG Memoir 82, pp 65-90
- Dahl PS (1996) The crystal–chemical basis for Ar retention in micas: inferences from interlayer partitioning and implications for geochronology. *Contributions to Mineralogy and Petrology* 123:22-39
- Dalla Salda L, Varela R (1984) El metamorfismo en el tercio sur de la sierra Pie de Palo, San Juan. *Revista de la Asociación Geológica Argentina* 39(1-2):68–93
- Davis JS, Roeske SM, McClelland WC, Snee LW (1999) Closing the ocean between the Precordillera terrane and Chilenia: Early Devonian ophiolite emplacement and deformation in the southwest Precordillera. *Geological Society of America Special Papers* 336:115-138

- Dellapé D, Hegedus A (1995) Structural Inversion and Oil Occurrence in the Cuyo Basin in Argentina. In: Tankard AJ, Suárez Soruco R, Welsink HJ (eds) *Petroleum Basins of South America*. American Association of Petroleum Geologists Memoir, pp 369-382
- Demange M, Alvarez JO, Lopez L, Zarco JJ (1996) The Achala batholith (Cordoba, Argentina): a composite intrusion made of five independent magmatic suites. Magmatic evolution and deuteric alteration. *Andean Geodynamics. Journal of South American Earth Sciences* 9(1–2):11–25. doi:10.1016/0895-9811(96)00024-7
- Dodson M (1973) Closure temperatures in cooling geological and petrological systems. *Contributions to Mineralogy and Petrology* 40:259–274
- Dollase W (1986) Correction of intensities for preferred orientation in powder diffractometry: Applications of the March mode. *Journal of Applied Crystallography* 19:267–272
- Donelick RA, Ketcham RA, Carlson WD (1999) Variability of apatite fission-track annealing kinetics: II. Crystallographic orientation effects. *American Mineralogist* 84:1224-1234
- Donelick RA, O'Sullivan P, Ketcham RA (2005) Apatite Fission-Track Analysis. *Reviews in Mineralogy and Geochemistry* 58:49–94
- Dunkl I (2002) TRACKKEY: a Windows program for calculating and graphical presentation of fission-track data. *Computational Geosciences* 28:3–12
- Dunkl I, Mikes T, Simon K, Eynatten H von (2008) Brief introduction to the Windows program Pepita: data visualization, and reduction, outlier rejection, calculation of trace element ratios and concentrations from LA-ICPMS data. *Mineralogical Association of Canada, Short Course* 40:334–340
- Ehlers TA, Farley KA (2003) Apatite (U-Th)/He thermochronometry: methods and applications to problems in tectonic and surface processes. *Earth and Planetary Science Letters* 206:1–14
- Ehlers TA, Willett SD, Armstrong P, Chapman D (2003) Exhumation of the central Wasatch Mountains, Utah: 2. Thermokinematic model of exhumation, erosion, and thermochronometer interpretation. *Journal of Geophysical Research* 108:2173
- England P, Molnar P (1990) Surface uplift, uplift of rocks, and exhumation of rocks. *Geology* 18(12):1173-1177
- Farley KA (2000) Helium diffusion from apatite; general behavior as illustrated by Durango fluorapatite. *Journal of Geophysical Research* 105:2903–2914
- Farley KA (2002) (U-Th)/He Dating: Techniques, Calibrations, and Applications. *Reviews in Mineralogy and Geochemistry* 47(1):819–844. doi:10.2138/rmg.2002.47.18
- Farley KA, Kohn B., Pillans B (2002) The effects of secular disequilibrium on (U-Th)/He systematics and dating of quaternary volcanic zircon and apatite. *Earth and Planetary Science Letters* 201(1):117–125
- Farley KA, Wolf RA (1996) The effects of long alpha-stopping distances on (U-Th)/He ages. *Geochimica et Cosmochimica Acta* 60(21):4223-4229
- Fernandez Seveso F, Perez M, Brisson I, Alvarez L (1993) Sequence stratigraphy and tectonic analysis of the Paganzo Basin, western Argentina. *Comptes Rendus*(12):223–260
- Finney S, Gleason J, Gehrels G, Peralta S, Aceñolaza G (2003) Early Gondwanan connection for the Argentine Precordillera terrane. *Earth and Planetary Science Letters* 205(3-4):349–359
- Fitz Gerald JD, Harrison TM (1993) Argon diffusion domains in K-feldspar; I, Microstructures in MH-10. *Contributions to Mineralogy and Petrology* 113:367-380
- Fitzgerald PG (2002) Tectonics and landscape evolution of the Antarctic plate since the breakup of Gondwana, with an emphasis on the West Antarctic Rift System and the Transantarctic Mountains. *Royal Society of New Zealand Bulletin* 25:453–469
- Fitzgerald PG, Baldwin SL, Webb L, O'Sullivan P (2006) Interpretation of (U-Th)/He single grain ages from slowly cooled crustal terranes: A case study from the Transantarctic Mountains of southern Victoria Land. *Chemical Geology* 225(1-2):91-120. doi:10.1016/j.chemgeo.2005.09.001
- Fitzgerald PG, Muñoz J, Coney P, Baldwin SL (1999) Asymmetric exhumation across the Pyrenean orogen: implications for the tectonic evolution of a collisional orogen. *Earth and Planetary Science Letters* 173:167–170
- Friedrich D (1991) Eine neue Methode zur Bestimmung der Illit-Kristallinität mit Hilfe digitaler Messwerterfassung. Diploma thesis, Georg-August-Universität Göttingen

- Fuhrmann U, Lippolt HJ, Hess JC (1987) Examination of some proposed K-Ar standards: $^{40}\text{Ar}/^{39}\text{Ar}$ analyses and conventional K-Ar data. *Chemical Geology* 66:41-51
- Furque G (1968) Bosquejo geológico de la Sierra de Malanzan, La Rioja. Translated Title: Geology of the Sierra de Malanzan, La Rioja. *Actas de las Jornadas Geológicas Argentinas* 1:111-120
- Galbraith RF, Laslett GM (1993) Statistical models for mixed fission track ages. *Nuclear Tracks and Radiation Measurements* 21:459-470
- Galindo C, Casquet C, Rapela CW, Pankhurst RJ, Baldo E, Saavedra J (2004) Sr, C and O isotope geochemistry and stratigraphy of Precambrian and lower Paleozoic carbonate sequences from the Western Sierras Pampeanas of Argentina: tectonic implications. *Precambrian Research* 131(1-2):55-71
- Gallagher K (1995) Evolving temperature histories from apatite fission-track data. *Earth and Planetary Science Letters* 136(3-4):421-435. doi:10.1016/0012-821X(95)00197-K
- Gardini CE, Costa CH, Schmidt CJ (1999) Estructura subsuperficial entre las sierras de Las Quijadas-El Gigante y la sierra de Villa General Roca, San Luis. Translated Title: Underground structures between Sierras Las Quijadas-El Gigante and Sierra Villa General Roca, San Luis. In: 14° Congreso Geológico Argentino, vol 14, pp 219-221
- Gharrabi M, Velde B, Sagon J (1998) The transformation of illite to muscovite in pelitic rocks: constraints from x-ray diffraction. *Clays and Clay Minerals* 1:78-88
- Giambiagi L, Martinez A (2008) Permo-Triassic oblique extension in the Potrerillos-Uspallata area, western Argentina. *Journal of South American Earth Sciences* 26(3):252-260
- Gleadow AJW (1981) Fission-track dating methods: what are the real alternatives. *Nuclear Tracks and Radiation Measurements* 5:3-14
- Gleadow AJW, Duddy IR (1981) A natural long-term track annealing experiment for apatite. *Nuclear Tracks and Radiation Measurements* 5(1-2):169-174
- Gleadow AJW, Fitzgerald PG (1987) Uplift history and structure of the Transantarctic Mountains: new evidence from fission track dating of basement apatites in the Dry Valley area, southern Victoria Land. *Earth and Planetary Science Letters* 82:1-14
- Gohrbandt KH (1992) Paleozoic paleogeographic and depositional developments on the central proto-Pacific margin of Gondwana. *Journal of South American Earth Sciences* 6:267-287
- González Bonorino F (1950) Lagos problemas geológicas de las Sierras Pampeanas. *Revista de la Asociación Geológica Argentina* 5:81-110
- Gonzalez Diaz EF (1981) Geomorfología. In: Yrigoyen MR (ed) *Geología y Recursos Naturales de la Provincia de San Luis*. 8° Congreso Geológico Argentino Relatorio, pp 193-236
- González PD, Sato AM (2000) Los plutones monzoníticos cizallados El Molle y Barroso: dos nuevos intrusivos pos-orogénicos en el oeste de las sierras de San Luis, Argentina. In: 9° Congreso Geológico Chileno, 1, pp 621-625
- González RE (1971) Edades radiométricas de algunos cuerpos eruptivos de Argentina. *Revista de la Asociación Geológica Argentina* 26:411-412
- González RE, Toselli AJ (1973) Las rocas efusivas básicas de la Sierra de Las Quijadas al oeste de Hualtarán, Provincia de San Luis. *Acta Geológica Lilloana* 12:89-104
- Gonzalez RR, Aceñolaza G (1972) La Cuenca de deposición Neopaleozóica-mesozóica del oeste Argentino. *Fundación e Instituto Miguel Lillo, Tucumán, Miscelánea*(40):629-643
- Gordillo CE, Lencinas A (1967) Geología y petrología del extremo norte de la Sierra de Los Cóndores, Córdoba. *Boletín de la Academia Nacional de Ciencias*:73-108
- Gordillo CE, Lencinas A (1979) Sierras Pampeanas de Córdoba y San Luis. In: Turner JC (ed) *Segundo Simposio de Geología Regional Argentina*. Academia Nacional de Ciencias, pp 577-650
- Grathoff GH, Moore DM (1996) Illite polytype quantification using Wildfire calculated X-ray diffraction patterns. *Clays and Clay Minerals* 44(6):835-842
- Grathoff GH, Moore DM, Hay RL, Wemmer K (1998) Illite Polytype Quantification and K-Ar Dating of Paleozoic Shales: A technique to Quantify. In: Schieber J, Zimmerle W, Sethi P (eds) *Shales and Mudstones II*. E. Schweizerbart'sche Verlagsbuchhandlung (Nägele u Obermiller), Stuttgart, pp 161-175

- Grathoff GH, Moore DM, Hay RL, Wemmer K (2001) Origin of illite in the lower Paleozoic of the Illinois basin: Evidence for brine migrations. *Geological Society of America Bulletin* 113(8):1092–1104. doi:10.1130/0016-7606(2001)113<1092:OOIITL>2.0.CO;2
- Green PF, Duddy IR, Gleadow AJW, Tingate P, Laslett GM (1986) Thermal annealing of fission tracks in apatite 59:237–253
- Green PF, Durrani S (1978) A quantitative assessment of geometry factors for use in fission track studies. *Nuclear Track Detection* 2(4):207–213
- Gross W (1948) Cuadro tectónico del valle de Punilla. *Revista de la Asociación Geológica Argentina* 3(2):73–132
- Guereschi AB, Martino RD (2008) Field and textural evidence of two migmatization events in the Sierras de Córdoba, Argentina. *Gondwana Research* 13(2):176–188
- Guinier A, Bokij GB, Boll-Dornberger K, Cowley JM, Đurovič S, Jagodzinski H, Krishna P, Wolff PM de, Zvyagin BB, Cox DE, Goodman P, Hahn T, Kuchitsu K, Abrahams SC (1984) Nomenclature of Polytype Structures Report of the International Union of Crystallography Ad-Hoc Committee on the Nomenclature of Disordered, Modulated and Polytype Structures. *Acta Crystallographica Section A Foundations of Crystallography* 40(4):399–404. doi:10.1107/S0108767384000842
- Gutscher MA, Spakman W, Bijwaard H, Engdahl E (2000) Geodynamics of flat subduction; seismicity and tomographic constraints from the Andean margin. *Tectonics* 19(5):814–833
- Haines SH, van der Pluijm BA (2008) Clay quantification and Ar–Ar dating of synthetic and natural gouge: Application to the Miocene Sierra Mazatán detachment fault, Sonora, Mexico. *Journal of Structural Geology* 30(4):525–538. doi:10.1016/j.jsg.2007.11.012
- Hamilton PJ, Giles, Ainsworth P (1992) K–Ar dating of illites in Brent Group reservoirs: a regional perspective. In: Morton AC (ed) *Geology of the Brent Group*. Geological Society of London, Special Publications 61, pp 377–400
- Hamilton PJ, Kelley S, Fallick AE (1989) K–Ar dating of illite in hydrocarbon reservoirs. *Clay Minerals* 24(2):215–231
- Hay RL, Lee M, Kolata D, Matthews J, Morton JP (1988) Episodic potassic diagenesis of Ordovician tuffs in the Mississippi Valley area. *Geology Boulder* 16(8):743–747. doi:10.1130/0091-7613(1988)016<0743:EPDOOT>2.3.CO;2
- Hess JC, Lippolt HJ (1994) Compilation of K–Ar measurements on HD-B1 standard biotite; 1994 status report. In: Odin GS (ed) *Phanerozoic Time Scale*, Bulletin de Liaison et d'information, Paris, pp 19–23
- Hilley GE, Coutand I (2010) Links between topography, erosion, rheological heterogeneity, and deformation in contractional settings: Insights from the central Andes. From the trench to the arc: subduction along South America. *Tectonophysics* 495(1–2):78–92. doi:10.1016/j.tecto.2009.06.017
- Hodges KV (2003) Geochronology and Thermochronology in Orogenic Systems. In: Rudnick RL (ed) *Treatise on Geochemistry: The Crust*, Volume 3. Elsevier, Amsterdam, pp 263–292
- Hoffman J, Hower J (1979) Clay mineral assemblages as low grade metamorphic geothermometers; application to the thrust faulted disturbed belt of Montana, U.S.A. *Special Publication Society of Economic Paleontologists and Mineralogists* 26, Pages 55–79
- Hourigan JK, Reiners PW, Brandon MT (2005) U–Th zonation-dependent alpha-ejection in (U–Th)/He chronometry. *Geochimica et Cosmochimica Acta* 69(13):3349–3365
- House MA, Farley KA, Kohn B. (1999) An empirical test of helium diffusion in apatite: Borehole data from the Otway basin, Australia. *Earth and Planetary Science Letters* 170:463–474
- Hower J, Hurley PM, Pinson WH, Jr., Fairbairn HW (1963) The dependence of K–Ar age on the mineralogy of various particle size ranges in a shale. *Geochimica et Cosmochimica Acta* 27(5):405–410. doi:10.1016/0016-7037(63)90080-2
- Huene R von, Corvalán J, Flueh E, Hinz K, Korstgard J, Ranero CR, Weinrebe W (1997) Tectonic control of the subducting Juan Fernandez Ridge on the Andean margin near Valparaíso, Chile. *Tectonics* 16(3):474–488
- Hünicken MA, Azcuy CL, Pensa MV (1981) Sedimentitas Paleozoicas. In: 8° Congreso Geológico Argentino, pp 55–77
- Hünicken MA, Pensa MV (1980a) Estratigrafía y tectónica de las sedimentitas neopaleozoicas (Formación Chancani) y de las felitas (Formación La Mermela) del borde occidental de las sierras de Pocho y

- Guasapampa (Provincia de Córdoba, República Argentina). *Boletín de la Academia Nacional de Ciencias* 53(3-4):255-279
- Hünicken MA, Pensa MV (1980b) Formación Los Ranqueles (Carbónico) de Sampacho y Cerro Suco en el sudoeste de Córdoba, Argentina. *Bol. Proy* 42(3):5-6
- Hunziker JC, Frey M, Clauer N, Dallmeyer R, Friedrichsen H, Flehmig W, Hochstrasser K, Roggwiler P, Schwander H (1986) The evolution of illite to muscovite; mineralogical and isotopic data from the Glarus Alps, Switzerland. *Contributions to Mineralogy and Petrology* 92(2):157-180
- Hurford AJ, Green PF (1983) The zeta age calibration of fission-track dating. *Chemical Geology* 41:285-317
- Hurley PM (1954) The helium age method and the distribution and migration of helium in rocks. In: Faul H (ed) *Nuclear geology; a symposium on Nuclear phenomena in the earth sciences*. Wiley and Sons, New York, pp 301-329
- Introcaso A, Lion A, Ramos VA (1987) La estructura profunda de las Sierras de Córdoba. *Revista de la Asociación Geológica Argentina* 42:117-178
- Isacks BL (1988) Uplift of the Central Andean Plateau and bending of the Bolivian Orocline. *Journal of Geophysical Research* 93:3211-3231
- Jaboyedoff M, Bussy F, Kübler B, Thélin P (2001) Illite "crystallinity" revisited. *Clays and Clay Minerals* 49(2):156-167
- Jaboyedoff M, Kübler B, Sartori M (2000) Basis for meaningful illite crystallinity measurements : an example from the Swiss Prealps. *Schweizerische mineralogische und petrographische Mitteilungen*(80):75-83
- Jordan TE, Allmendinger RW (1986) The Sierras Pampeanas of Argentina: A modern analogue of Rocky Mountain foreland deformation. *American Journal of Science* 286:737-764
- Jordan TE, Alonso RN (1987) Cenozoic stratigraphy and basin tectonics of the Andes Mountains, 20 degrees -28 degrees south latitude. *AAPG Bulletin* 71(1):49-64. doi:10.1306/94886D44-1704-11D7-8645000102C1865D
- Jordan TE, Isacks BL, Allmendinger RW, Brewer JA, Ramos VA, Ando CJ (1983) Andean tectonics related to geometry of subducted Nazca plate. *Geological Society of America Bulletin* 94(3):341-361
- Jordan TE, Zeitler P, Ramos VA, Gleadow AJW (1989) Thermochronometric data on the development of the basement peneplain in the Sierras Pampeanas, Argentina. *Journal of South American Earth Sciences* 2(3):207-222
- Kay SM, Gordillo CE (1994) Pocho volcanic rocks and the melting of depleted continental lithosphere above a shallowly dipping subduction zone in the Central Andes. *Contributions to Mineralogy and Petrology* 117(1):25-44
- Kay SM, Mpodozis C, Ramos VA, Munizaga F (1991) Magma source variations for mid-late Tertiary magmatic rocks associated with a shallowing subduction zone and thickening crust in the Central Andes (28-33°S). In: Harmon RS, Rapela CW (eds) *Andean Magmatism and its Tectonic Setting*. Geological Society of America Special Paper 26, pp 113-137
- Keller M, Buggish W, Lehnert O (1998) The stratigraphic record of the Argentine Precordillera and its plate tectonic background. In: Pankhurst RJ, Rapela CW (eds) *The Proto-Andean Margin of Gondwana*, pp 35-56
- Kelley S (2002) K-Ar and Ar-Ar dating. *Reviews in Mineralogy and Geochemistry* 47:785-818
- Kendrick E, Brooks BA, Bevis M, Smalley RF, Jr., Lauría E, Araujo M, Parra H (2006) Active orogeny of the south-central Andes studied with GPS geodesy. *Revista de la Asociación Geológica Argentina* 61(4):555-566
- Kerrick R, Goldfarb R, Groves D, Garwin S The Geodynamics of World-Class Gold Deposits: Characteristics, Space-Time Distribution, and Origins. In: Hagemann S, Brown P (eds) *Gold in 2000*, vol 13, pp 501-551
- Ketcham RA (2005) Forward and inverse modeling of low-temperature thermochronometry data. *Reviews in Mineralogy and Geochemistry* 58:275-314
- Ketcham RA, Donelick RA, Carlson WD (1999) Variability of apatite fission-track annealing kinetics: III. Extrapolation to geological time scales. *American Mineralogist* 84:1235-1255
- Kirschner DL, Hunziker JC, Cosca M (1996) Closure Temperature of argon in micas; a review and reevaluation based on Alpine samples

- Kleiman LE, Japas MS (2009) The Choiyoi volcanic province at 34°S–36°S (San Rafael, Mendoza, Argentina): Implications for the Late Palaeozoic evolution of the southwestern margin of Gondwana. *Tectonophysics* 473(3–4):283–299. doi:10.1016/j.tecto.2009.02.046
- Koslowski E, Manceda R, Ramos VA (1993) Estructura. In: 12º Congreso Geológico Argentino y 2º Congreso de Exploración de Hidrocarburos, pp 235–256
- Kraemer PE, Tauber A, Schmidt CJ, Rame G (1993) Analisis cinemático de la "Falla de Nono"; evidencias de actividad neotectónica, Valle de San Alberto, Provincia de Córdoba. Translated Title: Kinematic analysis of the "Nono Fault"; evidence of neotectonic activity, San Alberto Valley, Córdoba Province. *Actas del Congreso Geológico Argentino* 12, 3:277–281
- Kralik M, Klima M, Riedmüller G (1987) Dating fault gouges. *Nature* 327:315–317
- Kübler B (1964) Les argiles indicateurs de métamorphisme. *Revue de l'Institut Français du Pétrolé* 19:1093–1112
- Kübler B (1967) La cristallinité de l'illite et les zones tout à fait supérieures du métamorphisme. *Etages Tectonique, Colloque de Neuchâtel, Neuchâtel*
- Kübler B (1968) Evaluation quantitative du métamorphisme par la cristallinité de l'illite. *Bull. Centre Recherches Pau-SNPA* 2:385–397
- Lamphere M, Dylruple G (2000) First-principles calibration of ³⁸Ar tracers: Implications for the age of ⁴⁰Ar/³⁹Ar fluence monitors. *US Geological Survey Professional Paper* 1621:10
- Laslett GM, Green PF, Duddy IR, Gleadow AJW (1987) Thermal annealing of fission tracks in apatite. *Chemical Geology; Isotope Geoscience Section* 65(1):1–13
- Layer P (2000) Argon40/argon39 age of the El'gygytyn impact event, Chukotka, Russia. *Meteoritics and Planetary Science* 35:591–599
- Layer P, Hall CM, York D (1987) The derivation of ⁴⁰Ar/³⁹Ar age spectra of single grains of hornblende and biotite by laser step heating. *Geophysical Research Letters* 14:757–760
- Le Corre C, Rossello E (1994) Kinematics of early paleozoic ductile deformation in the basement of NW Argentina. *Journal of South American Earth Sciences* 7(3–4):301–308
- Lee J, Ahn J, Peacor DR (1985) Textures in layered silicates; progressive changes through diagenesis and low-temperature metamorphism. *Journal of Sedimentary Petrology* 55(4):532–540. doi:10.1306/212F871F-2B24-11D7-8648000102C1865D
- Lencinas A, Timonieri A (1968) Algunas características estructurales del valle de Punilla, Córdoba. Translated Title: Structural characteristics of Punilla valley, Córdoba. *Actas de las Jornadas Geológicas Argentinas* 1:195–207
- Limarino CO, Spalletti LA (2006) Paleogeography of the upper Paleozoic basins of southern South America: An overview. *Journal of South American Earth Sciences* 22:134–155. doi:10.1016/j.jsames.2006.09.011
- Lippolt HJ, Leitz M, Wernicke R, Hagedorn B (1994) U+Th)/He dating of apatite: Experience with samples from different geochemical environments. *Chemical Geology* 112:179–191
- Lippolt HJ, Weigel E (1988) ⁴He diffusion in ⁴⁰Ar retentive minerals. *Geochimica et Cosmochimica Acta* 52:1449–1458
- Llambías EJ, Quenardelle S, Montenegro T (2003) The Choiyoi Group from central Argentina: a subalkaline transitional to alkaline association in the craton adjacent to the active margin of the Gondwana continent. *Journal of South American Earth Sciences* 16(4):243–257. doi:10.1016/S0895-9811(03)00070-1
- Löbels S (2012) The Structural and Morphotectonical Evolution of the Sierras Pampeanas constrained by a multichronometrical approach. PhD-thesis, Georg-August-Universität Göttingen
- Löbels S, Bense FA, Dunkl I, Wemmer K, Siegesmund S (in review B) Thermochronological constraints of the exhumation and uplift of the Sierra de Pie de Palo, NW Argentina
- Löbels S, Bense FA, Wemmer K, Dunkl I, Costa CH, Layer P, Siegesmund S (2011) Exhumation and uplift of the Sierras Pampeanas: preliminary implications from K–Ar fault gouge dating and low-T thermochronology in the Sierra de Comechingones (Argentina). *International Journal of Earth Sciences* 100(2–3):671–694. doi:10.1007/s00531-010-0608-0
- Löbels S, Sobel ER, Bense FA, Wemmer K, Dunkl I, Siegesmund S (2013) Refined thermochronological aspects of the Northern Sierras Pampeanas. *Tectonics* 32(3):453–472

- Lonker SW, Fitz Gerald JD (1990) Formation of coexisting 1M and 2M polytypes in illite from an active hydrothermal system. *American Mineralogist* 75:1282–1289
- López de Luchi MG, Siegesmund S, Steenken A, Wemmer K (2004) Highly fractionated Devonian granitoids of the Sierra de San Luis, Argentina; sources for Qz-W veins 29
- Lucero Michaut NH, Gamkosian A, Jarsun B, Zamora YE, Sigismodi M, Caminos R, Miró R (1995) Mapa Geológica de la Provincia de Córdoba, República Argentina 1:500.000. Ministerio de Economía y Obras y Servicios Públicos, SEGEMAR, Buenos Aires
- Lucero Michaut NH, Olsacher J (1981) Descripción Geológica de la hoja 19h, Cruz del Eje, provincia de Córdoba. Boletín, vol 179, Buenos Aires
- Lyons JB, Schnellenberg J (1971) Dating faults. *Geological Society of America Bulletin* 82:1749-1752
- Martínez A, Rodríguez Blanco L, Ramos VA (2006) Permo-Triassic magmatism of the Choiyoi Group in the cordillera Frontal of Mendoza, Argentina: geological variations associated with changes in Paleo-Benioff zone. In: Asociación Geológica Argentina and Geological Society of America (ed) Backbone of the Americas Symposium, Mendoza
- Martino RD (2003) Las fajas de deformación dúctil de las Sierras Pampeanas de Córdoba: Una reseña general. *Revista de la Asociación Geológica Argentina* 58(4):549–571
- Martino RD, Kraemer PE, Escayola MP, Giambastini M, Arnosio M (1995) Transecta de las Sierras Pampeanas de Córdoba a los 32°S. *Revista de la Asociación Geológica Argentina*(50):60–77
- Massabie A (1976) Estructura cenozoica entre Charbonier y Cosquín, provincia de Córdoba. In: 6° Congreso Geológico Argentino, Actas 1, Buenos Aires, pp 109-123
- Massabie A (1987) Neotectónica y sismicidad en la región de Sierras Pampeanas Orientales, sierras de Córdoba, Argentina. In: 10° Congreso Geológico Argentino, Actas 1, pp 271-274
- Massabie A, Szlafztein C (1991) Condiciones geomecánicas y edad del fallamiento neotectónico en las Sierras Pampeanas Orientales, Córdoba, Argentina. *Asociación Argentina de Geología Aplicada a la Ingeniería*, Actas(6):154–168
- Maxwell D, Hower J (1967) Highgrade diagenesis and low-grade metamorphism of illite in the Precambrian Belt Series. *American Mineralogist* 52:843–857
- McDougall I, Harrison TM (1999) *Geochronology and Thermochronology by the $^{40}\text{Ar}/^{39}\text{Ar}$ method*, 2nd. Oxford University Press, Oxford
- Meesters A, Dunai T (2002) Solving the production-diffusion equation for finite diffusion domains of various shapes Part I. implications for low-temperature (U-Th)/He thermochronology. *Chemical Geology* 186:333–344
- Meira V, Campos Neto M, González PD, Stipp Basei M, Varela R (2012) Ordovician klippen structures of the Sierra de Umango: New insights on Tectonic evolution of the Western Sierras Pampeanas, Argentina. *Journal of South American Earth Sciences* 37:154–174
- Miller H, Söllner F (2005) The Famatina complex (NW Argentina): back-docking of an island arc or terrane accretion? Early Palaeozoic geodynamics at the western Gondwana margin. *Geological Society, London, Special Publications* 246(1):241-256
- Miró R, Martos D (1999) Mapa Geológico De La Provincia De San Luis; Escala 1:500.000. Instituto de Geología y Recursos Minerales and Servicio Geológico Minero Argentino, Buenos Aires
- Moore DM, Reynolds RC (1997) *X-Ray Diffraction and the Identification and Analysis of Clay Minerals*, 2nd edn. Oxford University Press, New York
- Morata D, Castro Machuca Bd, Arancibia G, Pontoriero S, Fanning C (2010) Peraluminous Grenvillian TTG in the Sierra de Pie de Palo, Western Sierras Pampeanas, Argentina: Petrology, geochronology, geochemistry and petrogenetic implications. *Precambrian Research* 177(3-4):308–322
- Mortimer E, Carrapa B, Coutand I, Schoenbohm L, Sobel ER, Sosa GJ, Strecker MR (2007) Fragmentation of a foreland basin in response to out-of-sequence basement uplifts and structural reactivation; El Cajon-Campo del Arenal Basin, NW Argentina. *Geological Society of America Bulletin* 119:637–653. doi:10.1130/B25884.1

- Mpodozis C, Kay SM (1990) Provincias magmaticas acidas y evolucion tectonica de Gondwana; Andes chilenos, 28-31 degrees S. Translated Title: Acidic magmatic provinces and the tectonic evolution of Gondwana; Chilean Andes, 28-31 degrees S. *Revista Geologica de Chile* 17(2):153–180
- Mpodozis C, Ramos VA (1989) The Andes of Chile and Argentina. In: Ericksen GE, Canas Pinochet MT, Reinemund JA (eds) *Geology of the Andes and its Relation to Hydrocarbon and Mineral Resources*, vol 11, pp 59–90
- Mulcahy SR, Roeske SM, McClelland WC, Jourdan F, Iriondo A, Renne PR, Vervoort JD, Vujovich G (2011) Structural evolution of a composite middle to lower crustal section: The Sierra de Pie de Palo, northwest Argentina. *Tectonics* 30(1). doi:10.1029/2009TC002656
- Mulcahy SR, Roeske SM, McClelland WC, Nomade S, Renne PR (2007) Cambrian initiation of the Las Pirquitas thrust of the western Sierras Pampeanas, Argentina: Implications for the tectonic evolution of the proto-Andean margin of South America. *Geology* 35(5):443–446
- Müller MJ (1996) *Handbuch ausgewählter Klimastationen der Erde*, 5th edn. Universität Trier FB VI, Trier
- Naipauer M, Vujovich G, Cingolani CA, McClelland WC (2010) Detrital zircon analysis from the Neoproterozoic–Cambrian sedimentary cover (Cuyania terrane), Sierra de Pie de Palo, Argentina: Evidence of a rift and passive margin system? *Journal of South American Earth Sciences* 29(2):306–326. doi:10.1016/j.jsames.2009.10.001
- Noble DC, McKee EH, Mourier T, Megard F (1990) Cenozoic stratigraphy, magmatic activity, compressive deformation, and uplift in northern Peru. *Geological Society of America Bulletin* 102(8):1105–1113. doi:10.1130/0016-7606(1990)102<1105:CSMACD>2.3.CO;2
- Northrup CJ, Simpson C, Hodges KV (1998) Pseudotachylite in Fault zones of the Sierras de Córdoba, Argentina: Petrogenesis and ⁴⁰Ar/³⁹Ar Geochronology. In: Geological Society of America (ed) *GSA Annual Meeting, Abstracts with Program*, vol 30, Toronto, Ontario, pp A-325
- O’Sullivan P, Parrish R (1995) The importance of apatite composition and single-grain ages when interpreting fission track data from plutonic rocks: a case study from the Coast Ranges, British Columbia. *Earth and Planetary Science Letters* 132(1-4)
- Ortiz Suárez A, Prozzi CR, Llambías EJ (1992) Geología de la parte sur de la Sierra de San Luis y granitoides asociados, Argentina. *Estudios Geológicos* 48:269–277
- Pankhurst RJ, Rapela CW (1998) The proto-Andean margin of Gondwana: an introduction. In: Pankhurst RJ, Rapela CW (eds) *The Proto-Andean Margin of Gondwana*
- Pardo Casas F, Molnar P (1987) Relative Motion of the Nazca (Farallon) and South American Plates since late Cretaceous time. *Tectonics* 6(3):233–248
- Passchier CW, Trouw RAJ (2005) *Microtectonics*, 2nd edn. Springer, Berlin Heidelberg
- Peacor DR, Bauluz B, Dong H, Tillick D, Yan Y (2002) Transmission and analytical electron microscopy evidence for high Mg contents of 1M illite: absence of 1M polytypism in normal prograde diagenetic sequences of pelitic rocks. *Clays and Clay Minerals* 50:757–765
- Perez A, Martínez R (1990) Modelación de cuerpos litosféricos en el área Pie de Palo, San Juan. In: 11° Congreso Geológico Argentino, Actas 2, pp 353–356
- Pevear DR (1992) illite age analysis, a new tool for basin thermal history analysis. In: Kharaka YK, Maest AS (eds) *Water-rock interaction. The Netherlands: AA Balkema, Rotterdam*, pp 1251–1254
- Pevear DR (1999) Colloquium Paper: Illite and hydrocarbon exploration. *Proceedings of the National Academy of Sciences* 96(7):3440–3446. doi:10.1073/pnas.96.7.3440
- Pevear DR, Vrolijk P, Longstaffe F (1997) Timing of Moab Fault displacement and fluid movement integrated with burial history using radiogenic and stable isotopes. In: Hendry J, Carey J, Ruffell AH, Worden RH (eds) *Geofluids II*, pp 42–45
- Pilger RH (1981) Plate reconstruction, aseismic ridges, and low-angle subduction beneath the Andes. *Geological Society of America Bulletin* 92:448–456
- Pilger RH (1984) Kinematics of the South American subduction zone from global plate reconstructions. In: Cabre R (ed) *Geodynamics of the Eastern Pacific Region, Caribbean and Cotia Arcs. Geodynamic Series 9. American Geophysical Union, Washington D.C.*, pp 113–125
- Purdy JW, Jaeger E (1976) K-Ar ages on rock-forming minerals from the central Alps. *Mem. Instituti Geol. Mineral. Uni. Padova*(30):1–31

- Rabassa J, Carignano C, Cioccale M (2010) Gondwana Paleosurfaces in Argentina: An Introduction. *Geociências* 29(4):439–466
- Ramos VA (1982) descripción geológica de la Hoja 20f Chepes, provincia de La Rioja. *Boletín*, vol 184
- Ramos VA (1988) The tectonics of the central Andes (30°–33°S latitude). In: Clark S, Burchfiel D, Suppe D (eds) *Procesos in Continental lithospheric Deformation*
- Ramos VA (2001) The Southern Central Andes. In: Cordani U, Milani EJ, Thomaz Filho A, Campos DA (eds) *Tectonic Evolution of South America*, Rio de Janeiro, pp 561–604
- Ramos VA (2004) Cuyania, an Exotic Block to Gondwana: Review of a Historical Success and the Present Problems. *Gondwana Research* 7(4):1009–1026
- Ramos VA (2008) The Basement of the Central Andes: The Arequipa and Related Terranes. *Annu. Rev. Earth Planet. Sci.* 36(1):289–324. doi:10.1146/annurev.earth.36.031207.124304
- Ramos VA (2010) The Grenville-age basement of the Andes. *Journal of South American Earth Sciences* 29(1):77–91. doi:10.1016/j.jsames.2009.09.004
- Ramos VA, Cristallini EO, Pérez D (2002) The Pampean flat-slab of the central Andes. *Journal of South American Earth Sciences* 15:59–78
- Ramos VA, Dallmeyer R, Vujovich G (1998) Time constraints on the Early Palaeozoic docking of the Precordillera, central Argentina. In: Pankhurst RJ, Rapela CW (eds) *The Proto-Andean Margin of Gondwana*, pp 143–158
- Ramos VA, Escayola MP, Mutti D, Vujovich G (2001) Proterozoic - early Paleozoic ophiolites in the Andean basement of southern South America. In: *Ophiolites and Oceanic Crust: New insights from Field Studies and Ocean Drilling Program*. Geological Society of America Special Paper 349, pp 331–349
- Ramos VA, Folguera A (2009) Andean flat-slab subduction through time. *Geological Society, London, Special Publications* 327(1):31–54. doi:10.1144/SP327.3
- Ramos VA, Jordan TE, Allmendinger RW, Mpodozis C, Kay SM, Cortés JM, Palma M (1986) Paleozoic terranes of the Central Argentine–Chilean Andes. *Tectonics* 5(6):855–880
- Ramos VA, Kay SM (1991) Triassic rifting and associated basalts in the Cuyo basin, central Argentina. In: Harmon RS, Rapela CW (eds) *Andean Magmatism and its Tectonic Setting*. Geological Society of America Special Paper 26, pp 79–91
- Ramos VA, Vujovich G (2000) Hoja Geológica 3169-IV San Juan, provincial de San Juan. *Servicio Geológico Minero Argentino Bulletin* 243:1–82
- Ramos VA, Vujovich G, Dallmeyer R (1996) Los klippen y ventanas tectónicas de la estructura preándica de la sierra de Pie de Palo (San Juan): Edad e implicancias tectónicas. In: 13° Congreso Geológico Argentino, Actas V, pp 377–391
- Rapela CW, Pankhurst RJ, Casquet C, Baldo E, Saavedra J, Galindo C (1998) Early evolution of the Proto-Andean margin of South America. *Geology* 26(8):707–710
- Ravenhurst CE, Willett SD, Donelick RA, Beaumont C (1994) Apatite fission track thermochronometry from central Alberta: Implications for the thermal history of the Western Canada Sedimentary Basin. *J. Geophys. Res.* 99(B10):20023. doi:10.1029/94JB01563
- Regnier M, Chatelain J, Smalley RF, Jr., Ming Chiu J, Isacks BL, Puebla N (1992) Seismotectonic of the Sierra Pie de Palo, a basement block uplift in the Andean foreland, Argentina. *Bulletin of Seismological Society of America* 82:2549–2571
- Reiners PW, Brandon MT (2006) Using Thermochronology to Understand Orogenic Erosion. *Annu. Rev. Earth Planet. Sci.* (34):419–466
- Reiners PW, Spell TL, Nicolescu S, Zanetti KA (2004) Zircon (U-Th)/He thermochronometry; He diffusion and comparisons with (super 40) Ar/ (super 39) Ar dating. *Geochimica et Cosmochimica Acta* 68(8):1857–1887. doi:10.1016/j.gca.2003.10.021
- Reynolds RC (1963) Potassium-Rubidium ratios and polytypism in illites and microclines from the clay size fractions of Proterozoic carbonate rocks. *Geochimica et Cosmochimica Acta* 27:1097–1112
- Reynolds RC, Thomson CH (1993) Illite from the Potsdam sandstone of New York: A probable noncentrosymmetric mica structure. *Clays and Clay Minerals* 41:66–72

- Richardson T, Gilbert H, Anderson M, Ridgway KD (2012) Seismicity within the actively deforming Eastern Sierras Pampeanas, Argentina. *Geophysical Journal International* 188(2):408–420. doi:10.1111/j.1365-246X.2011.05283.x
- Rossello E, Moztetic ME (1999) Caracterización estructural y significado geotectónico de los depocentros creácicos continentales del centro-oeste argentino. 5° Simposio sobre el Cretácico del Brasil, *Boletim* 5:107–113
- Rovereto G (1911) *Studi di geomorfologia Argentina. I, La Sierra di Cordova*. E. Cuggiani, Roma
- Roy RCDP, Rossello E, Billa M, Bailly L, Lips A (2006) Predictive mapping for copper–gold magmatic–hydrothermal systems in NW Argentina: Use of a regional-scale GIS, application of an expert-guided data-driven approach, and comparison with results from a continental-scale GIS. *Ore Geology Reviews* 29(3–4):260–286
- Salfrity JA, Marquillas R (1981) Las unidades estratigráficas cretácicas del norte de la Argentina. Translated Title: Cretaceous stratigraphic units of northern Argentina. *Congreso Latinoamericano de Paleontología* 2, 1:303–317
- Santa Cruz EO (1979) Geología de las unidades sedimentarias aflorantes en el área de las cuencas de los ríos Quinto y Conlara, provincia de San Luis, República Argentina. Translated Title: Geology of sedimentary units outcropping in the region of the Quinto and Conlara river(7, Tomo I)
- Sato AM, Tickyj H, Llambías EJ, Sato K (2000) The Las Matras tonalitic–trondhjemitic pluton, central Argentina: Grenvillian-age constraints, geochemical characteristics, and regional implications. *Journal of South American Earth Sciences* 13(7):587–610
- Sato AM, Tickyj H, Llambías EJ, Stipp Basei M, González PD (2004) Las Matras Block, Central Argentina (37°S–67°W): the Southernmost Cuyania Terrane and its Relationship with the Famatinian Orogeny. *Gondwana Research* 7(4):749–764
- Schlagintweit O (1954) Una interesante dislocación en Potrero de Garay (Valle de Calamuchita), Sierra Chica y Grande de la Provincia de Córdoba. *Revista de la Asociación Geológica Argentina*(9):135–154
- Schmidt CJ, Astini RA, Costa CH, Gardini CE, Kraemer PE (1995) Cretaceous rifting, alluvial fan sedimentation, and Neogene inversion, southern Sierras Pampeanas, Argentina. In: Tankard AJ, Suárez Soruco R, Welsink HJ (eds) *Petroleum Basins of South America*. American Association of Petroleum Geologists Memoir, pp 341–358
- Schmitz MD, Bowring S (2001) U–Pb zircon and titanite systematics of the Fish Canyon Tuff: an assessment of high-precision U–Pb geochronology and its application to young volcanic rocks. *Geochimica et Cosmochimica Acta* 65:2571–2587
- Schumacher E (1975) Herstellung von 99,9997% ^{38}Ar für die $^{40}\text{K}/^{40}\text{Ar}$ Geochronologie. *Geochronologia Chimica* 24:441–442
- Shuster DL, Flowers RM, Farley KA (2006) The influence of natural radiation damage on helium diffusion kinetics in apatite. *Earth and Planetary Science Letters* 249(3–4):148–161. doi:10.1016/j.epsl.2006.07.028
- Siegesmund S, Steenken A, López de Luchi MG, Wemmer K, Hoffmann A, Mosch S (2004) The Las Chacras–Potrerillos Batholith, Pampean Ranges, Argentina; structural evidences, emplacement and timing of the intrusion 93(1). (Series) <http://link.springer.de/link/service/journals/00531/index.htm>
- Simpson C, Law R, Gromet LP, Miró R, Northrup CJ (2003) Paleozoic deformation in the Sierras de Córdoba and Sierra de Las Minas, eastern Sierras Pampeanas, Argentina. *Journal of South American Earth Sciences* 15(7):749–764
- Simpson C, Whitmeyer SJ, Paor DG de, Gromet LP, Miró R, Krol MA, Short H (2001) Sequential ductile to brittle reactivation of major fault zones along the accretionary margin of Gondwana in Central Argentina. *Geological Society, London, Special Publications* 186(1):233–255. doi:10.1144/GSL.SP.2001.186.01.14
- Sims JP, Ireland TR, Camacho A, Lyons E, Pieters PE, Skirrow RG, Stuart-Smith PG, Miró R (1998) U–Pb, Th–Pb and Ar–Ar geochronology from the southern Sierras Pampeanas, Argentina: implications for the Palaeozoic tectonic evolution of the western Gondwana margin. In: Pankhurst RJ, Rapela CW (eds) *The Proto-Andean Margin of Gondwana*, pp 259–281
- Smalley RF, Jr., Isacks BL (1987) A high resolution study of the Nazca plate Wadati–Benioff zone under western Argentina. *Journal of Geophysical Research* 92:13903–13912

- Smalley RF, Jr., Isacks BL (1990) Seismotectonics of thin- and thick-skinned deformation in the Andean foreland from local network data; evidence for a seismogenic lower crust. *Journal of Geophysical Research* 95:12,487-12,498
- Snellenberg J (1971) Dating faults. *Geological Society of America Bulletin* 82(6):1749–1752
- Sobel ER, Strecker MR (2003) Uplift, exhumation and precipitation: tectonic and climate control of late Cenozoic landscape evolution in the northern Sierras Pampeanas, Argentina. *Basin Research* 15:431-451
- Solá P Manifestaciones volcánicas de los cerritos Negros de los alrededores de las Chacras, Dto. San Martín, Prov. de San Luis - Unpubl. Degree Thesis
- Solum JG, van der Pluijm BA, Peacor DR (2005) Neocrystallization, fabrics and age of clay minerals from an exposure of the Moab Fault, Utah. *Journal of Structural Geology* 27(9):1563-1576. doi:10.1016/j.jsg.2005.05.002
- Sosa GM, Augsburger MS, Pedregosa JC (2002) Columbite-group minerals from rare-metal granitic pegmatites of the Sierra de San Luis, Argentina. *European Journal of Mineralogy* 14:627-636
- Środoń J (1999) Nature of mixed-layer clays and mechanisms of their formation and alteration. *Annu. Rev. Earth Planet. Sci.* 27:19–53
- Środoń J, Clauer N, Eberl DD (2002) Interpretation of K-Ar dates of illitic clays from sedimentary rocks aided by modeling. *American Mineralogist* 87:1528–1535
- Środoń J, Eberl DD (1984) Illite. *Reviews in Mineralogy and Geochemistry* 13(1):495-544
- Środoń J, Eberl DD, Drits VA (2000) Evolution of fundamental particle size during illitization of smectite and implications for reaction mechanism. *Clays and Clay Minerals* 48:446–458
- Sruoga P, Urbina N, Malvicini L (1996) El Volcanismo Terciario y los Depósitos Hidrotermales (Au, Cu) asociados en La Carolina y Diente Verde, San Luis, Argentina. In: 13° Congreso Geológico Argentino, Actas III, pp 89–100
- Stauder W (1973) Mechanism and spatial distribution of Chilean earthquakes with relation to subduction of the oceanic plate. *Journal of Geophysical Research* 78:5033
- Steenken A, Siegesmund S, Wemmer K, López de Luchi MG (2008) Time constraints on the Famatinian and Achalian structural evolution of the basement of the Sierra de San Luis (Eastern Sierras Pampeanas, Argentina). *Journal of South American Earth Sciences* 25(3):336-358. doi:10.1016/j.jsames.2007.05.002
- Steenken A, Wemmer K, López de Luchi MG, Siegesmund S, Pawlig S (2004) Crustal Provenance and Cooling of the Basement Complexes of the Sierra de San Luis: An Insight Into the Tectonic History of the Pro to-Andean Margin of Gondwana. *Gondwana Research* 7(4):1171–1195. doi:10.1016/S1342-937X(05)71092-3
- Steenken A, Wemmer K, Martino RD, López de Luchi MG, Guerreschi AB, Siegesmund S (2010) Post-Pampean cooling and the uplift of the Sierras Pampeanas in the west of Córdoba (Central Argentina). *N. Jb. Geol. Pal. A.* 256(2):235–255. doi:10.1127/0077-7749/2010/0094
- Steiger RH, Jaeger E (1977) Subcommittee on geochronology; convention on the use of decay constants in geo- and cosmochronology. *Earth and Planetary Science Letters* 36(3):359–362
- Stelzner A (1885) Beiträge zur Geologie und Paläontologie der Argentinischen Republik und des angrenzenden, zwischen dem 32° u 33° S. Br. gelegenden Teiles der Chilenischen Cordillere. I. Geologischer Theil, Cassel and Berlin
- Stipanovic P, Linares E (1975) Catálogo de edades Radiométricas determinadas para la República Argentina. Asociación Geológica Argentina, Publication Especial (Serie B) 3
- Stockli DF, Farley KA, Dumitru T (2000) Calibration of the (U-Th)/He thermochronometer on an exhumed fault block, White Mountains, California. *Geology* 28:983-986
- Surace IR, Clauer N, Thélin P, Pfeifer H (2011) Structural analysis, clay mineralogy and K–Ar dating of fault gouges from Centovalli Line (Central Alps) for reconstruction of their recent activity. *Tectonophysics* 510(1-2):80–93. doi:10.1016/j.tecto.2011.06.019
- Tagami T (2012) Thermochronological investigation of fault zones. *Tectonophysics* 538-540:67–85. doi:10.1016/j.tecto.2012.01.032
- Thomas W, Astini RA (2003) Ordovician accretion of the Argentine Precordillera terrane to Gondwana: a review. *Journal of South American Earth Sciences* 16(1):67–79

- Uliana MA (1989) Mesozoic Extension and the Formation of Argentine Sedimentary Basins. In: Tankard AJ, Balkwill HR (eds) *Extensional tectonics and stratigraphy of the North Atlantic margins*. American Association of Petroleum Geologists and Canadian Geological Foundation, Tulsa, OK
- Urbina N (2005) Cenozoic magmatism and mineralization in the Sierras Pampeanas of San Luis. In: Geological Society of Nevada (ed) *Geological Society of Nevada Symposium 2005: Window to the World*, Reno, pp 787–796
- Urbina N, Sruoga P (2008) K-Ar mineral age constraints on the Diente Verde porphyry deposit formation, San Luis, Argentina. In: *South American Symposium on Isotope Geology* (ed) 6^o South American Symposium on Isotope Geology - Extended Abstracts, vol 37. Bariloche, p 4
- Urbina N, Sruoga P (2009) La Faja Metalogenética de San Luis, Sierras Pampeanas: Mineralización y Geocronología en el Contexto Metalogenético Regional. *Revista de la Asociación Geológica Argentina* 64(4):635–645
- Urbina N, Sruoga P, Malvicini L (1997) Late Tertiary gold-bearing volcanic belt in the Sierras Pampeanas of San Luis, Argentina. *International Geology Review* 39:287–306
- Urreiztieta M de, Gapais D, Le Corre C, Cobbold P, Rossello E (1996) Cenozoic dextral transpression and basin development at the southern edge of the Puna Plateau, northwestern Argentina. *Tectonophysics* 354(1–2):17–39
- van Daalen M, Heilbronner R, Kunze K (1999) Orientation analysis of localized shear deformation in quartz fibres at the brittle-ductile transition. *Tectonophysics* 303:83–107
- van der Pluijm BA, Hall CM, Vrolijk P, Pevear DR, Covey M (2001) The dating of shallow faults in the Earth's crust. *Nature*(412):172–175
- van der Pluijm BA, Marshak S (2004) *Earth structure. An introduction to structural geology and tectonics*, 2nd edn. W.W. Norton, New York
- van Staal CR, Vujovich G, Currie KL, Naipauer M (2011) An Alpine-style Ordovician collision complex in the Sierra de Pie de Palo, Argentina: Record of subduction of Cuyania beneath the Famatina arc. *Flow of Rocks Field Analysis and Modeling - in celebration of Paul F. Williams' contribution to mentoring*. *Journal of Structural Geology* 33(3):343–361. doi:10.1016/j.jsg.2010.10.011
- Varela R, Cingolani CA, Dalla Salda L, Aragon E, Teixeira W (1993) Las monzodioritas y monzogabros de Cacheuta, Mendoza; edad, petrología e implicancias tectónicas. Translated Title: The monzodiorites and monzogabbros of Cacheuta, Mendoza; age, petrology and tectonic implications. *Actas del Congreso Geológico Argentino* 12, 4:75–80
- Varela R, Llambías EJ, Cingolani CA, Sato AM (1994) Datación de algunos granitoides de la Sierra de San Luis (Argentina) e interpretación evolutiva. In: *Actas del Congreso Geológico Chileno* 14, pp 1249–1253
- Velde B (1965) Experimental determination of muscovite polymorph stabilities. *American Mineralogist* 50:436–449
- Vigny C, Rudloff A, Ruegg JC, Madariaga R, Campos J, Alvarez M (2009) Upper plate deformation measured by GPS in the Coquimbo Gap, Chile. *Physics of the Earth and Planetary Interiors* 175:86–95. doi:10.1016/j.pepi.2008.02.013
- Villa IM (1998) Isotopic closure. *Terra Nova* 10:45–47
- Vita-Finzi C (2009) Pie de Palo, Argentina: A cataclastic diapir. *Geomorphology* 104(3–4):317–322
- Vujovich G, Kay SM (1998) A Laurentian? Grenville-age oceanic arc/back-arc terrane in the Sierra de Pie de Palo, Western Sierras Pampeanas, Argentina. In: Pankhurst RJ, Rapela CW (eds) *The Proto-Andean Margin of Gondwana*, pp 159–179
- Vujovich G, van Staal CR, Davis W (2004) Age Constraints on the Tectonic Evolution and Provenance of the Pie de Palo Complex, Cuyania Composite Terrane, and the Famatinian Orogeny in the Sierra de Pie de Palo, San Juan, Argentina. *Gondwana Research* 7(4):1041–1056
- Wagner GA, van Den Haute P (1992) Fission-track dating. Enke, Stuttgart
- Weber K (1972) Notes on the determination of illite crystallinity. *Neues Jahrbuch für Geologie und Paläontologie - Monatshefte* 6:267–276
- Webster R, Chebli G, Fischer J (2004) General Levalle basin, Argentina: A frontier Lower Cretaceous rift basin. *AAPG Bulletin* 88(5):627–652

- Wemmer K (1991) K-Ar-Alterdatierungsmöglichkeiten für retrograde Deformationsprozesse im spröden und duktilen Bereich - Beispiele aus der KTB-Vorbohrung (Oberpfalz) und dem Bereich der Insubrischen Linie (N-Italien). *Göttinger Arbeiten zur Geologie und Paläontologie* 51:1-61
- Wemmer K, Ahrendt H (1997) Comparative K-Ar and Rb-Sr age determinations of retrograde processes on rocks from the KTB deep drilling project. *International Journal of Earth Sciences* 86:272-285
- Wemmer K, Steenken A, Mueller S, López de Luchi MG, Siegesmund S (2011) The tectonic significance of K-Ar illite fine-fraction ages from the San Luis Formation (eastern Sierras Pampeanas, Argentina). *International Journal of Earth Sciences* 100:659–669
- Wolff R, Dunkl I, Kiesselbach G, Wemmer K, Siegesmund S (in press) Thermochronological constraints on the multiphase exhumation history of the Ivrea-Verbano Zone of the Southern Alps. *Tectonophysics*. doi:10.1016/j.tecto.2012.03.019
- Wölfler A, Kurz W, Danišik M, Rabitsch R (2010) Dating of fault zone activity by apatite fission track and apatite (U-Th)/He thermochronometry: a case study from the Lavanttal fault system (Eastern Alps). *Terra Nova*:no. doi:10.1111/j.1365-3121.2010.00943.x
- Wolf RA, Farley KA, Kass DM (1998) Modeling of the temperature sensitivity of the apatite (U-Th)/He thermochronometer. *Chemical Geology* 148(1-2):105-114
- Wolf RA, Farley KA, Silver LT (1996) Helium diffusion and low-temperature thermochronometry of apatite. *Geochimica et Cosmochimica Acta* 60(21):4231–4240. doi:10.1016/S0016-7037(96)00192-5
- Yañez G, Ranero GR, Huene R von, Díaz J (2001) Magnetic anomaly interpretation across a segment of the Southern Central Andes (32-34°S): implications on the role of the Juan Fernández Ridge in the tectonic evolution of the margin during upper Tertiary. *Journal of Geophysical Research* 106:6325-6345
- Ylagan RF, Altaner S, Pozzuoli A (2000) Reaction mechanisms of smectite illitization associated with hydrothermal alteration from Ponza Island, Italy. *Clays and Clay Minerals* 48(6):610–631
- Yoder HS, JR., Eugster HP (1955) Synthetic and natural muscovites. *Geochimica et Cosmochimica Acta* 8:225–280
- York D, Hall CM, Yanase Y, Hanes J, Kenyon W (1981) ⁴⁰Ar/³⁹Ar dating of terrestrial minerals with a continuous laser. *Geophysical Research Letters* 8:1136–1138
- Yrigoyen MR (1975) La edad Cretácica del Grupo Gigante (San Luis), su relación con cuencas circunvecinas. In: *Actas 2, 1° Congreso Geológico Argentino de Paleontología y Biostratigrafía*, pp 9-56
- Zambrano G, Suvires J (2008) Actualización en el límite entre Sierras Pampeanas occidentales y Precordillera Oriental; en la provincia de San Juan. *Revista de la Asociación Geológica Argentina* 63(1):110–116
- Zapata T (1998) Crustal structure of the Andean thrust front at 30° S latitude from shallow and deep seismic reflection profiles, Argentina. *Journal of South American Earth Sciences* 11(2):131–151
- Zapata T, Allmendinger RW (1996) La estructura cortical de la Precordillera Oriental y valle del Bermejo a los 30° de latitud sur. In: *13° Congreso Geológico Argentino, Actas 2*, pp 211–224
- Zeitler P, Herczig A, McDougall I, Honda M (1987) U-Th-He dating of apatite: A potential thermochronometer. *Geochimica et Cosmochimica Acta* 51:2865–2868
- Zhao G, Peacor DR, McDowell SD (1999) "Retrograde diagenesis" of clay minerals in the Precambrian Freda Sandstone, Wisconsin. *Clays and Clay Minerals* 47(2):119–130
- Zoeller M, Brockamp O (1997) 1M- and 2M₁-illites; different minerals and not polytypes; results from single crystal investigations at the transmission electron microscope (TEM). *European Journal of Mineralogy* 9(4):821–827
- Zwingmann H, Yamada K, Tagami T (2010) Timing of brittle deformation within the Nojima fault zone, Japan. *Chemical Geology* 275(3-4):176–185. doi:10.1016/j.chemgeo.2010.05.006

Acknowledgment

Die vorliegende Arbeit entstand unter Betreuung von Prof. Dr. Siegfried Siegesmund und Dr. Klaus Wemmer (GZG, Universität Göttingen). Für die Vergabe dieses interessanten Themas, für Ihr reges Interesse am Fortgang der Arbeit, ihre Hilfsbereitschaft sowie für Ihre Ratschläge und die anregende Diskussionen möchte ich mich hier bedanken.

Das Korreferat übernahm Dr. Georg Grathoff (Universität Greifswald), bei dem ich mich ebenfalls für sein Interesse sowie Anregungen und fachlichen Rat herzlich bedanken möchte.

Meinem Kollegen Stefan Löbens danke ich für die gute Zusammenarbeit über die Jahre.

Finanziell wurde die vorliegende Arbeit durch ein Kurzstipendium des Deutschen Akademischen Austausch Diensts (DAAD), in dessen Rahmen die sechsmonatige Geländearbeiten in Argentinien durchgeführt wurden, unterstützt. Dem DAAD (namentlich Fr. Karin Führ) sei an diese Stelle herzlich gedankt.

Mein besonderer Dank gilt Dr. István Dunkl für sein Engagement, sein Interesse, seine zahllosen Ratschläge sowie für seine ständige Bereitschaft fachliche Fragen zu diskutieren.

Dr. David C. Tanner danke ich für zahlreiche Anregungen sowie die Diskussionen über strukturgeologische Probleme. Dr. Dennis Harries danke ich für die Möglichkeit TEM Untersuchungen an der Universität Bayreuth durchführen zu können, sowie seine Hilfe bei der Auswertung der Daten.

Dr. Stephan Kaufhold und Dr. Reiner Dohrmann danke ich für die IR, CEC und DTA Analysen.

Dra. Monica López de Luchi and Dr. Carlos H. Costa danke ich für Ihre freundliche Unterstützung und Hilfe in Argentinien und auch später. Dr. Emilio Ahumada danke ich für seine tatkräftige Unterstützung in Argentinien. Juan Antonio Palevecito danke ich für die gemeinsame, teils abenteuerliche Zeit im Gelände. Dr. André Steenken danke ich für seine Einführung in die Geologie der Sierras Pampeanas

Mein Dank gilt ebenfalls Günter Tondock und Marie-France Hesse.

Meinen Kollegen am Institut Reinhard Wolff, Annette Süssenberger, Alexander Michler, Manuela Morales Demarco, Wanja Wedekind, Victoria Shushakova und Felix Hüttenrauch danke ich für die teils sehr kurzweilige, gemeinsame Zeit.

Zum Schluss möchte ich mich besonders bei meinen Eltern bedanken, deren Beistand ich mir stets sicher sein konnte und die mir stets jedwede Unterstützung zukommen ließen. Und Heidrun....Danke!

